

AD-A022 116

LONG RANGE MATERIALS RESEARCH

Robert A. Huggins

Stanford University

Prepared for:

Defense Advanced Research Projects Agency

January 1976

DISTRIBUTED BY:

**NTIS**

**National Technical Information Service  
U. S. DEPARTMENT OF COMMERCE**

**BEST  
AVAILABLE COPY**



ADA022116

SEMI-ANNUAL TECHNICAL REPORT

LONG RANGE MATERIALS RESEARCH

Sponsored by

Defense Advanced Research Projects Agency

ARPA Order No. 3018



January 1976

The views and conclusions contained in this document are those of the authors and should not be interpreted as necessarily representing the official policies, either expressed or implied, of the Defense Advanced Research Projects Agency or the U. S. Government.

REPRODUCED BY  
NATIONAL TECHNICAL  
INFORMATION SERVICE  
U. S. DEPARTMENT OF COMMERCE  
SPRINGFIELD, VA. 22161

CENTER FOR MATERIALS RESEARCH

STANFORD UNIVERSITY • STANFORD, CALIFORNIA

## SEMI-ANNUAL TECHNICAL REPORT

Long Range Materials Research

Sponsored by  
Defense Advanced Research Projects Agency  
ARPA Order No. 3018

Program Code Number: 5D10

Contractor: Leland Stanford, Jr. University

Effective Date of Contract: June 1, 1975

Contract Expiration Date: June 30, 1976

Amount of Contract: \$125,000

Contract Number: N00014-75-C-1171

Principal Investigator: Robert A. Huggins  
Phone: (415) 497-4118

Short Title: Long Range Materials Research

January 1976

The views and conclusions contained in this document are those of the authors and should not be interpreted as necessarily representing the official policies, either expressed or implied, of the Defense Advanced Research Projects Agency or the U. S. Government.

Center for Materials Research  
Stanford University  
Stanford, California 94305  
(415) 497-4118

ACCESSION NO.
NTIS
DDC
UNANNOUNCED
JUSTIFIED
<i>Letter on file</i>
BY
DIST
D.H.
A

## TABLE OF CONTENTS

	Page
I. GENERAL INFORMATION	1
II. DETECTION OF X-RADIATION	3
C. W. Bates, Jr.	
A. <u>Introduction</u>	4
B. <u>EPR Studies</u>	4
C. <u>Optical Measurements Down to Liquid Helium Temperatures</u>	5
III. SUPERPLASTICITY AND WARM WORKING OF METALS AND ALLOYS	6
O. D. Sherby	
A. <u>Introduction and Summary</u>	7
B. <u>Superplasticity of Eutectoid Steel and an Iron-0.8% Alloy</u>	8
E. S. Kayali	
C. <u>Powder Consolidation under Superplastic Conditions</u>	20
R. D. Caligiuri	
D. <u>Superplastic Hot Pressing of White Cast Iron</u>	25
R. C. Caligiuri, R. T. Whalen, O. D. Sherby	
IV. SYNTHESIS OF NEW TYPES OF CATALYST MATERIALS	37
J. P. Collman, M. Boudart, and W. A. Little	
A. <u>Synthesis of New Types of Catalyst Materials</u>	38
J. P. Collman	
1. Introduction	38
2. Chelating Silica-Bonded Ligands	39
K. Neuberg	
3. Conducting Catalyst Supports	52
M. Marrocco	

4.	Face-to-Face Porphyrins	59
	T. Halbert and B. Tovrog	
B.	<u>Preparation of Highly Dispersed Palladium Samples</u>	84
	<u>Supported on SiO<sub>2</sub></u>	
	M. Boudart	
C.	<u>Preparation of Fine Particles</u>	107
	J. W. Brill and W. A. Little	
V.	DEVELOPMENT OF ELEVATED TEMPERATURES ELECTROCRYSTALLIZATION	108
	TECHNIQUES	
	R. S. Feigelson and R. A. Huggins	
A.	<u>Introduction</u>	109
B.	<u>New Material Studies</u>	111
	I. V. Zubeck and P. A. Pettit	
C.	<u>Continuous Growth</u>	116
	R. C. DeMattei	
D.	<u>Electrodeposition of Niobium Alloy Superconductors from</u>	120
	<u>Molten Fluorides</u>	
	U. Cohen	

## I. GENERAL INTRODUCTION

This semi-annual technical report on the research program entitled "Long Range Materials Research", covers the time June 1 through December 31, 1975. This program is composed of four separate programs as follows:

1. Detection of X-Ray Radiation
2. Superplasticity and Warm Working of Metals and Alloys
3. Synthesis of New Types of Catalyst Materials
4. Development of Elevated Temperature Electrocrystallization Techniques

Progress in each of the subareas during this report period will be described separately in the succeeding sections of this report.

**II. DETECTION OF X-RADIATION**

**C. W. Bates, Jr.**

**Associate Professor of Materials Science  
and Engineering  
and Electrical Engineering**

### A. Introduction

The work during this period has been devoted to electron paramagnetic resonance studies of ultrapure CsI and CsI(Na) and to extending the measurement of the optical properties of these materials down to liquid helium temperatures.

### B. EPR Studies

All measurements were made on a Varian Associates EPR Spectrometer, E-112 E-Line Century Series. These studies were undertaken to throw additional light on the temperature cycling luminescence observed in ultrapure CsI. It appears that there is a strong correlation between the temperature cycling luminescence and the appearance of epr signals in these pure specimens. At room temperature before temperature cycling there is no epr signal. After temperature cycling to liquid nitrogen and back to room temperature, an epr signal which is observed at liquid nitrogen temperature is retained when the sample is warmed back to room temperature. The epr signal has two components. One component is a single line with a g-value  $< 2$ , presumably due to an F-center. The tentative assignment to an F-center is based on the fact that it is isotropic with a g-value very close to that of the F-center. The second component appears to be a hole-like or V-center, based on its g-value being  $> 2$  and the fact that it is anisotropic. The crystals used in these experiments were single crystals with two faces oriented along the (100) axis. It was not possible to ascribe this hole-center to  $V_k$ -centers as the structure was fairly complex. After annealing at about 200°C for 48 hours both signals disappeared at room temperature, so one can attribute them to lattice deformations of the host CsI. As a similar phenomena occurred during our luminescent studies, it suggests that these centers are connected with the room temperature - after cooling luminescence (RTAC) observed in this system. The picture that is beginning to emerge is that in CsI cooling to liquid nitrogen produces traps for both electrons and holes which do not release them upon warming back to room temperature and that these centers are responsible for the luminescence observed at room temperature after cooling.

C. Optical Measurements Down to Liquid Helium Temperatures

We have extended our measurements of optical absorption, excitation and emission spectral down to liquid helium temperatures. Excitation bands which were obscured because they were located in regions of high absorption have all been resolved. The shift of the absorption edge is linear with temperature from room to liquid helium temperatures. The interpretation of all this data will be included in our final report.

**III. SUPERPLASTICITY AND WARM WORKING  
OF METALS AND ALLOYS**

**O. D. Sherby  
Professor of Materials Science  
and Engineering**

#### A. Introduction and Summary

Our research has centered on plain carbon steels containing 0.8 to 2.3% carbon (twelve to thirty-five volume percent cementite respectively). Steels above 1.0%C and below 2.3%C have rarely, if ever, been considered for broad industrial applications. During the past two years we have developed various thermal mechanical processing procedures for developing particulate composites of cementite in ferrite containing ferrite grains finer than one micron in size and cementite particles finer than 0.1 $\mu$ m. We were able to show that ultrahigh carbon steels can be made superplastic (over 700% elongation has been achieved). Furthermore, they can be made strong and ductile at room temperature. These results suggest exciting possibilities in the application of inexpensive steels for many new structural applications.

Eutectoid composition steels contain twelve percent cementite. Such steels have not been made truly superplastic to date. In the past six months Mr. Sabri Kayali has concentrated in trying to make an iron-carbon alloy and a steel of eutectoid composition superplastic. By a cold working and recrystallization treatment it was possible to obtain fine ferrite grains in the order of one micron. Furthermore, these specially processed materials contained a large fraction of high angle boundaries. Mechanical tests in the temperature range 600-700°C revealed these materials to be superplastic, with the strain rate sensitivity exponent equal to 0.5, and elongations as high as 400% (on thin samples) were obtained. These results are described in part A of this report.

We have initiated a study on the consolidation of powders utilizing the superplastic characteristics associated with fine structures. This subject is the basis of a thesis by Robert Caligiuri and is described in part C of this report. A few critical experiments were initiated to determine if hot pressing could be accelerated by the presence of a fine structure in ultrahigh carbon iron powders. The results obtained were very encouraging and this aspect of our work is described in part D of this report.

## B. Superplasticity of Eutectoid Steel and an Iron - 0.8% Alloy

E. S. Kayali

### ABSTRACT

Superplasticity of a eutectoid steel and an iron - 0.8%C alloy was investigated. These materials were spheroidized and made fine grained by several thermal-mechanical treatments. Fine spheroidized structures of cementite in a ferrite matrix containing ferrite grains and cementite particles finer than one micron were obtained by warm working, but the grain boundaries in this microstructure were a mixture of low and high angle boundaries. The results of elevated temperature strain rate-stress and elongation tests showed that the maximum strain rate sensitivity exponent ( $m$ ) is about 0.3 for both materials and the maximum elongations are about 150% and 200% for the Fe-0.8%C alloy and the eutectoid composition steel respectively. Fine spheroidized structures containing only high angle boundaries were also obtained by a cold rolling and recrystallization process in both materials; the results of elevated temperature tests showed that higher strain rate sensitivity exponents ( $m \approx 0.5$ ) and higher elongations (250-400%) are achievable in recrystallized structures than in warm rolled structures. These results indicate the importance of the type of grain boundaries in fine grained equiaxed structures on superplastic deformation.

Metallographic studies on these materials before and after superplastic deformation indicated that grain growth occurred during high temperature deformation. The grain growth rate was higher for the Fe-0.8%C alloy than the eutectoid composition steel. This result indicates the importance of impurities (the principal impurities in steel are Si and Mn) in controlling grain size and retarding grain growth.

### INTRODUCTION

Many investigations have been made on the phenomenon of superplasticity in recent years (Johnson 1970; Davies, Edington, Cutler and Padmonabhan 1970; Nicholson 1972; Alden 1975). Certain alloys are known to exhibit extreme elongations when extended at high temperature. The large elongation values observed have been associated with a high strain rate sensitivity exponent ( $m$ ) expressed in the phenomenological equation  $\sigma = K\dot{\epsilon}^m$ , where  $\sigma$  is the flow stress,  $K$  is a material constant for a given temperature,  $\dot{\epsilon}$  is the strain rate. Studies

on superplastic alloys have revealed that certain prerequisites are generally required for superplastic behavior. These are: fine stable grains with equiaxed structure\*, and test temperature greater than half the absolute melting temperature.

---

\* It is generally believed that fine grains permit extensive plastic flow by grain boundary sliding, a mechanism which apparently dominates superplastic deformation. (Geckinl: 1973; Dingley 1970)

---

Fine grained structures generally cannot be maintained in single phase alloys at high temperatures, and two phase materials are preferred for attaining superplasticity. The presence of a second phase stabilizes the fine grain structure and prevents rapid grain growth. An additional requirement for superplasticity is that the strength of the matrix and second phase should be nearly the same at the temperature where superplastic deformation occurs.

Superplasticity is usually observed in eutectic or eutectoid alloys, because these alloys can be spheroidized and made fine grained by appropriate thermal-mechanical processing. Thus, superplastic behavior might be expected in iron-carbon alloys of eutectoid composition.

Many investigations have been made on superplasticity associated with the allotropic transformation in iron and the eutectoid transformation in steel (Sherby and Goldberg 1961; Clinard and Sherby 1964; Oelschlagel and Weiss 1966). Some investigations have also been made on superplasticity in several steels in the two phase region (Schadler 1968; Morrison 1968; Marder 1969; and Sherby, Walser, Young and Cady 1975). Some investigators (Marder 1969; Yoder and Weiss 1972; Kasir and Rosen 1969; Young, Bly and Sherby 1972) also studied superplasticity of eutectoid steels and found only limited success. Marder studied Fe-C alloys in the composition range from 0.2 to 1.0% C and observed a maximum strain rate sensitivity exponent ( $m = 0.35$ ) and a maximum elongation (98%) at the eutectoid composition. Yoder and Weiss found higher  $m$  values ( $m = 0.42$ ) and higher elongations (133%) in their eutectoid composition steel than did Marder. We believe the difference is primarily due to the background impurity content of the steels studied. Marder's iron alloys only contained carbon as an additive whereas Yoder and Weiss worked with conventional eutectoid composition steel (0.45%Mn, 0.12%Si).

The purpose of this investigation on the eutectoid composition steel and the Fe-0.8% C alloys are to examine: a) the effects of temperature, strain rate

and grain size on the tensile ductility of these materials; b) the effect of the thermal-mechanical treatment (TMT) used to produce fine grained structure on these materials [i.e., the effect of TMT on grain shape, nature of grain boundaries and texture (structural anisotropy)]; c) the influence of manganese and silicon, the principal impurities in steel, on superplastic behavior; and d) grain growth behavior in these materials during high temperature deformation and its effect on the test results.

#### MATERIALS AND EXPERIMENTAL PROCEDURES

A near eutectoid composition plain carbon steel and an Fe-0.8C alloy have been used in this investigation and the chemical compositions are given in Table 1.

Table 1

Chemical Compositions of Materials Tested (Wt pct.)

<u>Material</u>	<u>C</u>	<u>Mn</u>	<u>Si</u>	<u>Mo</u>	<u>Cu</u>	<u>Cr</u>	<u>Ni</u>	<u>S</u>	<u>P</u>	<u>Fe</u>
Eutectoid steel	0.75	0.75	0.24	<0.1	0.56	0.06	0.43	0.01	0.012	bal.
Fe-0.8%C alloy	0.82	<0.01	<0.01	<0.01	<0.05	0.01	0.02	--	--	bal.

The eutectoid steel was received in the form of a 1 cm thick plate and the Fe-0.8%C alloy was received in the form of a 2.5 cm thick plate. Both plates exhibited microstructures consisting of fine pearlite.

Two different thermal-mechanical processing techniques were developed to obtain fine grained spheroidized structures in these materials. One of the methods is by isothermal rolling at warm temperatures; the other method is by cold rolling and recrystallization.

The eutectoid composition steel was warm rolled to a true strain of  $\epsilon = -2.76$  at 500°C and the Fe-0.8%C alloy was warm rolled to a true strain of  $\epsilon = -2.0$  at 550°C. Fine spheroidized structures were obtained with this warm rolling procedure for both materials.

Another warm-rolling process was performed on the Fe-0.8%C alloy to obtain a fine spheroidized structure. First the plate (the dimensions were 2.5 cm x 2.5 cm x 7.5 cm) was homogenized at 1150°C for one half hour, then rolled continuously during cooling. True strain of  $\epsilon = -0.81$  was achieved as the original casting cooled to about 600°C. With further isothermal rolling at 575°C to a true strain of  $\epsilon = -1.52$  a spheroidized structure was obtained. The microstructure of the alloy rolled with this thermal-mechanical process, however, revealed elongated grains along the rolling

direction.

Fine recrystallized structures were obtained by a severe cold rolling and recrystallization heat treatment process. The Fe-0.8%C alloy, originally warm rolled at 550°C to  $\epsilon = -2.0$ , was annealed at 700°C for 10 minutes. The purpose of this treatment was to reduce the dislocation substructure thus permitting large amounts of cold working without cracking. After this heat treatment, the fine spheroidized Fe-0.8%C alloy was cold rolled at room temperature to various amounts (50%, 65%, 75%, 85% reduction in thickness), then fully recrystallized at 500°C for 150 hrs. Spheroidized and recrystallized fine grained structures (grain sizes from 0.5 $\mu\text{m}$  to 2.5 $\mu\text{m}$ ) were produced with this thermal-mechanical process. A similar procedure was established for the eutectoid steel. Thus, the 1 cm thick eutectoid composition plate was annealed at 700°C for 15 minutes (originally in pearlitic structure) then cold rolled at room temperature to 75% reduction in thickness. The cold rolled plate was annealed at 700°C for 1 hr. to obtain a spheroidized and recrystallized structure. The structure was not fully spheroidized after this heat treatment. Therefore further cold rolling (70% reduction) followed by recrystallization (500°C for 125 hours) was performed and a very fine structure was obtained (about 0.5 $\mu\text{m}$  ferrite grains and about 0.2 $\mu\text{m}$  cementite particles).

Longitudinal tensile specimens were machined from the rolled plates with different gage lengths. One inch gage length specimens were used in change-in-strain rate tests and 0.5 inch or 0.25 inch gage length specimens were used in ductility tests. All specimens were flat and had different thicknesses.

Elevated temperature tensile tests were performed on an Instron machine with constant cross-head speed. The tests were carried out over a wide range of strain rates (from  $10^{-5} \text{ sec}^{-1}$  to  $10^{-2} \text{ sec}^{-1}$ ) and temperatures (550, 600, 650 and 700°C). A dual-elliptical reflector infrared furnace was used with an electronic temperature controller and the specimen was contained in an inert or reducing atmosphere within a quartz tube during testing. Good temperature distribution along the sample length was achieved using shields on the quartz tube. The temperature gradient was within  $\pm 0.5\%$  of the desired temperature over a length of more than 3 inches for the duration of the test.

Two different testing schemes were developed i) change-in-strain-rate tests (or differential cross-head speed tests) to establish the strain rate-stress relations and to determine the strain-rate sensitivity exponent ( $m$ ) over a wide range of strain rates. ii) Constant cross-head speed (decreasing true strain rate) tests to fracture

to measure the tensile ductilities.

Stress relaxation tests were also performed during change-in-strain rate tests and constant cross-head speed tests. Strain rate sensitivity exponent ( $m$ ) values were obtained from change-in-strain rate tests and stress relaxation tests.

Because of the difficulty of resolving very fine structures with optical microscopy, electron microscopy was used. After polishing and etching with 2 pct. nital, the surface was examined by replication using acetyl cellulose. The plastic replica was shadowed with chromium at 35-45° and backed with a carbon layer. Thin foils for transmission electron microscopy were also prepared from a surface parallel to the rolling direction by hand polishing and chemical thinning in a solution of 5 pct. HF, 15 pct. H<sub>2</sub>O and 80% H<sub>2</sub>O<sub>2</sub> to 0.015 cm. The specimens were then electro-thinned in a solution of 15 parts Na<sub>2</sub>CrO<sub>4</sub>, 7.5 parts CrO<sub>3</sub> and 77.5 parts of glacial acetic acid. The foils were examined at 100 kv in a Philips 200 electron microscope. Grain size was measured using a line intercept method from electron-micrographs.

#### EXPERIMENTAL RESULTS AND DISCUSSION:

##### The results of tensile tests and change-in-strain rate tests

The effective strain rate decreases with increasing strain during constant cross-head speed testing. Therefore, constant strain rate (CSR) true stress/true strain curves were calculated from constant cross-head speed (CCHS) tests using the known strain rate sensitivity exponent. Such data are plotted in Figure 1 where one can observe the differences in deformation behavior when comparisons are made under these two conditions of testing. Figure 1 shows the true stress/true strain curves for the warm-rolled eutectoid steel and the warm-rolled Fe-0.8%C alloy for different cross-head speeds and temperatures. The true stress/true strain curves reveal that the flow stress does not reach a steady state value but is a function of the strain at a given cross-head speed and temperature. Strain hardening is evident at all strain rates up to about 0.2 true strain. Grain growth occurred during high temperature deformation of the materials studied. It is believed that this grain growth leads to strain hardening. This strain hardening, of course, has nothing to do with the accumulation of dislocations in the microstructure; such a process is specifically absent during superplastic flow. These ideas will be described in greater detail later.

The influence of strain rate on the flow stress was obtained from change-in-strain rate tests. There exists considerable controversy on the usefulness and interpretation of change-in-strain rate tests in the literature (Rai and Grant 1975) especially if

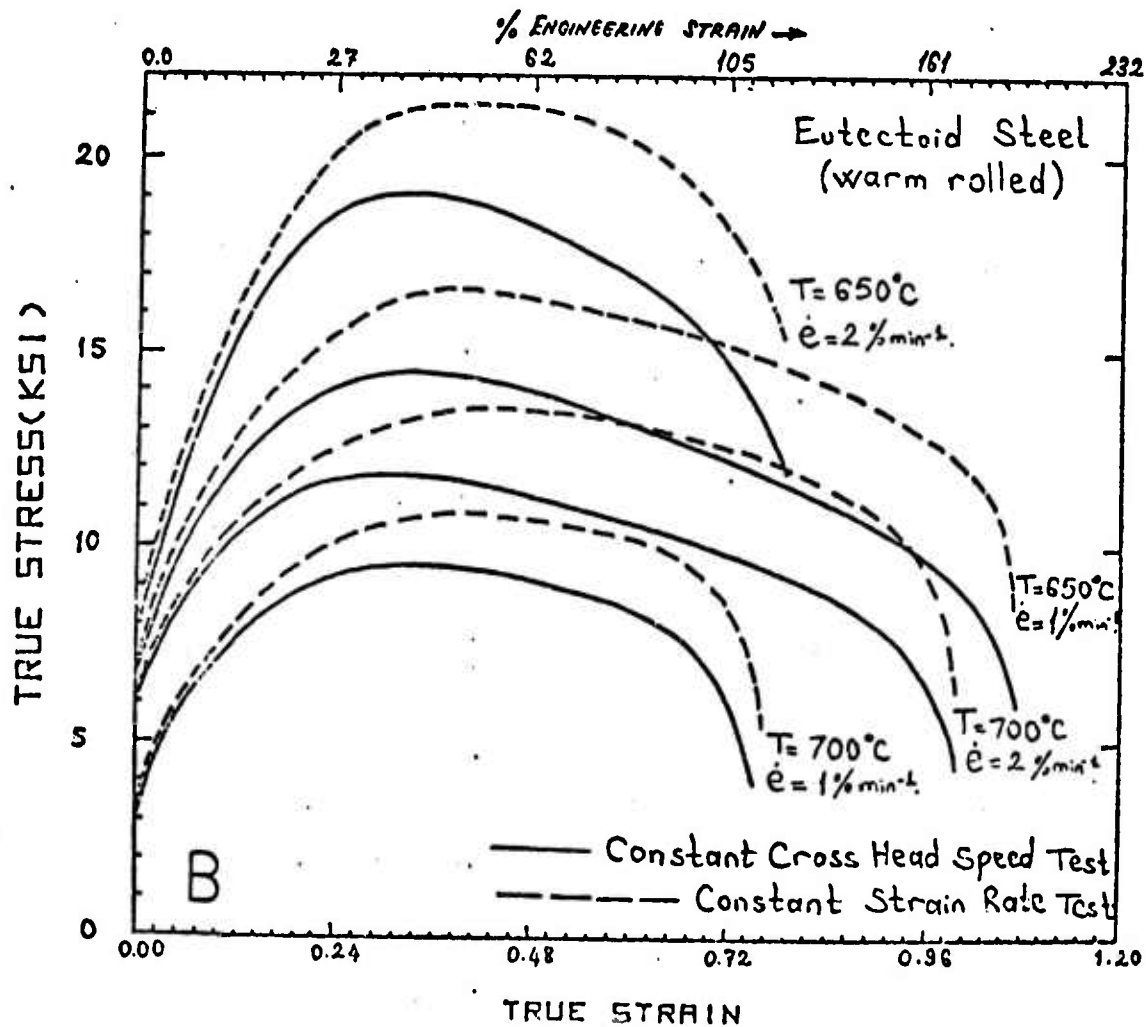
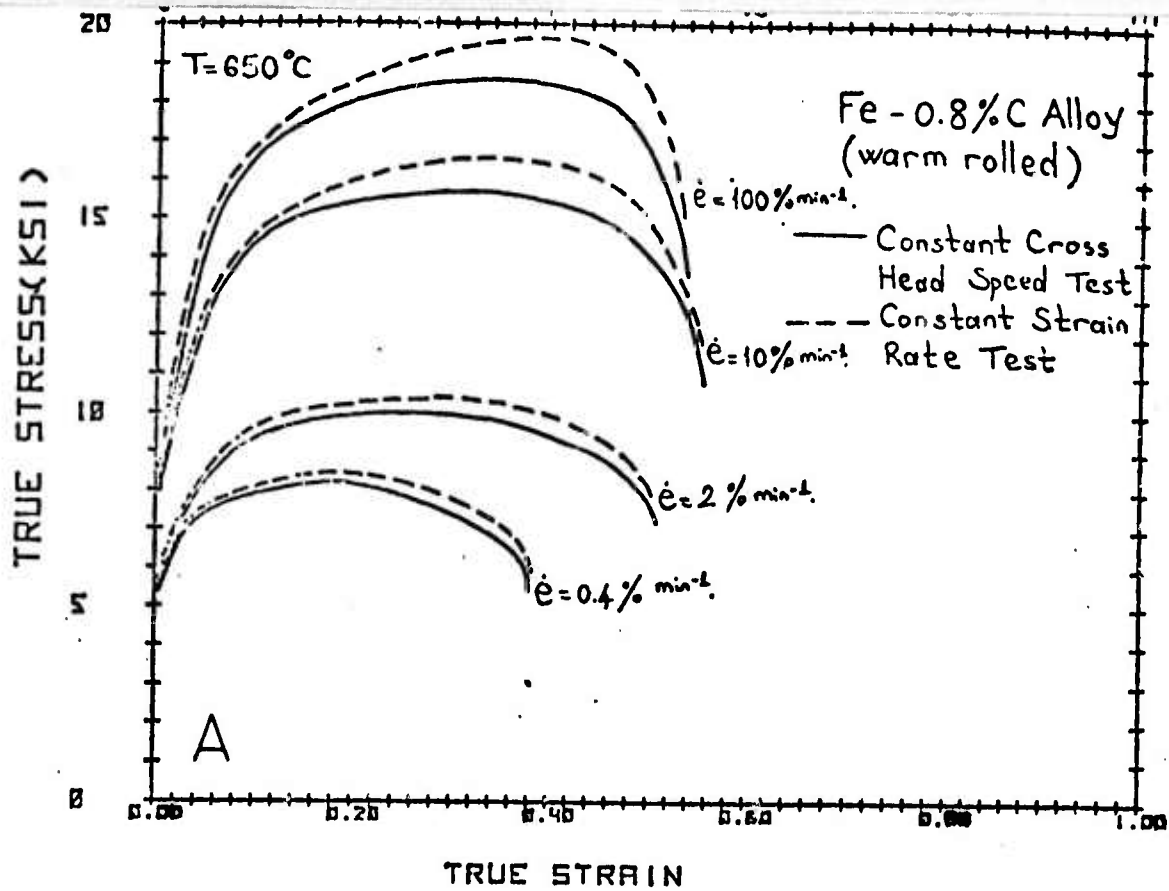


Figure 1. True stress-true strain curves for various cross-head speeds and temperatures. (A) Warm-rolled Fe-0.8%C alloy, and (B) Warm rolled eutectoid steel.

they were measured in the early stages of deformation where the structure is changing rapidly (i.e. grain growth). The elevated temperature tension test true stress/true strain curves show that maximum flow stresses are not achieved until about 20-30% deformation. These considerations led to the development of a testing scheme for change-in-strain rate testing. After reaching the test temperature, a specimen is pulled at a low strain rate to about 20-30% deformation to establish a more or less constant structure. Then the cross-head speed is changed repeatedly with only a small increment of strain at each change. Figure 2 represents a typical curve for this type of change-in-strain rate test and a plot of the log strain rate-log stress curve obtained from Figure 2 is shown in Figure 3. As can be seen the strain rate sensitivity exponent ( $m$ ) values are continuously increasing with decreasing strain rate, approach  $m = 0.5$  at the lowest strain rates used (it is often assumed that true superplasticity in fine structures is achieved when  $m = 0.5$ )

The effect of temperature on the strain rate-stress relation.

The effect of increased temperature is to increase the strain rate for optimum superplasticity. An example is given in Figure 4 which represents the true strain rate-true stress relation of warm rolled eutectoid steel (initial grain size  $\approx 0.5\mu\text{m}$ ) at various temperatures (550, 600, 650 and 700°C). High strain rate sensitivity was clearly evident at low strain rates. All the test temperatures were near or above half the absolute melting temperature, [at 700°C,  $T/T_m = 0.54$ ; at 650°C,  $T/T_m = 0.52$ ; at 600°C  $T/T_m = 0.48$ ; at 550°C,  $T/T_m = 0.46$ ; where  $T_m = 1530^\circ\text{C}$ ]. Figure 5 is a plot of the strain rate sensitivity exponent, as a function of strain rate for the various test temperatures. It appears that  $m$  increases with increasing temperature and the highest  $m$  values for all strain rates are obtained at 700°C. It should be noted that the value of  $m$  for this material never exceeds 0.33 whereas the ideal fine-structure superplastic material exhibits  $m = 0.5$ . Later, it will be shown that the thermal mechanical treatment given this material leads to low angle grain boundaries which we believe inhibits superplastic flow. Nevertheless, the data shown in Figure 5 indicates that higher  $m$  values can be expected at 650-700°C than at 550-600°C. For this reason, subsequent tests on the materials investigated were generally restricted to 650 and 700°C.

The effect of thermal-mechanical processing used to produce fine grain structures on the strain rate-stress relation.

It is generally believed that superplasticity is enhanced by the presence of fine

### CHANGE IN CROSS HEAD SPEED TEST

MATERIAL: Fe-0.8% C ALLOY (G.S = 2.2  $\mu$ m)

TEST TEMP: 700 °C

Cross Head Speeds:

- 1 = 0.17"/min.
- 2 = 0.002"/min.
- 3 = 0.005"/min.
- 4 = 0.01"/min.
- 5 = 0.02"/min.
- 6 = 0.05"/min.
- 7 = 0.1"/min.
- 8 = 0.2"/min.
- 9 = 1"/min.

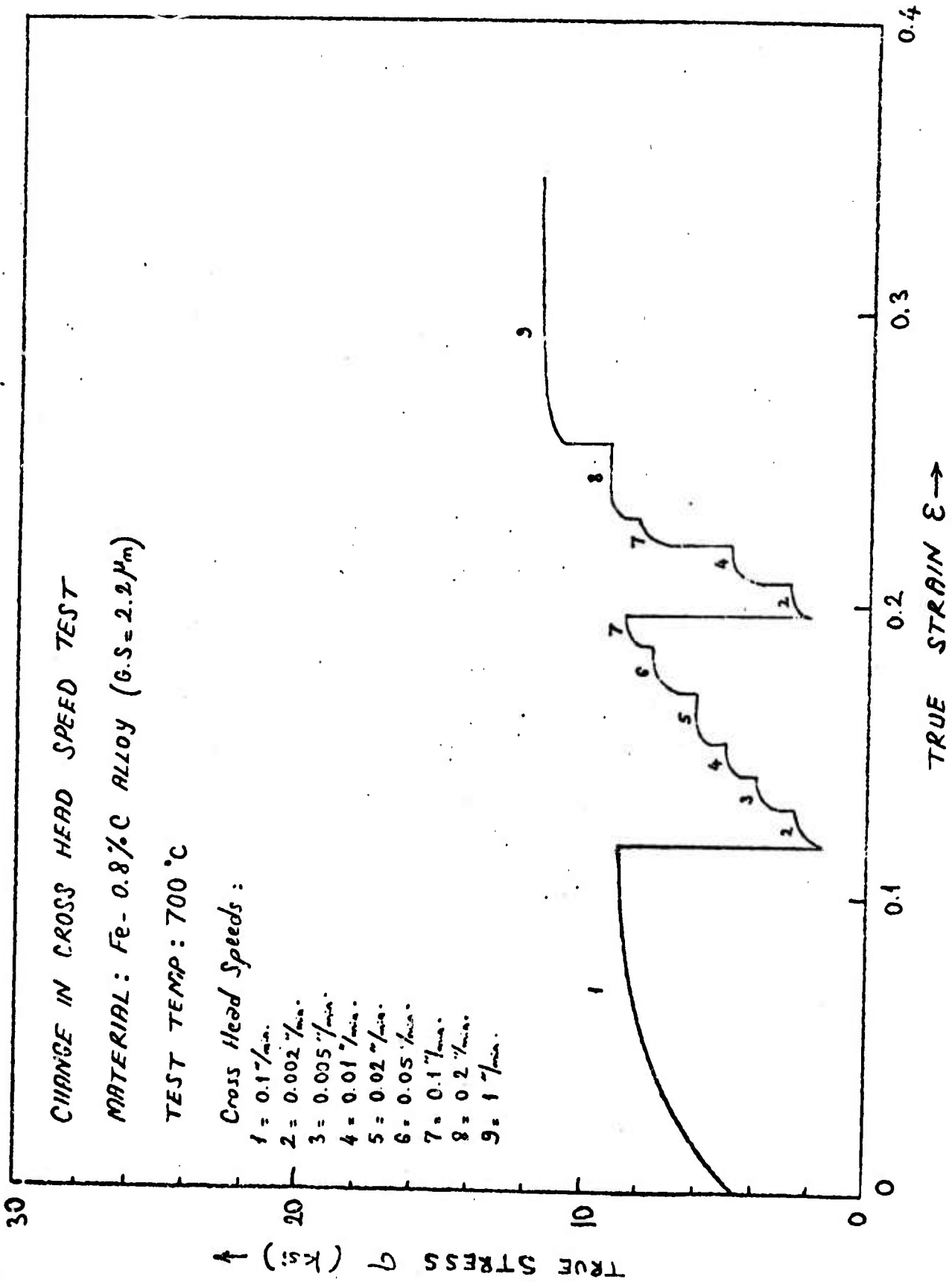


Figure 2. Change-in-strain-rate tests performed on an Fe-0.8% C alloy in tension at 700°C. Such tests on a single sample permit plotting the flow stress as a function of the strain rate as shown in Figure 3.

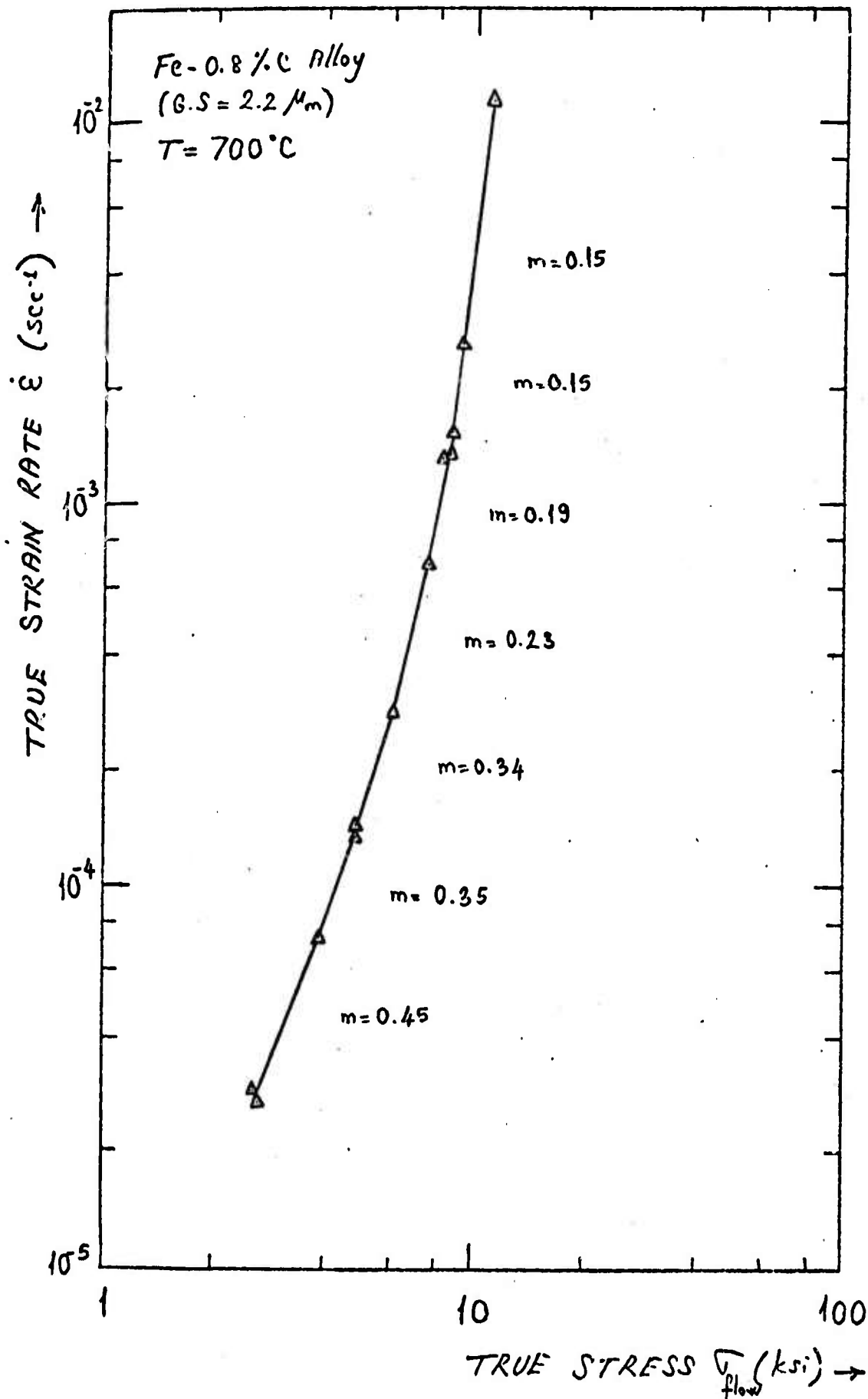


Figure 3. Flow stress-strain rate relationship for an Fe-0.8% C alloy tested at 700°C. Strain rate sensitivity exponent (m) values are continuously increasing with decreasing strain rate and approach  $m = 0.5$  (ideal fine structure superplasticity) at the lowest strain rates used. This material was prepared by a cold working and recrystallization process.

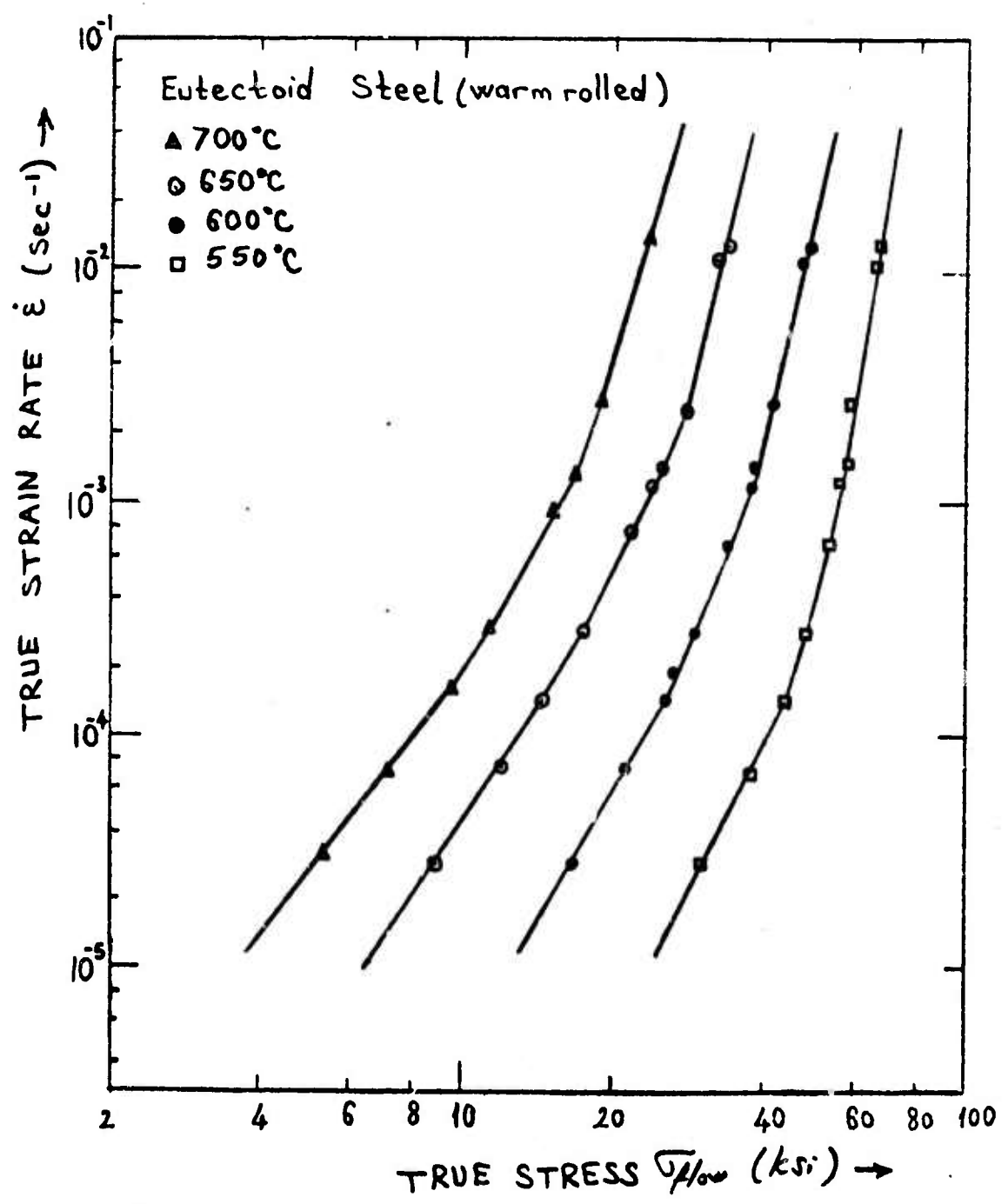


Figure 4. Flow stress-strain rate relationship for a eutectoid steel at various temperatures. The material was prepared in a fine spheroidized state by warm working.

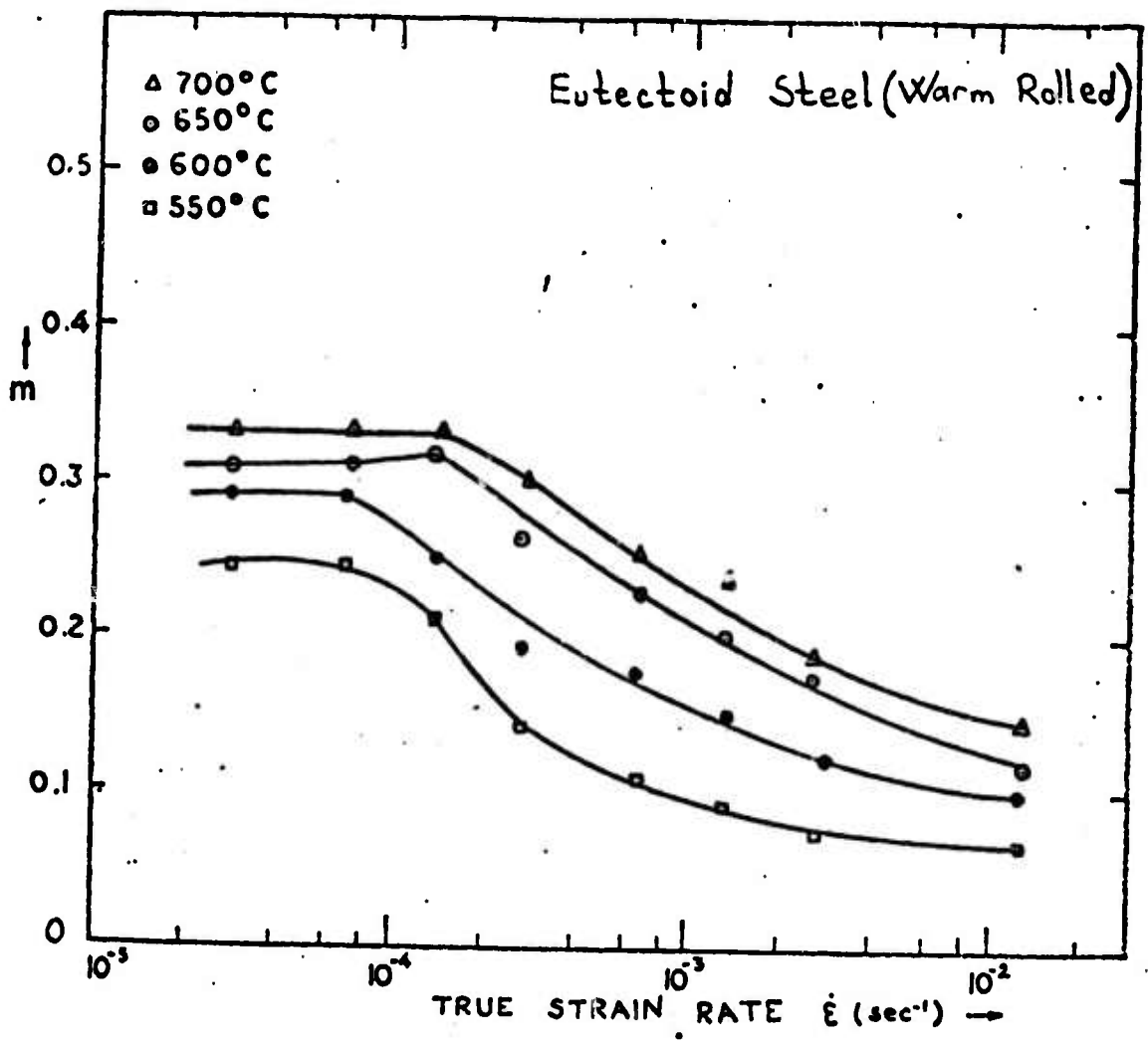


Figure 5. Dependence of strain rate sensitivity exponent (m) values on strain rate ( $\dot{\epsilon}$ ), for various test temperatures in a eutectoid steel prepared by warm working.

equiaxed grains in a non-textured matrix. There are several methods which have been used to obtain fine-grained structures. In this study, warm rolling and cold rolling and recrystallization processes have been used to obtain fine grained microstructures on both materials. The microstructures of the eutectoid steel are shown as warm rolled (A) and as cold rolled then recrystallized (B) in Figure 6 and the high temperature strain rate-stress relation for these two processing conditions are given in Figure 7. The microstructures of the Fe-0.8%C alloy as warm rolled (A) and cold rolled then recrystallized (B) are shown in Figure 8 and the strain rate-stress relation for these two processing conditions are given in Figure 9.

Transmission electron microscopy studies revealed that warm rolled structures contain fine spheroidized cementite particles and a high density of dislocations in the ferrite matrix (Figures 6A and 8A). Transmission diffraction studies also revealed that the ferrite grain boundaries were a mixture of high and low angle boundaries in the warm rolled structures. On the other hand, the microstructure of the cold rolled and recrystallized structures of the eutectoid steel and the Fe-0.8%C alloy contains fine spheroidized particles and dislocation free fine equiaxed ferrite grains (Figures 6B and 8B). These fully recrystallized structures contain only high angle boundaries (i.e. no subgrain boundaries were observed).

It is very clear from Figures 7 and 9 that cold rolled and recrystallized structures of the eutectoid steel and the Fe-0.8%C alloy are more rate sensitive ( $m = 0.5$ ) than warm rolled structures ( $m = 0.3$ ) at low strain rates. Tests taken to fracture also showed that higher elongations (250-400%) are achievable in cold rolled and recrystallized structures than in warm rolled structures (150-200%). These results can be related to the importance of the type of grain boundaries on superplastic deformation. Since grain boundary shearing appears to dominate the deformation process during superplastic flow, the nature of the grain boundary would be an important consideration. In studies on bicrystals, the ease of grain boundary sliding has been shown to increase as the misorientation of the boundary increases (Rhines, Bond and Kissel 1956). These observations fit in well with the results of this study. Thus, the high strain rate sensitivity exponent observed for the recrystallized steels can be attributed to the presence of high angle boundaries which would contribute to a large amount of grain boundary shearing. On the other hand, the warm rolled steels exhibit only moderate values for the strain-rate



A

1 μm



B

Figure 6. The microstructure of a eutectoid steel, (A) as warm rolled at 500°C to a true strain of  $\epsilon = 2.76$ , and (B) cold rolled then recrystallized.

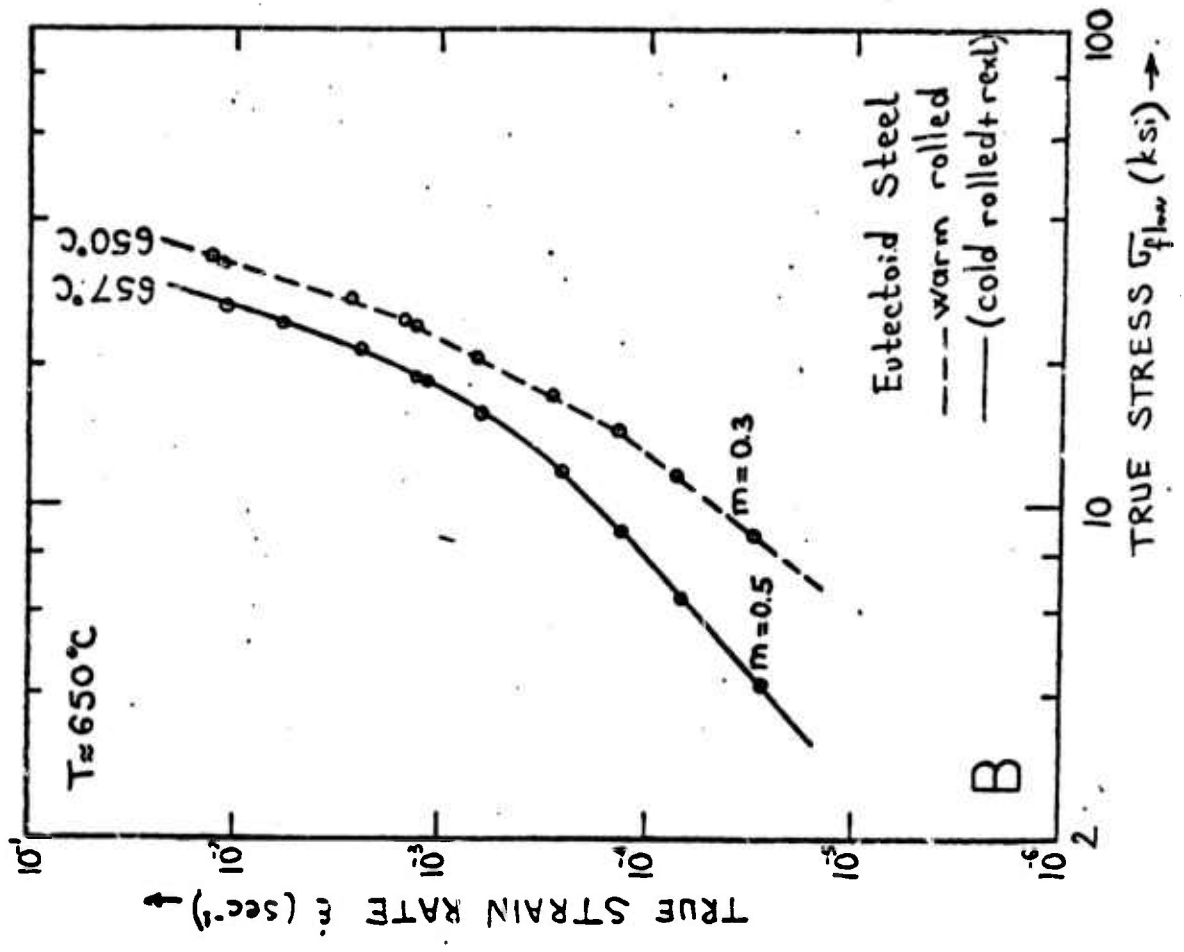
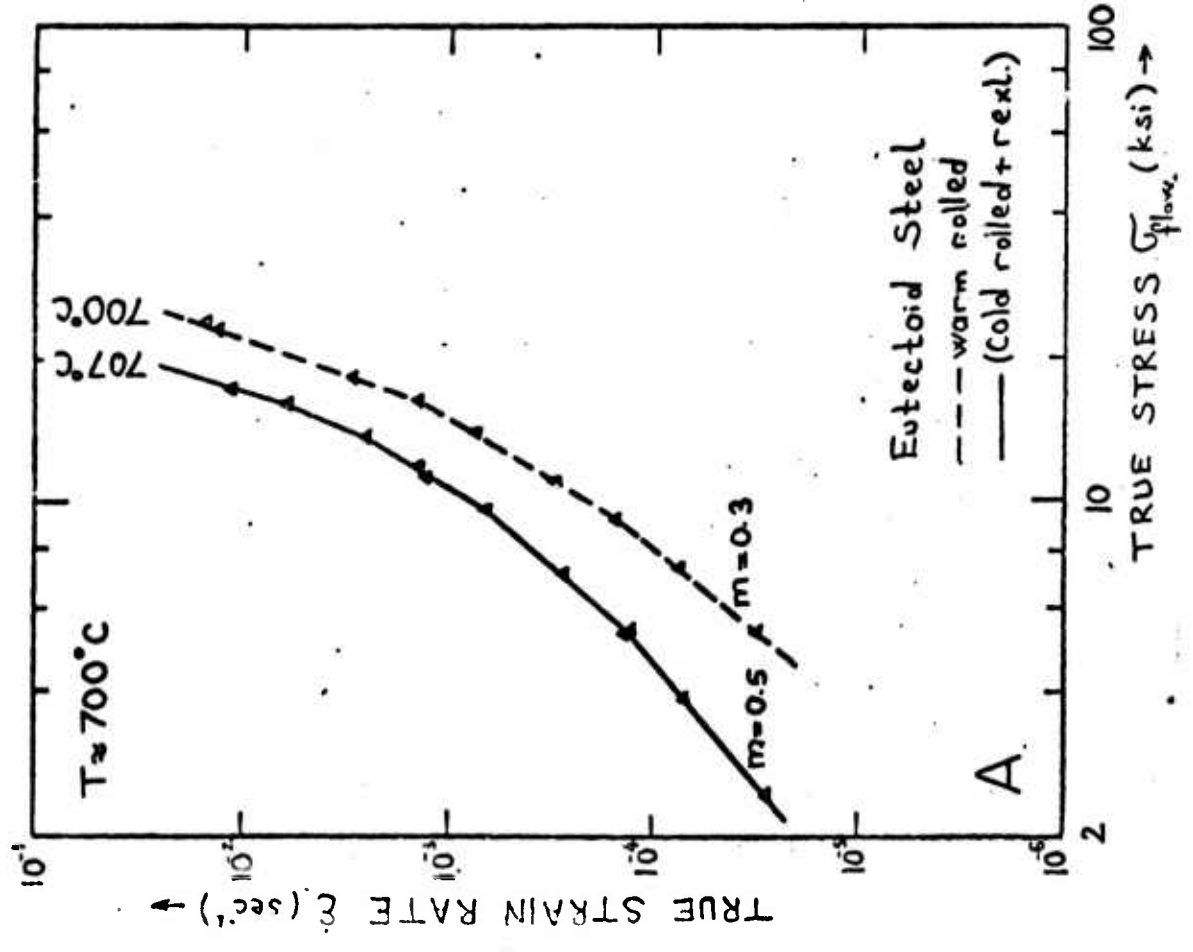


Figure 7. Flow stress-strain rate relationship for a eutectoid steel as warm rolled and as cold rolled then recrystallized. (A) at  $\approx 700^\circ\text{C}$  and (B) at  $\approx 650^\circ\text{C}$ .



A

1 μm



B

2 μm

Figure 8. The microstructure of an Fe-0.8%C alloy, (A) as warm rolled at 550°C to a true strain of  $\epsilon = 2.0$  and (B) cold rolled then recrystallized.

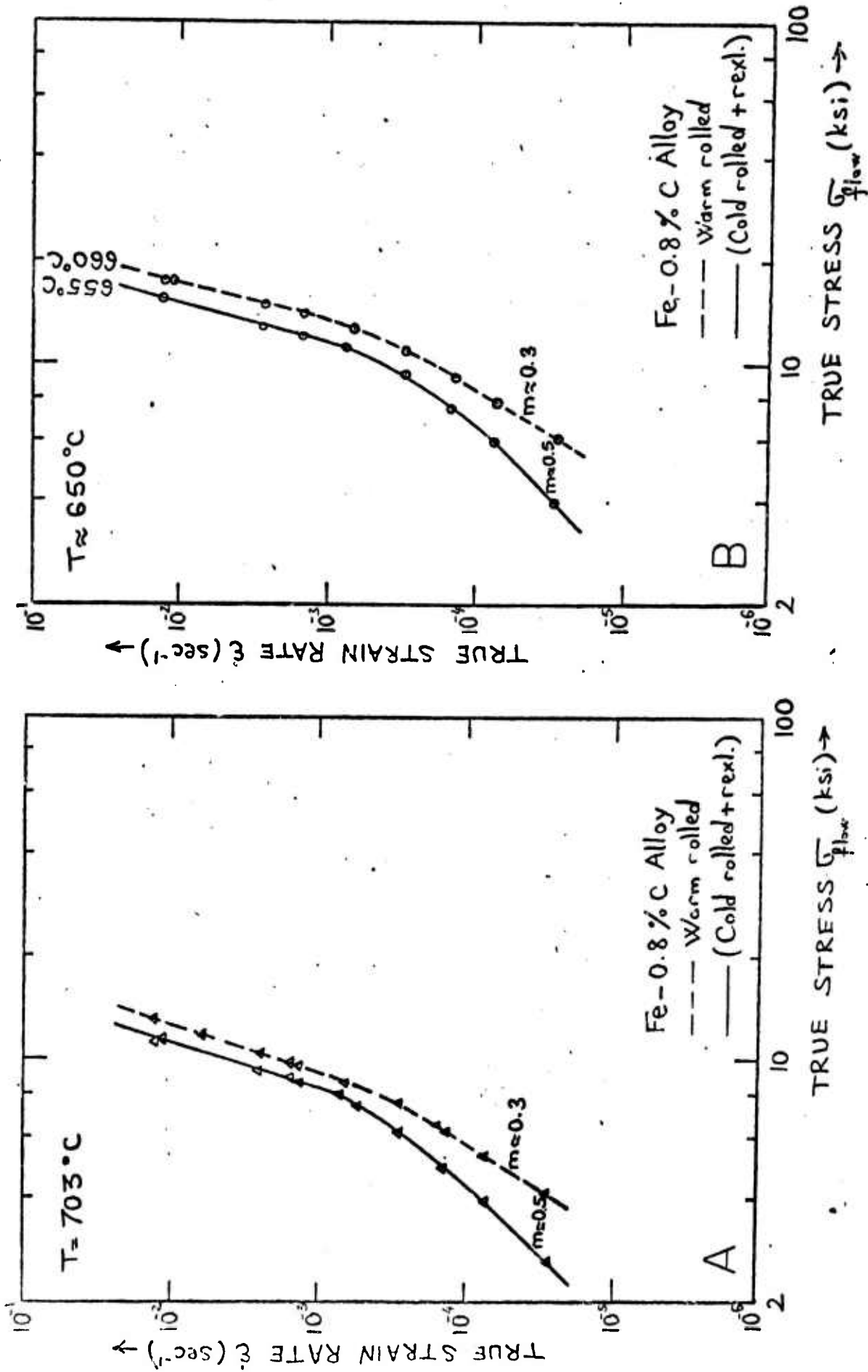


Figure 9. Flow stress-strain rate relationship for an Fe-0.8% C alloy as warm rolled and as cold rolled then recrystallized. (A) at 703°C and (B) at  $\approx$  650°C.

sensitivity exponent, which can be attributed to the presence of a large fraction of low angle boundaries and therefore a correspondingly small contribution to grain boundary shearing. It is believed our results are the first to show that the nature of the grain boundary is an important variable in superplastic flow.

Another difference between warm rolled structures and recrystallized structures of the materials used in this study is that warm rolled structures were equiaxed but banded\* (i.e. coarse and fine structures were obtained along the rolling direction). Such structural anisotropy was obvious for all warm-rolled structures, but recrystallized structures were equiaxed and isotropic. Microstructural examinations after deformation revealed that superplastic deformation tends to destroy structural anisotropy, the deformed structure becoming nearly isotropic.

---

\* Bands are metastable and therefore according to Russian investigators they may be important in superplastic flow (Underwood 1962). It is difficult to determine the effect of banding per se since heat treatments which reduce banding also tend to increase grain size. Cold rolling plus recrystallization eliminates banding and an isotropic structure is produced. Isotropic structures produced by cold rolling plus recrystallization might enhance high elongations and high strain rate sensitivity, possibly by leading to the presence of high-angle boundaries.

---

Warm rolling, preceded by hot rolling, also has been used to obtain fine grained structure in the Fe-0.8%C alloy. In this case, however, the microstructure revealed elongated grains along the rolling direction. Comparison of the elevated temperature strain rate-stress relation of the material with elongated grains (hot and warm rolled) with material consisting of equiaxed grains (warm rolled) for the Fe-0.8%C alloy is given in Figure 10. As can be seen a low value of  $m$  is observed for the elongated grain structure for all strain rates ( $m \approx 0.15$ ) but the equiaxed structure shows fairly high strain rate sensitivity at low strain rates ( $m = 0.3$ ). These results show that the elongated grain structure does not show any superplastic behavior and indicates that fine equiaxed structure is necessary for the existence of superplasticity in Fe-C alloys in agreement with previous results on superplastic alloys (Marder 1969).

#### The effect of impurities on grain growth during superplastic deformation.

Because superplastic deformation of ultrafine grained materials involves considerable holding time at high temperature, grain growth can be expected to occur. Grain growth behavior during superplastic deformation has been studied for various superplastic alloys (Franti and Wilsdorf 1975; Lindinger, Gibson and Brophy 1969; Clark and Alden 1973; Walser and Sherby 1975) and the results of these studies revealed that grain growth usually occurs at an enhanced rate during deformation.

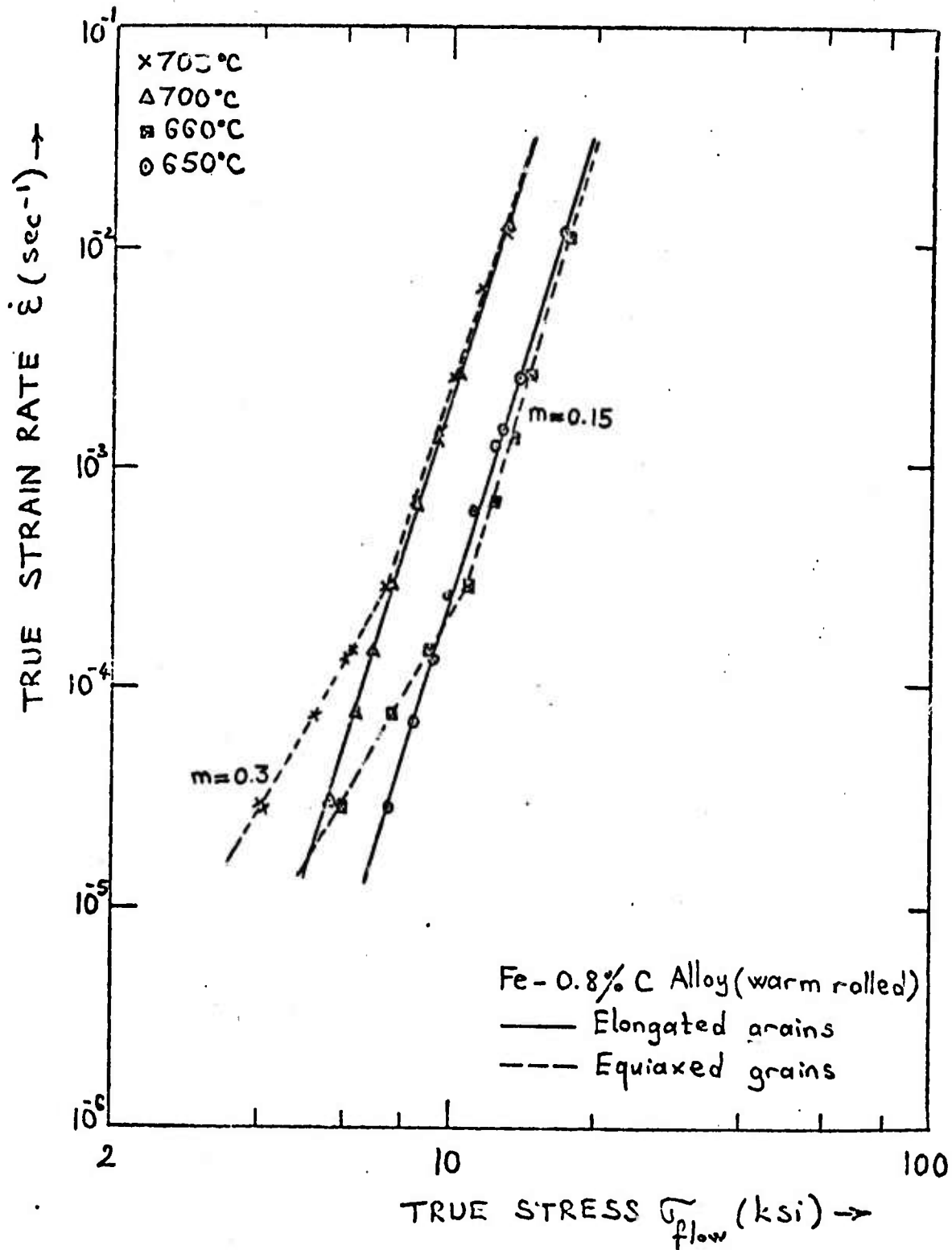


Figure 10. Comparison of the elevated temperature strain rate-stress relation of the material with elongated grains (hot and warm rolled) with material consisting of equiaxed grains (warm rolled) for an Fe-0.8% C alloy.

Microstructural studies of our samples after deformation also revealed that grain growth occurred and it is definitely enhanced by concurrent deformation. Comparison of the grain size between the deformed region (gage) and undeformed region (grip) of all samples after superplastic deformation showed that the deformed regions have larger grain size than the undeformed regions. These results can be seen in Figure 11 which shows the microstructures of the eutectoid steel before and after high temperature deformation. Similar photomicrographs are shown for the Fe-0.8%C alloy in Figure 12.

It is very difficult to calculate the average growth rate during superplastic deformation because there are many variables which affect the growth rate. The work of several investigators would suggest that the grain growth rate ( $J$ ) =  $f(T, t, \dot{\epsilon}, \epsilon, L_1)$  where  $T$  is the temperature of test,  $t$  is the time of test,  $\dot{\epsilon}$  is the strain rate,  $\epsilon$  is strain and  $L_1$  is the initial grain size.

In order to determine the effect of impurities on grain growth behavior of the eutectoid steel and the Fe-0.8%C alloy, a grain growth rate analysis was made on both materials and the data are listed in Table 2.

Table 2  
Grain Size and Grain Growth Data

Material	Test #	$\bar{L}_{initial}$	$\bar{L}_{grip}$	$\bar{L}_{gage}$	T(°C)	$\dot{\epsilon}(\text{min}^{-3})$	Time of test t (min)	Total time t(min)* total
Eutectoid Steel	57	0.6	1.2	1.8	700	0.8%	394	424
Fe-0.8%C Alloy	61	2.2	3.3	5.5	700	0.8%	313	343

\*  $t_{total}$  = time of test (t) + annealing time (30 min) before start to test

Material	growth rate during dynamic annealing $J \propto \left[ \frac{L_{gage} - L_{grip}}{t} \right] (\mu\text{m}/\text{min})$	growth rate during static annealing $J \propto \left[ \frac{L_{grip} - L_{initial}}{t_{total}} \right] (\mu\text{m}/\text{min})$
Eutectoid Steel	0.00152	0.00142
Fe-0.8%C Alloy	0.00703	0.00321

In this analysis, the average grain growth rate ( $J$ ) is usually assumed to be proportional to  $\left( \frac{L_f - L_o}{t} \right)$ , following the analysis of Lindinger, Gibson and Brophy, where  $L_f$  is the final grain size,  $L_o$  is the initial grain size and  $t$  is the time of

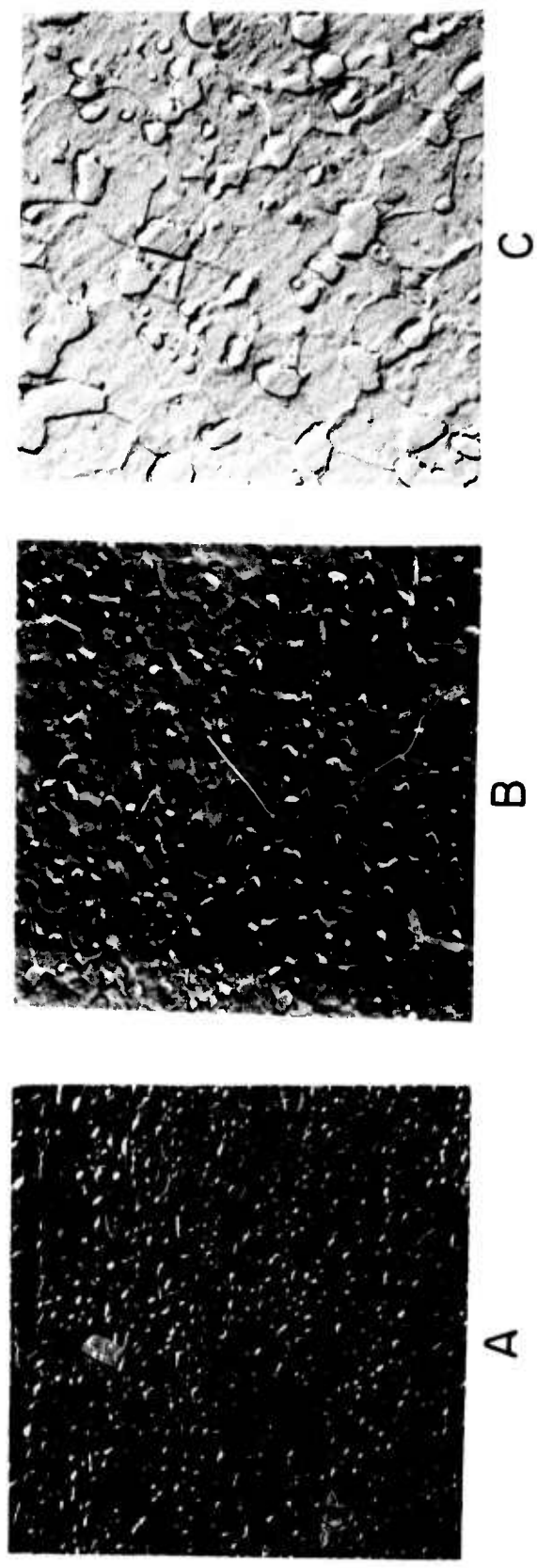


Figure 11. Carbon replica micrographs of a eutectoid steel illustrating the grain growth that occurs during superplastic flow. (A) Steel in as warm rolled condition (at 500°C,  $\epsilon = -2.76$ ), (B) sample held at 650°C for 7 hours [grip region of sample shown in (C)] and (C) gage region of sample deformed superplastically at 650°C and  $\dot{\epsilon} = 0.4\%/min$  to  $\epsilon \approx 170\%$ .

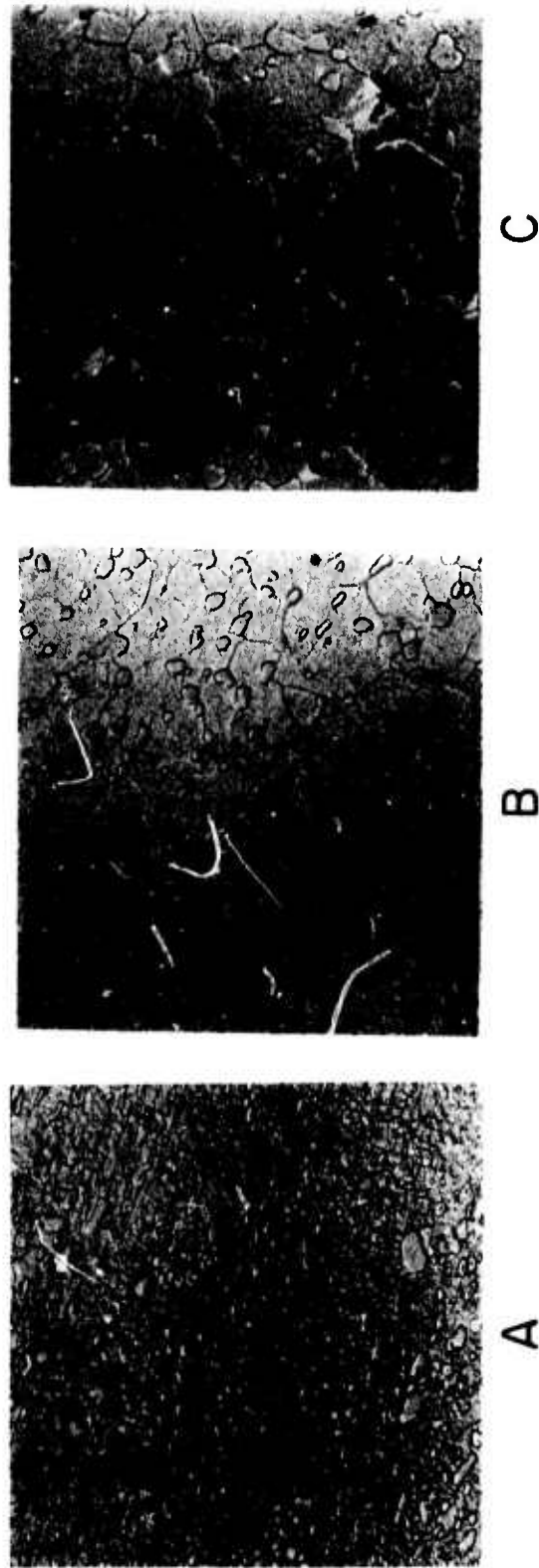


Figure 12. Carbon replica micrographs of an Fe-0.8%C alloy illustrating the grain growth that occurs during superplastic flow. (A) Alloy in as warm rolled condition (at 550°C,  $\epsilon = -2.0$ ), (B) sample held at 670°C for 3 hours [grip region of sample shown in (C)] and (C) gage region of sample deformed superplastically at 670°C and  $\dot{\epsilon} = 1\%/min$  to  $\epsilon \approx 150\%$ .

test. It should be emphasized, however, that  $J$  is a function of strain and therefore the discussion that follows is correct in a qualitative sense only.

The growth rate during dynamic annealing (high temperature deformation) was modified from the analysis of Lindinger et al. by using  $J \propto \frac{L_{\text{gage}} - L_{\text{grip}}}{t}$ .

The grain growth rate during static annealing was calculated using  $J \propto \frac{L_{\text{grip}} - L_{\text{initial}}}{t}$ .

Comparison of the grain growth data of the eutectoid steel with the Fe-0.8%C alloy, given in Table 2, shows that the grain growth rate of the Fe-0.8%C alloy is higher than the eutectoid steel. This result can be attributed to the presence of impurities in the eutectoid steel such as Mn, Si and Ni. These impurities control grain size and retard grain growth which in turn results in better superplastic behavior in the eutectoid steel. Comparison of the grain growth rates during dynamic annealing of both materials with growth rates during static annealing, given in Table 2, also shows that growth rate is enhanced during deformation.

REFERENCES

- Alden, T. H., 1975, in *Treatise on Materials Science and Technology*, Vol. 6, ed. R. J. Arsenault, Academic Press, New York, p. 225.
- Clark, M. A., and Alden, T. H., 1973, *Acta Met.*, 21, 1195.
- Clinard, F. W., and Sherby, O.D., 1964, *Acta Met.*, 12, 911.
- Davies, G.J., Edington, J. W., Cutler C.P. and Padmanabhan, K.A., 1970, *J. Mater. Sci.*, 5, 1091.
- Dingley, D. J., 1970, in *Proc. of the 3rd Annual Scanning Electron Microscope Symposium*, Chicago, p. 329.
- Franti, G. W., and Wilsdord, H.G. F., 1975, Final Report to Office of Naval Research, Department of Materials Science, University of Virginia, Charlottesville, Virginia.
- Geckinli, A. E., 1973, Ph.D. Thesis, Dept. of Materials Science, Stanford University, Stanford, California.
- Johnson, R.H., 1970, *Met. Rev.*, 15, 115.
- Kazir, J., and Rosen, A., 1969, in *Quantitative Relations Between Properties and Microstructure*, ed. D. G. Brandon and A. Rosen, Israel Universities Press, p. 351.
- Lindinger, R.J., Gibson, R.C., and Brophy, J. H., 1969, *Trans. ASM*, 62, 231.
- Marder, A.R., 1969, *Trans. Met. Soc. of AIME*, 245, 1337.
- Morrison, W.B., 1968, *Trans. ASM*, 61, 423.
- Nicholson, R.B., 1972, in *Electron Microscopy and Structure of Materials*, ed. G. Thomas, R. M. Fulrath and R. M. Fisher, University of California Press, Berkeley, p. 689.
- Oelschlagel, D., and Weiss, V., 1966, *Trans. ASM*, 59, 143.
- Rai, G., and Grant, N.J., 1975, *Met. Trans.*, 6A, 385.
- Rhines, F.N., Bond, W.E., and Kissel, M.A., 1956, *Trans. ASM*, 48, 919.
- Schadler, H.W., 1968, *Trans. TMS-AIME*, 242, 1281.
- Sherby, O.D., and Goldberg, A., 1961, *Acta Met.*, 9, 510.
- Sherby, O.D., Walser, B., Young, C.M., and Cady, E.M., 1975, *Scripta Met.*, 9, 569.
- Underwood, E.E., 1962, *J. Metals*, 14, 914.

Walser, B., and Sherby, O.D., 1975, Second Annual Progress Report to Advanced Research Projects Agency, Center for Materials Research, Stanford University, Stanford, California.

Yoder, G.R., and Weiss, V., 1972, Met. Trans., 3, 675.

Young, C.M., Bly, D. L., and Sherby, O.D., 1972, Semi-Annual Progress Report to AISI, Department of Materials Science and Engineering, Stanford University, Stanford, California.

### C. Powder Consolidation Under Superplastic Conditions

R. D. Caligiuri

The purpose of this research has been to propose and demonstrate a method of accelerating the sintering process by taking advantage of the unique properties of superplastic materials. Specifically the method utilizes the low flow stress (i.e. weakness) of superplastic materials at warm temperatures. This permits easy flow into pores and results in high densification. The advantages here are immediately obvious. First, since superplastic behavior is observed at warm temperatures, full densification of powder metallurgy parts can be achieved at temperatures much lower than those required for conventional sintering. Second, since the superplastic structures exhibit much higher creep rates at low flow stresses, densification can be achieved at pressures much lower than those required for conventional hot pressing. Third, the final compact is a fine grained product which is generally a desirable structural feature for low (normal) temperature applications.

The above ideas form the basis of this research program on superplastic hot pressing. A literature search revealed superplastic hot pressing to be a novel idea. Powder metallurgy techniques have been used in the past to produce superplastic materials specifically IN-100 superalloy<sup>(1)</sup>, but no one to our knowledge has attempted to use superplastic characteristics to enhance the densification process itself.

Figure 1 gives an outline of the current research program. Although the concept of superplastic hot pressing is applicable to all systems that exhibit superplasticity, we have restricted ourselves to ferrous based powders for two reasons: 1) we already have accumulated extensive knowledge about superplasticity in the iron-carbon system from earlier work here at Stanford<sup>(2,3)</sup> 2) ferrous based powders are relatively inexpensive, easily obtained, and simple to work with. The only real requirement a material must meet before it exhibits the weakness characteristic of superplastic systems is that it must have a high strain rate sensitivity exponent ( $m \approx 0.5$ )<sup>(4-7)</sup>. As outlined in Figure 1 this high  $m$  value can be achieved in one of two ways. One method is to prepare a material which contains a fine structure<sup>(4-7)</sup> (classified as fine structure superplasticity). The second method is to develop internal stresses of sufficient magnitude during plastic deformation (classified as internal stress superplasticity). The conditions

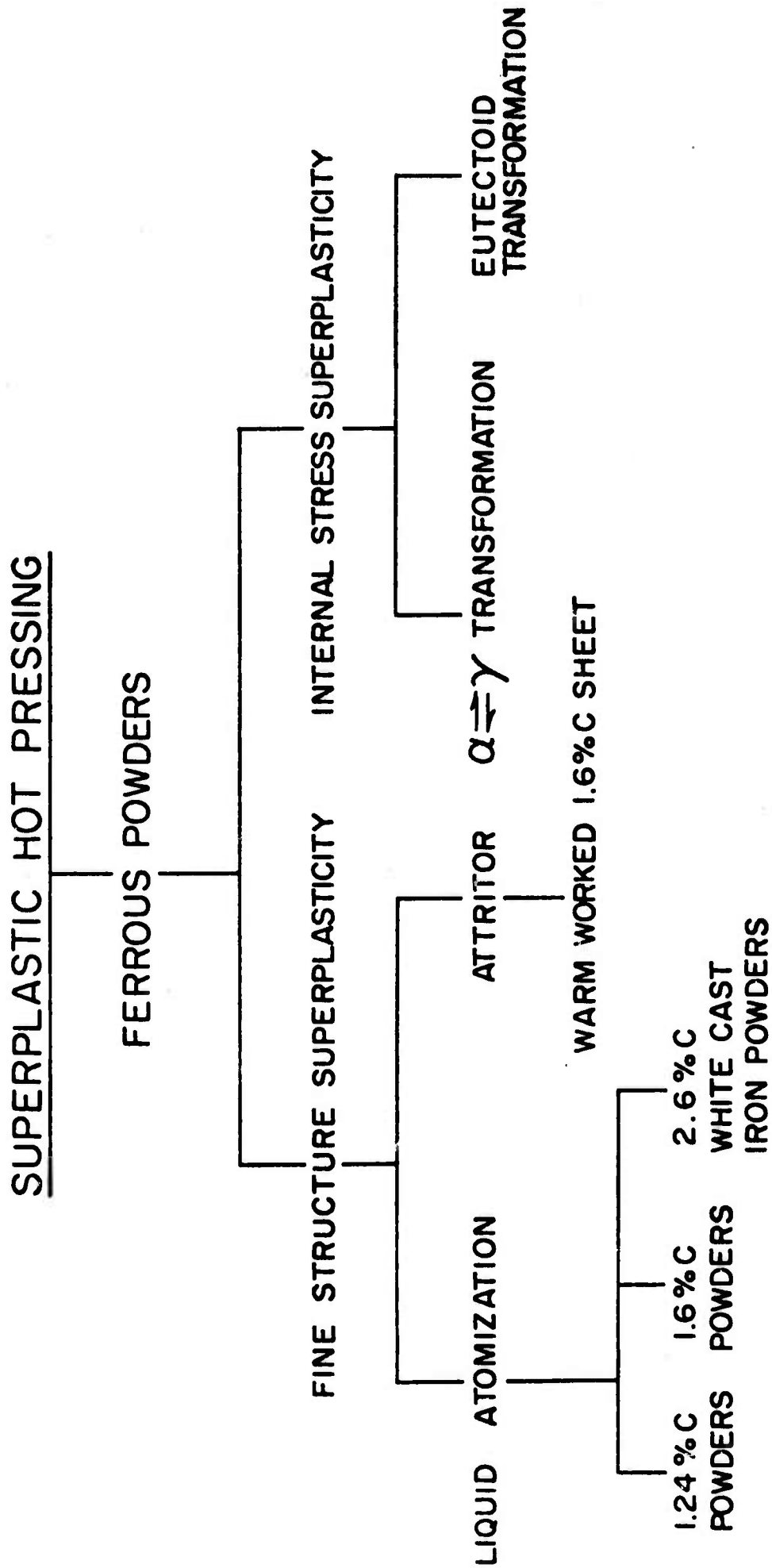


Figure 1. Outline of current and proposed research studying powder consolidation under superplastic conditions. Details are given in text.

necessary for fine structure superplasticity are described in the third section of this report. The second method, involving internal stress, can be obtained by cycling pure iron powders through the  $\alpha \rightleftharpoons \gamma$  transformation<sup>(8)</sup> or by cycling 0.8%C steel powders through the eutectoid transformation. Such transformations will introduce strains from volume changes which in turn develop internal stresses ( $\sigma_i$ ). If thermal cycling is carried out under constant load creep conditions, then it can be shown<sup>(9)</sup> that the strain rate sensitivity exponent will be affected by the internal stresses according to:

$$m_{\text{cyc}} = \frac{m_{\text{iso}}(\sigma_a + \sigma_i)}{\sigma_a}$$

Where  $m_{\text{cyc}}$  is the strain rate sensitivity exponent under cyclic conditions,  $m_{\text{iso}}$  is the exponent under isothermal conditions, and  $\sigma_a$  is the applied stress. If  $\sigma_i$  is large enough ( $\sigma_i \approx 2\sigma_a$ ), then  $m_{\text{cyc}}$  will approach 0.5. The powders at this point will be very weak and should densify readily. It is expected that much of the next six months will be spent studying internal stress superplasticity and its application to ferrous powder metallurgy. Since research to date has dealt only with fine structure superplasticity, however, the rest of this progress report will deal only with this subject.

How can a fine structure be introduced into a powder? There are two basic methods. The first method involves liquid or gas atomization wherein liquid droplets are cooled rapidly by a liquid or gas medium. The impurities in the liquid present many nucleation sites for austenite grains and cementite particles. Furthermore, the cooling rate is so fast that the fine austenite grains will transform to a fine structure which will not have a chance to grow. This results in a fine structure at room temperature. White cast iron powders (2.6%C) produced by such a liquid atomization process were obtained and studied extensively. The results of this study, along with more detailed information on the relation between fine structure superplasticity and powder metallurgy, are described in the next section. Quantities of 1.24%C and 1.6%C liquid atomized high carbon powders have recently been obtained from A. O. Smith Inland, Inc. and International Nickel, Inc., and are presently being studied. Results should be available within the next few months.

The second method of producing fine structures in powders involves the use of the attritor. The attritor is a commercially available device which, among other things, pulverizes material into fine powder form. With the attritor we can

attrit bulk material into powder form. We thus have the capability to run a controlled experiment: 1) take bulk material and process a portion of it in such a manner that it consists of a fine structure and another portion processed in such a manner that it consists of a coarse structure; 2) attrite both the coarse and fine structure material identically into powder form; 3) hot press both types of powder for the same amount of time at the same pressure and temperature. If the fine structure powders develop a higher density than the coarse structure powders it is likely due to the weakness characteristic of the superplastic fine structure since all other variables are equivalent between the coarse and fine powders.

Based upon earlier work here at Stanford<sup>(2,3)</sup>, the ideal choice for bulk material for such an experiment is ultrahigh carbon steels. High carbon steels can be made super weak at warm temperatures by warm rolling operations. We obtained a 1.6% C casting which contained the microstructure shown in Figure 2a. Note the massive cementite interwoven in the ferrite matrix. The as-cast material, then, is an example of a material containing a coarse structure. A fine structure was developed in the casting by the following procedure. The casting was annealed at 1100°C to dissolve all the cementite. It was then rolled continuously as the material cooled to 750°C. Further warm rolled at 550°C to a strain of  $\epsilon = 2.0$  lead to a microstructure as shown in Figure 2b. Note how the cementite has been broken up into very fine ( $\approx 1\mu\text{m}$ ) particles with ferrite grains in the order of 1-5 $\mu\text{m}$ . Previous work<sup>(2,3)</sup> indicates such a microstructure should be superplastic at warm temperatures (600 to 700°C). This is indeed the case. Mechanical testing gives a strain rate sensitivity exponent of about 0.45, in close agreement with earlier work (Figure 3).

This warm worked sheet was then milled into chips 0.12 inches long and 0.010 inches thick. These chips were then attrited dry at 360 RPM for 10 hours. The remaining portion of the casting (coarse structure) was similarly milled and attrited. Both sets of powders were then hot pressed at 650°C and 10,000 psi. The results were plotted as density versus time of hot pressing and curves for both powders are shown in Figure 4. The density scale is given as percent of theoretical density. The results reveal that the fine structure powders are more dense at any given time than the coarse structure powders. This difference in density can only be related to the degree of structural refinement because all other parameters are



Figure 2a. Microstructure (at 1800X) of the 1.6%C casting prior to warm rolling. Note the massive proeutectoid cementite structure interwoven in the ferrite matrix. This is said to be a very coarse structure.



Figure 2b. Microstructure (at 1800X) of the 1.6%C casting after annealing at 1100°C,  $\gamma$  working between 1100°C and 750°C, and  $\alpha$  working at 550°C. Total final strain was  $\epsilon = 2.0$ . Note that the cementite is now in a fine spheroidized form, with occasional larger precipitates which did not break up during warm rolling.

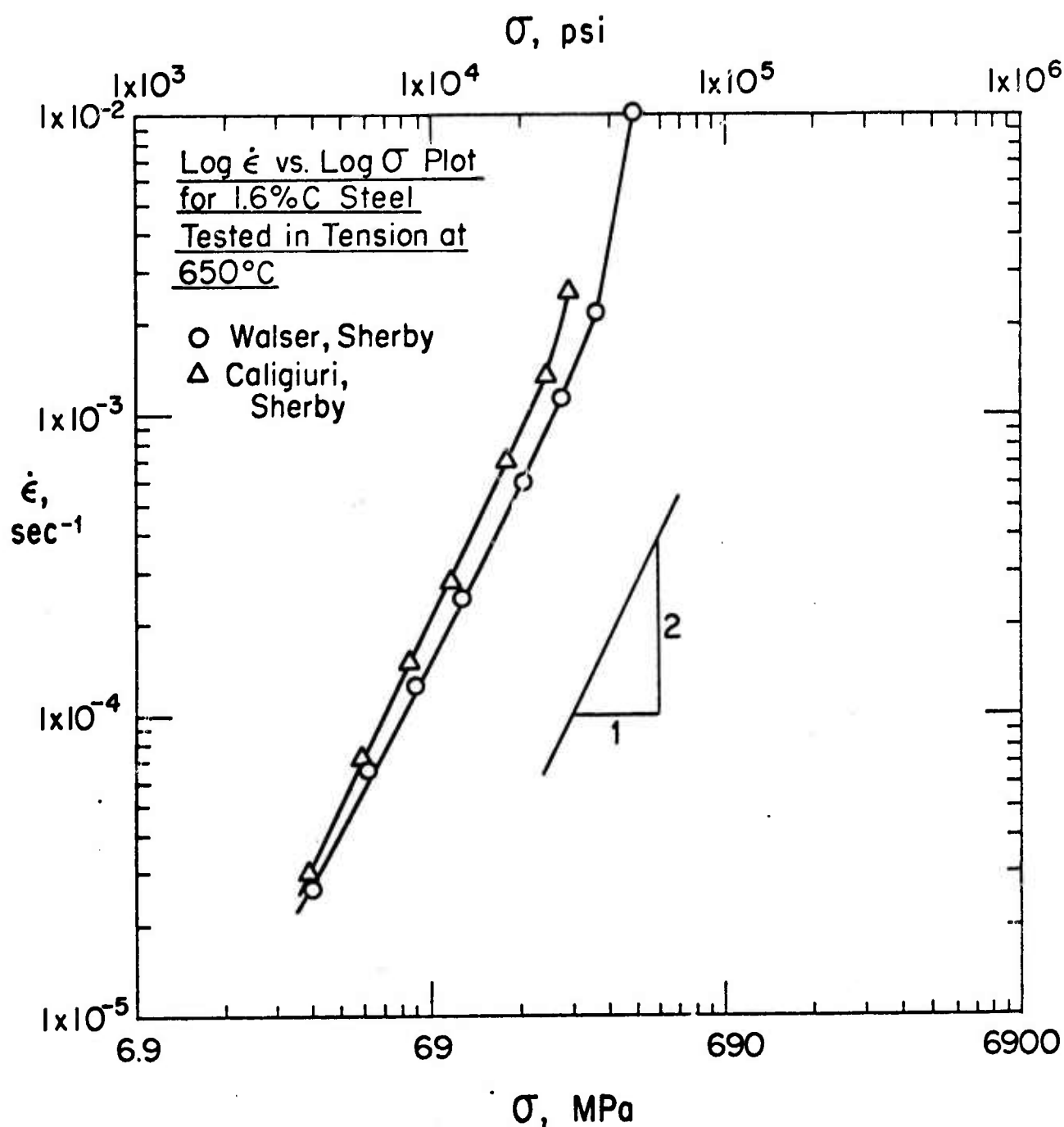


Figure 3. Log  $\dot{\epsilon}$ -Log  $\sigma$  plots for warm rolled 1.6% C castings tested previously at Stanford<sup>(2,3)</sup> (○) and this research (△). As this figure shows, the material used in this study behaved similarly to the material studied previously which was shown to be superplastic<sup>(2,3)</sup>. Note the high strain rate sensitivity exponent of both materials ( $m \sim 0.5$ ).

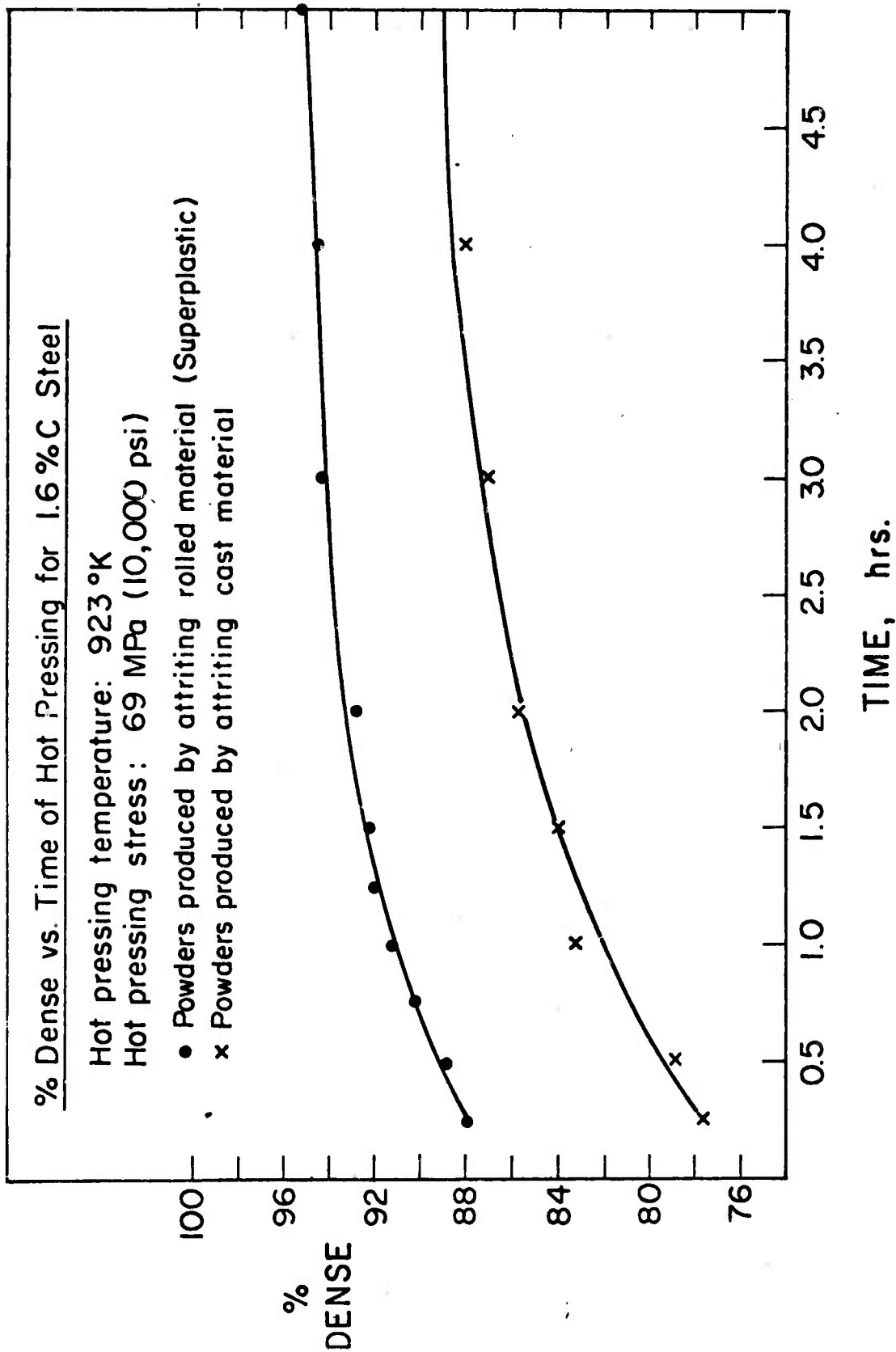


Figure 4. Density versus time curve for 1.6% C steel hot pressed at 650°C and 10,000 psi. The fine structure powder (•) is more dense at all times.

the same. Since the fine structure material was shown to be superplastic at the temperature and stress of hot pressing (Figure 3), the difference in density can further be attributed to the characteristic weakness of superplastic materials which permits easy plastic flow into existing pores. That is to say, "superplastic hot pressing" appears to be a real phenomenon.

Figure 5 shows the effect of increasing the compacting stress to 20,000 psi on the difference in density between the two types of powders. The fine structure powders are still more dense, but the difference is not as large as at 10,000 psi. This can possibly be attributed to the fact that the difference in creep rates between the two types of materials is not as great at 20,000 psi as it is at 10,000 psi. In addition, both density-time curves shown in Figure 5 are shifted upwards because the overall steady state creep rates of both materials increases as stress increases.

There are still many unanswered questions. What effect does temperature have on the density-time curve? How can we be certain power law creep is the controlling densification mechanism? Perhaps the fineness of the structure acts to enhance diffusion, and the higher density is due to increased diffusion and not to the weakness associated with superplasticity. Can a mathematical model be developed which will describe the densification process? These and other questions will be considered in detail during the next six months.

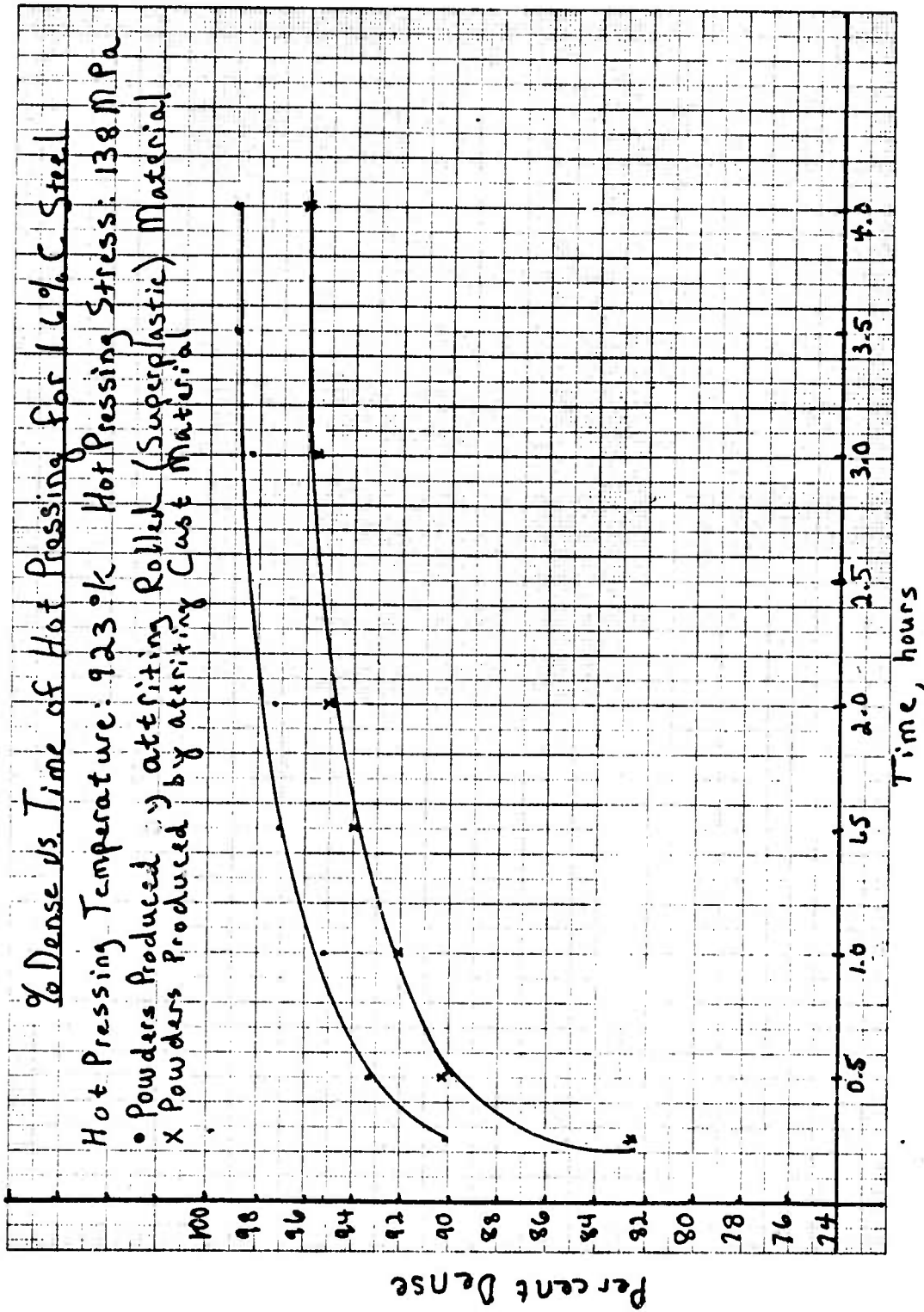


Figure 5. Density versus time curve for 1.6% C steel hot pressed at 650°C and 20,000 psi. The fine structure powder is still more dense at all times, but the difference is not as great as at 10,000 psi.

References

1. S. H. Reichman and J. W. Smythe, International Journal of Powder Metallurgy, 6, 65 (1970).
2. B. Walser and O. D. Sherby, Superplastic Ultra-High Carbon Steels; Second Annual Report to Advanced Research Projects Agency, Washington, D.C., August 1975.
3. O. D. Sherby, B. Walser, C.M. Young, and E. M. Cady, Scripta Met., 9, 569 (1975).
4. H. W. Hayden, R. C. Gibson, and J. H. Brophy, Scientific American, 28, March (1969).
5. R. H. Johnson, Metallurgical Reviews, 15, 115 (1970).
6. O. D. Sherby, Science Journal, 5, 75 June (1969).
7. G. J. Davies, J. W. Eddington, C. P. Cutler, and K. A. Padmanabhan, Jnl. Mats. Sci., 5, 1091 (1970).
8. F. W. Clinard, and O. D. Sherby, Acta Metallurgica, 12, 911, August (1964).
9. O. D. Sherby, unpublished research.

D. Superplastic Hot Pressing of White Cast Iron\*

R. D. Caligiuri, R. T. Whalen, O. D. Sherby

ABSTRACT

A new method of sintering high carbon ferrous powders using hot press techniques is described. We designate this process as "superplastic hot pressing". This technique utilizes the exceptional weakness of superplastic structures, permitting the production of dense compacts at low temperatures and pressures. White cast iron powders (2.6%C) are hot pressed in air for 2 - 5 hours at 69 - 193 MPa (10,000 - 28,000 psi) and 600 - 700°C (1112 - 1292°F) into compacts 90 to 99% dense. The mechanical properties of this hot pressed material are shown to be commensurate with as-cast white cast iron (a fracture strength at room temperature of 1241 MPa (180,000 psi)). Strain rate change and stress relaxation tests on the hot pressed white cast iron at 650°C revealed it to be highly strain rate sensitive ( $m = 0.3$  in  $\sigma = Ke^m$ ) suggesting that sintering by superplastic type flow mechanisms occurred. It is predicted that a finer structure than that developed in our cast iron powders would lead to  $m = 0.5$  (ideal superplastic state) and therefore would result in ideal superplastic hot pressing.

---

\* This portion of the progress report was submitted to the International Journal of Powder Metallurgy and will appear in a forthcoming issue.

### INTRODUCTION

The purpose of this paper is to propose and demonstrate a method of accelerating the sintering process by taking advantage of the unique properties of superplastic materials. It is our contention that powders containing superplastic microstructures can be readily hot pressed at warm temperatures (warm is defined as  $0.4$  to  $0.65T_m$  where  $T_m$  is the absolute melting temperature) under small externally applied pressures. Some of the basic principles that relate to the development and understanding of superplastic materials will be described. These principles will be used to illustrate how powders with such fine structures should have unique characteristics during hot pressing. The ideas presented will then be applied to an experimental study of superplastic hot pressing of white cast iron.

Superplastic Alloys - Studies in recent years<sup>(1-4)</sup> have revealed the prerequisites needed for superplastic behavior. These are: high strain rate sensitivity\* and fine stable grains with equiaxed structure (grain size in the order of 1 to 10 microns). High strain rate sensitivity is achievable at warm temperatures ( $0.4$  to  $0.65T_m$ ) and low strain rates ( $10^{-6}$  to  $10^{-4}$  sec<sup>-1</sup>), and fine grain materials can be stabilized by the presence of a second phase. Another important requirement for superplasticity is that the strength of the matrix and second phase should be nearly the same at the temperature where deformation occurs. Superplastic flow is characterized by high tensile ductility and very low strengths. The latter property, that of low strength, is important

---

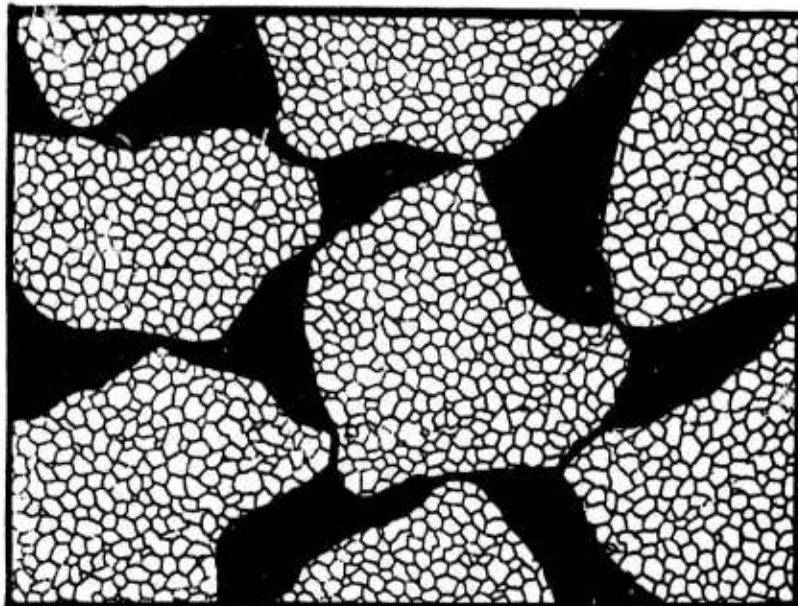
\* Strain rate sensitivity is measured by means of the flow stress ( $\sigma$ )- strain rate ( $\dot{\epsilon}$ ) relation  $\sigma = K\dot{\epsilon}^m$  where  $m$  = strain rate sensitivity exponent and  $K$  is a material constant. Superplastic metallic alloys generally exhibit  $m$  values in the range  $0.3 - 0.6$ <sup>(1-4)</sup>.

for its potential usefulness in hot pressing.

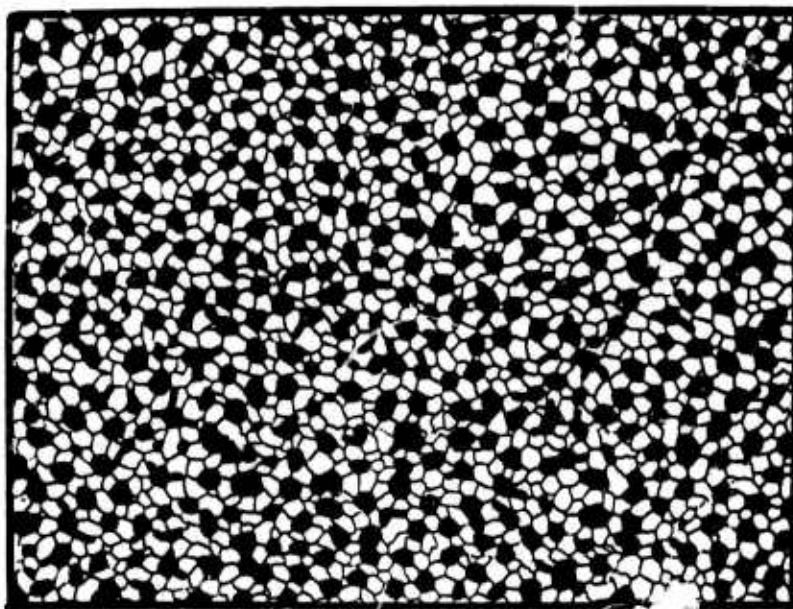
Accelerated Sintering by Superplastic Flow - Figure 1 illustrates the two types of powders which should be amenable to superplastic hot pressing. Figure 1A illustrates relatively coarse powders which, however, are prepared in such a way that they contain fine grains in them. Such structures may be attainable during normal atomization of many materials especially those that contain alloying elements and impurities; thus, the presence of a second phase could provide the nucleation sites for grain growth during atomization or during heat treatment after atomization (IN 100 powders are an example of such a material<sup>(5)</sup>). Another method of obtaining fine structures is by splat cooling<sup>(6)</sup>. Powders consisting of fine, equiaxed structures should be extremely weak at warm temperatures and low applied pressures and should fill the pores readily. The mechanism of densification here would be by boundary shearing of the grains within the particles, a mode of deformation which apparently dominates the superplastic flow process<sup>(7-9)</sup>.

Oftentimes it is difficult to prepare medium size powders (i.e. 50-100 microns) with fine grain structures within them. In order to superplastically hot press such powders it is necessary to refine them into smaller sizes (1 to 10 microns); one common method is by means of the attritor which simply mechanically comminutes powders to virtually any desired size. Thus, powders such as those sketched in Figure 1B should readily bond and sinter under warm temperatures and low pressures to high densities.

A major advantage of "superplastic hot pressing" in ferrous-base materials is that only warm temperatures would be needed to obtain high densification. Thus oxidation, a major problem in sintering of iron base powders, would be minimized during hot pressing at 550-700°C (1022-1292°F), a temperature range where superplastic flow is known to occur<sup>(10-11)</sup>. It is even feasible to consider hot pressing without a protective atmosphere at such temperatures. Another advantage of warm



(A)



(B)

25 $\mu$ m

Figure 1. A schematic illustration of two types of powders which should be amenable to superplastic hot pressing. (A) Illustrates powders of normal size containing a fine structure (about 5 microns) within each powder and (B) illustrates powders of a size on the order of 5 microns. Both powders should hot press readily at warm temperatures due to ease of superplastic flow by boundary shearing.

temperature pressing is that grain growth will not be excessive under such conditions.

### MATERIALS

The choice of material for investigation requires that it have superplastic characteristics. With the exception of a special grade of stainless steel<sup>(12)</sup>, the only known ferrous material that exhibits superplastic properties are ultra high carbon steels<sup>(11)</sup>. These steels contain 1.3 to 1.9%C (a range which lies between and overlaps ordinary high carbon steels and cast irons) and have been shown to be superplastic when containing a fine grained structure. High strain rate sensitivity exponents of  $m = 0.4$  to  $0.6$  were observed. The fine structures were obtained by a number of different methods; a common one involved extensive warm working of the original casting to develop a fine spheroidized structure with accompanying fine grains ( $0.5$  to  $1.5\mu\text{m}$ ). The high volume fraction of cementite contained in the 1.3 to 1.9%C steels (20 and 29 volume percent respectively) does not lead to brittle tendencies at warm temperatures since cementite exhibits high plasticity at these temperatures<sup>(13)</sup>.

The most logical choice of powders for the proposed superplastic hot pressing experiments are those based on the above mentioned ultra-high carbon steels. Such powders are not available commercially. It was, however, possible to obtain a white cast iron containing 2.6% carbon (40 volume percent cementite). This powder, screened out at  $70\mu\text{m}$ , was donated by Cleveland Metal Abrasive Co., of Cleveland, Ohio (courtesy of Dr. John Vasein of Wheelabrator-Frye Co, of Mishwaka, Indiana). The powders were atomized from the liquid state and were considered to contain a fine structure of cementite in a fine ferrite matrix. It was therefore decided to use the cast iron powders in the as-received state.

### EXPERIMENTAL METHODS

The experimental work consisted of three distinct phases: the production of compacts, mechanical testing, and metallography and density calculations.

Compact Production - The P/M processes by which dense material was produced from the cast iron powders are now described. The compacts were produced by essentially a "hot pressing" technique<sup>(14-18)</sup>. That is to say, densification was the result of simultaneous application of temperature and pressure. However, our method differed from conventional hot pressing in two distinct ways: (1) the powders were poured directly into a cold 3.81 cm bore die and heated to the temperature of testing without the benefit of a protective atmosphere; (2) the temperatures and pressures employed were well below those normally associated with the hot pressing of cast irons<sup>(21,22)</sup>. Compaction loads were applied with a 267KN (60,000 pound) capacity Riehle testing machine.

Mechanical Testing - The purpose of mechanically testing samples cut from the compacts was two-fold: determination of room temperature mechanical properties and computation of strain rate sensitivity exponents ( $m$ ) at 650°C (1202°F). All testing was done in compression on a 44.5 KN (10,000 lb) capacity Instron, model TTCL. Specimen size and shape were limited by the compacts to square cross-section, .343cm (0.135 inches) wide and .508cm (0.200 inches) long. The compact size precluded any tensile testing. In order to simplify analysis, all mechanical testing was done on samples cut from the same compact which was hot pressed to a density of 97% in two hours at 650°C (1202°F) and 193 MPa (28,000 psi).

Strain rate sensitivity exponents at 650°C (1202°F) were determined by two basic methods: changes in strain rate and stress relaxation. Explicit detail of  $m$  calculations by both techniques are given elsewhere<sup>(1-4,19)</sup> and will not be discussed further here.

Metallography and Density Measurements - Samples were prepared metallographically by cutting, mounting in bakelite, grinding, polishing, and etching in a 2.5% Nital solution for 5 seconds. Samples were examined under a Lietz microscope (50X to 1000X and photographed through a polaroid camera attachment. High magnification

surface studies were made using standard scanning electron microscopy techniques.

Density measurements were made by the "weight in water-weight in air" method. The compact is first weighed dry and then weighed while immersed completely in water. The density was calculated from the following:

$$\rho_{\text{compact}} = \frac{(W_{\text{dry}}) (\rho_{\text{H}_2\text{O}})}{W_{\text{dry}} - W_{\text{wet}}} \quad (1)$$

where  $\rho_{\text{H}_2\text{O}}$  is the density of water corrected for temperature. The weight wet is corrected for the weight of the supporting basket.

The calculation of the theoretical density of white cast iron was based upon the fact that our cast iron contains 2.6% C which converts to 40 volume percent cementite and 60 volume percent ferrite. Since the density of cementite is 7.40 gm/cm<sup>3</sup> and the density of ferrite is 7.87 gm/cm<sup>3</sup>, a simple proportional calculation gives the maximum density of white cast iron as 7.68 gm/cm<sup>3</sup>. From chemical analysis, however, the powders are known to contain 1.3 wt% Si. The density of silicon is 2.3 gm/cm<sup>3</sup> and assuming that all of the silicon is in solution, it is readily calculated that the maximum density of our white cast iron is 7.47 gm/cm<sup>3</sup>. This value, of course, is only approximate and this should be kept in mind when considering the percent dense values given in Figure 2.

#### RESULTS AND DISCUSSION

The experimental results of this research are given in Figures 2-5. Figure 2 summarizes all the different compacts produced as to previous mechanical treatment, time, temperature, stress of hot pressing, and the resulting density. This graph exhibits several general trends: (1) the higher the stress and temperature of hot pressing the higher the resulting density; (2) longer times increase the density only up to a certain limit - that is, a compact may achieve its maximum density in 2 hours with no change in density beyond that time; (3) high densities (>90%) are observed at temperatures between 600 and 700°C (1112 and 1292°F) and pressures

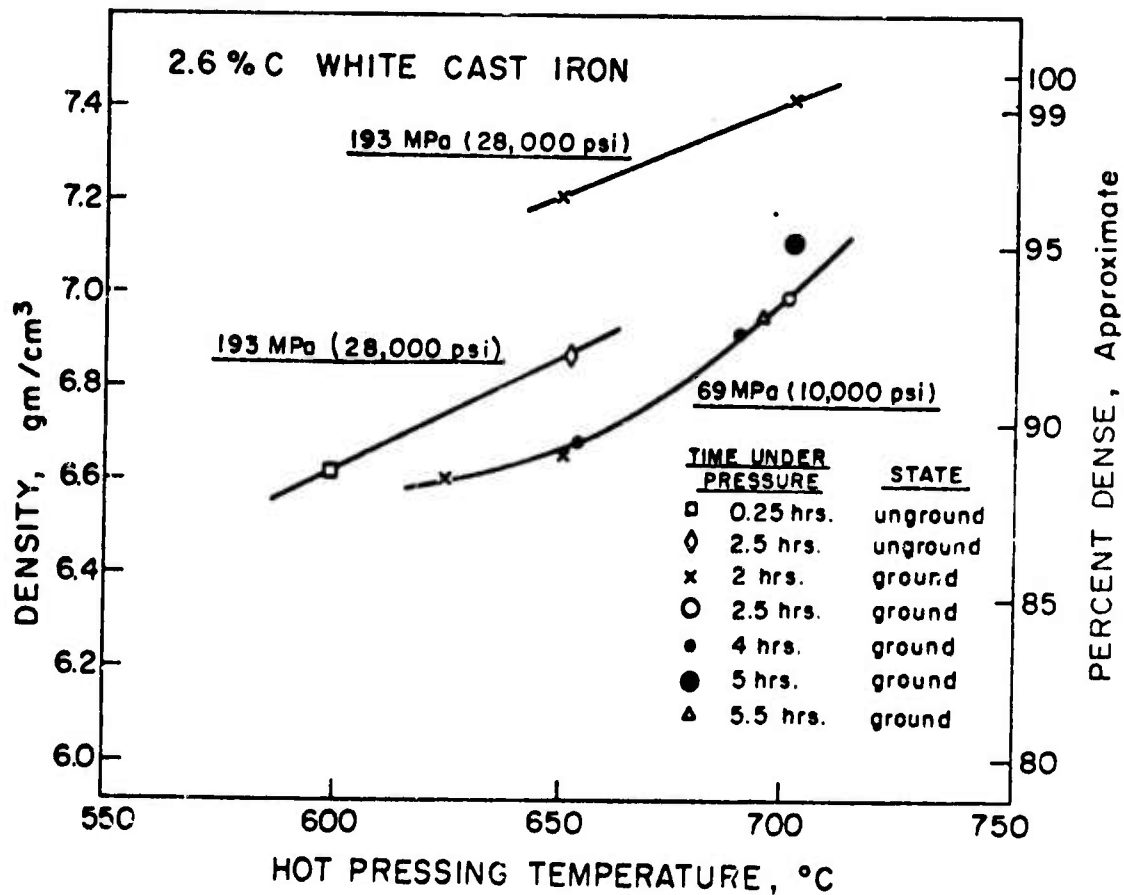


Figure 2. A summary of the experimental work done on 2.6% C white cast iron. The stresses are the applied stresses during hot pressing. The state refers to whether or not the particles were ground by hand in a mortar and pestle prior to hot pressing.

between 69-193 MPa (10,000 - 28,000 psi); (4) grinding of powders by mortar and pestle, prior to hot pressing, gave higher densities than without such grinding.

Figure 3 gives the results of the strain rate change tests for determination of  $n$  values. Twelve different changes in strain rates from two different tests are shown. A slope calculated from the mean values yields an  $n$  value of 0.31. Data from four different stress relaxation tests indicated an  $n$  value of 0.30, in close agreement with the change in strain rate tests. These are high values for the strain rate sensitivity exponent and are typical of the low end of values for superplastic materials quoted in the literature<sup>(1-4)</sup>.

Figure 4 shows the microstructure of a compact hot pressed to a density of 95% at 702°C (1296°F) and 69 MPa (10,000 psi) for 5 hours. Figure 4A, taken at 200X, demonstrates the low degree of porosity attained; on the average, the pores are widely spaced and less than 50 $\mu$ m in diameter. Figure 4B, taken at 1000X, shows a somewhat fine structure interspersed in a network of massive cementite. At room temperature, material compacted to 97% dense exhibited a hardness of 39R<sub>c</sub>, a fracture strength in compression of 1241 MPa (180,000 psi), and a compression ductility of 4.7%; these results are comparable to as-cast white cast iron. Our hot pressed material can thus be considered to be fully bonded.

The regions of fine structure shown in Figure 4B are further examined in the scanning electron micrograph shown in Figure 5. As shown in Figure 5 (taken at 5000X), the ferrite grain size (recessions) appears to be 2 $\mu$ m and the cementite structure (protrusions) is on the order of 1 $\mu$ m. This fine cementite and ferrite structure is well within the range required for superplasticity in ultra high carbon steels<sup>(11)</sup>.

Sauerwald and Kubik<sup>(21)</sup> hot-pressed white cast iron at 370 MPa (54,000 psi) for 30 seconds at 800°C (1472°F). They reported a very porous compact, less than half

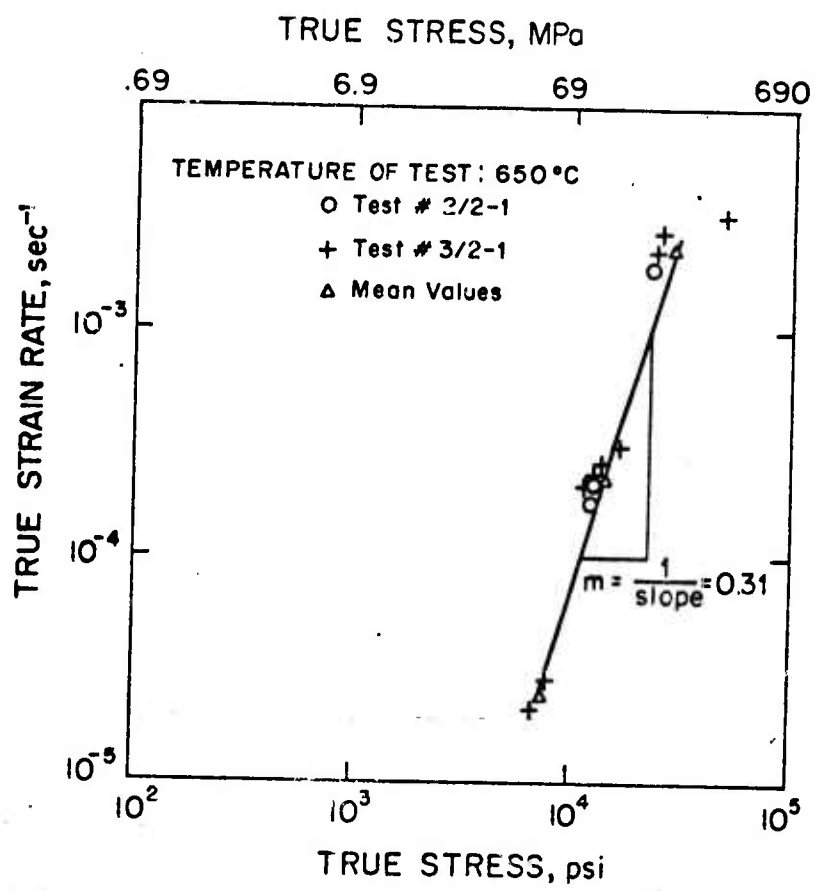
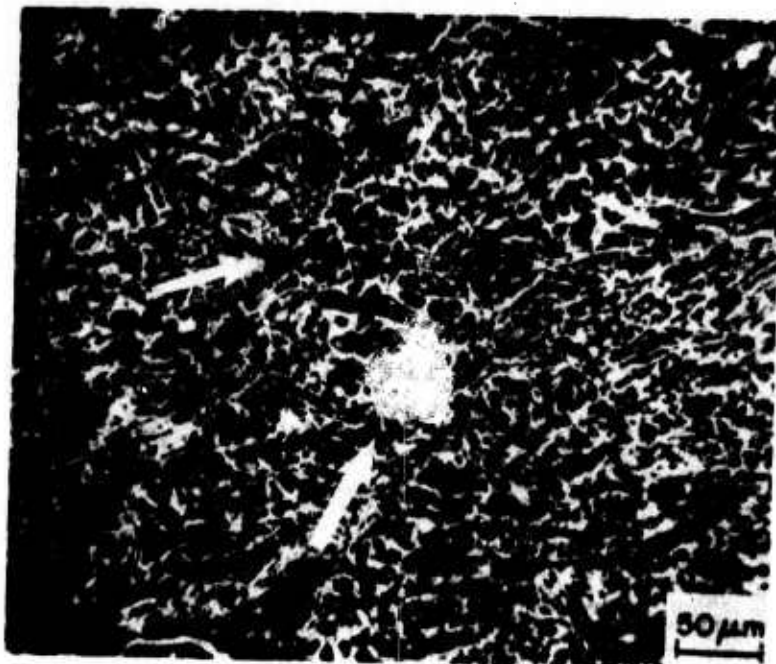
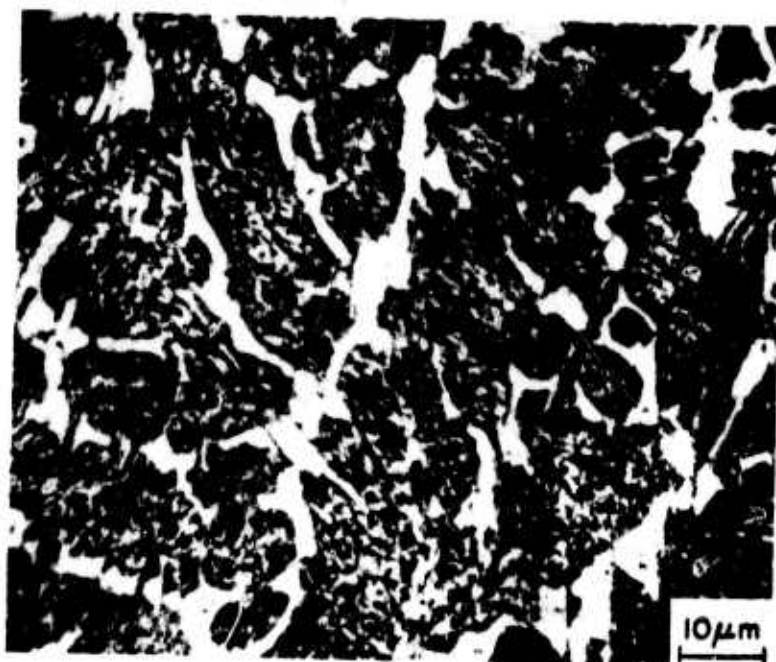


Figure 3. The flow stress-strain rate curve for hot pressed white cast iron as obtained by changes in strain rate tests. The slope observed is equal to 1/m, yielding  $m = 0.31$ . Twelve separate tests were run on two different sized samples, and the mean values taken over both samples.



(A)



(B)

Figure 4. Photomicrographs of a compact hot pressed 95% dense at 69 MPa (10,000 psi) and 702°C for 5 hours. (A) At 20X, shows the pores to be small and widely spaced. (B) At 1000X, shows a lack of pores even at high magnification and reveals the microstructure to be one of regions of fine structure broken up by a network of massive cementite.

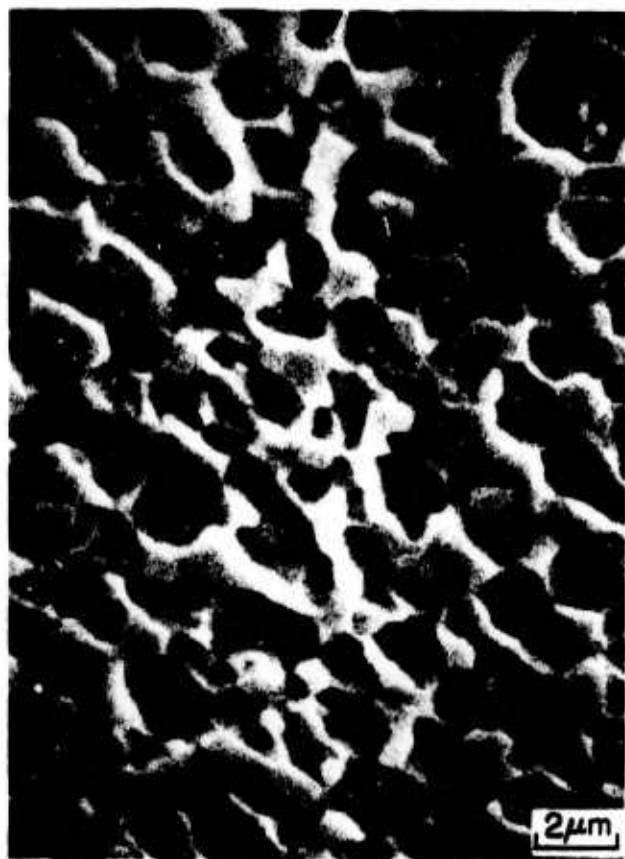


Figure 5. A scanning electron micrograph taken at 5000X detailing the fine structure observed in Figure 4B. Note that the ferrite grain size (recessed regions) appears to be 2µm and the cementite structure (protruding regions) is on the order of 1µm. Not shown is the massive cementite network surrounding such regions of fine structure.

as hard as the original material. Jones<sup>(22)</sup> reported a density of  $6.3 \text{ gm/cm}^3$  (80% dense) when he hot pressed powdered gray cast iron (3.16%C) at  $800^\circ\text{C}$  ( $1472^\circ\text{F}$ ) and 124 MPa (18,000 psi). Furthermore, recent experimental and theoretical work<sup>(15,23-25)</sup> has revealed that densification by hot pressing at high temperatures and pressures is primarily the result of plastic flow through dislocation glide. Specifically, it can be concluded that the primary mechanism of densification in cast iron above  $800^\circ\text{C}$  ( $1472^\circ\text{F}$ ) is plastic flow by dislocation glide. However, comparison of the results of Sauerwald and Kubik and Jones with the data reported in Figure 2 of this paper strongly suggests that a different mechanism of densification is operating in the  $600\text{--}700^\circ\text{C}$  ( $1112\text{--}1292^\circ\text{F}$ ) range for the atomized powders studied. We believe that the mechanism is that of mass flow of matter by grain and interphase boundary shearing. We term this new mechanism as "superplastic hot pressing" and suggest the following observations to support this concept.

First, the 2.6%C white cast iron does exhibit superplastic characteristics. An  $n$  value of 0.31 is high, well above the norm of 0.15 to 0.2 found for ferrous materials tested at  $600\text{--}700^\circ\text{C}$  ( $1112\text{--}1292^\circ\text{F}$ )<sup>(26)</sup>. The high strain rate sensitivity exponent obtained is consistent with the fine structure observed in the cast iron (Figure 5). Ideally superplastic materials exhibit  $n = 0.5$ , however, and it is likely that this high value was not obtained in our study because of the presence of massive cementite regions in the structure (Figure 4B). It is our contention that powders of cast iron containing only fine structures (as in Figure 5) will lead to 100% densification at lower pressures and temperatures than used in this investigation.

Second, the relationship between the material's superplastic nature and the densification mechanism is demonstrated by the fact that even grinding the  $70\mu\text{m}$  powders by hand in a mortar and pestle (thereby refining the structure and enhancing the superplastic response) increases the density of the final product (cf. Figure 2).

Thus, particle and grain refinement leads to greater ease of densification in agreement with the expected enhancement of superplastic flow by a decrease in grain size. It may be argued that refinement of the particles simply increases the surface area of contact, thereby accelerating the diffusional bonding process. As an initial attempt to answer this question, a sample of the 2.6% white cast iron powders was ground by hand in a mortar and pestle. One-half of the powders was hot pressed at 650°C (1202°F) and 193 MPa (28,000 psi) for two hours and the other half simply placed in a sintering furnace at 650°C (1202°F) for three hours with a protective atmosphere. The resulting hot pressed compact was 97% dense and the sintered compact was only 79% dense. Although this experiment suggests rejection of the diffusion bonding from an increased surface area argument, further research on this and other points (including the application of superplastic hot pressing to HIP equipment) is currently in progress.\*

---

\* After preparation of this paper for publication, the authors became aware of a very interesting patent by Volin et al. (27). This patent, entitled "Thermoplastic Prealloyed Powder", describes a process by which strain energy is introduced into superalloy powders, specifically IN-100, by means of an attritor. These attrited powders were hot pressed at 1900°F to 99% dense and then the hot hardness was measured as a function of temperature. Unattrited powders were similarly hot pressed at 1900°F to 99% dense and the hot hardness measured as a function of temperature. The compact made from attrited powders exhibited a much lower hardness at a given high temperature than the compact made from unattrited material. Volin et al. state that the attriting action introduces large amounts of strain energy into the powders which in turn induces recrystallization upon heating. A fine gamma prime precipitate apparently maintains the fine recrystallized grain size throughout hot pressing. The authors state that the presence of fine grain size contributes to the ease of densification. We agree with this analysis and specifically would like to suggest that densification with the attrited powders occurred by superplastic flow mechanisms in the following way. The attrited powders could be like those sketched in Figure 1A prior to application of the load and hence could have superplastically hot pressed to the reported density of 99%. Or, the attriting action could have refined the particle size to such a degree that powders like those sketched in Figure 1B (although more in the form of flakes) were produced and superplastic flow occurred during hot pressing. The limited mechanical property data reported by Volin et al., however, suggest that the attrited and compacted IN-100 does not exhibit high values of the strain-rate sensitivity exponent ( $m = 0.15$ ). These results would imply that greater ease of densification through superplastic flow is possible if structural features were developed in IN-100 such that higher strain-rate sensitivity is obtained.

SUMMARY AND CONCLUSIONS

This research has proposed a mechanism for the hot pressing of cast iron powders to high densities at low temperatures and pressures by taking advantage of their superplastic characteristics in the warm working range (600-700°C) (1112-1292°F). The possible existence of such a mechanism has been demonstrated in the hot pressing of 2.6%C white cast iron powders. The results we have presented suggest that "superplastic hot pressing" is a possible means of accelerating sintering although additional studies are needed to prove the quantitative feasibility of this concept. However, no matter what the mechanism turns out to be, we believe the production of a ferrous material 90 to 99% dense by hot pressing powders, without a protective atmosphere, at 600-700°C (1112-1292°F) and 69-193 MPa (10,000-28,000 psi) to be remarkable in itself and worthy of further study.

REFERENCES

1. H. W. Hayden, R. C. Gibson, and J. H. Brophy, *Scientific American*, 28, March (1969).
2. R. H. Johnson, *Metallurgical Reviews*, 15, 115, (1970).
3. O. D. Sherby, *Science Journal*, 5, 75, June (1969).
4. G. J. Davies, J. W. Eddington, C. P. Cutler, and K. A. Padmanabhan, *Jnl. Mats. Sci.*, 5, 1091 (1970).
5. S. H. Reichman and J. W. Smythe, *International Journal of Powder Metallurgy*, 6, 65 (1970).
6. H. Jones, *Rep. Prog. Phys.*, 36, 1425 (1973).
7. T. H. Alden, *Act. Met.*, 15, 469 (1967).
8. D. L. Holt, *Trans. AIME*, 242, 25 (1968).
9. A. E. Geckinli, Ph.D. Dissertation, Department of Materials Science and Engineering, Stanford University, Stanford, California 94305, Feb. 1973.
10. G. R. Yoder and V. Weiss, *Metallurgical Transactions*, 3, 675 (1972).
11. O. D. Sherby, B. Walser, C. M. Young and E. M. Cady, *Scripta Met.*, 9, 569 (1975).
12. H. W. Hayden, S. Floreen, and P. D. Goodell, *Metallurgical Transactions*, 3, 833 (1972).
13. J. L. Robbins, O. C. Shepard, and O. D. Sherby, *Jnl. Iron and Steel Inst.*, 202, 804 (1964).
14. C. G. Goetzel, *Principles and Present Status of Hot Pressing*, published in the Physics of Powder Metallurgy, McGraw-Hill Publishing Co., New York, (1951).
15. J. D. McClelland, Powder Metallurgy (AIME Publication) (1960).
16. O. H. Henry and J. J. Cordiano, *Trans. AIME*, 166, 520 (1946).
17. P. Schwarzkopf and C. G. Coetzel, *The Iron Age*, 148, 37 (Sept. 4, 1941).
18. C. G. Goetzel, Treatise on Powder Metallurgy, Volume 1, Interscience Publishers, Inc., New York (1949).
19. S. L. Robinson and O. D. Sherby, *Mechanical Behavior of Dispersion Hardened Materials at Elevated Temperatures*, First Annual Report to NASA Lewis Research Center, Cleveland, Ohio (July 1974).

20. Metals Handbook, Volume 1, Eighth Edition, p. 401 (1961).
21. F. Sauerwald and S. Kubik, Z. Elektrochemie, 38, 33 (1932).
22. W. D. Jones, Foundry Trade Journal, 39, 401 (1938).
23. L. Ramqvist, Powder Metallurgy, 9, 1 (1966).
24. J. Williams, The Hot Compacting of Metal Powders, published in Symposium on Powder Metallurgy, p. 112 (1954).
25. F. V. Lenel and G. S. Ansell, Creep Mechanisms and Their Role in the Sintering of Metal Powders, published in Modern Development in Powder Metallurgy, Volume 1, p. 281 (1965).
26. T. Watanabe and S. Karashima, Metallurgical Transactions, 2, 1359 (1971).
27. T. E. Volin, J. S. Benjamin, R. M. Larson and L. Cairns, U. S. Patent 3,865,575, February 11, 1975.

**IV. SYNTHESIS OF NEW TYPES  
OF CATALYST MATERIALS**

**J. P. Collman**

**Professor of Chemistry**

**M. Boudart**

**Professor of Chemical Engineering  
and Chemistry**

**and**

**W. A. Little**

**Professor of Physics**

## A. Synthesis of New Types of Catalysts Materials

J. P. Collman

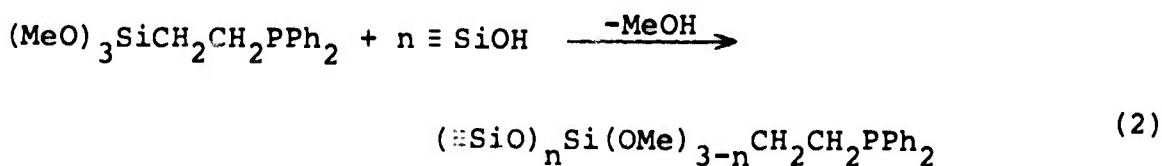
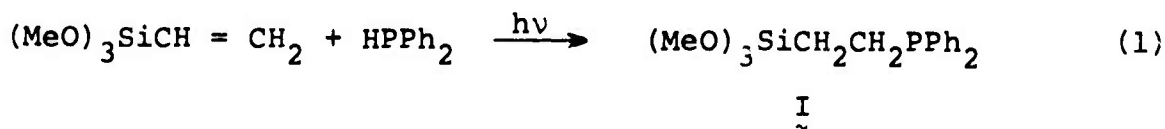
### 1. Introduction

Contained in this report are summaries of three activities we have in the area of catalyst materials: a study of silica bonded heterogeneous-homogeneous catalysts, studies of group V dichalcogenides as catalyst supports, and the preparation of face-to-face (cyclophane) porphyrins. These three seemingly diverse subjects are a part of a general theme whereby we are trying to prepare new catalyst materials--for use in classic catalytic hydrogenation and as catalytic electrodes. The work on silica is directed towards the development of immobilized mononuclear catalytic centers in a material which is chemically inert and has a very high surface area. This project has been frustrated by synthetic difficulties which have no precedent in the chemical literature since this represents the first attempted synthesis of a chelating silated bis phosphine. The second topic, the group V dichalcogenides, deals with attempts to place catalytic centers on molecular dispersions of these highly conducting substances. The third topic is an attempt to make specific binuclear catalysts in order to promote multi-electron redox reactions--ultimately to be applied to a high conducting surface acting as an electrode.

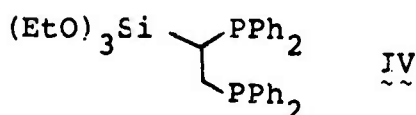
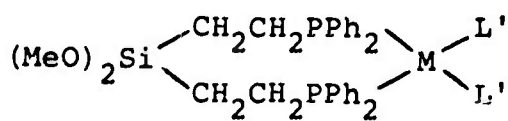
2. Chelating Silica-Bonded Ligands (K. Neuberg)Introduction.

For some time we have been interested in preparing catalysts in which the active centers are discrete transition metal complexes anchored on a silica support. One of the difficulties in preparing such catalysts has been that during preparation or under the reaction conditions of a catalytic experiment some of the complexes lose their integrity and the metal atoms aggregate into active clusters. To overcome this problem a very stable surface complex is needed. With this in mind we have been attempting to synthesize bidentate ligands which can be covalently bound to the silica surface. A support functionalized with these chelating groups should coordinate transition metals more strongly than a silica functionalized with monodentate ligands.

Silicas of the latter type have been prepared in this group<sup>1,2</sup> and by others<sup>3,4</sup>. The approach for a diphenylphosphino ligand is shown in eq. 1 and 2<sup>5</sup>. Unfortunately, this route



cannot be carried over into the bisphosphine system; a divinylsilane, if available, would yield a relatively unstable 8-membered chelate ring (II). We have, therefore, been forced to look for alternate synthetic schemes for bidentate ligands. Three considerations severely restrict the types of schemes which can be proposed: (1) the limited number of methods available for forming Si-C bonds; (2) the necessity of having easily substituted groups (Cl, OR) on the silicon; and (3) the ease of oxidation of many tertiary phosphines. In the previous report<sup>6</sup> we discussed several ligands which were in various stages of synthesis and actual utilization in catalysis. During this past period we have concentrated our efforts on one of these (III) and on a related ligand (IV).



### Results and Discussion.

#### 1. Ligand III

Ligand III was synthesized in this lab by D. Marquardt<sup>7</sup> by the reactions shown below (Fig. 1), where Y is a crystalline

material prepared in three steps from readily available materials. The ligand so obtained was not well-characterized and was very impure. It could not be crystallized or distilled, and purification by column chromatography was avoided at the time as it was believed that the siloxy groups would react with silica and alumina adsorbents<sup>8</sup>.

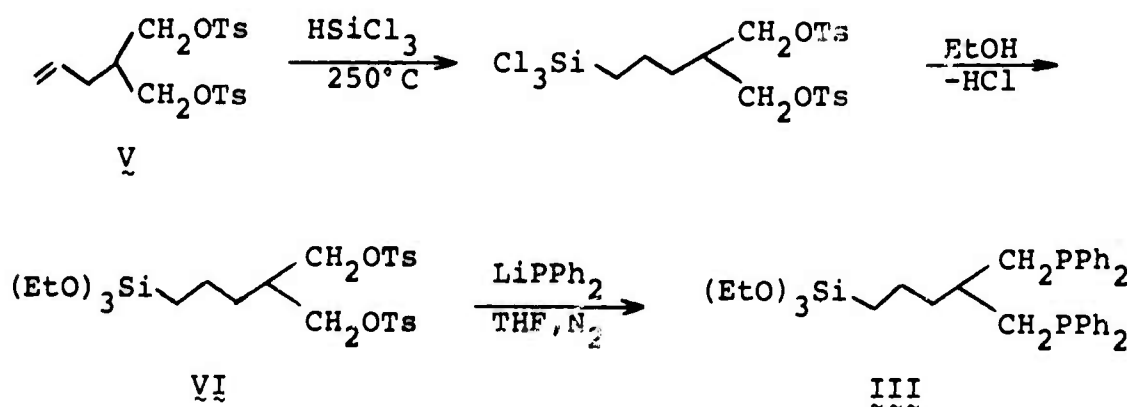
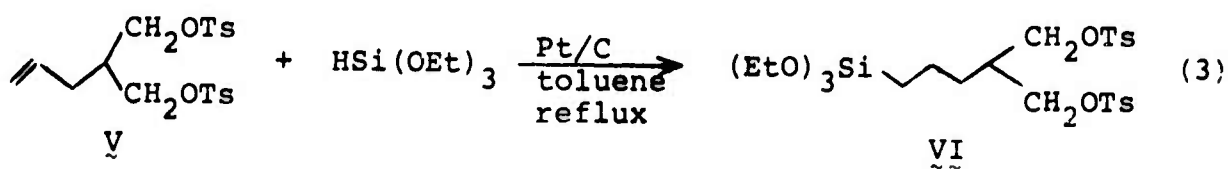


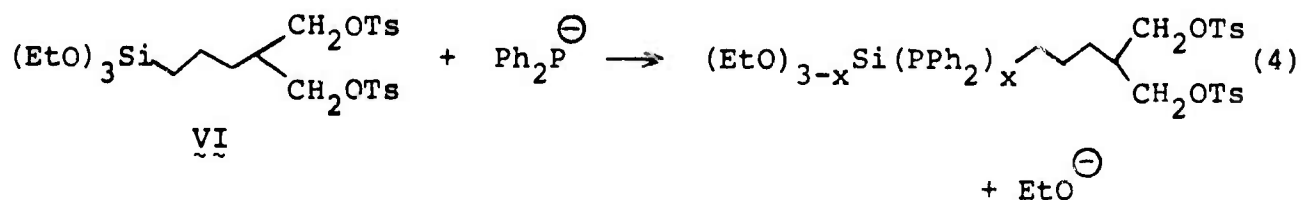
Figure 1

One of our goals has been to develop new methods of preparing and purifying III. In the last report we described a new approach to synthesizing the precursor VI. As shown in eq. 3, the compound can be prepared directly from V in a platinum-on-charcoal-catalyzed hydrosilylation using



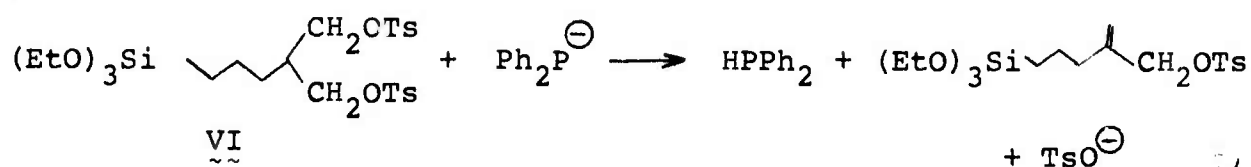
(EtO)<sub>3</sub>SiH (bp 131°C). By nmr, tlc, and C, H analysis, the product of the reaction probably contains less than 5% of the unreacted olefin. We have now extended this reaction to (MeO)<sub>3</sub>SiH (bp 89°C). The greatest degree of conversion to adduct (70-75%) was obtained using a closed reactor and mildly refluxing toluene. As in the case of VI the trimethoxy analog was an uncrystallizable oil.

In the last six month period a considerable amount of time has been devoted to the next step in the synthetic sequence, phosphination with LiPPh<sub>2</sub>. This step is complicated by two side reactions which apparently were not reported by Marquardt. One of these is substitution at silicon giving Si-P bonds (eq. 4).

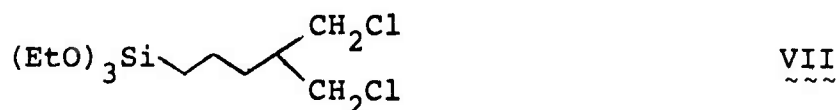


These bonds are easily cleaved by water and alcohols<sup>9</sup>. Therefore, it should be possible to ethanolyze any Si-P bonds which form by adding more than the theoretical amount of ethanol required to destroy the slight excess of LiPPh<sub>2</sub>.

The more serious side reaction is elimination producing HPPh<sub>2</sub> and an olefin (eq. 5). Using Marquardt's conditions (addition of LiPPh<sub>2</sub> solution to a solution of VI, THF, room



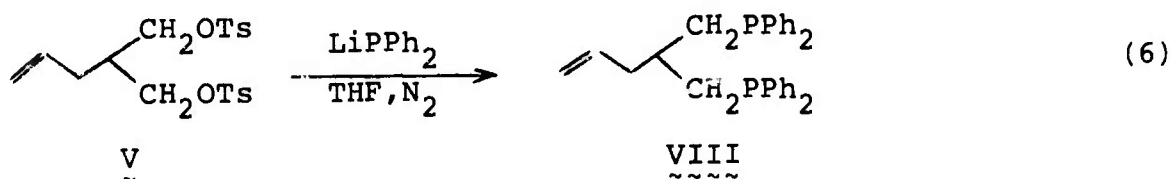
temperature, under  $\text{N}_2$ ) we obtained some of the desired product (III), which was identified by nmr. However, by tlc ( $\text{CHCl}_3$ , silica) the major components of the crude isolated material were  $\text{HPPh}_2$  and an unidentified compound, both of which had much larger  $R_f$  values than expected for III. Our failure to repeat Marquardt's results in this experiment, as well as other lines of evidence, have led us to suspect that Marquardt may have isolated VII rather than VI from the two-stage reaction sequence given in Fig. 1. The competition between elimination and nucleophilic displacement may differ for the two leaving groups  $\text{TsO}^\ominus$  and  $\text{Cl}^\ominus$ <sup>10</sup>.



Other workers were able to reduce the amount of elimination occurring in nucleophilic substitutions of  $\text{MPPh}_2$  on primary tosylates by employing  $\text{KPPh}_2$  rather than  $\text{LiPPh}_2$  or  $\text{NaPPh}_2$ <sup>11</sup>. We tried this reagent, but again  $\text{HPPh}_2$  was one of the major components of the reaction mixture.

With the hope of gaining selectivity for the desired substitution reaction over both elimination and attack at silicon,

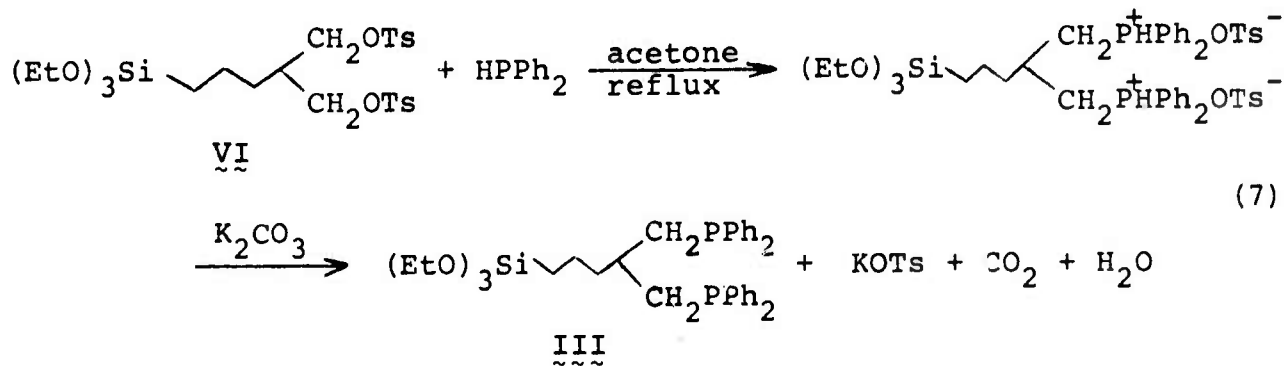
we carried out phosphination reactions at  $-77^{\circ}\text{C}$ . The first two low temperature reactions were worked up in the presence of air, since the work-ups for the model compounds VI and VIII (eq. 6)<sup>7</sup> did not require inert atmosphere. Although by tlc



the low temperature reaction was still not a clean one, for the first time the major components of the crude product were ones having low  $R_f$  values. This looked promising, but in fact nmr indicated that the material isolated in both attempts was not the desired product--the spectra were dominated by aromatic signals with little evidence of ethoxy groups. The crude product was not soluble in  $\text{C}_6\text{H}_6$  or  $\text{CHCl}_3$ , giving emulsions which sometimes formed a precipitate upon standing. Such behavior had first been observed in the  $\text{KPPH}_2$  reaction in which the work-up also was done in air. The behavior may be partially due to incomplete removal of inorganic salts, as a rapid aqueous extraction did increase the solubility of the product in  $\text{CHCl}_3$  in one case. But in the second case, the precipitate which settled out of a benzene solution and was collected by centrifugation was found to be very soluble in  $\text{CHCl}_3$ . We cannot explain these unexpected results. We suspected either polymerization of an alkoxy silicon compound or oxidation of the phosphine.

By repeating the low temperature reaction with the rigorous exclusion of air, we isolated a material which was soluble in  $\text{CHCl}_3$  and  $\text{C}_6\text{H}_6$  and which by nmr (under  $\text{N}_2$ ) appeared to be III in a purer state than was obtained using Marquardt's conditions. However, tlc in air of this crude product still showed the usual pattern of several spots, including a fast moving one which may be  $\text{HPPH}_2$  which was not completely removed by evacuation. We must consider the possibility that the compound is decomposing on the silica or on exposure to air. We, therefore, intend to try tlc in the inert atmosphere box with various adsorbents. We also plan to attempt to purify the crude III by crystallization and by column chromatography in the absence of oxygen. Finally, we are currently studying the low temperature phosphination of the model compound V to determine the best reaction conditions.

Because of the difficulties experienced using alkali metal phosphides, we are now considering an approach using  $\text{HPPH}_2$  as the nucleophile (eq. 7). The reaction of secondary phosphines



with alkyl halides is a known route for the preparation of tertiary phosphines. The intermediate phosphine hydrohalide salts are generally decomposed by use of concentrated sodium hydroxide, conditions which would cause polymerization of the alkoxy silicon compound in eq. 7. Our system would require a weak base such as  $K_2CO_3$ . A preliminary experiment using the model compound V seemed to yield a salt which did not decompose to give VIII upon treatment with  $K_2CO_3$ .

Two other routes to III are shown in Fig. 2. These were tried earlier but without success<sup>7</sup>. An example in the literature<sup>3</sup> involving the direct hydrosilylation of  $p\text{-Ph}_2\text{PC}_6\text{H}_4(\text{CH}_2)_2\text{CH}_2 = \text{CH}_2$  using  $\text{HSiCl}_3$  and UV irradiation prompted us to reinvestigate these approaches.

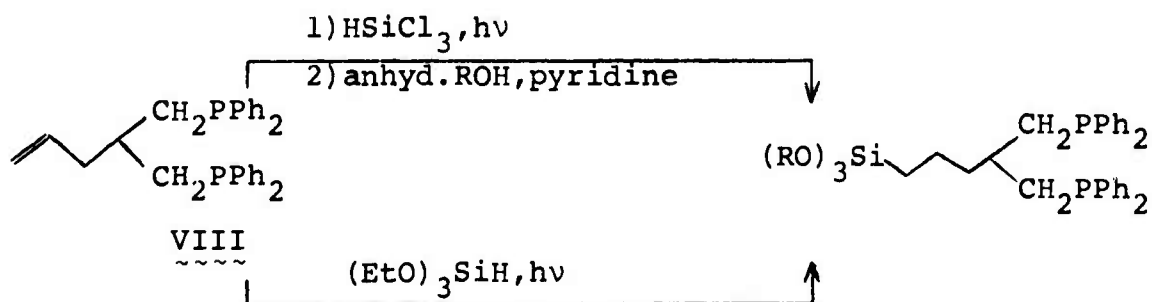


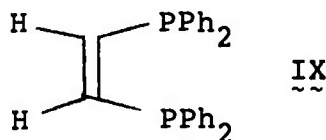
Figure 2

We previously reported that a silyl adduct could be obtained in an impure state by the two-step pathway where  $R = \text{Et}$ <sup>6</sup>. We have repeated this using anhydrous methanol in the

second step to yield the methoxy analog (also impure). Both reactions were worked up in air, but realizing now that compounds like III are very air-sensitive, future work will be done under inert atmosphere. The direct route using  $(\text{EtO})_3\text{SiH}$  did not appear to yield any adduct under the reaction conditions used.

## 2. Ligand IV

Olefin IX can be easily prepared from readily available materials and would be an ideal precursor for an organosilicon bisphosphine ligand (IV) using the routes shown in Figure 2. Again, early attempts to hydrosilylate IX were unsuccessful<sup>7</sup>, but we decided to reexamine the system. Unreacted starting material was recovered in experiments using  $(\text{EtO})_3\text{SiH}$  and (1) benzoyl peroxide as a free radical initiator or (2) platinum-on-charcoal. In the latter case the catalyst was ineffective due to poisoning by IX. Trichlorosilane has also been used. In one case unreacted IX was recovered. In a second attempt the residue after workup in air was insoluble in  $\text{C}_6\text{H}_6$ ,  $\text{CHCl}_3$ , and  $\text{EtOH}$  and may have been a polymer. Work will probably continue on this system.



### Experimental.

Reagents: The following solvents were distilled and stored under nitrogen: toluene (distilled from sodium), benzene (distilled from Aldrich Red-al), and THF (distilled from sodium-benzophenone ketyl). The silanes were distilled and freeze-pump-thaw degassed before use. Chlorodiphenylphosphine was distilled before use. Compound V was prepared as described<sup>7</sup>.

Preparation of VI: Platinum-on-charcoal (0.18 g,  $4.6 \times 10^{-6}$  mol assuming 5% Pt) was placed in a 100 ml side-arm round-bottom flask which was then fitted with a reflux condenser and gas inlet adaptor. The system was evacuated and filled with nitrogen several times and then toluene (20 ml) and  $\text{HSi(OEt)}_3$  (4.0 ml,  $2.2 \times 10^{-2}$  mol) were added by syringe. The reaction mixture was heated to reflux under nitrogen. A solution of V (4.99 g,  $1.18 \times 10^{-2}$  mol) in toluene (15 ml) was similarly prepared under nitrogen and added by syringe to the refluxing mixture during 15-20 min. Reflux was continued for 16 hr. After cooling, the solution was filtered through celite, the celite washed with benzene and ether, the colorless filtrates dried over  $\text{Na}_2\text{SO}_4$  and the solvent finally removed on the rotovap. The residue was heated to  $70^\circ\text{C}$  (bath temperature) under vacuum to remove residual solvent and silane. By tlc ( $\text{CHCl}_3$ , silica) the resulting crude product (6.90 g, 99% yield) contained a small amount of unreacted olefin and an impurity which remained at the origin.

The latter contaminant could be removed by stirring the material over a small amount of silica gel in  $\text{CHCl}_3$ . A portion of the product treated in this fashion gave, after removal of silica, evaporation of  $\text{CHCl}_3$  on the rotovap, and evacuation at  $80^\circ\text{C}$ , purified material having 52.72% C, 6.77% H; calc: C, 53.03%, H, 6.85%. The product had a satisfactory nmr. Note: In a number of preparations the overall yield including silica gel treatment was generally about 82%.

Preparation of the trimethoxy analog of VI: Using the procedure above with  $(\text{MeO})_3\text{SiH}$  and benzene as solvent, the material obtained after a 48 hr. reaction period contained about 40% of the adduct, about 60% unreacted olefin. When the hydrosilylation was carried out in mildly refluxing toluene in a sealed reactor over 48 hr. 70-75% conversion to the organosilicon compound was achieved.

Preparation of  $\text{LiPPh}_2$ : Lithium wire ( $0.41\text{ g}$ ,  $5.9 \times 10^{-2}$  mol) which had been scraped and rinsed with THF was placed in a nitrogen-filled 25 ml side-arm round bottom flask under a blanket of nitrogen. THF (15 ml) was added via needlestock, followed by  $\text{Ph}_2\text{PCl}$  (1.5 ml,  $8.0 \times 10^{-3}$  mol) and the mixture warmed to accelerate the reaction. After about 30 min. the solution had developed a yellow color and the heat was removed. After a further 1 hr. at room temperature, the solution had darkened to orange. The reaction mixture was left overnight, during which

time a dark red color characteristic of  $\text{LiPPh}_2$  radical anion formed. This solution was transferred by needlestock into THF solutions of V or VI prepared under nitrogen. Reaction conditions and workups for these phosphinations will be described in the next report.

#### References

- (1) M. Takeda, Research Report, September, 1973.
- (2) M. Marrocco, Research Report, October, 1973.
- (3) G. Allum, et al., J. Organomet. Chem., 87, 203 (1975).
- (4) A. A. Oswald, L. L. Murrell, and L. J. Boucher, Abstracts, 167th National Meeting of the American Chemical Society, April 1974, Los Angeles, Calif., Petroleum Chem. Division, Items 34 and 35.
- (5) The abbreviation  $\equiv\text{SiOH}$  represents a free surface silanol group on the silica.
- (6) K. Neuberg, Research Report, June, 1975.
- (7) D. N. Marquardt, Ph.D. Thesis, Stanford University, May, 1974.
- (8) See, however, our description<sup>6</sup> of the successful use of silica gel chromatography to purify VI.
- (9) V. Bazant, V. Chvalovsky, and J. Rathousky, Chemistry of Organosilicon Compounds, Vol. I, Academic Press, N. Y. 1965, p. 89.

- (10) Note: The presence of  $\text{HPPh}_2$  is the only indication we have that elimination is occurring. It should be pointed out that  $\text{HPPh}_2$  will also be generated by the ethanolysis of Si-P bonds and by the destruction of unreacted  $\text{LiPPh}_2$ . We do not know to what extent these processes contribute to the observed  $\text{HPPh}_2$ . We have assumed that elimination is the major source.
- (11) J. D. Morrison, personal communication.

### 3. Conducting Catalyst Supports (M. Marrocco)

#### Introduction.

We have a general interest in group V transition metal dichalcogenides ( $MCh_2$ ) as catalyst supports. The potential advantages of these materials lie in their high surface area, the fact that they can be dispersed to the molecular level in organic solvents, in their metallic conductivity, and in their high thermal conductivity. We intend to employ these supports for two general purposes: firstly, as supports for hybrid homogeneous-heterogeneous catalysts comprised of transition metal complexes; and secondly, as supports for electrode catalysts.

In the first application, the hybrid coordination catalysts will be compared with examples using silica as a support. The further possibility of electrochemically activating catalysts on the conducting dichalcogenides is a matter we wish to ultimately examine. The use of group V dichalcogenides as supports for electrode catalysts will be somewhat limited by their electrochemical activity as discussed in our earlier reports. For that reason, we shall also be examining, in the future, graphite materials.

In our last report<sup>1</sup>, we described the introduction of  $RhCl_3$  and the fact that it seemed to have catalytic activity. We have experienced difficulty in introducing transition metal complexes on to these dispersed dichalcogenides. We are also still developing methods for dispersing the dichalcogenides. Beyond the

catalytic activity of the rhodium sites introduced into the dichalcogenides, we are also interested in the nature of these rhodium sites. The principle question is whether or not the rhodium atoms remain as mononuclear coordination complexes or become polynuclear metal crystallites. Following a criteria that we developed earlier with the silica catalysts, we have employed the reduction of aromatic substrates and the development of black coloration as indications of the presence of rhodium metal. The dichalcogenide surfaces might be expected to form coordinate complexes with the rhodium, but we have not yet examined this point experimentally.

In the last report, we briefly described conditions for dispersing  $TaS_2$ . Only two solvents: N-methyl formamide (NMF) and N-methyl acetamide (NMA) can be used to disperse these dichalcogenides. In each case preintercalation of a stoichiometric amount (based on  $TaS_2$ ) of organic material has been found to be necessary. We have employed N-propyl amine in this step for most preparations. Primary amines seem to be the reagent of choice because of their high rate of intercalation. Both amines and amides are known to form complexes with rhodium(III) and some of these are hydrogenation catalysts<sup>4,5</sup>. Formamides are easily decomposed to CO and an amine. The anomalous behavior of amide intercalation is probably due to this decomposition. This could account for Ruthardt's<sup>2</sup> serendipitous

discovery of  $TaS_2$  in MMF dispersions since pure NMR free of methyl amine is not effective. This decomposition is a further problem since carbon monoxide can act as a catalyst poison. The following experiments deal with our preliminary exploration of rhodium catalysts introduced into dispersed group V dichalogenides for dispersing these materials.

#### Experimental.

$TaS_2$  and  $NbSe_2$  were prepared from the elements as described by Di Salvo<sup>3</sup>.  $NbTe_2$  was purchased from Alfa as a freely flowing, black powder and used as obtained. NMR and dimethyl formamide (DMF) were freely distilled from BaO and stored over molecular sieve. N-methyl acetamide was fractionally recrystallized by freezing at 25° and discarding the remaining liquid. Cyclooctene was distilled from CaH and passed through an activated alumina column under nitrogen before use. Cyclooctane, methyl cyclohexane, toluene n-propyl amine and cyclohexyl amine were used as received from Aldrich. Hydrogenations were carried out in Fischer-Porter type pressure bottles having a volume of ca. 90 ml.  $MCh_2$  dispersions were prepared as previously described. All gas chromatography was carried out using an OV-101 column at 100°.

#### Hydrogenation of cyclooctene with $TaS_2$ - $RhCl_3$ NMF.

A:  $RhCl_3 \cdot H_2O_x$  3 mg ( $1.2 \times 10^{-5}$  mol) was dissolved in ca. 5 ml DMF in a Fischer-Porter bottle equipped with a magnetic stir

bar. After flushing the system with  $N_2$ , 0.5 ml (ca. 10-20 mg  $TaS_2$  .04-.08 mmol) of freshly prepared  $TaS_2$  dispersion was added by syringe. This mixture was sonicated for 30 sec. Cyclooctene 0.2 ml (1.55 mmol) was added by syringe. The system was flushed with  $H_2$  and pressurized to 44 psi  $H_2$ . The mixture was stirred at 25°. After 1-2 hr. the pressure no longer dropped. After 12 hr. products were analyzed by GC. Two peaks were observed of nearly equal height. These were identified as cyclooctene and cyclooctane by coinjection with authentic compounds.

B: This experiment was identical to (A) but with 100 mg  $TaS_2$ . No cyclooctane was detected by GC.

Hydrogenation in N-methyl acetamide. C:  $RhCl_3 \cdot H_2O_x$  5 mg ( $2 \times 10^{-5}$  ml) was dissolved in ca. 5 ml N-methyl acetamide in a Fischer-Porter bottle.  $TaS_2$  powder 50 mg (0.2 mmol) was dispersed in N-methyl acetamide with N-propyl amine (16  $\mu$ l (0.2 mmol). N-methyl acetamide freezes at 28°. Mixtures which froze were melted by placing the vessel in a warm water bath. As in (A) 0.5 ml of this dispersion was added under  $N_2$  to  $RhCl_3$  solution. Cyclooctene 0.2 ml (1.55 mmol) was added by syringe and the system was pressurized to 44 psi  $H_2$  after a  $H_2$  flush. After 12 hr. GC indicated complete conversion to cyclooctane. The mixture has turned from the characteristic orange-brown color of  $TaS_2$  dispersion to black.

D: Identical to (C) except 0.2 ml (1.9 mmol) toluene was used as substrate in place of cyclooctene. GC analysis found methyl cyclohexane and no toluene. The mixture was black after 12 hr.

Hydrogenation of arenes in NMF. E: The experimental conditions were identical to those in (A) with 0.2 ml (1.9 mmol) toluene replacing the cyclooctene substrate. No significant pressure drop was observed after 12 hr. The solution was still orange-brown in color at this time. GC analysis was complicated as methyl cyclohexane has a retention time similar to that of NMF which is present in large excess. Addition of water (25 ml) and extraction with diethyl ether (3 x 25 ml) followed by removal of ether resulted in an improved gc analysis. Added methyl-cyclohexane could easily be detected, however, its absence in the reaction mixture could still not be unambiguously ruled out.

F: The experimental conditions were identical to those in (A) with 0.2 ml (2.2 mmol) aniline (passed over activated alumina) replacing the cyclooctene substrate. No significant pressure drop was observed over 12 hr. The solution was still orange-brown. GC analysis showed aniline and no cyclohexyl amine.

Dispersion of MCh<sub>2</sub>. G: NbSe<sub>2</sub> 0.1 g (.4 mmol) crystals were treated with 30  $\mu$ l n-propyl amine (.4 mmol) in 5 ml N-methyl acetamide. Sonication of this system for 5 min. had no visible effect. After 24 hr. in contact with n-propyl amine the NbSe<sub>2</sub> still did not disperse on sonication.

H: NbTe<sub>2</sub> 0.1 g (.29 mmol) powder was treated with 30  $\mu$ l n-propyl amine in 5 ml NMF. Sonication failed to produce a dispersion.

I: NbSe<sub>2</sub> 0.1 g (.4 mmol) crystals were treated with 30  $\mu$ l n-propyl amine (.4 mmol) in 5 ml NMF. Sonication for 1 min. had no effect. After allowing the mixture to stand for 24 hr. sonication for 1 min. produced a reddish dispersion.

#### Discussion.

After demonstration of activity in experiment (A) a number of experiments were carried out using various substrates. In these experiments no hydrogenation was observed. It was subsequently discovered that the unsuccessful runs differed from the original recipe in that the unsuccessful experiments contained an order of magnitude more MCh<sub>2</sub>, as in (B). This is 0.12 equivalent % Rh compared with 1.2 equivalent % Rh in (A). What was first thought to be suspect was the unstable nature of the solvents, NMF and DMF, both of which are known to produce CO by decomposition. Consequently N-methyl acetamide was substituted as in experiments (C) and (D). The MCh<sub>2</sub> component was also reduced to the original concentration. These experiments afforded complete hydrogenation of olefin where as in NMF it was often found that up to half the olefin had not reduced. In experiment (D), however, an aromatic compound was completely hydrogenated. This is disappointing as this result suggests reduction of rhodium to metal particles. This was corroborated by the black color of the material at the end of a run suggesting the presence of rhodium particles, although this has not been verified by electron microscopy. This black color had not been

noted except in N-methyl acetamide. This led to experiments (E) and (F) in which toluene and aniline were subjected to the same conditions except in the NMF-DMF solvent system. The results suggest that the NMF-DMF system is not susceptible to the formation of Rh metal. It remains to be demonstrated that aniline can be reduced in N-methyl acetamide.

It seems at this point that changing the solvent system dramatically effects the nature of the catalytic site. If this is substantiated by further experiments, we will have two extreme cases to study electrochemically. This may prove to be an asset in the interpretation of electrolytic data.

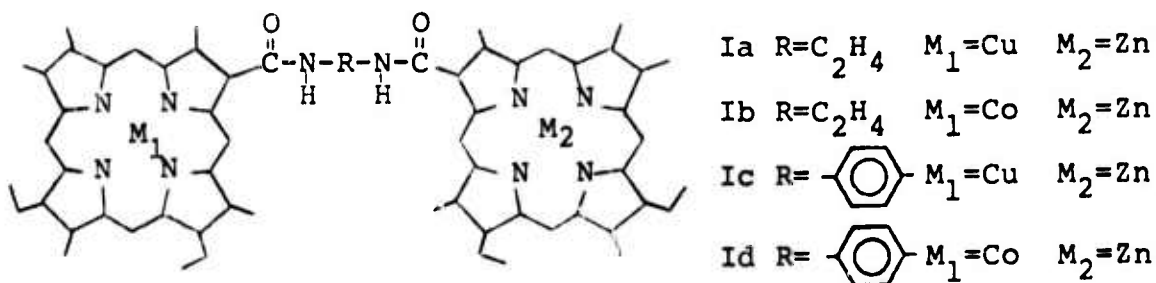
#### References

- (1) M. Marrocco, Long Range Materials Research, ARPA Program, 4010, p. 63, June (1975).
- (2) R. Ruthardt, Ph.D. Thesis, Ludwig Maximilian University (1968).
- (3) F. J. DiSalvo, Ph.D. Thesis, Stanford University (1971).
- (4) I. Jardine and F. J. McQuillin, Chem. Comm., 477 (1969).
- (5) B. R. James and G. J. Rempel, Discuss. Faraday Soc., 46, 48 (1968).

4. "Face-to-Face Porphyrins" (T. Halbert and B. Trovrog)Introduction.

The multi-electron reduction of small diatomic molecules such as  $O_2$  and  $N_2$  is a topic of much current interest. Sequential reduction of such molecules in one electron steps produces thermodynamically unfavorable intermediates, thus ruling out such pathways in the search for rapid and efficient reduction systems. It has been a goal of this group to synthesize bimetallic complexes in which both metals can simultaneously coordinate and reduce diatomic substrate molecules. Such complexes would, hopefully, enable direct four and six electron reduction, thus avoiding the unfavorable intermediates.

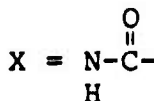
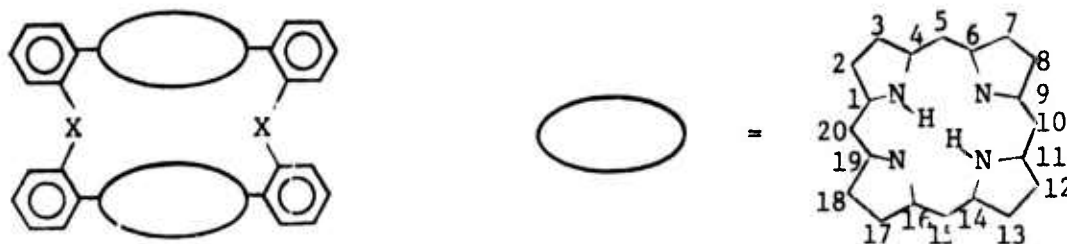
The search for such complexes has led us to propose a new class of so-called "face-to-face" porphyrins. These "face-to-face" porphyrins should contain two porphyrins, covalently linked in such a fashion as to bring the two metal containing sites close together. The only previously known examples of covalently linked bis-porphyrins are those of Dolphin and Gouterman<sup>1</sup>, shown below.



Studies on the lifetimes of the Zn porphyrin triplet states at 77°K in 2-methyl THF glasses have led to the conclusion that in the binary porphyrins Ia and Ib, there is an electronic interaction between the two porphyrins. This interaction, it is argued, requires orbital overlap of the two porphyrins. The binary porphyrins Ic and Id, which are geometrical constrained from such overlap, exhibit no electronic interaction.

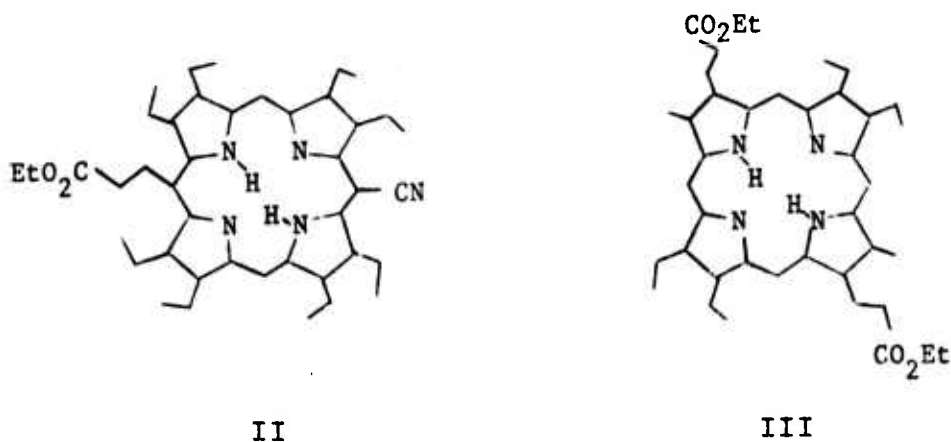
Synthetic considerations have given rise to three different approaches in our group to the construction of bis-porphyrins with more clearly defined "face-to-face" geometry.

1. Two covalent linkages, "trans" disposed.



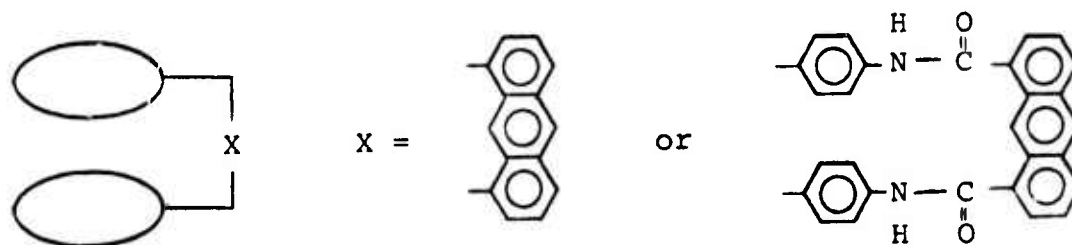
This approach involves the synthesis and condensation of 5 $\alpha$ , 15 $\alpha$  di(o-aminophenyl) and 5 $\alpha$ , 15 $\alpha$  di(o-carboxy phenyl) porphyrins. Synthetic routes to such porphyrins have been

proposed, but actual synthesis has just been initiated. Fuhrhop has reported<sup>2</sup> the small scale synthesis of a similar "trans" disposed difunctional porphyrin(II) as has Ogoshi<sup>3</sup>(III).



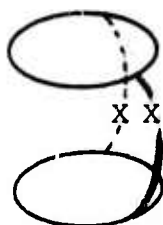
An earlier attempt to synthesize "face-to-face" porphyrins in our laboratories by bridging at four positions between two tetra *o*-substituted phenyl porphyrins was abandoned because of the high probability for polymerization.

## 2. One covalent linkage.

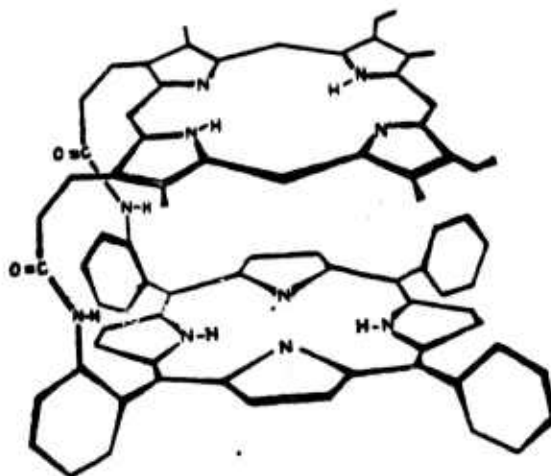


Synthetic work on this approach has again, just begun, and will not be discussed further in this report.

3. Two covalent linkages, "cis" disposed.



The main representative of this class, IV, is shown below.

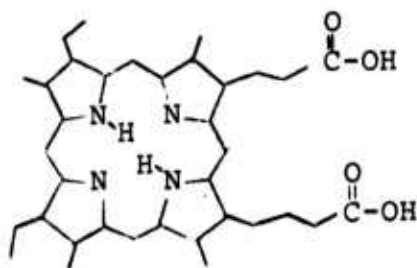


IV

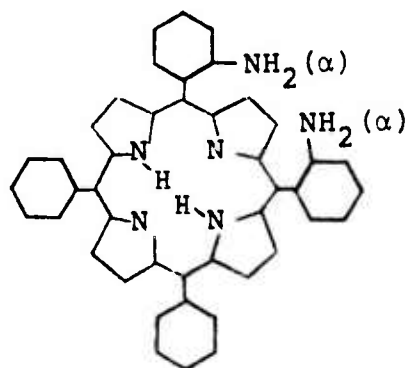
This approach was designed to take advantage of the available biological porphyrins, which have "cis" disposed propionic acid side chains. The synthesis of IV and its  $\text{Cu}^{\text{II}}$  and  $\text{Co}^{\text{II}}$  derivatives has recently been completed, and will be the subject of the remainder of this technical report.

### Results and Discussion.

Synthesis of the Ligand. The synthesis of the "clam-shell" porphyrin (IV) is convergent, involving the separate synthesis of a biological half (V) and a tetra-aryl half (VI) followed by their ultimate combination. The synthesis of (V), known commonly as mesoporphyrin IX, has been described in detail in the literature<sup>3</sup>.



V (mesoporphyrin IX)



VI (5 $\alpha$ , 10 $\alpha$  di(o-aminophenyl)  
15,20-diphenyl porphyrin)

The synthesis of the diamino porphyrin VI was approached by the "mixed" condensation of o-nitrobenzaldehyde, benzaldehyde, and pyrrole. Similar "mixed aldehyde" condensations have been reported recently by Ibers, Anton, and coworkers<sup>5</sup>. This condensation produces a mixture of tetra-aryl porphyrins which can be easily separated chromatographically into four components. The first is the well known tetraphenyl porphyrin (TPP), and the second is 5-(o-nitrophenyl)-10,15,20-triphenyl porphyrin (VII). Although VII is of no value for the "face-to-face"

porphyrin synthesis, the corresponding amino porphyrin, resulting from reduction of the nitro group, is of interest in the synthesis of hemoprotein models and has, therefore, been isolated and characterized. The third component contains a mixture of dinitro porphyrin isomers from which the diamino porphyrin VI is ultimately derived. The fourth component contains a mixture of di and trinitro porphyrins.

Reduction of the third component with  $\text{SnCl}_2$  in HCl gives two major diamino porphyrins VIIIa and VIIIb. After chromatographic separation, each was subjected to heating in refluxing toluene solution for  $\frac{1}{2}$  hour. Isomer VIIIa is converted to an equal mixture of VIIIa and VI, an atropisomeric diamino porphyrin with small r.f. on silica T.L.C. The isomer VIIIb is converted to an equal mixture of VIIIb and VIIIc, again an atropisomeric diamino porphyrin, but with larger r.f. on silica T.L.C.

The nmr spectra in the pyrrole proton region of diamino isomers VIIIa and VIIIb are shown in Figure 1. Based on these nmr, and on the relative T.L.C. r.f. values, the four compounds have been assigned the structures shown schematically below. The desired diamino porphyrin atropisomer, VI, can be produced by thermal equilibration of VIIIa, followed by silica gel chromatography.

64-A

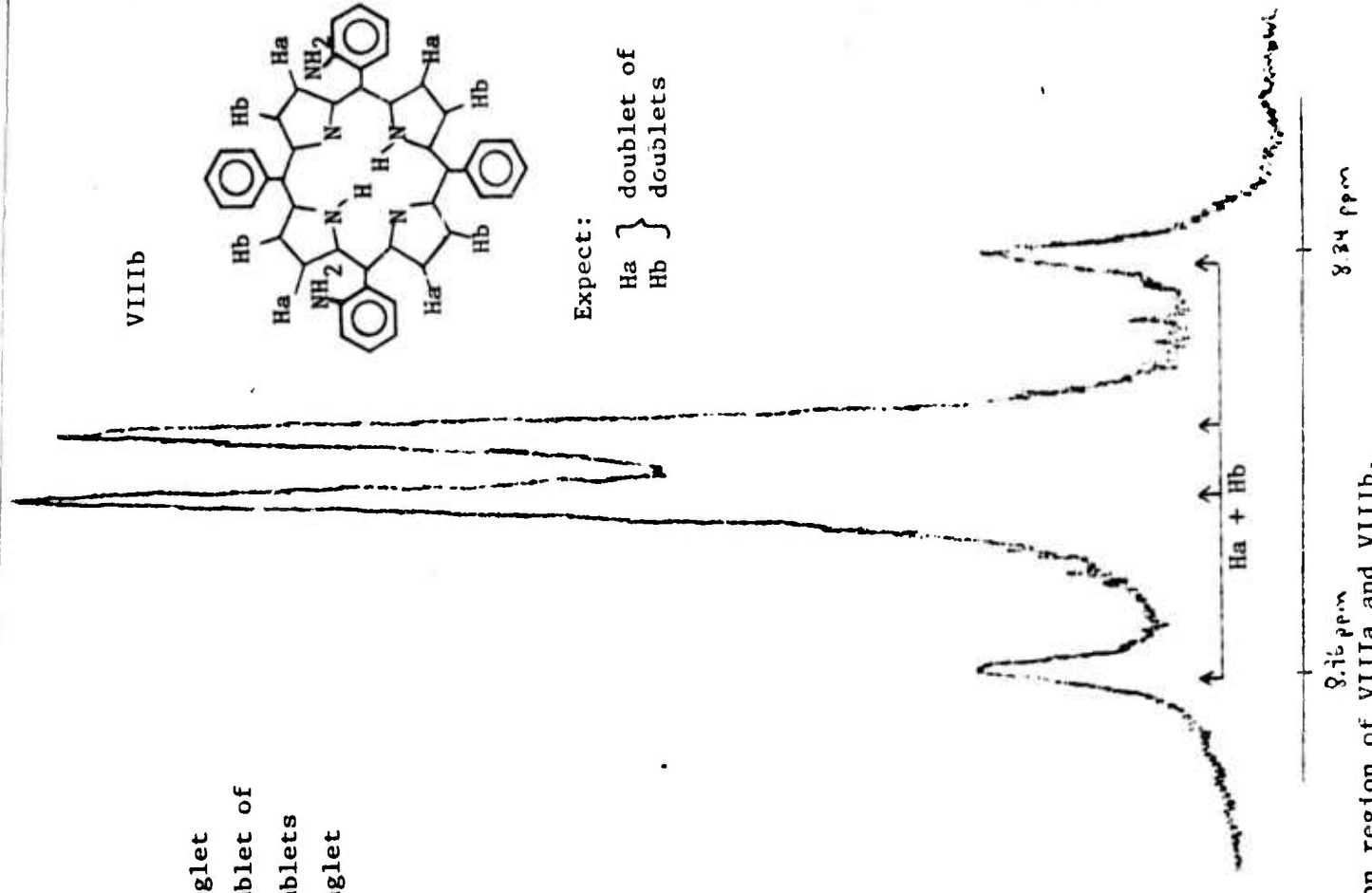
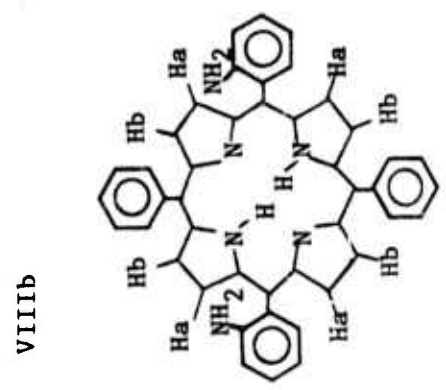
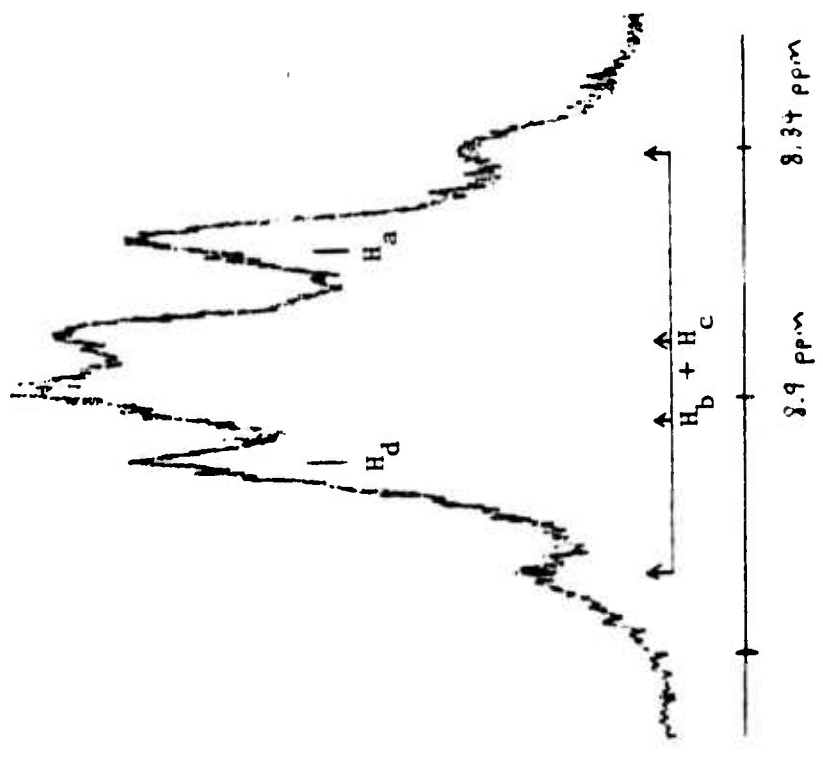
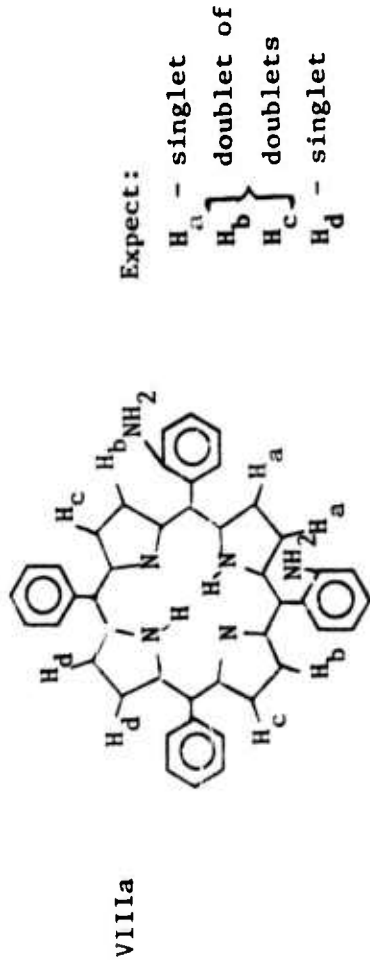


Figure 1. Nmr of pyrrole proton region of VIIIa and VIIIb.



Table I. Electronic Spectra

<u>Porphyrin</u>	<u>Solvent</u>	<u>Ligand</u>	<u>Soret</u>	<u>Visible</u>
diaminoporphyrim VI	benzene	--	422	515, 549, 590, 647
Meso PDME*	benzene	--	402	500, 532, 570, 624
clamshell (IV)	benzene	--	403,422	500(s), 509,530(s), 545(s)
	benzene			
Cu <sup>II</sup> TPP	benzene	--	417	537
Cu <sup>II</sup> Meso PDME*	benzene	--	399	524, 561
Cu <sup>II</sup> clamshell (IV)	benzene	--	399,417	537, 562
Co <sup>II</sup> TPP	toluene <sup>‡</sup>	--	412	528
Co <sup>II</sup> Meso PDME*	toluene <sup>‡</sup>	--	395	518, 553
Co <sup>II</sup> clamshell (X)	toluene <sup>‡</sup>	--	394,413	524, 552

\*Meso PDME = mesoporphyrin IX dimethylester.

<sup>‡</sup>Inert atmosphere.

perturbation of the visible spectra of either the meso or tetra-aryl porphyrin half. The infrared spectra (KBr pellet) show a single broad carbonyl band centered at  $1688\text{ cm}^{-1}$ , characteristic of an amide.

Metal Derivatives and Visible Spectra. Molecular models of the "clamshell" porphyrin IV indicate that the distance between the porphyrin centers can vary from 4 to 12 Å. Because the "face-to-face" conformation of IV is not rigidly enforced by the structure, initial studies have been directed toward demonstrating an interaction between the two metal sites in the  $\text{Cu}^{\text{II}}$  and  $\text{Co}^{\text{II}}$  derivatives. The  $\text{Cu}^{\text{II}}$  derivative (IX) was prepared by the procedure of Adler<sup>6</sup> and purified chromatographically. The  $\text{Co}^{\text{II}}$  derivative (X) was prepared by reaction of IV with anhydrous  $\text{CoCl}_2$  and 2,6 lutidine in THF. The procedure was carried out in inert atmosphere, and the product purified by chromatography and recrystallization.

The peak positions in the visible spectra of Cu "clamshell", IX, and Co "clamshell", X, in noncoordinating solvents are indicated in Table 1. The spectra of  $\text{Cu}^{\text{II}}$  and  $\text{Co}^{\text{II}}$  TPP, and  $\text{Cu}^{\text{II}}$  and  $\text{Co}^{\text{II}}$  mesoporphyrin dimethylester are included for comparison. The "clamshell" spectra appear as a simple superposition of the spectra of the two independent halves. Therefore, no information about possible metal-metal interaction or "clamshell" geometry has been obtained from visible spectroscopy.

### ESR of Metalloporphyrins

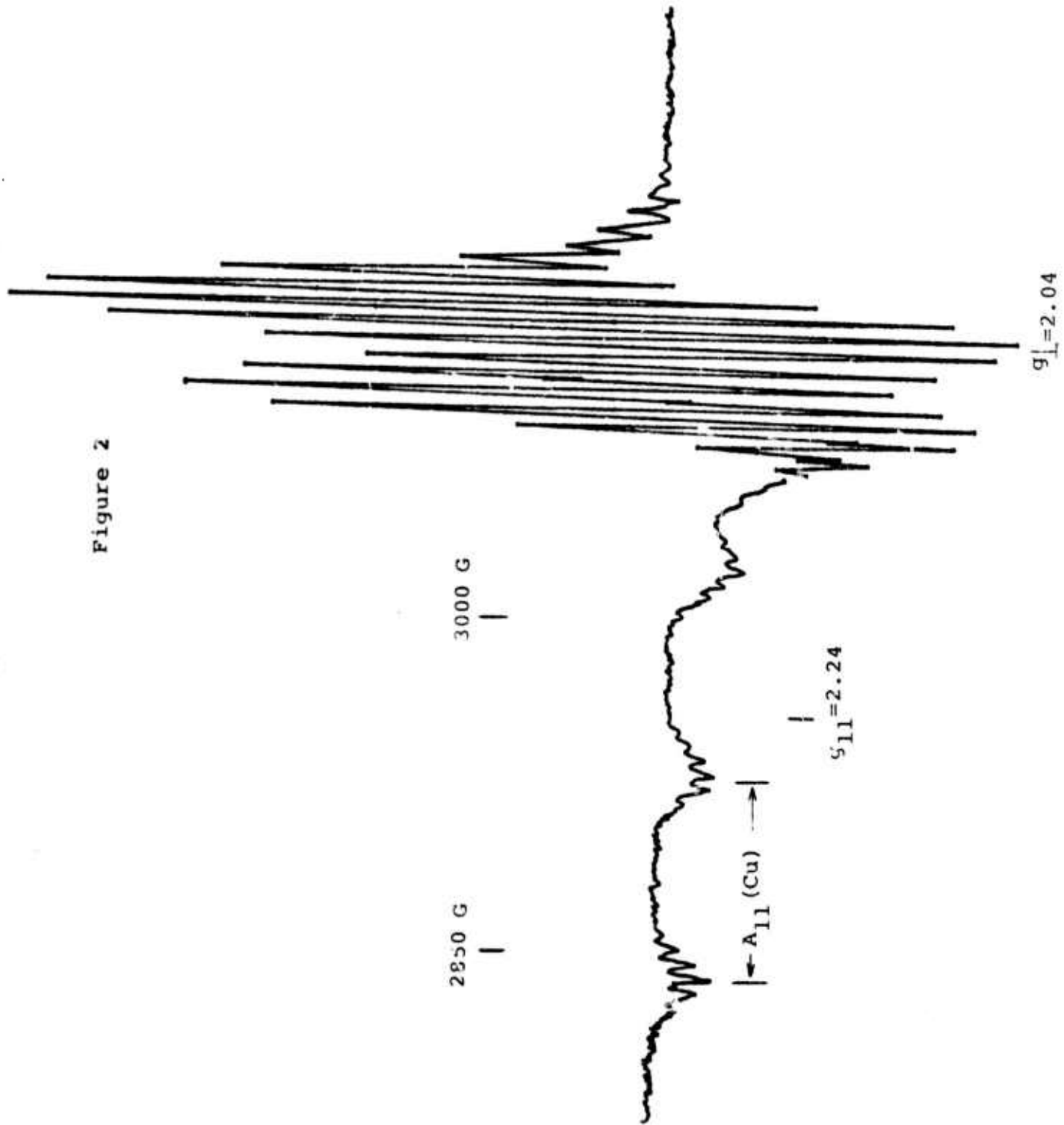
A primary objective in the study of the bimetallic clamshell derivatives is the determination of the metal-metal internuclear separation.

Electron spin resonance spectroscopy (esr) of derivatives containing two paramagnetic metal centers can yield such information. The esr of the Cu(II) clamshell and the Co(II) clamshell will be discussed below.

### ESR of Metalloporphyrin Monomers

Before the esr of bimetallic derivatives are presented, it is necessary to understand the origin of spectral features of monomeric metalloporphyrins. The esr at  $-170^{\circ}\text{C}$  of Cu(TpivPP) (TpivPP is meso-tetra( $\alpha$ -pivalamidophenyl) porphyrin) in a N-methylimidazole (N-MeImid.)/toluene glass is shown in Figure 2. Cu (TpivPP) is a  $d^9$  complex whose one unpaired electron resides in a predominantly copper  $d_{x^2-y^2}$  orbital. The spectrum is axial in appearance due to the  $C_{4v}$  symmetry of the complex and shows low field parallel and high field perpendicular regions. The fact that copper possesses  $I=3/2$  splits both the parallel and perpendicular regions into four hyperfine lines, as indicated. Additionally, since the copper  $x^2-y^2$  orbital overlaps with the porphyrin ligand orbitals, unpaired spin is delocalized onto the porphyrin nitrogen, resulting in the appearance of nitrogen superhyperfine ( $N\ I=1$ ). This superhyperfine is the source of the splitting in the parallel components (partially unresolved) and

Figure 2



in the perpendicular components. The spin Hamiltonian parameters which describe this as well as other systems studied are listed in Table II. The changes observed within this table are typical for adduct formation of Cu(TpivPP) with the nitrogen donors present.

The esr spectrum of Co(TPP) at  $-170^{\circ}\text{C}$  in toluene glass is shown in Figure 3. This spectrum is that of an  $S=\frac{1}{2}$  system and also shows axial symmetry. Cobalt, which possesses  $I=7/2$ , causes an eight-fold splitting in both the parallel and perpendicular regions. The spin Hamiltonian parameters;  $g_{\parallel}=2.05$ ,  $A_{\parallel}=142 \times 10^{-4} \text{ cm}^{-1}$ ,  $g_{\perp}=2.85$ ,  $A_{\perp}=206 \times 10^{-4} \text{ cm}^{-1}$  are characteristic of a cobalt  $(d_z^2)^1$  orbital occupation.

Addition of N-MeImid to the cobalt(II) porphyrins causes a dramatic change in the esr (Figure 4). An obvious feature is the three-fold splitting in the eight cobalt parallel hyperfine components. This is indicative of coordination of one N-Me Imid. along the z axis ( $I=1$  for nitrogen). The spin Hamiltonian values for these cobalt systems are also listed in Table II.

#### ESR of Bimetallic Clamshell Derivatives

When two metal centers possessing spin moments  $\bar{S}_1$  and  $\bar{S}_2$  are present in the same molecule, it is possible these spins can interact to give a total resultant spin  $\bar{S}$ , given by  $\bar{S}=\bar{S}_1+\bar{S}_2$ . This coupling gives rise to a singlet ( $S=0$ ) and a triplet ( $S=1$ ) state, separated by an energy,  $J$  (Figure 5a). Within the triplet state, the three-fold  $m_s=+1, 0, -1$  manifold is often split by a

Table II  
 Metalloporphyrin ESR Spectra at  $-170^{\circ}\text{C}$

<u>Complex</u>	<u>Solvent</u>	<u><math>g_{11}</math></u>	<u><math>g_{\perp}</math></u>	<u><math>\frac{A_{11}}{4} \text{ cm}^{-1}</math> (<math>\times 10^4 \text{ cm}^{-1}</math>)</u>	<u><math>\frac{A_{\perp}}{4} \text{ cm}^{-1}</math> (<math>\times 10^4 \text{ cm}^{-1}</math>)</u>
Cu(TpivPP)	toluene	2.20	2.03	210	30
Cu(TpivPP)	toluene/N-MeImid	2.24	2.04	197	30
Cu(TpivPP)	toluene/pyridine	2.23	2.04	192	30
Co(TPP)	toluene	2.05	2.85	142	206
Co(TPP)	toluene/N-Me-Imid	2.09	2.32	76	$\leq 10$

Figure 3

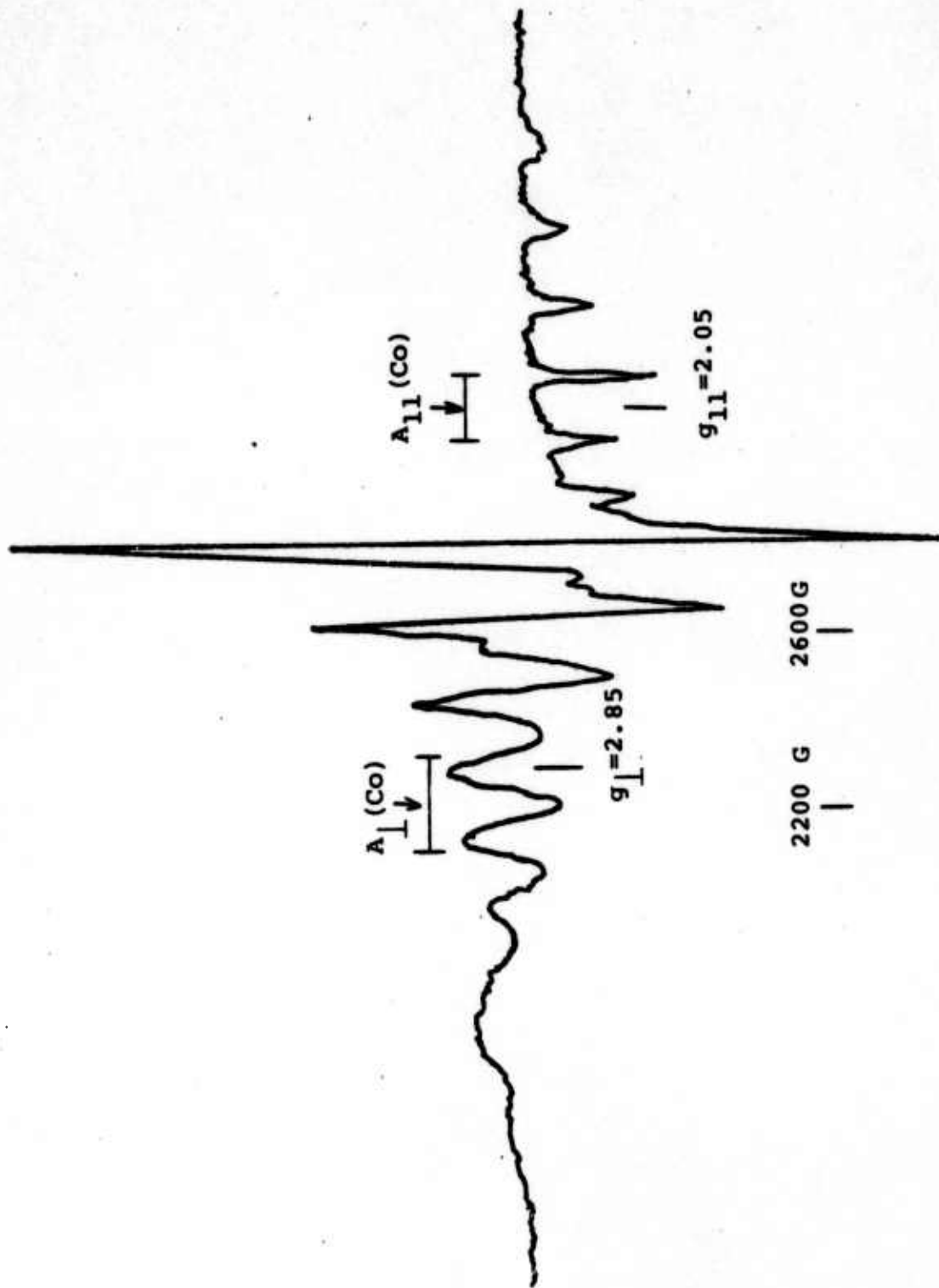
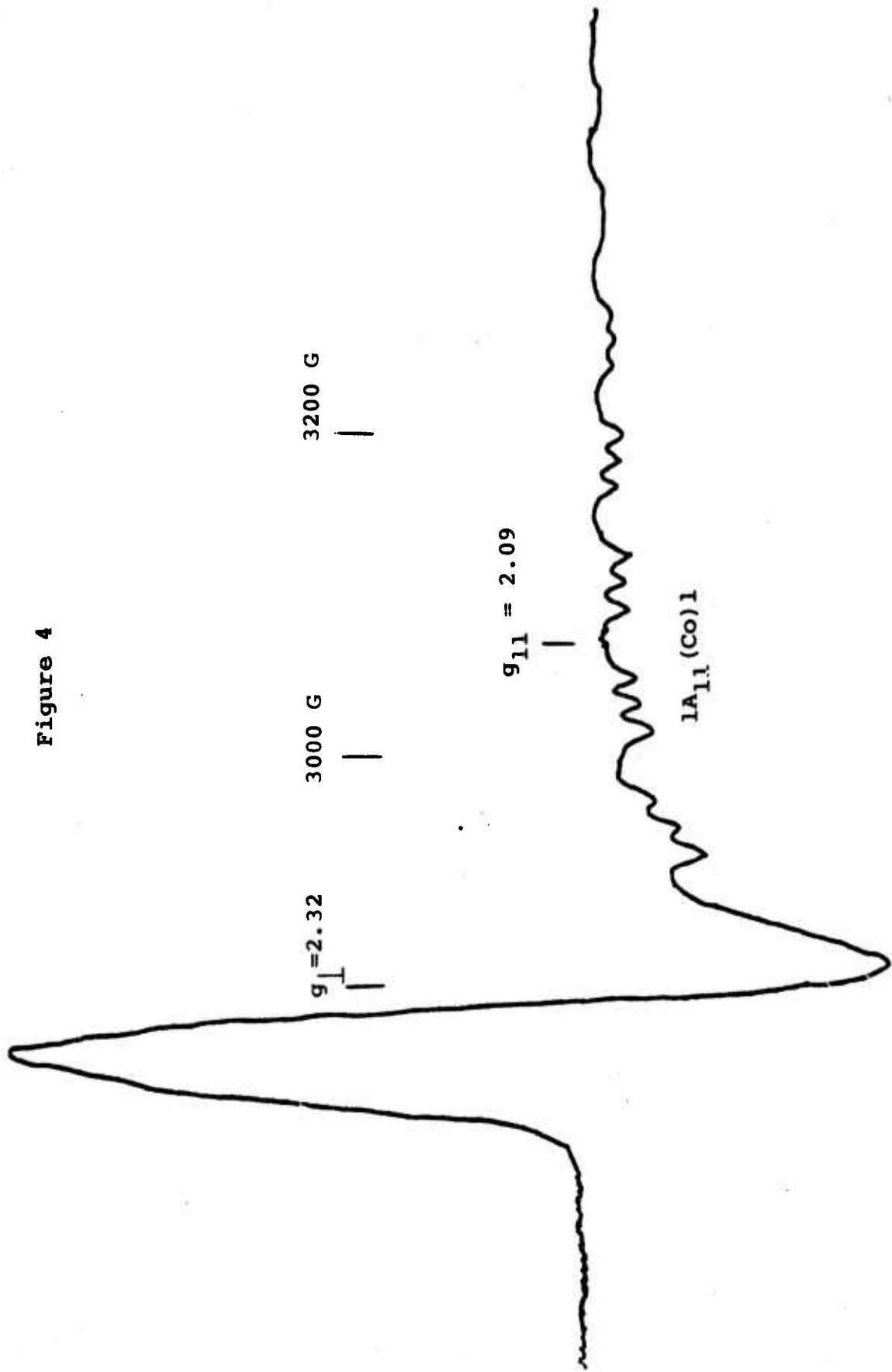


Figure 4

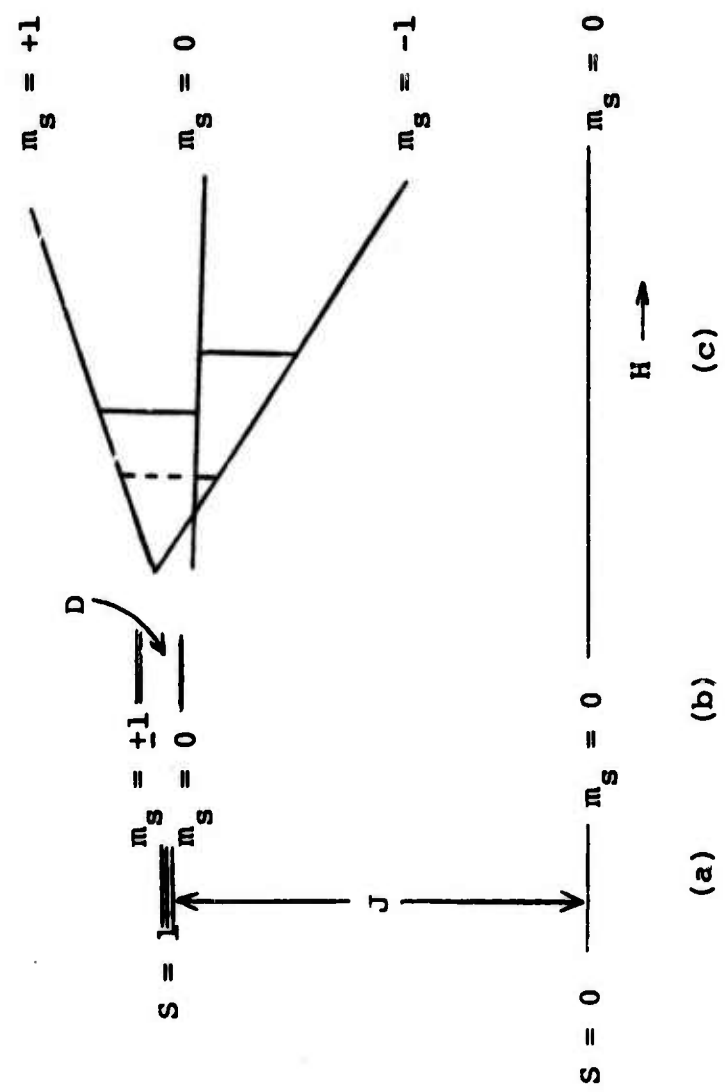


"zero field splitting" parameter,  $D$  (Figure 5b). Figure 5c shows the effect of a magnetic field on such a system. Allowed esr transitions, which are characterized by  $\Delta M_s = \pm 1$ , are shown by solid vertical lines. The " $\Delta M_s = 2$ " transition, which gains some allowedness in transition metal dimers is depicted by a dotted line. Returning to the  $\Delta M_s = \pm 1$  transitions, it is important to note that when  $D=0$ , both transitions (i.e.  $M_s = -1 \rightarrow 0$  and  $m_s = 0 \rightarrow +1$ ) occur at the same magnetic field strength. It should be pointed out that in the particular case of copper(II) porphyrins, each vertical line in this figure represents a spectrum similar to that in Figure 2. Thus when  $D \neq 0$ , one expects to observe two parallel regions and two perpendicular regions. It should also be noted that within the  $S=1$  triplet state,  $I=3$  giving rise to  $M_I = 3, 2, 1, 0, -1, -2, -3$ . Thus, each parallel and perpendicular region should be split into seven copper hyperfine components instead of four from the  $S=\frac{1}{2}$ ,  $I=3/2$  system of Figure 2. Such features have been observed in a variety of  $d^1$  and  $d^9$  systems<sup>7-12</sup>, however this study constitutes the first of this kind on a bimetallic porphyrin system.

Within the  $S=1$  esr, the separation between parallel regions is approximately  $2D$ , that between perpendicular regions approximately  $D$ . The "zero field splitting" parameter  $D$  can be analyzed to yield metal-metal distances. Briefly, the  $D$  value observed,  $D_{\text{obs}}$ , is a sum of two terms<sup>8,9</sup>,

$$D_{\text{obs}} = D_{\text{pseudo}} + D_{\text{dd}}$$

Figure 5



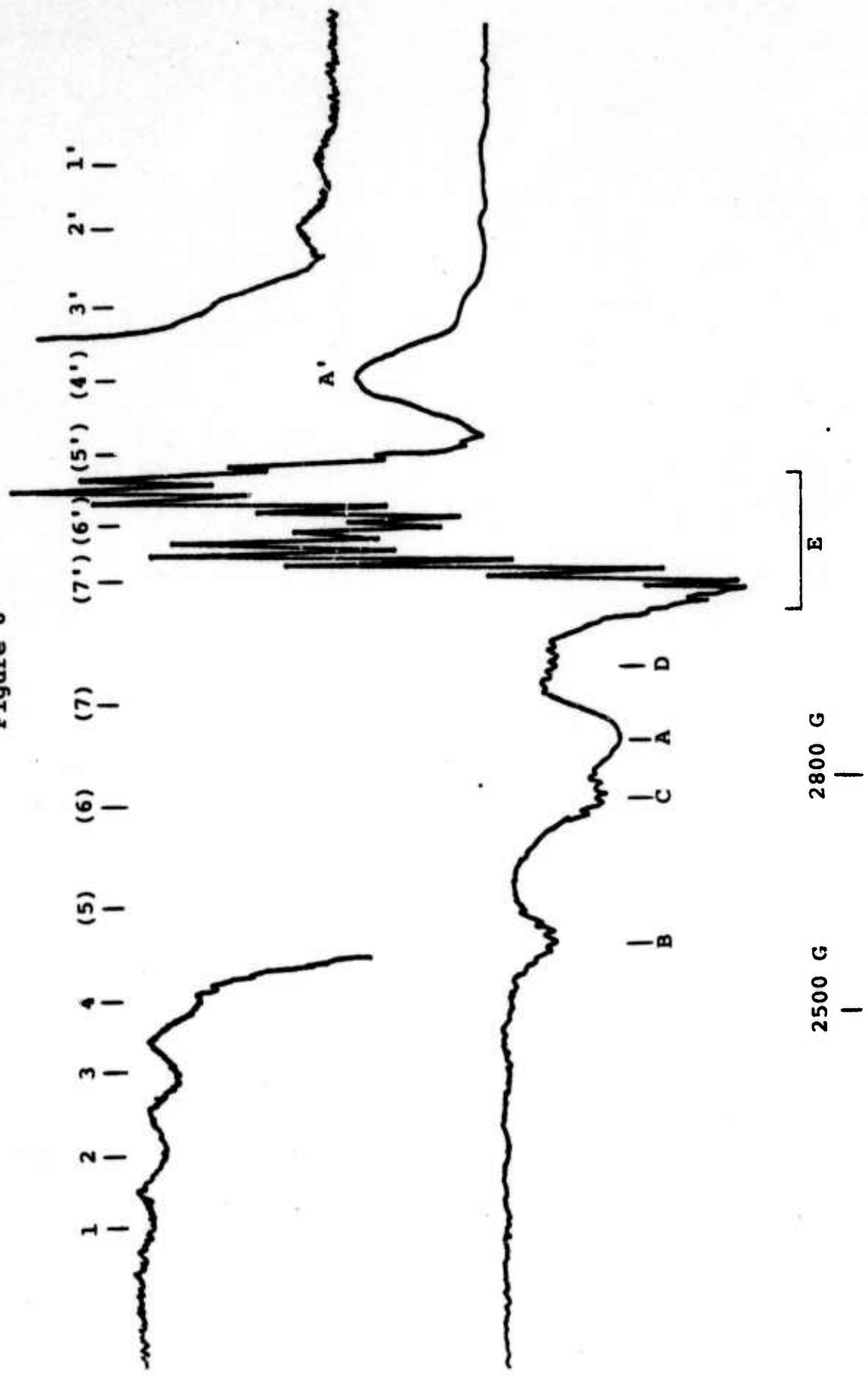
$D_{dd}$  arises from the dipole-dipole interaction of the two spins.  $D_{psuedo}$  arises from spin orbit coupling with the singlet state and is directly proportioned to  $J$ . In previous work it has been found that  $D_{dd}$  was from five to thirty times the magnitude of  $D_{psuedo}$ <sup>8,9</sup>.  $D_{psuedo}$  could then be neglected without a major effect on the metal-metal distances calculated. With this assumption,  $R$ , the metal-metal distance, is given by:

$$R = (0.650 g_{11}^2 / D_{dd})^{1/3}$$

Figure 6 shows the esr of the Cu(II) clamshell in a N-MeImid./toluene glass at -170 C. The spectrum is complex, but can be interpreted as a composite of two signals; one characteristic of two interacting metal centers and another of very weakly interacting centers. Resonances 1,1', 2,2', 3,3' and 4 appear to arise from a signal due to two interacting metal centers and are the outermost components of the two parallel regions. The likely positions of the other parallel lines are indicated in parentheses. Resonances A and A' are tentatively assigned to the two perpendicular components arising from the interacting species. The splitting between the parallel regions is  $842 \times 10^{-4} \text{ cm}^{-1}$ , that between the perpendicular regions  $387 \times 10^{-4} \text{ cm}^{-1}$ .

Resonances B, C, and D are tentatively assigned to those of the parallel components arising from a species where the two metals are interacting very weakly, if at all, and appear very similar to those of Cu(TpivPP) in Figure 2. The perpendicular region, E, also appears very similar to that in Figure 2.

Figure 6



Further evidence for the presence of a species containing interacting metal centers comes from the appearance of the " $\Delta m_s = 2$ " transition (see Figure 7). This region of the spectrum can also be analyzed for R utilizing the relation

$$H_{\min} = [ \omega_0^2 - \frac{4}{3} D_{dd}^2 ]^{1/2} / 2g_{11}\beta$$

where  $H_{\min}$  is the position of the  $M_I = 0$  line in the " $\Delta M_S = 2$ " transition,  $\omega_0$  is the esr spectrometer frequency and  $\beta$  is the bohr magneton.

One can then calculate D, and subsequently R by three methods; the  $\Delta M_S = \pm 1$  parallel region, the  $\Delta M_S = \pm 1$  perpendicular regions, and the " $\Delta M_S = 2$ " region. These parameters are listed in Table III. It should be emphasized that in view of the assumptions discussed above, these values are lower limits to the actual internuclear separation. The R value calculated, 4.2 - 4.4 Å, however, is approximately that for the closest approach for the two porphyrins, based on molecular models. In addition to the esr in Figure 6, two other Cu clamshell systems have been studied; a pyridine/toluene solution and a base free toluene solution. Both systems exhibit spectra very similar to that in Figures 6 and 7.

The esr of the Co(II) clamshell in toluene at  $-170^\circ\text{C}$  is shown in Figure 8. It is interesting to note that zero-

Figure 7

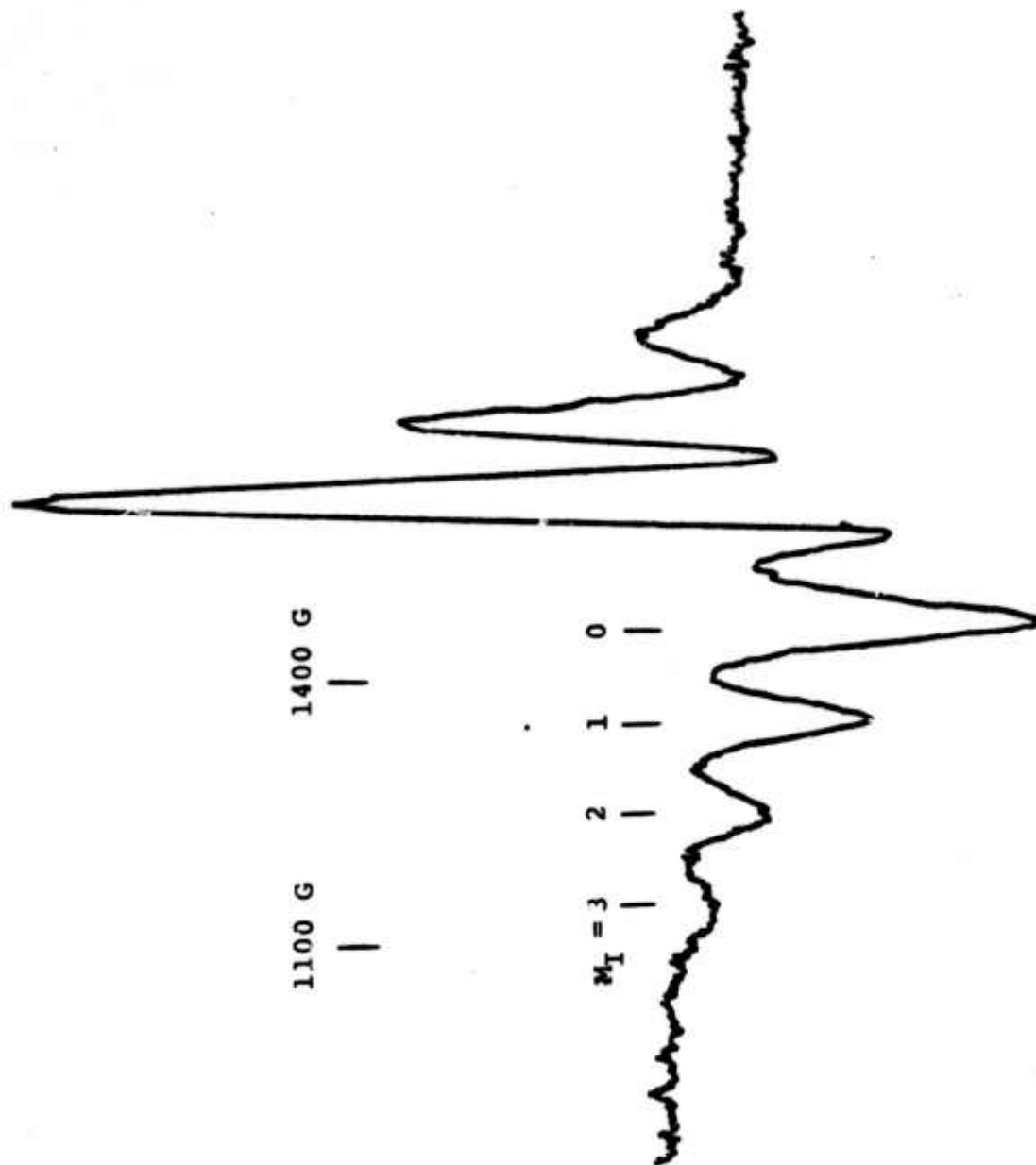


Table III

ESR of Paramagnetic Bimetallic Clamshell Porphyrins at  $-170^{\circ}\text{C}$ 

<u>Complex</u>	<u>Solvent</u>	$g_{\parallel}$	$g_{\perp}$	$A_{\parallel}^a$	$A_{\perp}^a$	$D^a$	$R^b$
Cu(II) clamshell	N-MeImid./toluene						
Features due to weakly interacting metals:		2.21	2.04	201	30	--	--
Features due to interacting metals:		2.19	2.06	92	-- <sup>c</sup>	421 <sup>d</sup>	4.22 <sup>d</sup>
						387 <sup>e</sup>	4.34 <sup>e</sup>
						382 <sup>f</sup>	4.37 <sup>f</sup>
Co(II) clamshell	toluene	2.03	2.53	111	94	--	--

<sup>a</sup>In  $10^{-4} \text{ cm}^{-1}$ .

<sup>b</sup> $R$  in Å.

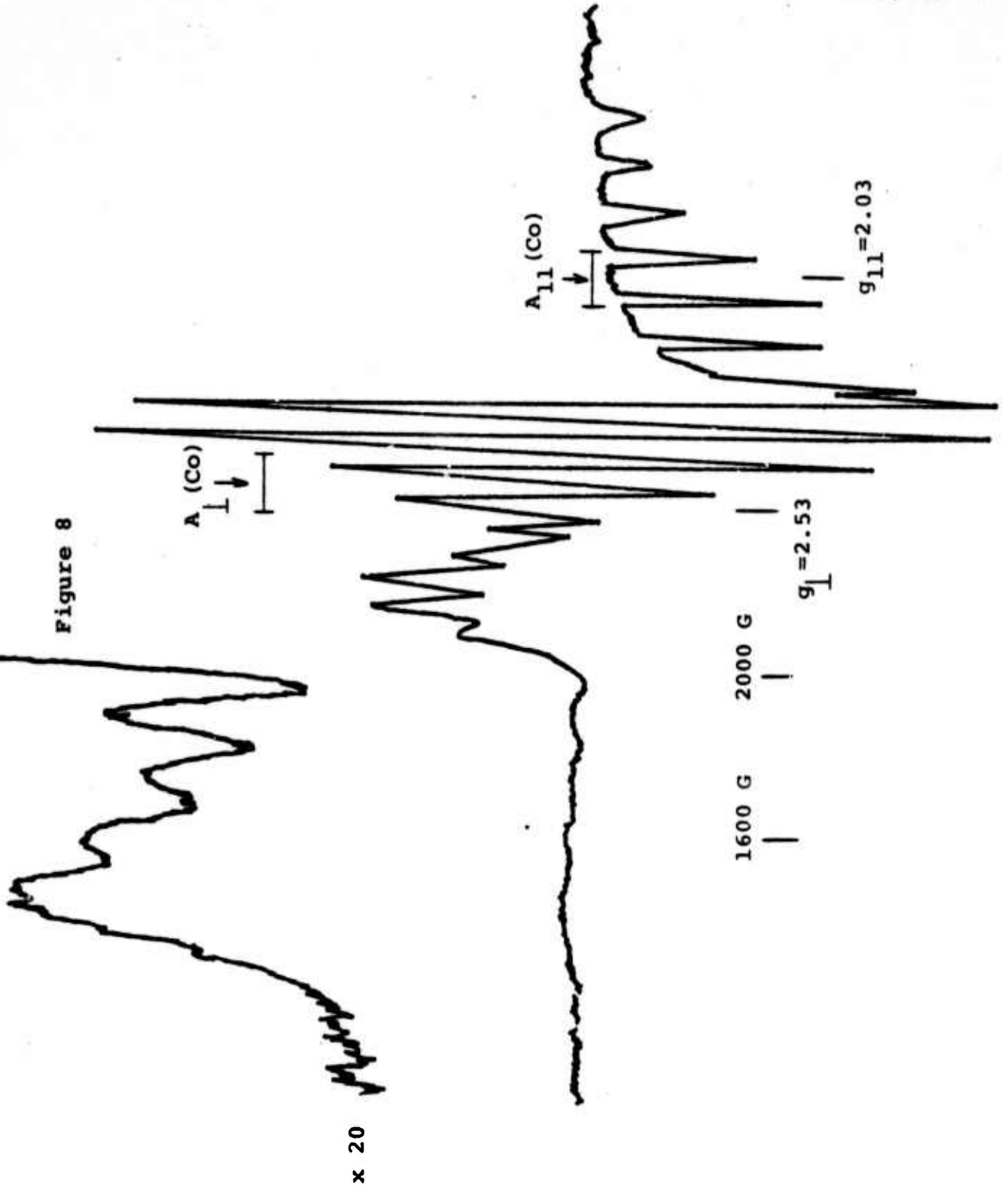
<sup>c</sup>Too small to observe  $\leq 15 \times 10^{-4} \text{ cm}^{-1}$ .

<sup>d</sup>Determined from  $\Delta m_s = \pm 1$  parallel region.

<sup>e</sup>Determined from  $\Delta m_s = \pm 1$  perpendicular region.

<sup>f</sup>Determined from " $\Delta m_s = 2$ " region.

Figure 8



field splitting of the parallel and perpendicular regions of the  $\Delta m_s = \pm 1$  regions does not occur. Further, only one type of cobalt is observed and the resonances observed are very narrow compared to the separated monomers under similar conditions. These observations suggest the metals are interacting weakly. In the triplet state, the  $S=1$  designation encompasses the entire molecule and any discrimination between the tetraaryl porphyrin and biological porphyrin is lost, hence the one type of cobalt. The phenomenon of "exchange narrowing" reduces the linewidths in weakly interacting paramagnetic dimers<sup>12</sup>. Additional support for some interaction between the metals in the observation of a weak signal in the " $\Delta m_s = 2$ " region.

When N-MeImid. is added, a spectrum very similar to that in Figure 4 is obtained. The hyperfine due to coordinated N-MeImid is obvious, but the spectrum is broad and there appears to be no interaction between the metals. It is a fair assumption that adduct formation has induced a conformational change increasing the metal-metal distance. The presence of different conformations in the Co(II) clamshell substantiates the earlier claim that the Cu(II) clamshell can possess different conformations. In summary, Co(II) clamshell, in the absence of base, at  $-170^\circ\text{C}$  appears to exist predominantly in a conformation exhibiting weak metal-metal interactions. The presence of N-MeIm. induces a conformational change which completely eliminates any interactions, i.e. the metal-metal distance has increased. A likely

cause is the coordination of the N-MeIm occurs on the "inside" at one or both of the metalloporphyrin "halves". It is clear that further studies on the Co(II) clamshell are needed. Since the unpaired electron resides in the  $d_z^2$  orbital of cobalt, the coordination of an unsaturated ligand simultaneously at both cobalts (e.g. pyrazine) is likely to promote very interesting exchange interactions.

### Experimental.

Mesoporphyrin IX (V). Hemin (equine, type III, Sigma Chem. Co.) was converted to protoporphyrin IX DME by a modification of the procedure of Grinstein<sup>13</sup>. 1g of hemin, dissolved in 5 ml 1 N. NaOH was diluted with 200 ml methanol. 2g powdered FeSO<sub>4</sub> were added, and dry HCl bubbled through the solution vigorously for 10 minutes. The initial black precipitate gave way rapidly to a deep red-violet solution. After cooling in ice, the solution was diluted with 300 ml H<sub>2</sub>O, and extracted twice with 300 ml CHCl<sub>3</sub>. The CHCl<sub>3</sub> extracts were washed twice with 300 ml H<sub>2</sub>O, once with 300 ml 2N NH<sub>4</sub>OH, and twice more with 300 ml H<sub>2</sub>O. After crude drying by filtration through NaCl, the product was crystallized by slowly removing solvent under vacuum and adding MeOH. Filtration with a medium frit and drying at 100°C gave 655 mg of violet-black crystalline material. Visible spectra agreed with literature reports.

Protoporphyrin IX DME was then reduced to mesoporphyrin IX DME following the procedure outlined by Falk<sup>4</sup>. The mesoporphyrin DME was purified by chromatography on activity IV alumina with 10:1 benzene/CHCl<sub>3</sub> eluent. 150 mg was run at one time on a 100 g alumina column. The column could be reused several times.

The dimethylester (200 mg) was dissolved in 10 ml 25% aqueous HCl. On standing, the bright violet solution produced a dark precipitate. After 12 hours, the mixture was neutralized

to pH 4.5 with 10% aqueous NaOH, and filtered. The filter cake was dried in air at 100°C, broken up and further dried under vacuum at 60°C for 12 hrs. The yield of mesoporphyrin IX (V) was nearly quantitative.

5,10-Di( $\alpha$ -2-aminophenyl)-15,20-diphenyl porphyrin (VI)

Benzaldehyde (35.4 g, 0.33 mole) and *o*-nitrobenzaldehyde (50.5 g, 0.33 mole) were dissolved in 2  $\ell$  hot acetic acid. The mixture was brought to reflux and 46.5 ml pyrrole (0.66 mole) added as rapidly as was possible without causing uncontrollable exothermic reaction. The resulting black solution was heated at reflux for 20 minutes, then cooled in ice to 35°C. Filtration through a coarse sintered glass funnel, followed by methanol washes and drying at 100°C in air, gave 9.8 g fine purple crystals. This mixture of porphyrins was stirred in 250 ml benzene until the solution was saturated, then diluted with 250 ml cyclohexane. After filtration, the solution was poured onto a 4" x 24" column of W. R. Grace 60-200 mesh silica, and eluted with 1:1 benzene/cyclohexane. The first two bands (TPP and mono(*o*-nitrophenyl)triphenylporphyrin) were set aside, and the third band collected and crystallized from benzene/methanol. This chromatographic procedure was repeated with the crude mixture that remained undissolved in the first run. The combined yield of mixed di-nitro isomers was 2.3 g, or 2.0% based on starting pyrrole.

One g of this mixture was dissolved in 50 ml concentrated HCl and 2.5 g (.011 mole) of  $\text{SnCl}_2 \cdot 2\text{H}_2\text{O}$  (Baker and Adamson reagent grade) was added. The bright green solution was stirred at 25°C for 1 hour, then at 75° to 85°C for 2 hours. After cooling to room temperature in an ice bath, concentrated  $\text{NH}_4\text{OH}$  was added slowly with stirring, until the mixture turned brown-violet. The pH was then adjusted to 10, and 50 ml  $\text{CHCl}_3$  added. After stirring 1 hour, the  $\text{CHCl}_3$  layer was separated and the aqueous layer extracted 2 times with 50 ml  $\text{CHCl}_3$ . The combined  $\text{CHCl}_3$  extracts were washed once with 100 ml 10%  $\text{NH}_4\text{OH}$ , twice with 100 ml water and dried over  $\text{Na}_2\text{SO}_4$ .

The solvent was then removed on a rotary evaporator, the residue dissolved in 5 ml  $\text{CH}_2\text{Cl}_2$ , and loaded onto a 1½" diameter chromatography column packed with 200 g PF-254 silica (E. Merck). Elution with  $\text{CH}_2\text{Cl}_2$  produced 5 major bands. The first two bands were shown to be unreacted starting material and partially reduced material. The third band, on crystallization from  $\text{CH}_2\text{Cl}_2/\text{MeOH}$ , gave 415 mg diamino porphyrin VIIIa as fine purple crystals. The fourth band gave 70 mg diamino porphyrin VIIIb, which was set aside. The final band gave 100 mg diamino porphyrin VI, apparently produced by atropisomerization of VIIIa during heating of the reduction mixture. The 415 mg of VIIIa was equilibrated to a statistical 1:1 mixture of the atropisomers VIIIa and VI by heating for 2 hours in refluxing

benzene solution, and then separated by chromatography with  $\text{CH}_2\text{Cl}_2$  on a column of 200 g PF-254 silica. Successive repetitions of this procedure gave nearly quantitative conversion of diamino porphyrin VIIIa to the desired  $\alpha, \alpha$  atropisomer VI. The overall yield of 5,10 di( $\alpha$ -o-aminophenyl)-diphenyl porphyrin (VI) is 515 mg or 56% based on starting dinitroporphyrin mixture. The overall yield based on starting pyrrole is 1.1%.

"Clamshell" porphyrin IV. Mesoporphyrin V (50 mg,  $8.85 \times 10^{-5}$  mole) was dissolved in 15 ml N-methylpyrrolidinone (NMP) under nitrogen in the dark. Thionyl chloride (50  $\mu\text{l}$ ,  $6.8 \times 10^{-4}$  mole) was added and the solution heated to  $50^\circ\text{C}$  for 30 minutes. Upon cooling the solution to room temperature, 10 ml degassed toluene was added. The toluene and excess thionyl chloride were distilled off under reduced pressure at room temperature. Diamino porphyrin, VI (57.5 mg,  $8.85 \times 10^{-5}$  mole) was dissolved in 5 ml NMP and then added to the solution of V by means of a syringe. After allowing the mixture to react for one hour at room temperature, 30 ml benzene was added. The benzene solution was washed 5 x 15 ml 5% aqueous  $\text{K}_2\text{CO}_3$ . The benzene layer was dried by filtration through NaCl, then filtered through celite, and taken to dryness on a rotary evaporator.

The crude reaction mixture was chromatographed on PF-254 silica, utilizing 7% ethyl acetate in  $\text{CH}_2\text{Cl}_2$  as the elutant. "Clamshell" porphyrin appears as a slower moving band than starting diamino porphyrin VI.

Cu<sup>II</sup> "clamshell" IX. The introduction of Cu<sup>II</sup> is based on the general metalloporphyrin synthesis of Adler<sup>6</sup>. 25 mg Cu(OAc)<sub>2</sub>·H<sub>2</sub>O (B. and A. reagent grade) and 25 mg IV ("clamshell") were dissolved in 10 ml dry DMF. The solution was stirred in an oil bath at 90°C for 1 hour. After cooling, 25 ml benzene and 25 ml H<sub>2</sub>O were added and stirred vigorously. The water layer was separated and extracted once with 25 ml benzene. The combined benzene layers were washed 3 times with 25 ml H<sub>2</sub>O and then evaporated to dryness under vacuum. The resulting bright red solid was purified by chromatography with 2% MeOH in benzene on a column containing 10 g PF-254 silica. The single major band, after evaporation under vacuum and crystallization from benzene/MeOH, gave 18 mg bright red solid.

Co<sup>II</sup> "clamshell" X. Anhydrous CoCl<sub>2</sub> (50 mg, Alfa Inorganics) and clamshell porphyrin, VI (50 mg) were heated gently with a heat gun under vacuum for 5 min. The reaction vessel was taken into an inert atmosphere box and the dry, solid mixture was dissolved in 10 ml THF and 40 μl 2,6 lutidine. After stirring at ambient temperature for 4 hours, the solvent volume was reduced to about 3 ml under vacuum, and the remaining solution subjected to chromatography on a ¼" x 1" column of neutral alumina (EM Reagents, activity grade I) with THF eluent. The resulting red-violet solution was allowed to crystallize

slowly by evaporation and addition of hexane. In this manner, 35 mg dark purple crystals were obtained.

### References

- (1) F. P. Schwarz, M. Gouterman, Z. Muljiani, and D. Dolphin, Bioinorg. Chem., 2, 1 (1972).
- (2) L. Witte, J-H Fuhrhop, Angew. Chem. Int. Ed., 14 (5), 361 (1975).
- (3) H. Ogoshi, H. Sugimoto, S. Sanada, E. Watanabe, Z. Yoshida, Chem. Let., 427 (1975).
- (4) J. E. Falk, Porphyrins and Metalloporphyrins, Elsevier Publishing Co., New York, pp. 177-178 (1964).
- (5) a. R. G. Little, J. A. Anton, P. A. Loach, and J. A. Ibers, J. Heterocycl. Chem., 12 (2), 343 (1975).  
b. J. A. Anton and P. A. Loach, J. Heterocycl. Chem., 12 (3) 573 (1975).
- (6) A. D. Adler, F. R. Longo, F. Kampus, and J. Kim. J. Inorg. Nucl. Chem., 32, 2443 (1970).
- (7) J. Lewis, F. E. Mabbs, L. K. Royston, and W. R. Smail, J. Chem. Soc. (A), 291 (1969).
- (8) R. L. Belford, N. D. Chasteen, and R. E. Tapscott, J. Amer. Chem. Soc., 91, 4675 (1969).

- (9) N. D. Chasteen and R. L. Belford, Inorg. Chem., 9, 169 (1970).
- (10) J. B. Boas, J. R. Pilbrow, and T. D. Smith, J. Chem. Soc. (A), 721 (1969).
- (11) J. F. Boas, J. R. Pilbrow, and T. D. Smith, J. Chem. Soc. (A), 723 (1969).
- (12) G. F. Kokoszka and R. W. Duerst, Coord. Chem. Revs., 5, 209 (1970).
- (13) M. Grinstein, J. Biol. Chem., 167, 515 (1947).

## B. Preparation of Highly Dispersed Palladium Samples Supported on SiO<sub>2</sub>

M. Boudart

### 1. Introduction

The dispersion of palladium in supported samples can be successfully measured by hydrogen or deuterium titration at 373 K. Previously, Benson and Boudart (1) have reported that the hydrogen titration, which measures the total hydrogen uptake at room temperature on a Pt surface covered with chemisorbed oxygen, can successfully determine the dispersion of supported Pt catalysts. However, it was later found that the ratio oxygen adsorption:hydrogen adsorption:hydrogen titration changes with metal particle size (2). For this reason it is necessary to know whether this ratio also changes with palladium particle size  $d$ . Furthermore, Aben (3) studied the total sorption (both adsorption and absorption) at 195 K on a 2% Pd/SiO<sub>2</sub> ( $d = 2.5$  nm) catalyst and on palladium black ( $d > 50$  nm) and found that the total hydrogen uptake decreased as the particle size decreased. He attributed this to decreased hydrogen absorption in the  $\beta$ -phase. To study possible variations in absorption or adsorption with particle size require Pd catalysts of different particle size, especially important are well dispersed catalysts with Pd particles of about 2 nm diameter or less, since it is in this particle size range that the particle surface is significantly different from that of a plane surface. Because well-dispersed commercial palladium catalysts are not available, it was necessary to prepare such samples. This report deals with the development of a technique for the preparation of well-dispersed Pd/SiO<sub>2</sub> samples and the parameters that may affect the resulting high dispersion such as high temperature oxidation or reduction.

The general methods for preparation of supported metal catalysts have been extensively reviewed in the literature (4, 5). Supported metallic catalysts are most commonly prepared by either impregnation or cation exchange. Impregnation consists of wetting the support with a solution of the metal salt or acid, boiling off the solvent, and drying the sample in air at about 393 K. The sample is subsequently either calcined at about 773 K or reduced in hydrogen at about 673 K or both (3, 6). Another frequently employed impregnation method, the incipient wetness technique, uses the minimum amount of solution to fill the pores of the support during impregnation(7). The cation exchange method (8, 9) involves exchanging the  $H^+$  (Brønsted site) of the support with  $NH_4^+$  in ammonia solution, followed by exchange of the  $NH_4^+$  ions with cations of the metal. In these latter procedures the solid is separated from the solution by filtration, washed with distilled water and then dried. The solid can then be treated in any number of ways including calcination in air or reduction in hydrogen.

Only limited data are available on the preparation of highly dispersed Pd/SiO<sub>2</sub> catalysts. Aben (3) compared the metal dispersion of Pd/SiO<sub>2</sub> catalysts and reported that a 0.53% Pd/SiO<sub>2</sub> sample prepared by cation exchange was 83% dispersed while a 2% Pd/SiO<sub>2</sub> impregnated catalyst was only 40% dispersed. Platinum, however, has been extensively studied and procedures for the preparation of well dispersed Pt/SiO<sub>2</sub> catalysts may also be applied to the preparation of well dispersed Pd/SiO<sub>2</sub> catalysts. Dorling, Lynch and Moss (6) studied the effect of preparation and pretreatment conditions on the metal dispersion of Pt/SiO<sub>2</sub> samples. They found

that the mean crystallite size of samples prepared by cation exchange was independent of the support area and Pt content (up to 4.45% Pt). However, for samples prepared by impregnation, the mean crystallite size showed a strong dependence on the support area and Pt content. Benesi, Curtis and Studer (9) report the preparation of very highly dispersed platinum catalysts prepared by ion exchange of  $\text{Pt}(\text{NH}_3)_4^{++}$  onto silica gel. Samples made by impregnation with aqueous chloroplatinic acid showed much lower metal dispersion.

Boronin, Nikulina and Poltorak (8) also studied the preparation of Pt/SiO<sub>2</sub> samples. Several factors such as increasing the time allowed for the cation exchange to occur to two days, washing to remove any residual ammonia solution present on the support, and drying at a low temperature such as 323 K were the most important factors in obtaining well-dispersed Pt/SiO<sub>2</sub> samples. The effect of pretreatment on the dispersion of platinum supported on Ca-Y zeolite has been studied by Dalla Betta and Boudart (2). When the exchanged  $\text{Pt}(\text{NH}_3)_4^{++}$  ions were first decomposed in an anhydrous and oxidizing atmosphere before reduction, a well-dispersed Pt sample was obtained.

From the results discussed above, a preparation procedure to obtain well-dispersed supported Pd samples can be outlined. In this study, several Pd/SiO<sub>2</sub> samples were prepared by ion exchange using an aqueous solution of  $\text{Pd}(\text{NH}_3)_4^{++}$ . The pretreatment of the exchanged sample involved first decomposition in flowing oxygen up to a minimum decomposition temperature and then reduction in a dilute hydrogen in nitrogen gas stream (1.08% hydrogen) up to a minimum reduction temperature.

## 2. Experimental

The source, purity and purification of the gases used are given in Table 1. The silica support used here was obtained from Davison Chemical Co. (grade 62), and has a surface area of  $340 \text{ m}^2 \text{ g}^{-1}$  and a pore volume of  $1.15 \text{ cm}^3 \text{ g}^{-1}$ .

The procedure for the preparation of Pd/SiO<sub>2</sub> samples, and the choice of the pretreatment conditions are described below.

### PREPARATION OF SAMPLES BY CATION EXCHANGE

#### (a) Method A:

A 2.40% Pd/SiO<sub>2</sub> sample was prepared by the ion exchange method of Benesi, Curtis and Studer (9). The first step of the preparation was to exchange  $\text{NH}_4^+$  onto the silica gel surface. A 9.982 g sample of SiO<sub>2</sub> was immersed in 250 cm<sup>3</sup> of 0.1 M ammonium nitrate solution in a beaker and the resultant slurry was stirred for 600 s at room temperature (R.T.). A 400 cm<sup>3</sup> solution containing 0.1 M ammonium nitrate and 0.1 M ammonium hydroxide was slowly added to the stirred slurry at R. T. The solid was filtered from the solution, washed with 250 cm<sup>3</sup> distilled water and dried in a vacuum oven overnight at R. T.

The second step of the preparation consisted of exchanging  $\text{Pd}(\text{NH}_3)_4^{++}$  ions for the surface  $\text{NH}_4^+$  ions. The  $\text{NH}_4^+$  exchanged silica gel prepared above was immersed in 200 cm<sup>3</sup> of 0.001M  $\text{Pd}(\text{NH}_3)_4\text{Cl}_2$  solution. This slurry was stirred while the 190 cm<sup>3</sup> of a solution

Table 1 Purification of Gases

Gas	Source	Purity/%	Further Purification
H <sub>2</sub>	Liquid Carbonic	99.93	Pd-diffused
D <sub>2</sub>	Matheson (CP)	99.5	Pd-diffused
He	Liquid Carbonic (Grade A)	99.995	Passed over hot Cu wire and through a liquid nitrogen trap
O <sub>2</sub>	Liquid Carbonic	99.5	Passed over a Linde 5A molecu- lar sieve trap at 195 K.
H <sub>2</sub> /N <sub>2</sub> (1.08% H <sub>2</sub> )	Matheson (Certified Standard)		Passed over a Linde 5A molecu- lar sieve trap at 195 K.

0.01 M in  $\text{Pd}(\text{NH}_3)_4(\text{OH})_2$  and 0.001 M in  $\text{Pd}(\text{NH}_3)_4\text{Cl}_2$  was added.

After this addition was completed the slurry was stirred for an additional  $1\frac{1}{2}$  h at R.T. The slurry was filtered, washed with  $250 \text{ cm}^3$  distilled water and dried in a vacuum oven overnight at R.T.

(b) Method B:

Three  $\text{Pd}/\text{SiO}_2$  samples (3.20%, 0.57% and 3.75% Pd) were prepared according to the procedure of Boronin, Nikulina and Poltorak (8). A  $\text{Pd}(\text{NH}_3)_4^{++}$  solution was prepared by first dissolving 1.340 g of palladium chloride (Engelhard Co.) in  $200 \text{ cm}^3$  of a concentrated  $\text{NH}_4\text{OH}$  solution (approximately 58%) at 343 K and then diluting to one liter. A 21.097 g sample of the silica gel support was immersed in  $300 \text{ cm}^3$  of 28%  $\text{NH}_4\text{OH}$  solution and the resultant slurry was stirred for about 600 s at 343 K. The Pd salt solution prepared above was slowly added to the  $\text{SiO}_2$  slurry at 343K and stirred for one hour. The final slurry was filtered, the solid was washed with  $250 \text{ cm}^3$  of distilled water and dried in a vacuum oven overnight at R.T.

Each of the above four samples was separately pretreated by the standard procedure to be described later. The samples were then exposed to air. The weight % Pd in the samples was determined by atomic absorption after drying in a vacuum oven for at least 4 h at 393 K.

DETERMINATION OF THE MINIMUM DECOMPOSITION TEMPERATURE IN OXYGEN

The minimum decomposition temperature of the  $\text{Pd}(\text{NH}_3)_4^{++}$  ions supported on the  $\text{SiO}_2$  in flowing oxygen was studied by monitoring the weight loss of the sample in a vacuum electrobalance (10). A sample of the 2.40%  $\text{Pd}/\text{SiO}_2$  catalyst (0.474 g) was loaded into a bucket made of aluminum foil. It was outgassed for one hour at R. T. before oxygen was passed through the sample at R. T. and at a space velocity of  $1 \text{ s}^{-1}$ . The sample was heated to 368 K in  $\frac{1}{2}$  h and held at this temperature for  $\frac{1}{2}$  h. It was then heated to 773 K at a rate of 4.5 degrees per minute and the weight loss was monitored as a function of temperature. Since the weight loss of the sample was the sum of the weight loss due to the decomposition of the exchanged  $\text{Pd}(\text{NH}_3)_4^{++}$  and  $\text{NH}_4^+$  ions, and that due to the dehydration of the support, a blank run on 0.483 g of  $\text{SiO}_2$  was performed to monitor the weight loss from the support under the same experimental conditions. As will be discussed later, the minimum decomposition temperature is about 673 K. Once this temperature had been determined, a standard decomposition procedure was chosen.

DETERMINATION OF THE MINIMUM REDUCTION TEMPERATURE OF THE DECOMPOSED SAMPLES

The minimum reduction temperature of the above decomposed and oxidized sample was determined by a volumetric method in an apparatus discussed elsewhere (1). A sample of 0.469 g of a 3.75%  $\text{Pd}/\text{SiO}_2$  catalyst was first decomposed in oxygen according to the standard procedure discussed below. It was treated for one hour in static hydrogen at approximately 40 kPa and at R.T. A hydrogen isotherm at R.T. was measured and the total hydrogen uptake obtained. With the same

dosed amount of hydrogen in the system, the temperature of the sample was raised in static hydrogen to a higher reduction temperature, i.e. 350 K, and reduced at that temperature for 1 h at approximately 40 kPa. It was then cooled to R.T. and the hydrogen isotherm at R.T. was measured. The hydrogen isotherms at R.T. were again measured after reducing the sample in a similar manner at 408 K and at 453 K. The total hydrogen consumed during the reduction could be plotted against the pretreatment temperature. The minimum reduction temperature was chosen to be the minimum pretreatment temperature at which the total hydrogen uptake becomes constant. As will be discussed later, the minimum reduction temperature was 408 K.

After complete reduction, this sample was exposed to air, the dispersion of Pd was determined by hydrogen titration at 373 K, and the solubility of hydrogen was measured by hydrogen-back sorption at R.T. (11).

#### THE STANDARD PRETREATMENT PROCEDURE

Once the minimum decomposition and minimum reduction temperatures were determined, the following steps were adopted as the standard pretreatment of the cation exchanged samples : (a) Outgas a fresh sample at R.T. for at least 2 h. (b) Flow oxygen at R.T. for  $\frac{1}{2}$  h and at a space velocity of  $3.2 \text{ s}^{-1}$ . (c) Heat to 673 K in 8 h, maintain for another 3 h at 673 K, then cool to R.T. in flowing oxygen. (d) Outgas sample briefly, flow  $\text{H}_2/\text{N}_2$  ( 1.08% hydrogen ) for 2 h at R.T. and at a space velocity of  $3.2 \text{ s}^{-1}$ . (e) Heat to 408 K in 4 h and maintain at this temperature for 2 h. (f) Stop the gas flow at 408 K and cool to R.T. in vacuo.

THE EFFECT OF PRETREATMENT ON DISPERSION

The effect of the different pretreatment procedures on the dispersion of palladium supported on  $\text{SiO}_2$  was briefly studied. Unless otherwise specified, freshly exchanged samples reported as the dry weight of the samples were used in these studies. The specific treatment for a given sample is described below and also listed in Table 2. (1) A 2.40% Pd/ $\text{SiO}_2$  sample, designated as sample A, was pretreated by the standard procedure described above. (2) Sample A was further reduced in flowing hydrogen at 653 K for 1 h (space velocity  $1 \text{ s}^{-1}$ ), then outgassed for 2 h at 653 K. The sample was then designated as sample B. (3) Sample B was further reduced in flowing deuterium at 653 K for  $\frac{1}{2}$  h (space velocity  $0.3 \text{ s}^{-1}$ ) and outgassed for 1 h at 653 K. The sample was designated as sample C. (4) A 2.40% Pd/ $\text{SiO}_2$  sample, designated as sample D, was briefly outgassed at R.T. before hydrogen was admitted at R.T. and at about 71 kPa. The temperature was increased to 653 K in  $1\frac{1}{2}$  h and the sample was allowed to stay in static hydrogen for an additional 2 h. It was further reduced in flowing hydrogen (space velocity  $1 \text{ s}^{-1}$ ) for 12 h at 653 K before being outgassed for 2 h at the same temperature. (5) Two 3.20% Pd/ $\text{SiO}_2$  samples, designated as sample E and F, were pretreated separately by the standard procedure. (6) A portion of sample F, designated as sample G, was further reduced in static hydrogen at about 40 kPa and 373 K for 3 h, then exposed to air overnight at R.T. (7) A 3.75% Pd/ $\text{SiO}_2$  sample, designated as sample H, was pretreated according to the standard procedure. (8) A 3.75% Pd/ $\text{SiO}_2$  sample, designated as sample I, was decomposed in oxygen according to the standard procedure but was reduced in about 53 kPa of hydrogen up to 451 K and then exposed to air

Table 2 Variation of Palladium Dispersion With Pretreatment For Pd/SiO<sub>2</sub> Samples

Sample	Weight/g	Pretreatment	Dispersion /%
(A) 2.40%	1.005	Standard procedure.	78
(B) 2.40%	1.005	Sample A + reduction for 1 h at 653 K.	73
(C) 2.40%	1.005	Sample B + reduction for $\frac{1}{2}$ h at 653 K.	65
(D) 2.40%	1.337	Heat to 653 K in about 71 kPa of H <sub>2</sub> + reduction for 12 h at 653 K.	51
(E) 3.2%	2.096	Standard procedure.	81
(F) 3.2%	4.467	Standard procedure.	86
(G) 3.2%	1.40	Portion of sample F + reduction in about 40 kPa of H <sub>2</sub> at 373 K.	85
(H) 3.75%	0.398	Standard procedure.	82
(I) 3.75%	0.469	Decomposed in oxygen up to 673 K + reduction in H <sub>2</sub> up to 451 K.	63
(J) 0.57%	0.795	Standard Procedure.	77

at R.T. Sample I was the sample which was used to determine the minimum reduction temperature as described above. (9) A 0.57% Pd/SiO<sub>2</sub> sample, designated as sample J, was pretreated by the standard procedure.

Following the pretreatment of each sample as described above, the sample was exposed to air for at least 1 h at R.T. After outgassing the sample for about 2 h at 373 K, the dispersion of palladium for the sample was determined either by hydrogen or deuterium titration at 373 K (11).

### 3. Results

The weight loss of the  $\text{Pd}(\text{NH}_3)_4^{++}$  exchanged  $\text{SiO}_2$  and that of the  $\text{SiO}_2$  blank in mg per gram sample ( $\text{mg g}^{-1}$ ) are plotted against temperature in Fig. 1. The difference in weight loss of the two curves in the diagram is the weight loss due to the decomposition of the exchanged  $\text{Pd}(\text{NH}_3)_4^{++}$  and  $\text{NH}_4^+$  ions. When the temperature is higher than 673 K, the two curves are parallel to each other, indicating the weight loss in this region is due to the dehydration of the support alone. Therefore, it is clear from the figure that the decomposition has been completed at about 673 K and the minimum decomposition temperature is 673 K.

Fig. 2 is a plot of the total hydrogen uptake of the decomposed and oxidized sample vs. the reduction temperature. The uptake is constant when the temperature is 408 K or higher, indicating that the minimum reduction temperature is 408 K.

The dispersions of palladium for each sample determined by either hydrogen or deuterium titration at 375 K are listed in Table 2. The results of samples A, F, H and J show that all four samples prepared by ion exchange and pretreated by the standard procedure as described above are highly dispersed samples. The results for samples E and F show the good reproducibility of the dispersion of Pd, if we start with the same bath of freshly cation exchanged sample and the same standard pretreatment. As shown by the results for samples A, B and c, the dispersion of Pd for a reduced sample will decrease upon further reduction in flowing hydrogen or deuterium at 653 K. Also, from Pd dispersions of samples H and I, we

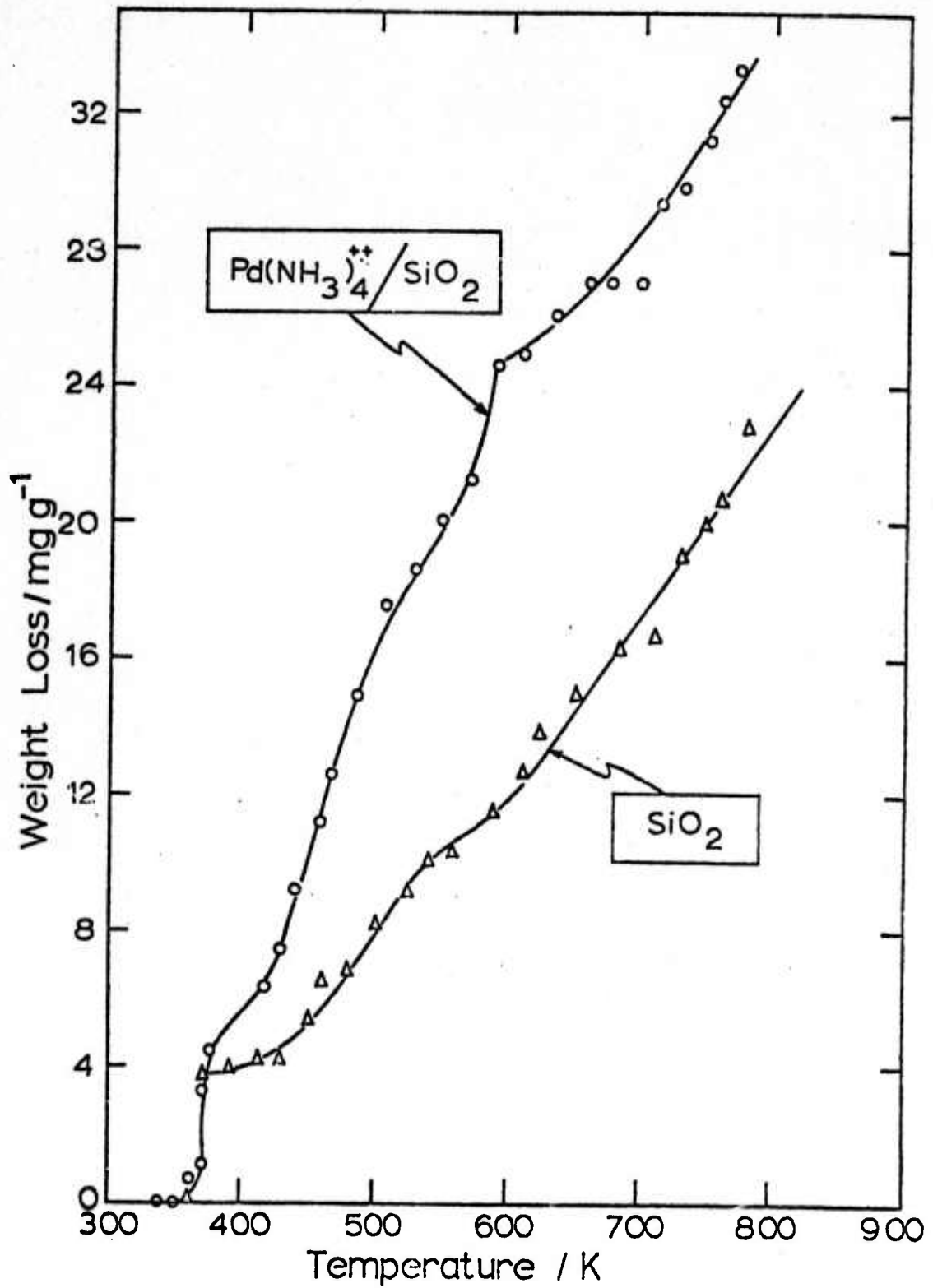


Figure 1. Weight Loss During Decomposition of  $\text{Pd}(\text{NH}_3)_4^{++} / \text{SiO}_2$  and  $\text{SiO}_2$

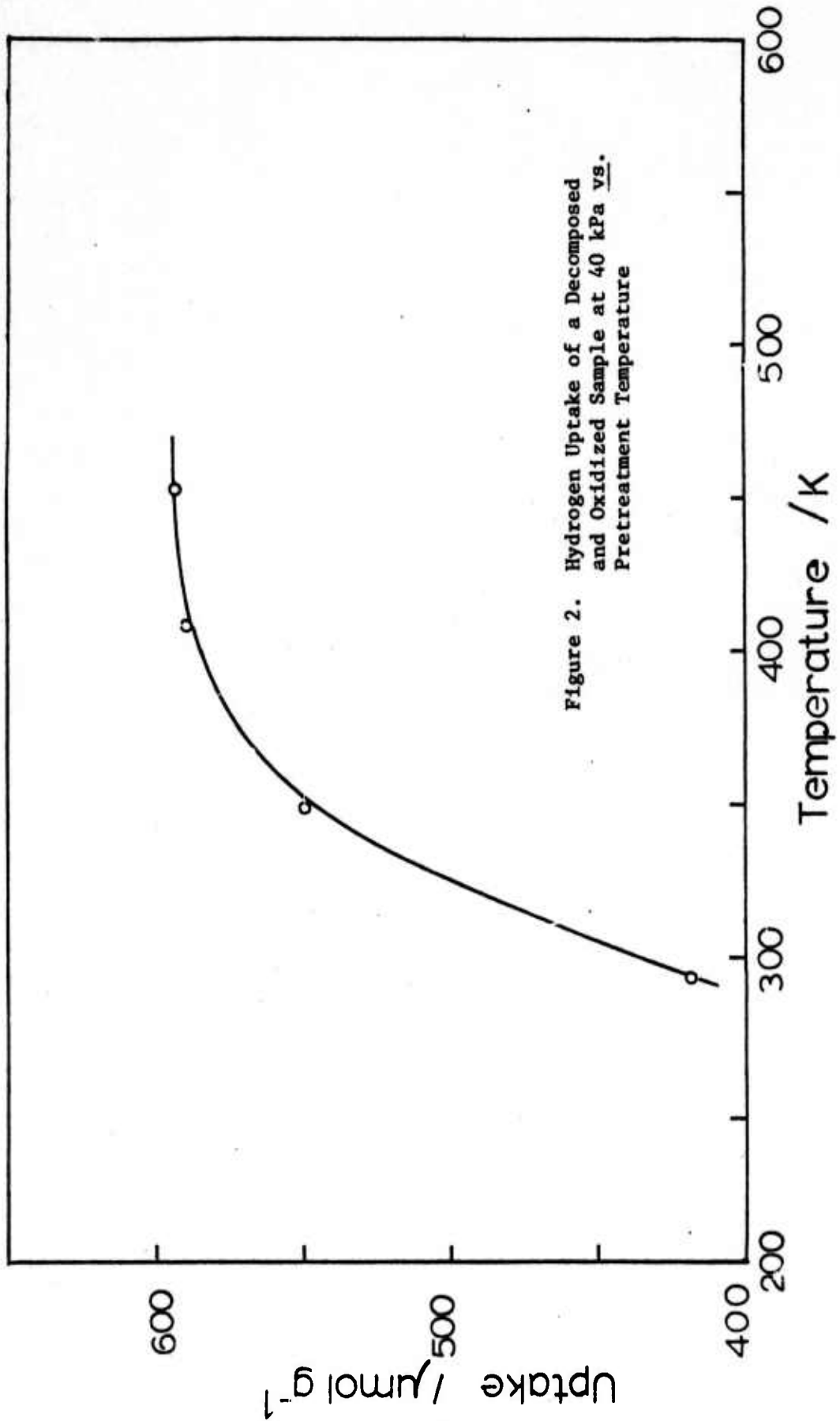


Figure 2. Hydrogen Uptake of a Decomposed and Oxidized Sample at 40 kPa vs. Pretreatment Temperature

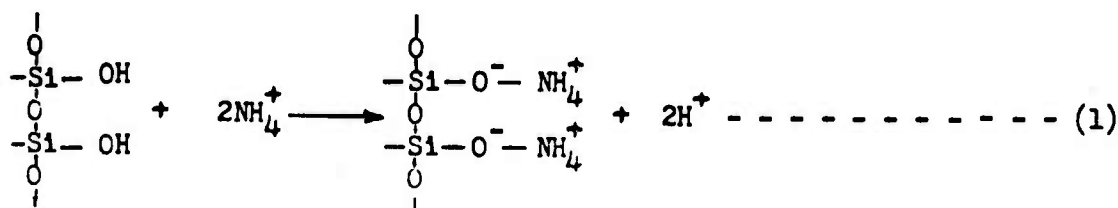
know direct reduction of the decomposed and oxidized sample in static hydrogen can cause severe sintering of palladium even at a temperature as low as 453 K. Therefore, in order to obtain a highly dispersed Pd/SiO<sub>2</sub> catalyst, it is necessary to reduce the sample at the minimum reduction temperature.

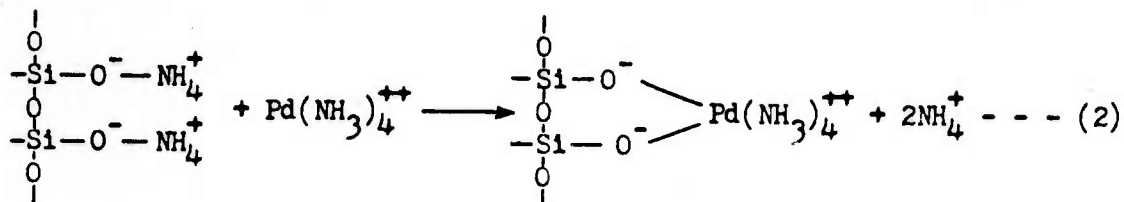
After taking the titration isotherm on sample F, the sample was maintained in about 40 kPa of hydrogen and at 373 K for an additional 2 h. This sample, now designated as sample G, was briefly outgassed at 373 K, cooled to R.T. and subsequently exposed to air. The dispersion of Pd for this sample was essentially the same as that of sample F. Therefore, we can conclude that hydrogen titration at 373 K does not cause any sintering and that the standard reduction procedure can effectively reduce all the oxidized palladium atoms.

4. DiscussionCATION EXCHANGE

Cation exchange between surface protons of aluminosilicate supports and transition metal cations has been reported in the literature (5). Although the protons on aluminosilicate surfaces could not be directly exchanged with transition metal cations or ammine complexes of the metal, this exchange could be achieved if the surface protons were first substituted by ammonium ions. The extent of the exchange between the surface protons and ammonium ions in solution depends on the acidity of the support and the pH of the slurry during exchange. It has been found that stronger support acidity (9) and higher slurry pH (9, 14) result in greater  $\text{NH}_4^+$  exchange. Similar trends are expected in the case of Pd exchange on silica. For example, 97% of the Pd ammine complexes in solution were taken up by silica if the pH of the slurry was between 9.5 and 10.5, while only about 15% of the cations were taken up at pH 8.0 (12). For this reason, controlling the pH of the slurry during the addition of the palladium ammine solution is very important. In this work, the pH of the slurry was controlled by adding an appropriate amount (of a given concentration) of  $\text{Pd}(\text{NH}_3)_4(\text{OH})_2$  solution in method A, while in method B, the pH was adjusted by simply adding more  $\text{NH}_4\text{OH}$  solution (approximately 28%  $\text{NH}_4\text{OH}$ ) to the slurry.

The cation exchange reactions can be expressed as





The exchange reaction (2) is reversible and is assumed to be able to reach equilibrium (14). Sulcek, Vařák and Doležal (12) studied reaction (2) by passing 25 cm<sup>3</sup> of Pd(NH<sub>3</sub>)<sub>4</sub><sup>++</sup> solution through a column filled with silica gel at a rate of 60 cm<sup>3</sup> h<sup>-1</sup>. The column was subsequently washed with approximately 0.01 M NH<sub>4</sub>OH solution and then with water. About 98% of the Pd(NH<sub>3</sub>)<sub>4</sub><sup>++</sup> ions were exchanged onto the silica when the pH is 10.0. These data indicate Pd(NH<sub>3</sub>)<sub>4</sub><sup>++</sup> ions can be rapidly exchanged onto a silica surface and once exchanged, they are tightly held so that washing with 0.01 M NH<sub>4</sub>OH solution or water does not remove a significant amount of the ammine complex. The forward exchange reaction (2) appears to be fast and the equilibrium lies far to the right. However, these exchanged ions can easily be eluted by 2.5 M nitric acid (12).

#### PRETREATMENT CONDITIONS

The results in Table 2 show that further reduction of the reduced sample (sample A) at 653 K in hydrogen, direct reduction of the palladium ammine complex ions in hydrogen (sample D), and direct reduction in static hydrogen of the decomposed sample up to 451 K (sample I) cause sintering of the catalyst. The above sintering phenomenon, especially at high temperature may be attributed to the high mobility of palladium in hydrogen, or intermediate compounds formed during reduction. The high

mobility of palladium in hydrogen has also been observed for Pd catalysts supported on charcoal (12). Therefore, to make well-dispersed Pd/SiO<sub>2</sub> samples, it is necessary to avoid the formation of the highly mobile palladium intermediate compounds during the pretreatment, and to reduce the sample at the lowest possible temperature.

A good example of the complex processes occurring during the decomposition of the ammine complex has been reported by Dalla Betta and Boudart (2). They studied the effect of the pretreatment procedure on the dispersion of Pt supported on Ca-Y zeolite. It was found that direct reduction of the Pt ammine complex for 2 h in hydrogen at 673 K produced a sample with a metal dispersion of only 6%. This result was attributed to the formation of an unstable hydride, such as Pt(NH<sub>3</sub>)<sub>2</sub>H<sub>2</sub> during reduction. The high mobility of this compound, especially with water present in the zeolite led to the migration and agglomeration of platinum. However, if the exchanged Pt ammine complex was first decomposed in oxygen at 623 K and then reduced by the same procedure, a well dispersed sample was obtained. In fact, the resulting catalyst consisted of Pt clusters of about 6 atoms located inside the zeolite supercages. The effect of water in the zeolite during the pretreatment was also investigated. It was found that efficient removal of water before direct hydrogen reduction increased the dispersion two-fold, that addition of water to the oxidized but unreduced sample decreased the dispersion, and that addition of water to the reduced sample did not cause any sintering at all. By summing all the results, they concluded that decomposing the Pt ammine complex in an anhydrous environment and oxidizing atmosphere before reduction is a very effective way to prevent the formation of the mobile intermediate compound.

In studying catalytic reactions, especially structure sensitive and structure insensitive reactions, it is frequently required to prepare several samples with different metallic dispersion. As shown by samples A, B and D in Table 2, an attractive way to prepare such samples is to start with the same batch of a cation exchanged catalyst, and to change the pretreatment procedure in any number of ways to obtain catalysts of widely varying dispersion.

#### CRYSTALLITE SIZE vs. PERCENTAGE Pd CONTENT

As shown in Table 2, when samples A, E, H and I are individually pretreated by the standard procedure, the dispersion of Pd for each sample is approximately the same. Thus, the dispersion is not a function of Pd content of the supported catalysts, if the weight % Pd is between 0.57% and 3.75%. In other words, the number of Pd crystallites increases with increasing Pd content, but the average crystallite size is approximately constant. A similar result was also found for Pt/SiO<sub>2</sub> catalysts prepared by cation exchange (6).

The crystal growth during pretreatment depends on : (1) the distribution and location of the Pd(NH<sub>3</sub>)<sub>4</sub><sup>++</sup> ions originally exchanged on the silica, (2) the probability of collision among the Pd intermediate compounds, the Pd atoms and/or the Pd crystallites, and (3) the probability of agglomeration through the formation of metallic bonds upon collision.

The location of the exchanged Pd ammine complex ions on the silica surface depends strongly on the original distribution and acidity of

the Brønsted sites, and the accessibility of the sites to the cations. Because the cations are rapidly exchanged on the surface, the small fraction of the stronger sites in easily accessible regions will be exchanged first when the Pd ammine solution is added to the slurry. These exchanged sites may induce changes in the support surface by either increasing the acidity of the neighboring sites or creating new weak protonic sites. Such an induction effect would be similar to the formation of proton acidity on a silica surface observed for sodium exchanged silica samples (16). This may imply that further addition of the Pd ammine complex ions to the slurry leads to preferential exchange with neighboring sites such that the exchanged cation will initially form independent islands surrounding the most active Brønsted sites on the easily accessible surface. However, the cation exchange reaction is reversible and is at equilibrium. Thus, the redistribution of the exchanged cations on the silica surface will certainly occur. As the exchange time increases, the stronger sites in the less accessible regions will be exchanged with the residual cations in the solution, and the cations previously exchanged on the weaker sites of the silica will desorb into the solution to maintain the exchange equilibrium. Hence, as the exchange time increases, the exchanged cations will become more evenly distributed on the support surface and the number of islands will be increased. For example, in preparing Pt/SiO<sub>2</sub> samples, Boronin, Nikulina and Poltorak (8) varied the exchange time while keeping other conditions constant, and found Pt dispersions of 65% and 88% for the exchange time of 180 s and 2 days respectively. Also, increasing the exchange time from 2 days to 17 days had no significant effect on the

metallic dispersion. The results can be interpreted by a rapid exchange of  $\text{Pt}(\text{NH}_3)_4^{++}$  on silica which reaches exchange equilibrium in 180 s. By increasing the exchange time to two days, the redistribution of the surface exchanged cations occurs and thus metallic dispersion increases after reduction. However, after two days, no further redistribution occurs.

The probability of collision between the Pd intermediate compounds, the Pd ions and/or Pd crystallites depends on their mobility (or diffusivity) on the support surface. The mobility will in turn depend on the interaction of the Pd compounds with the support and the pre-treatment environments. When a freshly exchanged sample is heated in oxygen, the Pd ammine complex ions exchanged with the weaker sites will first start to move on the support surface, because the interaction between the cation and the support is weaker than that for the stronger exchange sites. As ions diffuse on the surface, they will collide with the neighboring ions and agglomeration may occur through the formation of the metallic bonds. Since both the  $\text{Pd}(\text{NH}_3)_4^{++}$  and PdO are planer, the agglomeration probably occurs during the decomposition through formation of PdO, and further formation of the larger Pd crystallite probably occur during reduction due to the high mobility of the latter in hydrogen. Certainly, the total number of crystallites and the size of each crystallite strongly depend on the mobility and the distance between the Pd ions or Pd compounds on the support surface. Each cation exchanged island may form several crystallites if the mobility is low, or several islands may eventually become

a large particle if the mobility is high.

Now, in order to explain why the dispersion of Pd is not a function of Pd content, we assume that the redistribution of the Pd ammine ions on the silica surface cannot further occur for the four samples prepared above, even if we extend the exchange time. In other words, the cations will be exchanged on the sites strictly according to the relative acidities. For 0.57% Pd/SiO<sub>2</sub> sample, the number of cations exceeds the number of the most active protonic sites, and the formation of islands around the more active sites occurs. During pretreatment, the Pd or its compound starts to agglomerate from the boundary of the islands and within a certain distance depending on the mobility over the support surface, all Pd will eventually agglomerate to form a crystallite. In this way, the Pd dispersion of 77% is obtained. When more cations are added to the slurry, the exchange onto the slightly less active sites having the same acidity as that of the neighboring sites created by the induction effect, will also occur on the surface. The formation of islands around these sites will then follow. Therefore, for 3.75% Pd/SiO<sub>2</sub> sample, the number of cation exchanged islands is greater and the island area surrounding the most active sites is probably larger than that for 0.57% Pd/SiO<sub>2</sub> sample. Because of the increase in the number of exchanged islands and the limitation of the mobility, a dispersion of 82% of Pd is obtained after pretreatment.

## 5. Conclusion

By controlling the pH of the final slurry at about 10.2, the palladium ammine ions are readily exchanged with surface  $\text{NH}_4^+$  ions, thereby being deposited on the support. The initially exchanged cations will probably form several islands located in the easily accessible regions of the support surface. Because the exchange reaction is equilibrated, redistribution of the exchanged cations on the surface will occur, and the number of exchanged islands will increase as the exchange time is extended.

The crystal growth of the Pd particles strongly depends on the distribution of the exchanged cations on the support surface and the mobility of Pd or its compounds during the pretreatment. It is necessary, therefore, to extend the exchange time to allow the redistribution of the exchanged cations on the support surface to take place, and to minimize the mobility of Pd or its compound during the pretreatment. As shown in Table 2, palladium has a high mobility in the presence of hydrogen and at high temperature. Thus, in order to make a well dispersed Pd sample, the Pd ammine ions exchanged onto the silica must be decomposed first in oxygen to avoid the formation of the highly mobile intermediate compound. Thus, the sample can be reduced in  $\text{H}_2/\text{N}_2$  ( 1.08%  $\text{H}_2$  ) up to the minimum reduction temperature.

The minimum decomposition temperature of the Pd ammine complex ions in flowing oxygen was monitored by the weight loss of the sample upon heating and was found to be 673 K. The minimum reduction temperature of the decomposed and oxidized sample was determined by measuring

the hydrogen uptake at room temperature after treating the sample for 1 h at progressively higher temperatures, and was determined to be 408 K.

The Pd dispersions for the four samples were 78%, 86%, 82% and 77% for 2.40%, 3.2%, 3.75% and 0.57% Pd/SiO<sub>2</sub> respectively. As discussed above, the number of cation exchanged islands will increase as the % Pd content for a supported sample increases. Because Pd agglomeration is limited by the Pd mobility on the support surface, the dispersion of Pd for the above four samples are found not to be a function of Pd content.

## REFERENCES

1. Benson, J.E., and Boudart, M., J. Catal. 4, 704 (1965).
2. Dalla Betta, R.A., and Boudart, M., Proc. 5th Int. Congr. Catal. J.W.Hightower, Ed., Vol. 2, p.1329, North Holland, Amsterdam 1973.
3. Aben, P.C., J. Catal. 10, 224 (1968).
4. Sinfelt, J.H., Annu. Rev. Mater.Sci. 2, 641 (1972).
5. Morikawa, K., Shirasake, T., and Okada, M., Advan. Catal. Relat. Subj. 20, 97 (1969).
6. Dorling, T.A., Lynch, W.J., and Moss, R.L., J. Catal. 20, 190 (1971).
7. Sinfelt, J.H., J. Catal. 29, 308 (1973).
8. Boronin, V.S., Nikulina, V.S., and Poltorak, O.M., Russ. J. Phys. Chem. 37, 626 (1963).
9. Benesi, H.A., Curtis, R.M., and Studer, H.P., J.Catal. 10, 328 (1968).
10. Levy, R.B., and Boudart, M., J. Catal. 32, 304 (1974).
11. Benson, J.E., Hwang, H.S., and Boudart, M., J. Catal. 30, 146 (1973).
12. Sulcek, Z., Vašák, M., and Doležal, J., Microchemical J. 16, 210 (1971).
13. Pope, D., Smith, W.L., Eastlake, M.J., and Moss, R.L., J. Catal. 22, 72 (1971).
14. Samanos, B., Boutry, P., and Montarnal, R., C. R. Acad. Sc. Ser. C 274, 575 (1972).
15. Miall, L.M., and Sharp, D.W.A. (ed.), "A New Dictionary of Chemistry". John Wiley & Sons. Inc. N.Y. 1968.
16. Szczepańska, S., and Malinowski, S., J. Catal. 15, 68 (1969).

### C. Preparation of Fine Particles

J. W. Brill and W. A. Little

Recent work on fine particles, prepared by gas evaporation, has concentrated on measuring the energy loss of electrons bombarding the particles in an electron microscope. Parsons and Hoelke [Phil. Mag. 30, 135 (1974)], have measured energy loss in thin films by measuring the resulting chromatic aberration of the electron beam. If this technique could be used for single fine particles, the energy loss spectrum could be measured without the usual confusion caused by having an unknown size distribution of particles. The technique does require, however, having a sharp loss spectrum for each particle. I tried to repeat the work of Parsons and Hoelke, using both thin film and fine particle targets. For fine particle targets, I looked for chromatic aberration both in the image of the entire particle and in the phase contrast image of the crystalline atomic planes. However, instabilities in the electron microscope high voltage supply made it impossible to observe the effect at present.

**V. DEVELOPMENT OF ELEVATED TEMPERATURES  
ELECTROCRYSTALLIZATION TECHNIQUES**

**R. S. Feigelson**

**Director, Crystal Technology  
Center for Materials Research**

**and**

**R. A. Huggins**

**Professor of Materials Science  
and Engineering**

## A. Introduction

The major emphasis of the Electrocrystallization phase of this program is to develop a more sophisticated understanding of the principles involved in the use of molten salt electrochemistry for crystal growth. Such an indepth study is designed to ultimately lead to a better control of both nucleation and growth processes which will allow the production of both single crystals and polycrystalline layers of a wide range of materials. To date, little attention has been paid to this aspect of molten salt electrochemistry. Most of the previous work on the use of molten salt electrochemistry for the growth of solids has been concerned with compound synthesis in powder form.

During the past few years, we have made significant progress toward our objectives. Several papers have been published or have been accepted for publication including epitaxial deposition of silicon on silicon substrates<sup>(1)</sup>, a theoretical analysis of the rate-controlling process during electrolytic growth and dissolution<sup>(2)</sup>, and a study of the conditions necessary for stable growth<sup>(3-5)</sup>. One of the important findings resulting from this work has been that by using an appropriate pulse technique the stable growth rate can be increased by factors of 30-50<sup>(6)</sup>. Large single crystals of  $\text{LaB}_6$  have also been grown for the first time<sup>(7)</sup> and a potentially important process, the Electrochemical Czochralski Technique (ECT) has been developed for continuous growth<sup>(8)</sup>. In addition, several phases in the Nb-Ge alloy system have been synthesized from a molten salt bath.

During the current reporting period special emphasis has been placed on the synthesis and growth of new materials including  $\text{ScB}_2$ ,  $\text{PrB}_6$ , Si, sulfides, InP and GaP. The individual programs will be discussed separately in the following sections.

References

- (1) U. Cohen and R. A. Huggins, "Silicon Epitaxial Growth by Electrodeposition from Molten Salts", presented at the Electrochemical Society Meeting, Dallas, Texas, October 5-10, 1975.
- (2) D. Elwell, R. C. DeMattei, I. V. Zubeck, R. S. Feigelson and R. A. Huggins, "D.C. Resistances in Electrolytic Crystallization From Molten Salts", J. Crystal Growth (to be published).
- (3) D. Elwell, I. V. Zubeck, R. S. Feigelson and R. A. Huggins, "Surface Structure and Electrolytic Growth Stability of  $\text{LaB}_6$  Crystals", J. Crystal Growth 29, 65 (1975).
- (4) R. A. Huggins, "Interface Stability During Electrodeposition from Molten Salts", presented at Electrochemical Society Meeting, Toronto, Canada, May 11-16, 1975.
- (5) R. A. Huggins and D. Elwell, "Control of Interface Morphology During Electrocrystallization from Molten Salts - Electrochemical Analog to Constitutional Supercooling", J. Crystal Growth (to be published).
- (6) U. Cohen and R. A. Huggins, "High Rate Electrodeposition of Niobium from Molten Fluorides Using Alternating Square Wave Pulses", presented at Meeting of the Electrochemical Society, Dallas, Texas, October 5-10, 1975.
- (7) I. V. Zubeck, R. S. Feigelson, R. A. Huggins and P. A. Pettit, "The Growth of Lanthanum Hexaboride Single Crystals by Molten Salt Electrolysis", J. Crystal Growth (to be published).
- (8) R. C. DeMattei, R. A. Huggins and R. S. Feigelson, "Crystal Growth by the Electrochemical Czochralski Technique (ECT)", J. Crystal Growth (to be published).

## B. New Material Studies

I. V. Zubeck and P. A. Pettit

### 1. Introduction

During the first part of this program the necessary processing and control equipment for producing useful bulk samples and single crystals was designed and constructed, and the effects of cell parameters such as voltage, temperature, and current density on deposit quality was studied and are now well understood. A study of crucible and electrode materials compatible with high temperature molten salt systems was undertaken and completed. The net result of these preliminary studies culminated in the successful seeded growth of large (5.5 mm on a side) crystals of  $\text{LaB}_6$ , demonstrating the advances made in the control of the electrochemical growth process. Knowledge gained in this project is currently being applied toward expansion of the group's capability to the deposition of other types of compounds.

### 2. Seeded Growth of Lanthanum Hexaboride

The first successful seeded growth of  $\text{LaB}_6$  was carried out on a rectangular slice of the compound 2 X 3 mm in cross section immersed to a depth of 2.5 mm in the melt. After a period of 87 hours the seed had well developed facets and measured 4 X 5 X 3 mm, an increase in size of  $\sim 300\%$ . The section of the seed which had remained above melt level during growth (where the holding wire was threaded through the seed) had deteriorated seriously. Subsequent runs showed similar behavior. It was therefore essential that the seed be totally immersed in the electrolysis bath. The same seed was reintroduced into the bath, and totally immersed below melt level. After an additional deposition period of 115 hours (current density  $18 \text{ mA/cm}^2$ ) the crystal measured 5 X 6 X 6 mm. By estimating the surface area of the seed the cell voltage could be adjusted so that the initial cathodic current density was  $\sim 20 \text{ mA/cm}^2$ . Small periodic adjustments in cell potential were then made to control the slope of the current vs. time curve. A large well developed crystal of  $\text{LaB}_6$  is shown in Fig. 1.

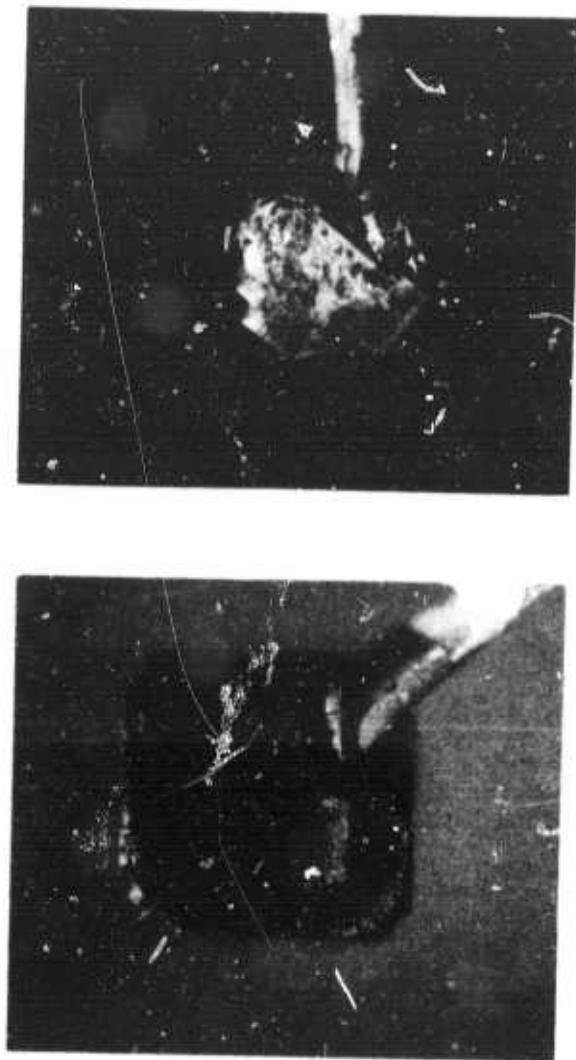


Figure 1. Seeded growth, suspended by gold wire ( $\sim 8X$ )  
(a) After 87 hours of growth  
(b) After 200 hours of growth

A paper reviewing the work was presented at the American Conference on Crystal Growth, Stanford University, July 1975, and has been accepted for publication in the Journal of Crystal Growth.

### 3. Scandium Borides

During the last report period, a program on the electrodeposition of  $\text{ScB}_2$  and other Sc-B compounds was in progress. Several molten salt solvents were explored including (1) an oxide bath similar to that used for  $\text{LaB}_6$  deposition, (2) a bath consisting of LiF-NaF-KF eutectic flux (Flinak) with a  $\text{Sc}_2\text{O}_3$ - $\text{B}_2\text{O}_3$  solute, and (3) a Flinak bath with a  $\text{ScF}_3$ - $\text{B}_2\text{O}_3$  solute. Cathode deposits obtained from these solvents as a function of individual bath composition were evaluated. For each bath composition the current vs voltage (I-V) characteristics of the bath were determined in the range 0-3V. Electrolysis was performed with an applied cell potential chosen on the basis of the I-V characteristics. Resulting deposits were examined by optical and/or scanning electron microscopy and analyzed by x-ray and electron microprobe techniques.

Complicated multiphase electrodeposits were obtained from these baths. While it is clear that Sc and B were being codeposited, no Sc-B compound could be identified. Because a prohibitive amount of time and work were considered necessary to provide a proper understanding of this system, the Sc-B project was terminated.

### 4. Praseodymium Hexaboride

Praseodymium hexaboride  $\text{PrB}_6$  crystallites in thin layers were electrodeposited from an oxyfluoride bath analogous to that used for  $\text{LaB}_6$  deposition. The bath was composed of 2.2 mole %  $\text{Pr}_2\text{O}_3$  ( $\text{Pr}_6\text{O}_{11}$ ), 1 mole %  $\text{B}_2\text{O}_3$ , 1 mole % LiF, and 1 mole %  $\text{Li}_2\text{O}$ . Initial deposition on a gold wire substrate showed the system to be well behaved. The violet  $\text{PrB}_6$  crystals, the largest  $\sim 1.0$  mm on a side, shown in Fig. 2, were deposited at  $\sim 2.16$ V in approximately three hours at  $800^\circ\text{C}$ .

Deposits of controlled weight per unit area were required for the Mossbauer studies. Initially, substrates were constructed by spot welding two layers of .05 mil Ni foil to a Ni support ring  $3/4$  in. OD by  $5/8$  in. ID by 10 mils thick. The thin Ni foils were impregnated



Figure 2.  $\text{PrB}_6$  deposit containing 1 mm cubes, gold wire substrate. ( $\sim 50\times$ )

with B during deposition, became brittle and could not support their own weight. The Ni substrates were replaced by 3 mil graphite discs 3/4 in. in diameter. The nominal thickness of the deposits made on the graphite substrates was .5 - 1.7 mg/cm<sup>2</sup>. The thin (.5 mg/cm<sup>2</sup>) deposits could be produced in approximately 15 minutes at ~40 mA/cm<sup>2</sup> at potentials on the order of 2.16V. Fig. 3 shows such a deposit containing crystallites 1 - 5μ on a side. Deposition of thicker films required increases in potential with time to maintain the desired current level. It was found that the graphite substrate could be removed by heating in air to 700°C without oxidizing the PrB<sub>6</sub>. Praseodymium deficient material was deposited from a bath containing .75 mole % Pr<sub>2</sub>O<sub>3.7</sub>. The material deposited from the Pr deficient bath consisted of much smaller cubes < 1 mm on a side which were a deeper violet in color.

#### 5. Sulfides

A synthesis-growth program was started recently to explore the preparation of some commercially important sulfide compounds. A preliminary effort was undertaken to study the preparation of Fe-S compounds of potential use in solid state battery research programs. The first deposition experiments using an alkali sulfate eutectic-iron sulfate bath, operated in air, produced Fe<sub>3</sub>O<sub>4</sub>. It was found that the dissolved FeSO<sub>4</sub> decomposed slowly to iron oxide and SO<sub>2</sub> at a cell temperature of 700°C. Similar behavior can be expected from other metal sulfates. An effort will be made to control the oxygen activity in the melt.

#### 6. Phosphides

Major emphasis will be placed on a new program for bulk synthesis and epitaxial electrodeposition of metal phosphides. Binary and ternary phosphides are of current interest to the electronics industry. Electrodeposition of gallium and indium phosphide will be of primary interest. Although electrochemical literature contains reference to the electrodeposition of these compounds, to date no major effort has gone into the production of device quality material.

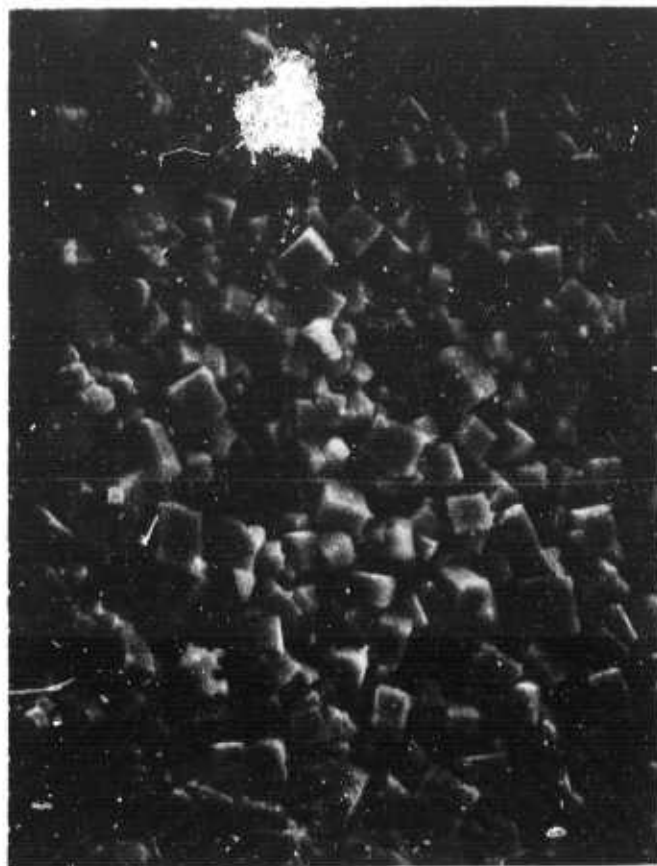
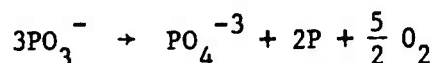


Figure 3.  $.5 \text{ mg/cm}^2$  deposit of  $\text{PrB}_6$  on graphite substrate.  
Crystallites 1 -  $5\mu$  on a side. ( $\sim 2000X$ )

Indium phosphide has been deposited on a Si cathode at 800°C from a sodium metaphosphate based melt consisting of 2.0 NaPO<sub>3</sub>-.25 In<sub>2</sub>O<sub>3</sub>-.5 NaF. The rapid decomposition of InP by P loss at elevated temperature (> 800°C) has been a major obstacle in the synthesis of the compound by traditional high temperature methods. In addition, indium oxide, In<sub>2</sub>O<sub>3</sub>, the source of In in the electrochemical bath, is known to be highly volatile at temperatures above 800°C. Indium phosphide electrodeposition from the lower melting chloride (or a fluoride) eutectic bath should significantly reduce these difficulties.

At the present time, deposition of the more easily controlled GaP system is under extensive investigation, and experience gained will then be applied to the InP system. Gallium phosphide has been deposited on a graphite cathode at 2.0V at 650°C from a chloride eutectic melt consisting of 1.2 LiCl-.8KCl-.1NaPO<sub>3</sub>-.05Ga<sub>2</sub>O<sub>3</sub>. Fig. 4 shows the current vs voltage (I-V) characteristics of the melt vs time. Sample #1 (0 - 24 hours) was grown at 1.0V, sample #2 (24 - 48 hours) at 1.3V, and sample #3 (48 - 72 hours) at 2.0V. Samples #1 and #2 yielded Fe metal and Li<sub>3</sub>PO<sub>4</sub> only, while sample #3 yielded GaP, Li<sub>3</sub>PO<sub>4</sub>, and Ga metal. Fe metal, a major contaminant in the reagent grade LiCl, KCl, and NaPO<sub>3</sub>, was depleted from the 50 gm. melt after 48 hours of electrolysis. This is indicated by the progressively lower initial currents in the three I-V curves. The PO<sub>4</sub><sup>-3</sup> is a by-product of phosphorous reduction:



Gallium metal deposition is seen to begin above 1.4V (I-V curve #3).

Fig. 5 shows I-V characteristics for three baths: (1) 1.2LiCl-.8KCl-.1NaPO<sub>3</sub>, (2) 1.2 LiCl-.8KCl-.05Ga<sub>2</sub>O<sub>3</sub>, and (3) 1.2 LiCl-.8KCl-.1NaPO<sub>3</sub>-.05Ga<sub>2</sub>O<sub>3</sub>. Phosphorous deposition, curve #1, begins below 1.0V. Gallium deposition, curve #2, begins at below 2.0V. The current flow in the Ga curve between .5 and 1.5V may be attributed to the Fe impurity in the chlorides. Curve #3, taken on a combined bath after 48 hours of electrolysis shows no current due to Fe deposition. The

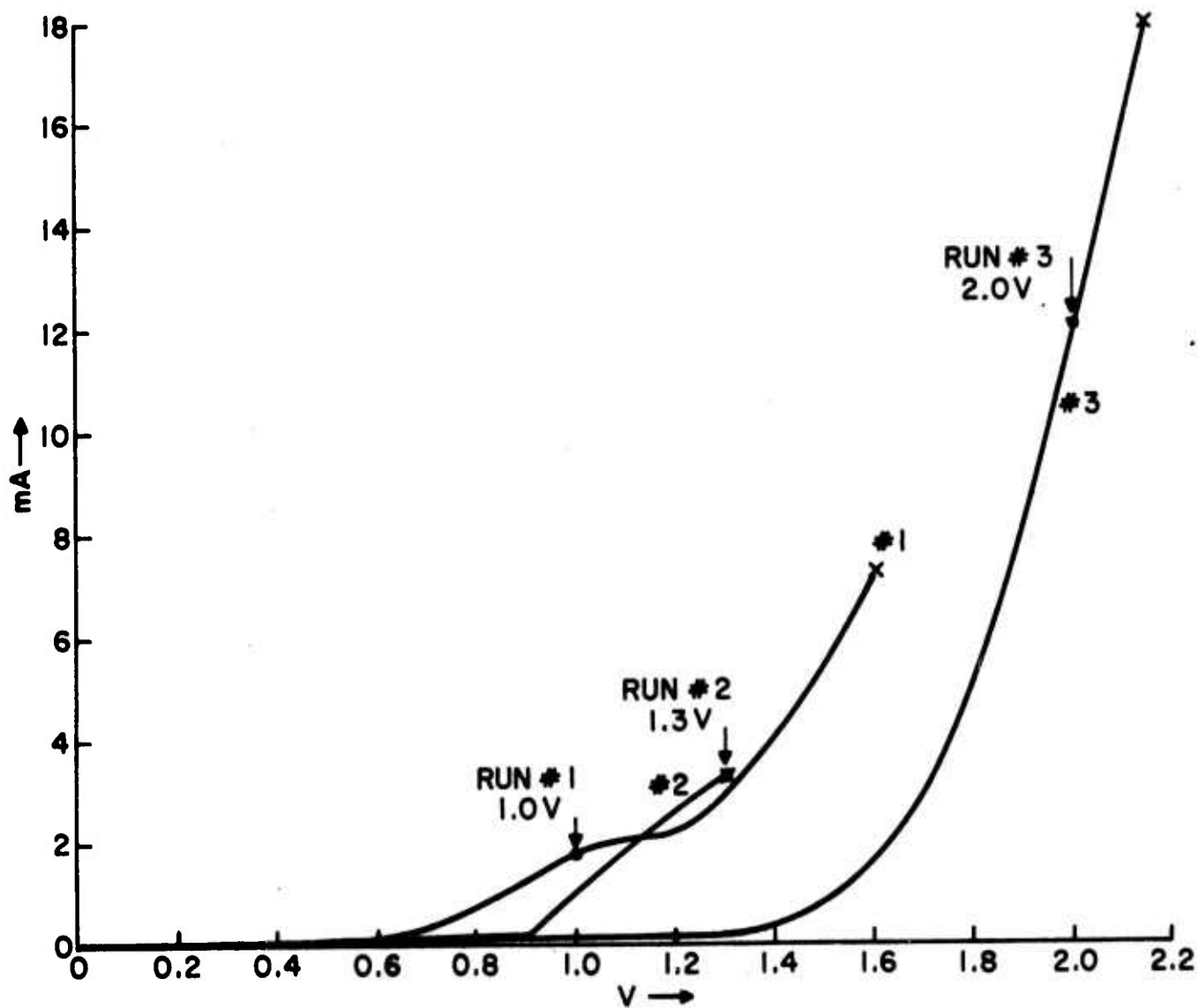


Figure 4. I-V characteristics vs time for  
 $1.2\text{LiCl}-.8\text{KCl}-.1\text{NaPO}_3-.05\text{Ga}_2\text{O}_3$  (moles)  
Curve #1 after 0 hours electrolysis  
Curve #2 after  $\sim 24$  hours electrolysis  
Curve #3 after  $\sim 48$  hours electrolysis

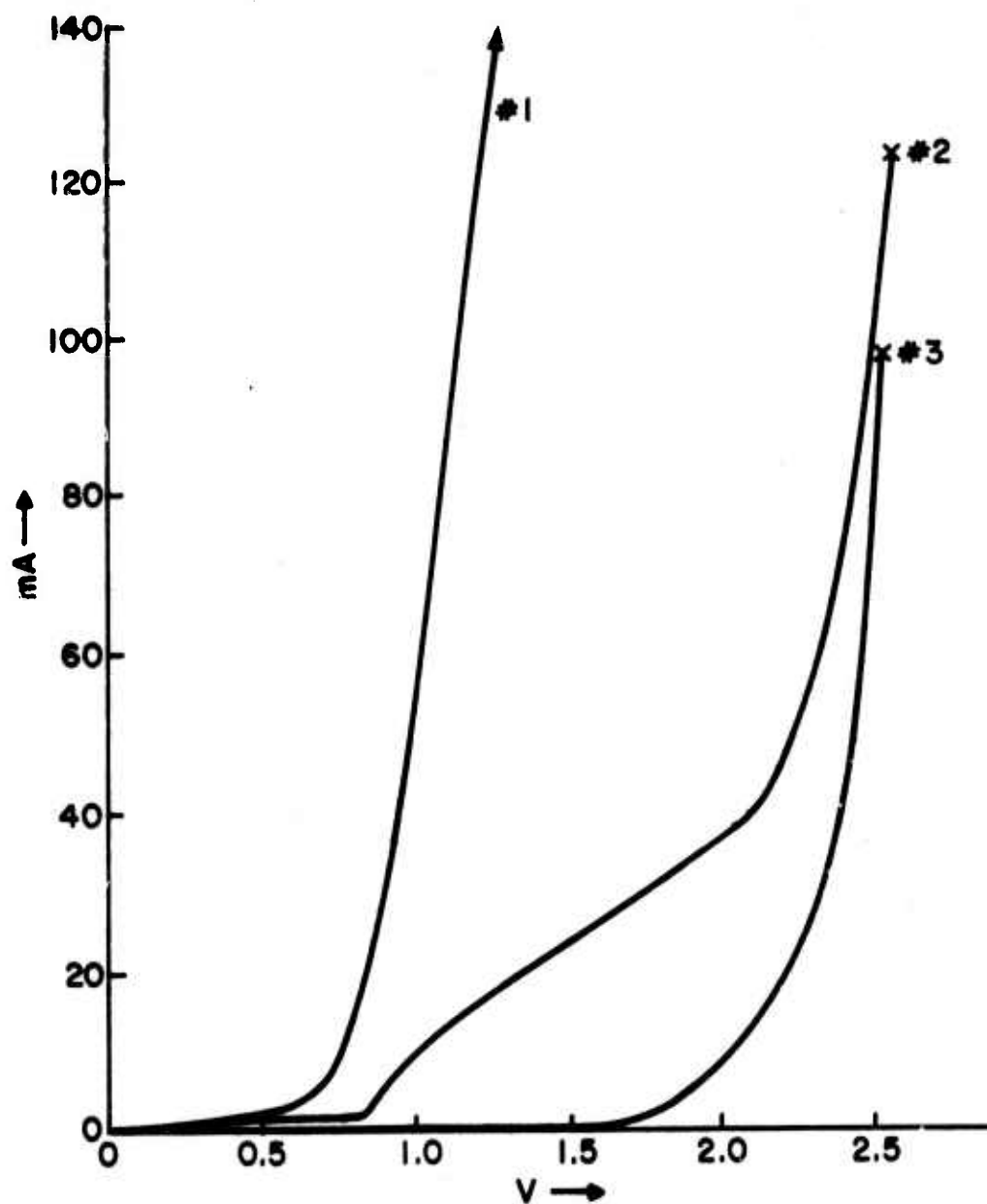


Figure 5. I-V characteristics

Curve #1  $1.2\text{LiCl}-.8\text{KCl}-.1\text{NaPO}_3$  (moles),  $600^\circ\text{C}$

Curve #2  $1.2\text{LiCl}-.8\text{KCl}-.05\text{Ga}_2\text{O}_3$ ,  $850^\circ$

Curve #3  $1.2\text{LiCl}-.8\text{KCl}-.1\text{NaPO}_3-.05\text{Ga}_2\text{O}_3$ ,  $650^\circ$

absence of two current waves, one due to P reduction, the other due to Ga reduction, indicates that there may be some complexing reaction between the two components.

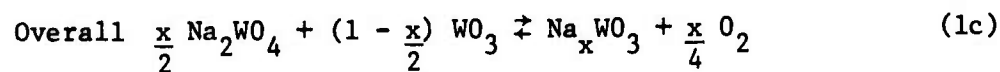
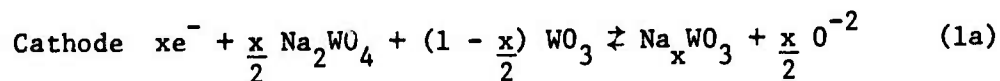
### C. Continuous Growth

R. C. DeMattei

#### 1. Introduction and Summary of Results to Date

Since electrochemical crystallization is a Faradaic process, material is deposited at the growth interface at a controlled rate. This is similar to the condition necessary for stable growth using the Czochralski technique. In principle, therefore, it appeared likely that electrochemical crystallization and crystal pulling could be combined. Since such a technique would be isothermal the diameter of the growing crystal should depend only on current and pull rate. Effort over the last eighteen months has led to the development of the Electrochemical Czochralski Technique (ECT)<sup>(1-2)</sup>.

The feasibility of ECT has now been conclusively demonstrated using sodium tungsten bronze ( $\text{Na}_x\text{WO}_3$ ,  $0.1 < x < 1$ ) as a model compound. This well-characterized compound<sup>(3-11)</sup> can be synthesized in its cubic phase ( $0.38 < x < 0.9$ ) at the cathode of an electrochemical cell over a melt composition range 5-58 m/o tungstic oxide ( $\text{WO}_3$ ) - sodium tungstate ( $\text{Na}_2\text{WO}_4$ ) according to the reactions:



Numerous crystals have been grown using 25 m/o  $\text{WO}_3$  -  $\text{Na}_2\text{WO}_4$  melts ( $\text{Na}_{0.82}\text{WO}_3$ ) at  $750^\circ\text{C}$  with  $\langle 111 \rangle$  oriented seeds in an apparatus designed for pulling under a controlled atmosphere. These crystals exhibited a three-fold axial symmetry with convex sides; and, unlike normal Czochralski growth, the interface region was faceted with well-developed  $\{100\}$  planes. The cross section of these crystals was controllable and depended only on the current and pull rate. This

dependence follows the relation:

$$d_{[111]} = \left[ \frac{ME}{nFc} \frac{I}{0.75(dy/dt)} \right]^{1/2} \quad (2)$$

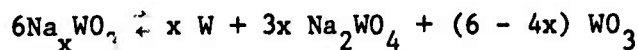
where  $d_{[111]}$  is the distance across the side of the crystal,  $M$  the molecular weight of the depositing species,  $\epsilon$  the faradaic efficiency (approximately 0.92 for  $\text{Na}_{0.82}\text{WO}_3$ ),  $I$  the total current,  $n$  the number of electrons transferred per depositing unit,  $F$  Faraday's constant,  $\rho$  the density of the crystal and  $dy/dt$  the pull rate. Attempts to grow along the other major directions ( $\langle 100 \rangle$  and  $\langle 110 \rangle$ ) with the same degree of control were not successful. Crystals grown in these directions widened uncontrollably owing to the inclination of the fast growth direction ( $\langle 111 \rangle$ ) to the pulling axis. Eventually these crystals lost contact with the melt. Preliminary experiments using a mechanical constraint to control lateral growth indicated that we may be able to grow  $\langle 100 \rangle$  or  $\langle 110 \rangle$  oriented crystals in this manner.

Seed rotation was shown to have a beneficial effect on growth stability up to about 32 rpm. In this region the relation between maximum stable pull rate and rotation rate ( $\omega$ ) in rpm may be expressed as

$$dy/dt = 2.25 + K\omega^{1.17} \quad (3)$$

where  $K$  is a constant. Above 48 rpm, the maximum pull rate increased three-fold, but the sides of the crystal became convex. This behavior is believed to be due to flow separation at the interface.

Small temperature changes ( $\pm 10^\circ\text{C}$  at  $750^\circ\text{C}$ ) had no visible effect on the growing crystals. Larger changes ( $+ 50^\circ\text{C}$ ) caused a visible decrease in the deposition rate and the formation of a grey, powdery tungsten deposit due to the reaction



which was reported by Randin<sup>(11)</sup>.

In order to complete the study with the tungsten bronze system, the effects of changes in melt composition needed to be investigated.

## 2. Experimental Results

To test the effect of composition on the growth of pulled sodium tungsten bronze crystals, several crystals were grown from 10 m/o  $WO_3 - Na_2WO_4$  ( $Na_{0.89}WO_3$ ) and from 45 m/o  $WO_3 - Na_2WO_4$  ( $Na_{0.6}WO_3$ ) melts. The higher sodium content crystals were grown at  $710^\circ C$  to avoid the thermal decomposition problem<sup>(11)</sup>, while those of lower sodium content were grown at  $800^\circ C$  to ensure a completely molten bath. All of the  $\langle 111 \rangle$  oriented crystals grown under these conditions exhibited cross sections which could be predicted by equation (2). The differences in the distance (d) among the crystals grown from different melt compositions was due to the differences in molecular weight (M), in number of electrons transferred (n,  $n = x$ ), and in the density ( $\rho$ ) of the depositing crystal.

## 3. Conclusions

The feasibility of the Electrochemical Czochralski Technique has been demonstrated. The parameters affecting growth by this technique have been studied using sodium tungsten bronze as a model. The results of this study should be directly applicable to the growth of other materials by ECT.

The Electrochemical Czochralski Technique should prove very useful for the growth of large crystals of electrically conducting materials with constant cross section which cannot be grown by the standard Czochralski Technique due to high melting point, thermal decomposition, or non-congruently melting systems.

## 4. Future Plans

While the feasibility of the Electrochemical Czochralski Technique has been established, controlled diameter growth along directions other than the fast growth direction needs further study, as does the application of this technique to other systems. Of particular interest would be a system with more isotropic growth kinetics which would allow a more complete study of the inherent diameter control capability of ECT. Growth from low solute concentration

systems would also be of interest. In addition, much of the technology developed with ECT could be applied to the development of another new technique: electrochemical, edge-defined, film-fed growth (EEFG). Such a technique would allow the growth of lengths of complex shaped materials that would be difficult to obtain by other means.

The hydrodynamic model which led to the development of equation (3) will be studied using a glycerine and water system. Because of its ease of growth, the sodium tungsten bronze system can also be used in a future study of methods of effecting crystal perfection or of increasing growth rate while maintaining crystal quality. This would include the use of electropolishing and applied a.c. deposition. Such a program would be two-pronged; one aimed at understanding of the progress, the other at equipment and technique development.

#### 5. References

- (1) R. DeMattei, Semi-Annual Technical Report, Long Range Materials Research, ARPA Order No. 2470-Amendment F, June 1975, p. 102.
- (2) R. C. DeMattei, R. A. Huggins and R. S. Feigelson, Crystal Growth by the Electrochemical Czochralski Technique, J. Crystal Growth, to be published.
- (3) K. D. Morris and P. L. Robinson, J. Chem. Eng. Data. 9, 444 (1964).
- (4) E. Banks and A. Wold, Prep. Inorg. React. 4, 237 (1968).
- (5) P. G. Dickens and M. S. Whittingham, Quart. Rev. 22, 30 (1968).
- (6) E. Banks, C. W. Fleischmann and L. Meites, J. Solid State Chem. 1, 372 (1970).
- (7) C. T. Hauck, A. Wold, and E. Banks, Inorg. Synth. 153 (1970).
- (8) R. A. Fredlein and A. Damjanovic, J. Solid State Chem. 4, 94 (1972).
- (9) M. S. Whittingham and R. A. Huggins, NBS Special Publication, 364, 51 (1972).
- (10) H. R. Shanks, J. Crystal Growth 13/14, VIII-4 (1972).
- (11) J.-P. Randin, J. Electrochem. Soc. 120, 1325 (1973).

D. Electrodeposition of Niobium-Germanium Alloys and Silicon from Molten Fluorides

U. Cohen

1. Introduction

The niobium intermetallic compounds  $Nb_3X$ , where X is Al, Sn, Ge, Si or Ga, are among the best-known superconductors. The compound  $Nb_3Ge$  was recently shown<sup>(1,2)</sup> to possess the highest known superconducting transition temperature,  $T_c = 23.2^\circ K$ .

These compounds have the A-15 crystal structure, and are highly brittle and non-machinable. Conventional metallurgical techniques, such as melting and casting, rolling, extrusion and wire-drawing, are therefore inadequate for their fabrication. The so-called "stoichiometric superconductors  $Nb_3Sn$ ,  $V_3Si$ , and  $V_3Ga$ , which are stable at their stoichiometric composition (75-25 mol. %) are commercially manufactured. They are produced by several sophisticated techniques such as chemical vapor deposition<sup>(3,4)</sup>, dipping-diffusion<sup>(5)</sup>, and diffusion through a copper-matrix medium<sup>(6-8)</sup>. The other "nonstoichiometric" superconductors such as  $Nb_3Al$ ,  $Nb_3Si$  and  $Nb_3Ge$  appear to be much more difficult to produce with homogeneous and reproducible properties. Thus, bulk prepared " $Nb_3Ge$ " has a composition corresponding to  $Nb_4Ge$ , with  $T_c \approx 6^\circ K$ <sup>(9)</sup>. In contrast, the samples prepared at lower temperatures by vapor phase deposition techniques, produce the compound with a closer composition to the stoichiometric  $Nb_3Ge$ , with  $T_c$  in excess of  $20^\circ K$ .

Electrodeposition of these compounds from molten fluorides may offer several unique advantages over the vapor phase techniques. The process is isothermal and of low temperature range ( $700 - 1000^\circ C$ ). Uniform deposit composition throughout the entire deposit is characteristic of the process. Either simple or complex shapes may be coated with thin or thick films. In contrast, the vapor phase techniques produce non-uniform coatings, with only a limited area of the right composition. This limitation is inherent in these techniques, whenever separated vapor sources are used. The rate of electrodeposition is easily controlled, and so are the composition, structure, and the

morphology of the deposit. Under proper conditions, the atomistic interface mechanisms involved in electrodeposition may offer easy surface rearrangement and therefore a lower concentration of crystal defects. The physical vapor deposition mechanism on the other hand, involves the arrival of molecular species, and sometimes clusters of appreciable size, at the interface, thereby increasing the possibility of defect incorporation. Lastly, the economical factor seems to be in favor of the electrodeposition process, as this technique is more familiar to industry.

Fluoride melts were chosen since they have been proved to yield superior coatings of niobium and other refractory metals<sup>(10-16)</sup>. The excellent bonding of the coatings is probably due to the fluxing effect of the fluoride solutions, exposing clean oxide-free metallic surfaces to the solution. This is essential for good adherency. Also, the fluoride complexes are stable enough to decrease diffusion-control effects, which are responsible for roughness increase, and eventually result in dendritic or powdery growth. Other attractive features of the alkali fluoride melts are their large decomposition potentials (> 3 volts), high ionic conductance (and negligible electronic conductance), as well as low melting point eutectics, low vapor pressure, and low viscosity. All of these make the fluorides ideal solvent electrolytes.

The most severe restriction on the electrodeposition of alloys is the compatibility of the components for simultaneous codeposition. To obtain a certain M-N alloy composition the standard electrode potentials of the two metals must not be too widely separated.

An estimate of the maximum standard potential separation can be made<sup>(17)</sup>. Assuming  $m = n$ ,  $T = 1000^\circ\text{K}$ ,  $a_m/a_N \leq 10$ , and  $a_N^{+n}/a_N^{+m} \leq 1000$ , we find that

$$|E_M^\circ - E_N^\circ| \leq 0.794/n \text{ volts}$$

Thus, for  $n = m = 4$ , any couple for which  $|E_M^\circ - E_N^\circ| > 0.2$  volts, may not be simultaneously co-deposited (under equilibrium conditions).

In addition to the requirement on the standard electrode potentials, a couple may not match due to different deposition kinetics.

These may be different electron transfer rates, or the interference of coupled chemical reactions, or catalytic or adsorption effects. It may also be noted that such interferences usually shift the actual deposition potentials from their equilibrium values.

Niobium and germanium were shown to be compatible for co-deposition in the first part of this research project<sup>(18)</sup>. This report describes the further investigation of this couple, the deposition of their various intermediate phases, and the improvement of deposit quality and morphology control. The related epitaxial growth of silicon by electrocrystallization from molten fluorides<sup>(19)</sup> will be discussed in Section E.

Of the four Nb-Ge intermetallic compounds three have been obtained as single phase coherent deposits. These are  $\text{NbGe}_2$ ,  $\text{Nb}_3\text{Ge}_2$  and  $\text{Nb}_5\text{Ge}_3$ . The fourth compound, the superconductor  $\text{Nb}_3\text{Ge}$ , was not obtained so far as a single phase deposit. It was obtained, however, as a mixture with either Nb or  $\text{Nb}_5\text{Ge}_3$ .

Attempts to improve deposit quality at high deposition rates by the application of alternating square wave pulses proved to be very successful for the deposition of niobium alone, but rather hard to control with the binary alloys. The technique involves the application of a cathodic pulse, followed by an anodic electropolishing pulse. The electrodeposition rate of niobium was improved by this technique by a factor of 10-50 over the steady state current value. The difficulties in the application of the pulse technique to the binary alloys are believed to be due to the different potentials at which the different phases are anodically stripped.

In addition to the previously described<sup>(18)</sup>  $\text{Au}/\text{F}^-$ ,  $\text{F}_2$  reference electrode, new practical reference electrodes were developed. The redox electrode  $\text{Cu}/\text{Nb}(\text{IV})$ ,  $\text{Nb}(\text{V})$  was used for solutions containing niobium solute only. When the solution contained both niobium and germanium solutes, the copper strip was covered with a Ge layer, and Mo was used instead. These reference electrodes are very practical and convenient in use, as they are simply established by the immersion of the inert metal strip in the bulk of the solution. The solution containing  $\text{K}_2\text{NbF}_7$  is first equilibrated with a niobium strip according

to the reaction



Senderoff and Mellors showed<sup>(10,13)</sup> that at equilibrium the ratio  $(\text{Nb(V)})/(\text{Nb(IV)}) \approx 1$ , which suggests a stable redox potential. These reference electrodes were found to be sensitive and reproducible within  $\pm 1$  mV.

Silicon epitaxial layers of the orientation (111) were grown on a single-crystal silicon substrate of the same orientation. Fluoride baths which contained the salt  $\text{K}_2\text{SiF}_6$  were used, and silicon was utilized as a dissolving anode.

## 2. Experimental Procedures for Growth of Niobium-Germanium Alloys

### (a) Materials

High purity and ultimate dryness are preconditions for successful electrodeposition from molten fluorides. Most of the chemicals which were used for this work were of 99.9% purity or better, and were kept in a vacuum desiccator prior to use. The hygroscopic KF was dried in a vacuum oven at 200°C for 48 hours.

Ultimate drying was achieved by adding the salt  $\text{KHF}_2$  to the salt mixture, and heating above the decomposition temperature of  $\text{KHF}_2$ . Slow heating, under vacuum, liberated HF which drove out the oxides according to the reaction:



The equilibrium was shifted to the right, as vacuum was maintained to remove the water vapor, and HF was continuously liberated in the melt. The process was completed with the expulsion of the dissolved excess HF by purging the melt with purified helium gas at 850°C.

The melt, containing  $\text{K}_2\text{NbF}_7$  in the KF-LiF solute, was further purified by a prolonged electrolysis using a niobium sheet as a dissolving anode. The more noble metallic impurities were substantially reduced by this procedure. Thus, the initial Nb-deposit contained 0.2% Fe, which dropped to below 0.05% after an overnight electrolysis.

Another source of Fe contamination was identified. The vapor over the melt could react with the inconel chamber walls, leaching the iron, and upon condensing, occasionally dripped back into the melt. A molybdenum liner was found useful in preventing this contamination.

Grade A helium was further purified by passing through a Linde 13X molecular sieve in a liquid nitrogen trap, and by flowing over heated titanium chips at 700°C.

(b) Apparatus

The experimental set-up is schematically shown in Fig. 1. A molybdenum crucible containing the salts is placed in an inconel chamber. Cathode, anode, reference electrode, thermocouple-well, and helium bubble tube are made to fit into the crucible. Lowering and raising of each one of these is independent of the other and is performed through vacuum-seal fittings. The electrodes are electrically insulated from the other components of the crucible. They may be removed through "rescue chambers" which are separated from the main chamber by circle seal valves. Thus, the electrodes may be replaced during an experiment without the need to cool the melt down and open the main chamber. A series of more than 60 experiments was performed without opening the main chamber.

Potentiostatic and galvanostatic control, as well as sweeping and pulsating signals, were obtained from a combination of a Potentiostat PAR 173 and a Universal Programmer PAR 175. Recording was performed with an X-Y Recorder and an oscilloscope.

(c) Procedures

The  $\text{KHF}_2$  drying procedure was described in detail in the Materials section, and in a previous report<sup>(18)</sup>. Further metallic purification by electrolysis was performed by the utilization of either steady-state current, or a pulsating square wave current. The application of the latter allowed shorter electrolysis periods, since higher currents were utilized. Following the purification, the melt was cooled, and a weighted amount of  $\text{K}_2\text{GeF}_6$  salt was introduced into the crucible through a long funnel. Remelting under vacuum, and admitting helium completed the procedure for solution preparation.

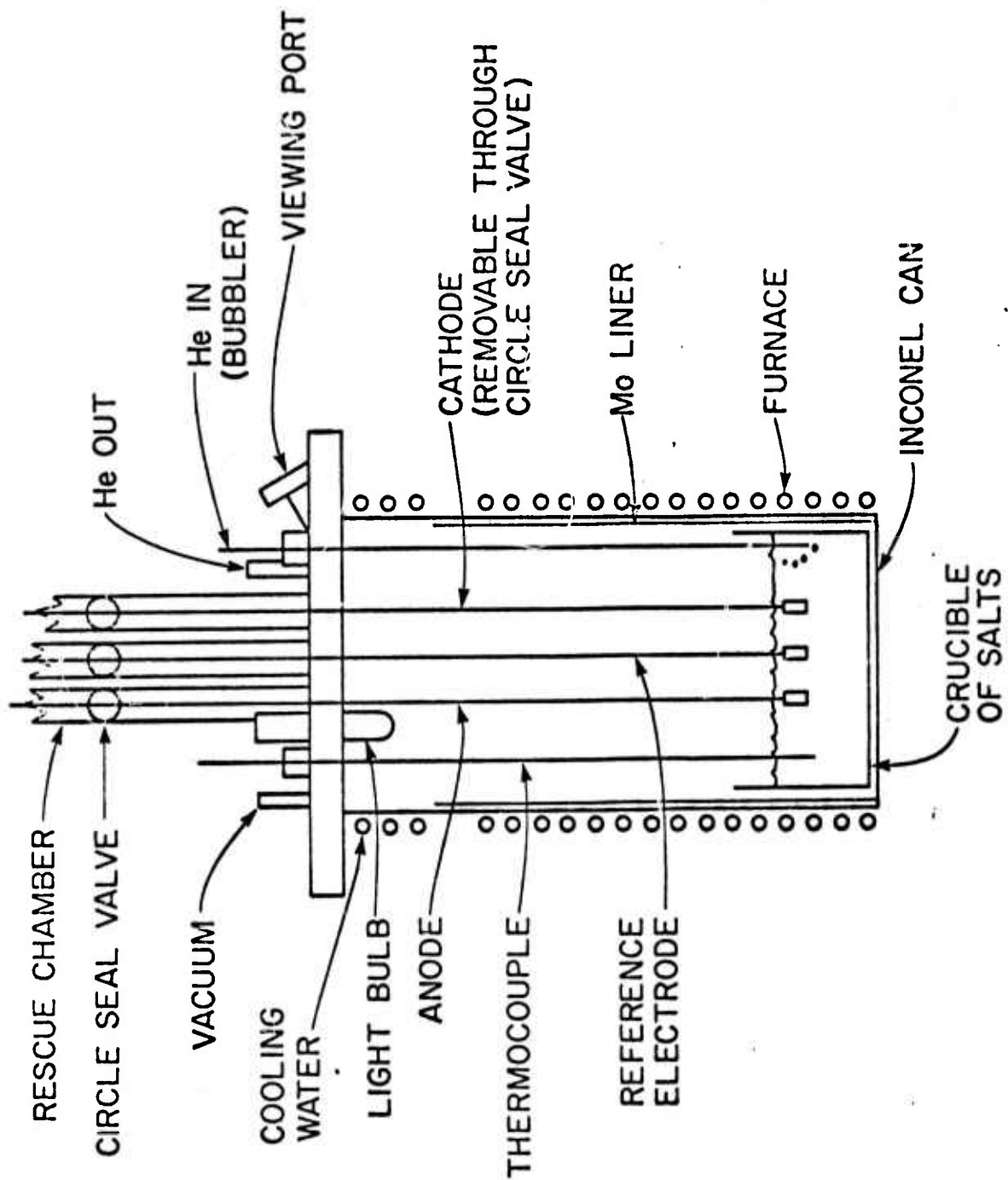


Figure 1. Experimental set up

A typical electrodeposition run was preceded by taking several cyclic voltammograms to reveal the potential regions of interest. Electrodeposition runs were mostly of the steady-state potential type, but other modes such as steady-state current, cyclic sweeping (current or potential controlled), as well as cyclic pulsating (current or potential controlled) were also used.

The samples deposited were subject to analysis consisting of x-ray diffraction, x-ray fluorescence, metallography, electron microprobe, scanning electron microscopy, and superconducting measurements. Rough estimates were also made of the bonding quality and the morphology.

### 3. Results and Discussion

#### (a) Nb and Ge Compatibility for Co-deposition

Compatibility of the pair Nb-Ge for a simultaneous co-deposition was shown in the first part of this research project<sup>(18)</sup>. Figs. 2 and 3 show the decomposition potentials of  $K_2NbF_7$  and  $K_2GeF_6$  in the KF-LiF eutectic. The decomposition potential values thus obtained may be corrected to the standard electrode potentials at 750°C to yield:

$$E_{Nb}^{\circ} = -1.78 \pm 0.10 \text{ volts}$$

and

$$E_{Ge}^{\circ} = -1.63 \pm 0.10 \text{ volts}$$

The uncertainty of  $\pm 0.10$  volts is attributed to the  $Au/F^-$ ,  $F_2$  reference electrode which was used in these measurements. From the criterion which was derived in the introduction, it is obvious that the pair may be simultaneously co-deposited.

#### (b) Cu/Nb(IV),Nb(V) and Mo/Nb(IV),Nb(V) Reference Electrodes

$K_2NbF_7$ -solutions were first equilibrated with regard to the niobium valence by reacting with a niobium sheet:  $Nb + 4Nb(V) = 5Nb(IV)$ . The mean valence was 4.5<sup>(10)</sup>, and a practical reference electrode was then established by simply immersing a Mo or Cu strip in the bulk of the solution. The redox potential of the couple is most stable at  $[Nb(IV)]/[Nb(V)] \approx 1$ , since fluctuations in concentration influence this ratio the least. The standard electrode potential for this redox

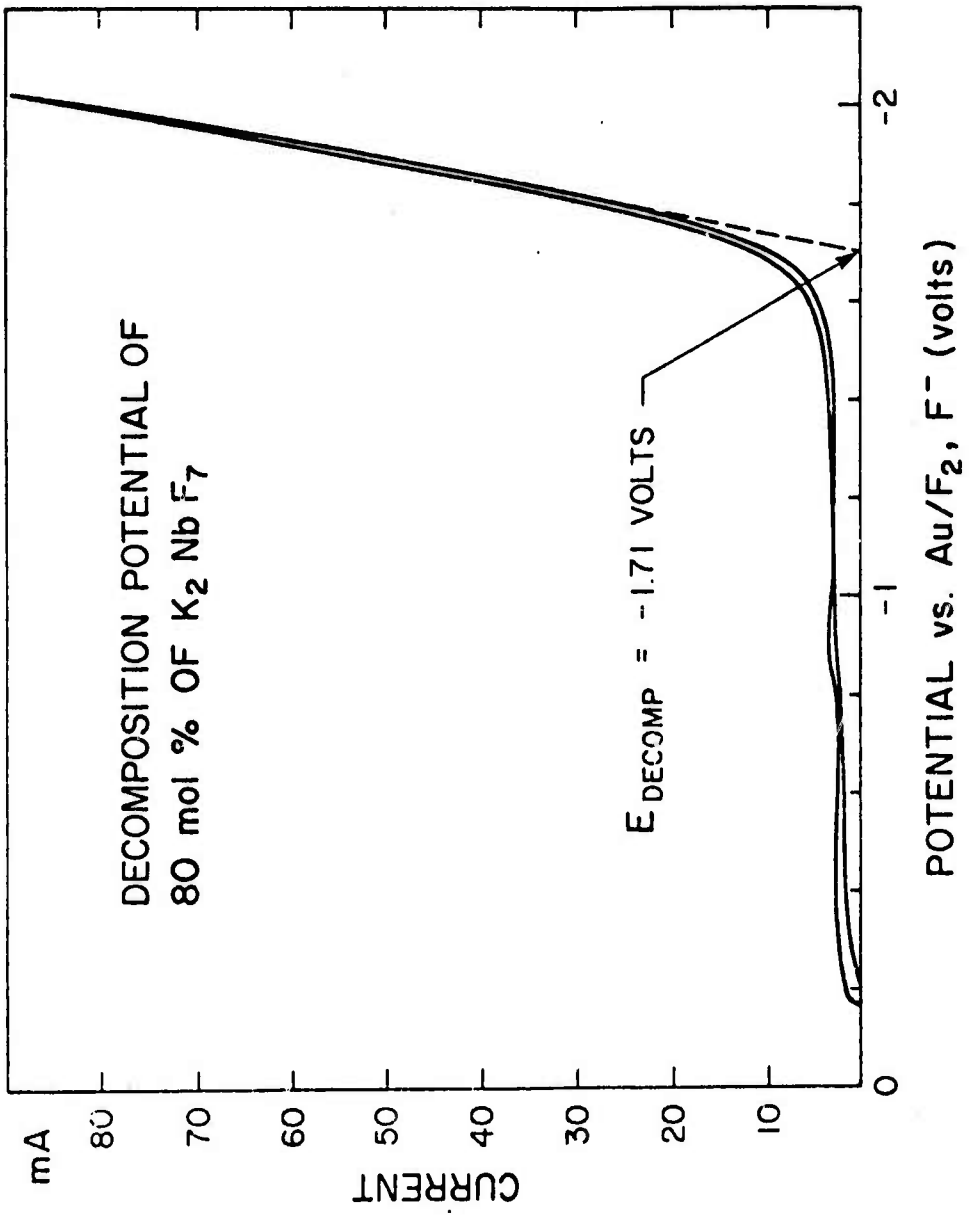


Figure 2. Decomposition potential of  $K_2 Nb F_7$  in  $KF-LiF$  eutectic.  
 $t = 812^\circ C, v = 1.66$  mV/sec

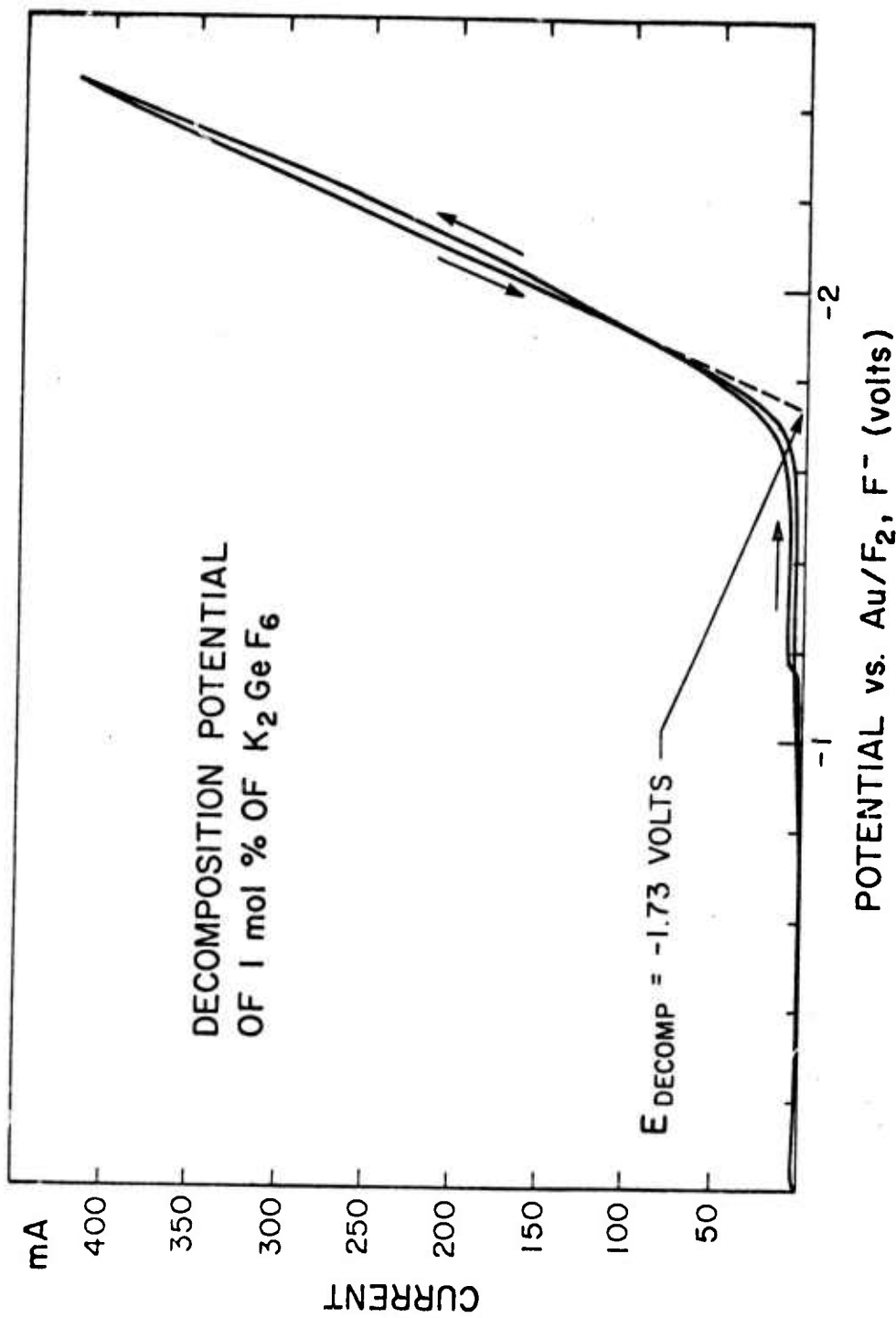


Figure 3. Decomposition potential of  $K_2GeF_6$  in  $KF-LiF$  solvent.  
 $t = 753^\circ C$ ,  $v = 16.6$  mV/sec

couple was reported by Senderoff and Mellors<sup>(13)</sup> to be -0.11 volts vs. the Ni/NiF<sub>2</sub> (1 mol. %) electrode. As this reference electrode has no separate compartment, there could be no liquid junction potentials of any kind. No adsorption effects could be observed on the Mo electrode, as indicated by the observation that a potential difference of less than 1 mV between the reference and a new Mo cathode was reached within a few minutes after the introduction of a fresh Mo cathode. Since the K<sub>2</sub>GeF<sub>6</sub> concentration was usually less than 10% of the K<sub>2</sub>NbF<sub>7</sub> concentration, it could have little effect only on the electrode potential. It was found, however, that if Cu strips were used in solutions that contained K<sub>2</sub>GeF<sub>6</sub>, they developed an adsorbed Ge layer, and they were, therefore, inappropriate for germanium-containing solutions. Copper reference electrodes were found to be suitable for solutions containing niobium only. The redox reference electrodes were found to be sensitive and reproducible within  $\pm 1$  mV.

(c) Electrochemical Investigation of the Nb-Ge Couple

Cyclic Voltammetry

Cyclic voltammetry involves sweeping the working electrode potential linearly with time to a new value, and then sweeping it back. The current response, as a function of the working electrode potential (versus some reference electrode) is recorded, and the curve is called a "cyclic voltammogram".

Cyclic voltammetry permits the study of the thermodynamic properties (such as  $E^\circ$ ), as well as the reaction kinetics. It provides criteria for reversibility, coupled chemical reactions, adsorption and catalysis interferences.

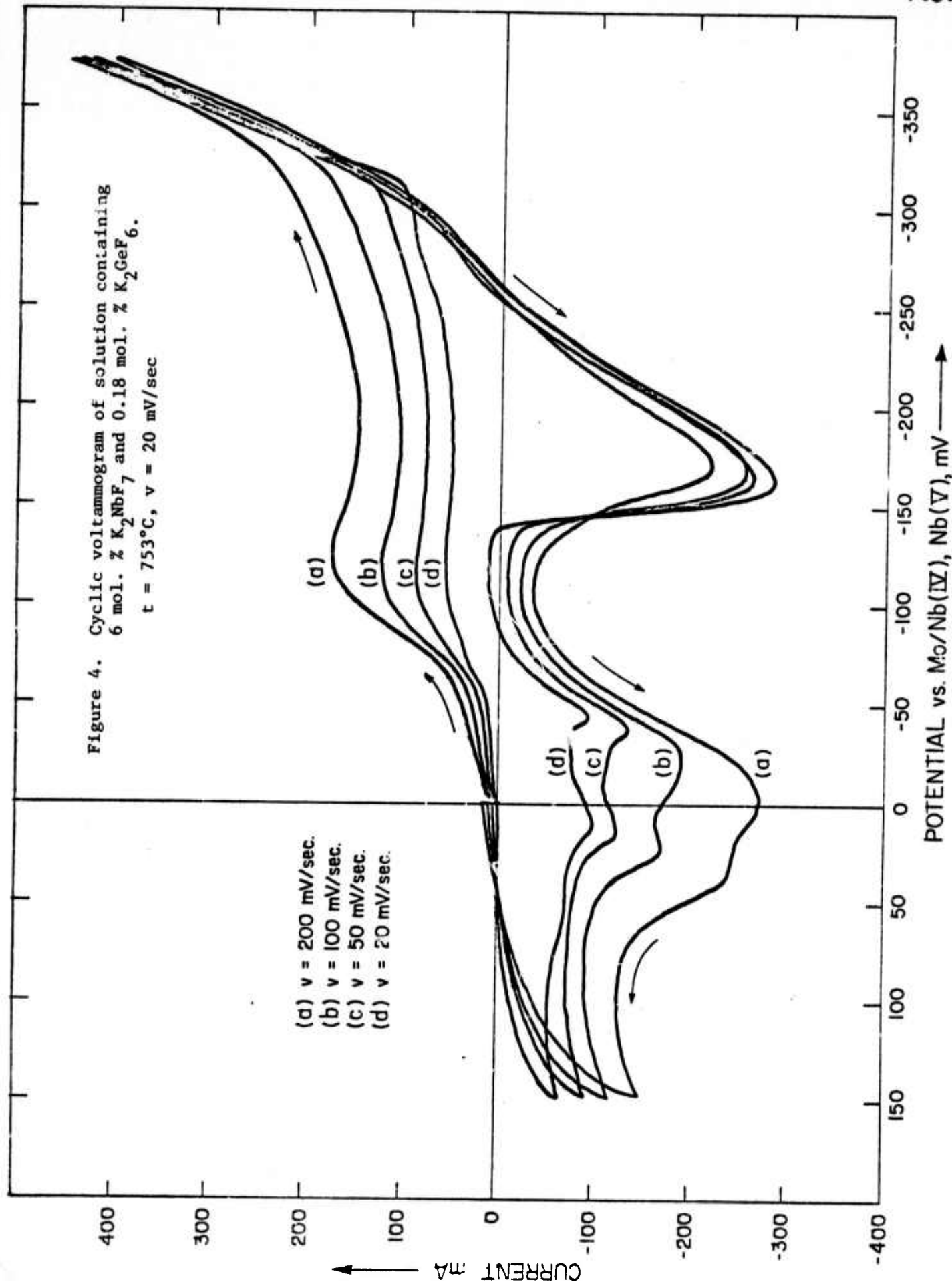
Experiments were performed with a Mo-working electrode, Mo/Nb(IV), Nb(V) reference, and Ge as a counter-electrode.

Two distinct cathodic waves could be observed, as shown in Fig. 4. The first wave starts at about -60 mV, and the second at about -300 mV.

Constant cathode potential (versus the Mo/Nb(IV), Nb(V) electrodes) electrolyses at potentials corresponding to the first cathodic wave yielded deposits of Nb-Ge compounds. Electrolyses under

Figure 4. Cyclic voltammogram of solution containing 6 mol. %  $K_2NbF_7$  and 0.18 mol. %  $K_2GeF_6$ .  $t = 753^\circ C$ ,  $v = 20$  mV/sec

- (a)  $v = 200$  mV/sec.
- (b)  $v = 100$  mV/sec.
- (c)  $v = 50$  mV/sec.
- (d)  $v = 20$  mV/sec.



constant cathode potential, at potentials corresponding to the second cathodic wave always resulted in a very thin transient layer rich in Ge, covered with a thick, almost pure Nb layer. The second cathodic wave is, therefore, attributed to Nb deposition, and its corresponding anodic peak is attributed to the Nb-stripping process. Electrolyses at potentials corresponding to the plateau between the two cathodic waves resulted in very thin adherent layers (less than 1  $\mu\text{m}$ ) and loose powders or dendrites of the same compound(s) obtained on the first wave. Attempts to electrolyze at potentials corresponding to the base of the second cathodic wave, or slightly to its left (anodically), resulted in a transient layer, containing the  $\text{Nb}_3\text{Ge}$  phase, underlying a niobium layer.

Relatively rich germanium solutions revealed more than one step (peak) on the first cathodic wave, see Fig. 5. It was found that each step corresponded to the deposition of a certain Nb-Ge alloy. The more cathodic the step, the richer the alloy in Nb. Cyclic voltammograms of lower germanium concentrations revealed only one step on the first cathodic potential, see Fig. 6. Constant potential electrolyses at this step yielded the alloys richer in Nb ( $\text{Nb}_3\text{Ge}_2$ ,  $\text{Nb}_5\text{Ge}_3$ , or  $\text{Nb}_5\text{Ge}_3 + \text{Nb}_3\text{Ge}$  mixture). At least two anodic peaks corresponding to the first cathodic wave, could always be observed. The relative magnitudes, separation, and locations of these peaks were dependent on the scanning rate, temperature, and solution concentration. The multiple anodic peaks corresponding to the first cathodic wave, even when it was composed of one step, as in Fig. 6, suggests a step-wise anodic stripping of the Nb-Ge deposit. The one on the right side corresponds to the richest niobium phase, and the one on the left corresponds to the stripping of the Ge-richest alloys.

The cyclic voltammetry was found to be very useful and convenient as it is a rapid technique, lacking the deleterious effects of prolonged electrolysis characteristic of the steady-state techniques. These are mainly the surface area increase, non-diffusional mass-transfer, time required, and errors if the process is irreversible (a fact which may not be detected by the steady-state techniques). Steady-state may be approximated by cyclic voltammetry to any degree which is consistent with the above interferences.

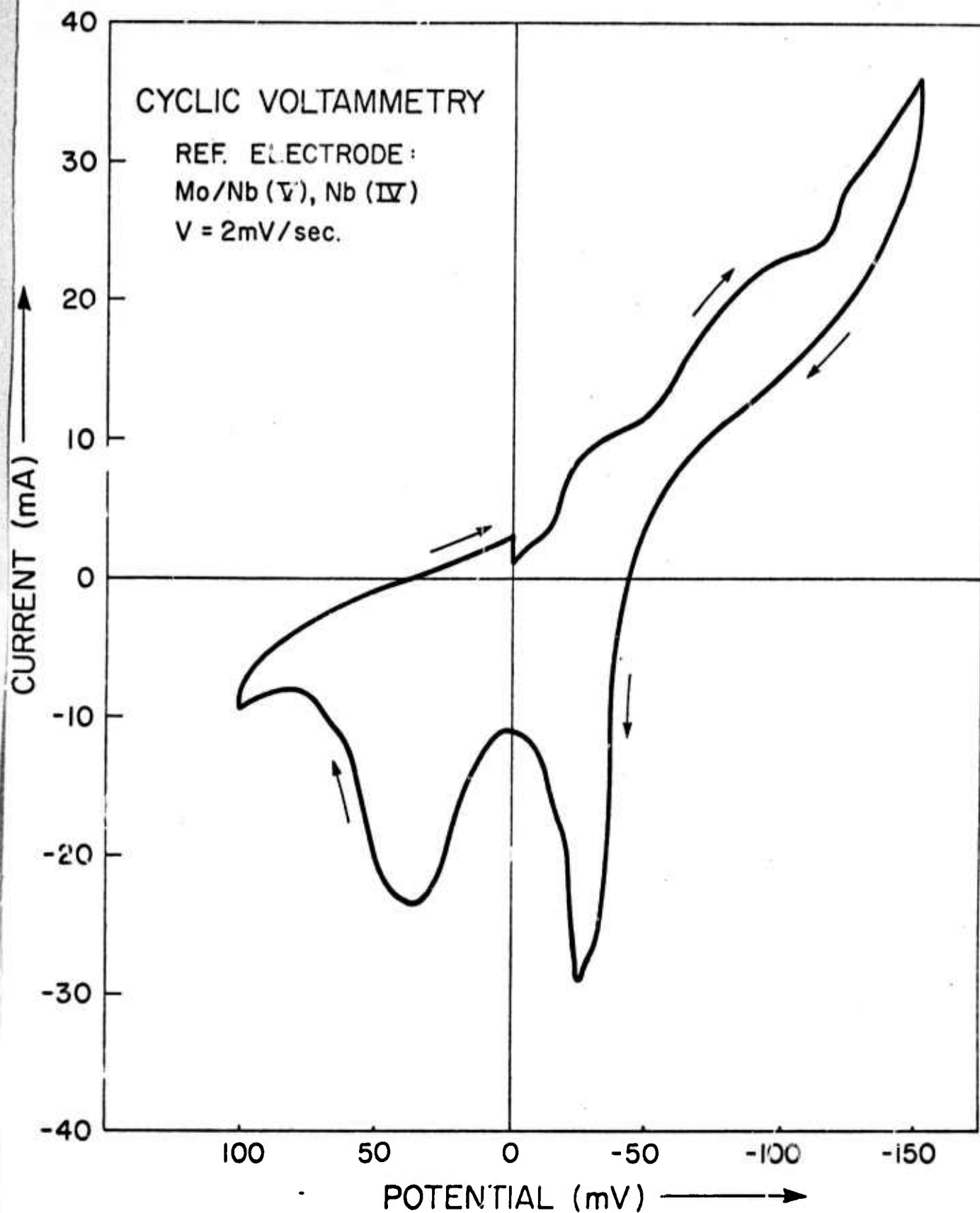


Figure 5. Cyclic voltammogram of the first wave. Solution containing 5 mol. %  $K_2NbF_7$  and 0.16 mol. %  $K_2GeF_6$ .  
 $t = 707^\circ C$

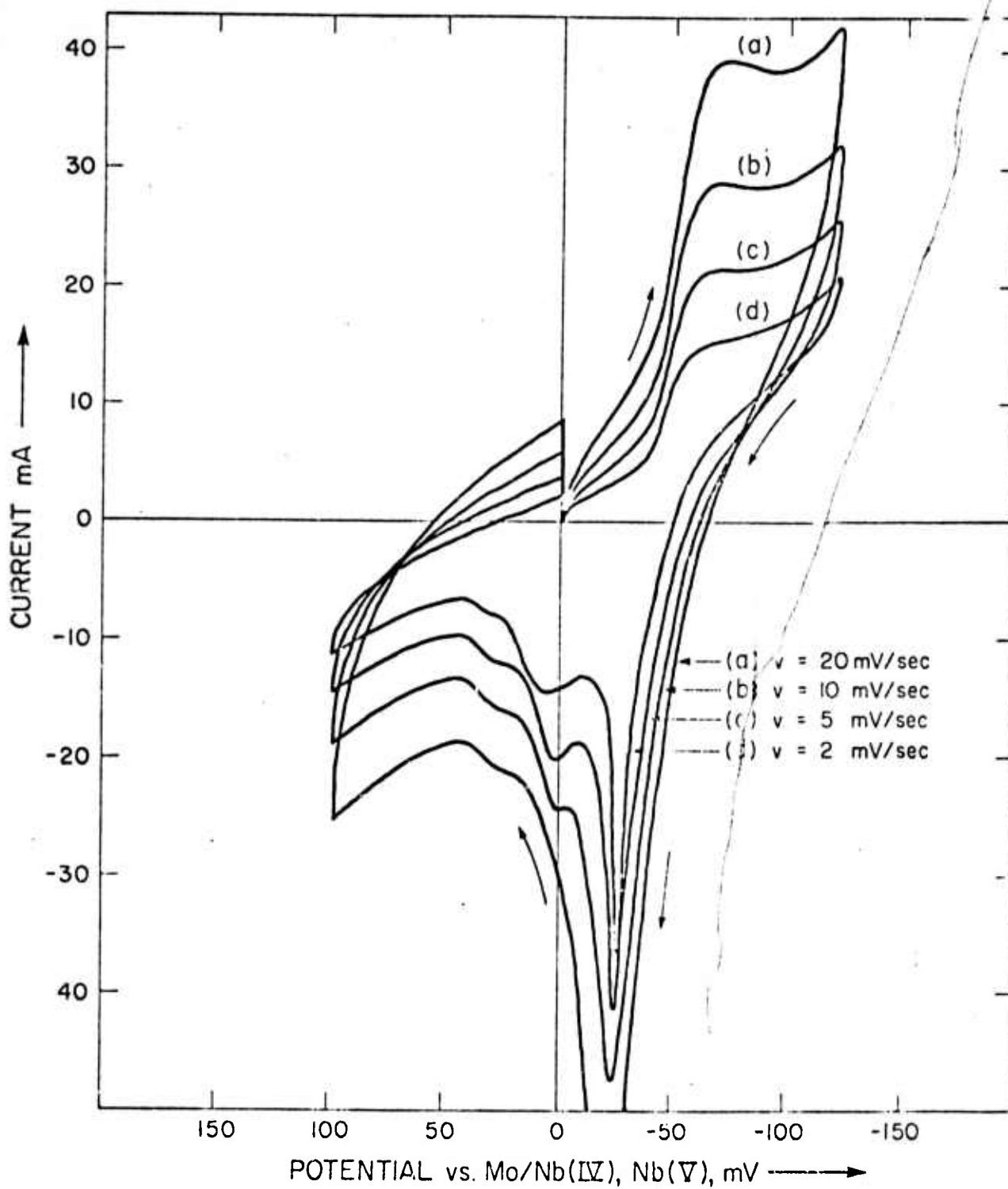


Figure 6. Cyclic voltammogram showing a first wave composed of one step (peak) only.

5 mol. %  $K_2NbF_7$ , 0.08 mol. %  $K_2GeF_6$ ,  $t = 756^\circ C$

(d) Nb-Ge Compound Co-deposition

Several cyclic voltammograms were usually taken preceding an electrolysis run, thus revealing the exact potential region at which the constant potential electrolysis was to be performed. High quality coatings could be obtained when the constant potential corresponded to the base of the first step (peak) of the first cathodic wave. Electrolysis at potentials cathodic to this base resulted in inferior coatings. The more cathodic the potential, the more roughness and coherency deterioration was observed. Potentials cathodic to  $E_{p/2}$  yielded deposits of thickness-limited nature, with many protrusions, eventually developing into dendrites and powders. Figure 7 shows a typical Mo cathode-substrate and its Nb-Ge coating. Coatings with thicknesses of more than 100  $\mu\text{m}$  were demonstrated.

NbGe<sub>2</sub>

This compound was deposited from the relatively rich germanium solutions. Fig. 8 shows SEM photographs of the coating surface. Note the growth of individual crystallites. This suggests difficult nucleation and therefore easy single crystal growth. The compound was obtained by electrolysis at a constant cathodic potential at the base (-18 mV) of the first step on the first cathodic wave shown in Fig. 5.

Nb<sub>3</sub>Ge<sub>2</sub>

This compound could be obtained from the relatively rich germanium solutions, when employing potentials corresponding to the second step on the first cathodic wave, such as in Fig. 5. This, however, resulted in a thickness limited coating which began to deteriorate after several microns of thickness. NbGe<sub>2</sub> crystallites were occasionally found in these coatings. A better procedure was to use the intermediate germanium concentrations, for which a single-step first cathodic wave, such as Fig. 6, was characteristic. Constant-potential electrolysis at the base of this step, yielded single phase coherent deposits of this compound. Fig. 9 shows SEM photographs of the coating surface. It was typically grown from a solution containing 5 mol. % K<sub>2</sub>NbF<sub>7</sub> and 0.05 mol. % K<sub>2</sub>GeF<sub>6</sub> at 750°C and under constant potential of -35 mV (versus the Mo/Nb(IV), Nb(V) electrode).

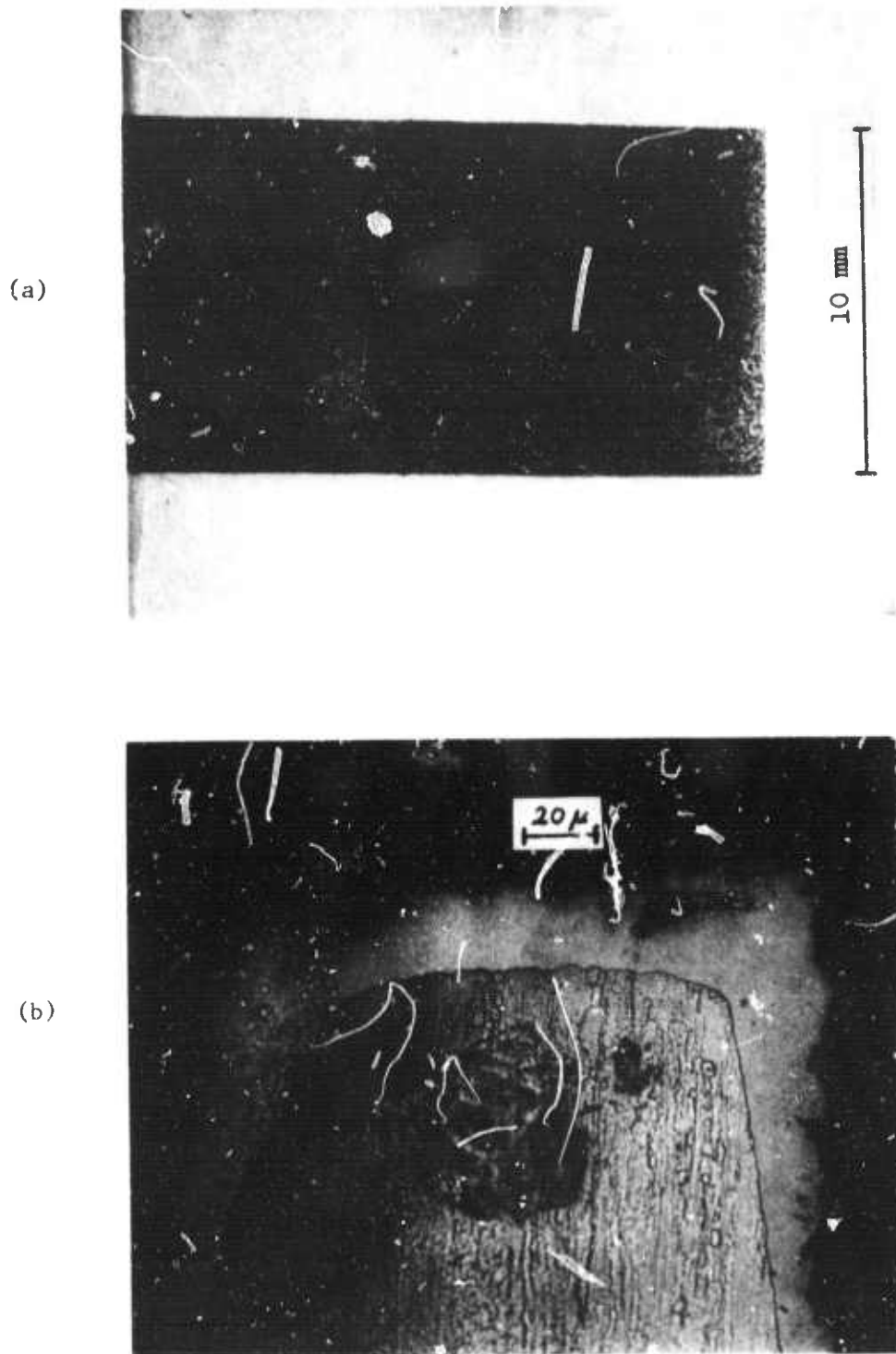
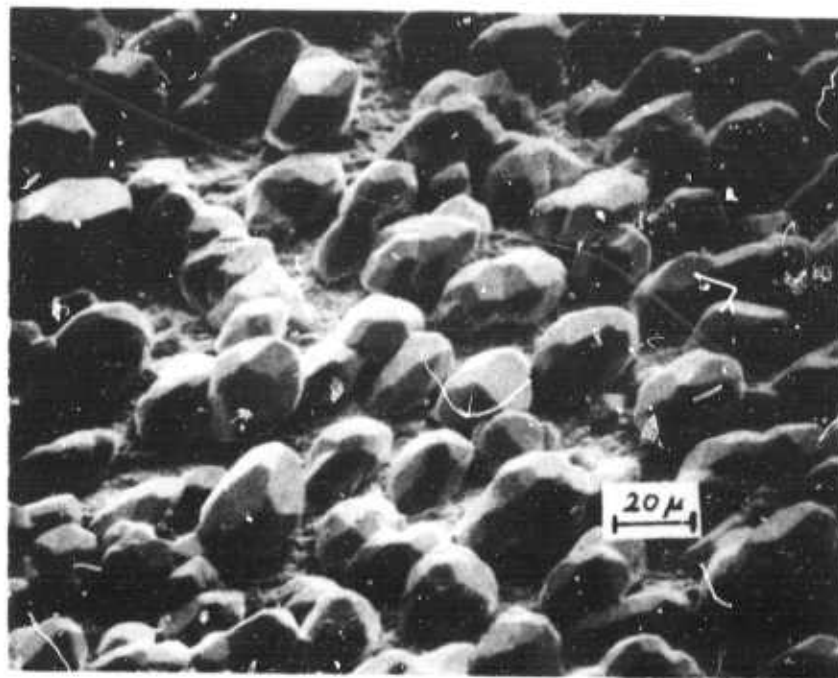


Figure 7. Typical molybdenum cathode and its Nb-Ge alloy coating. Strip width = 1 cm.

- (a) Full view. The deposit on the right side.  
(b) Vertical cross-section at the strip edge.

(a)



(b)

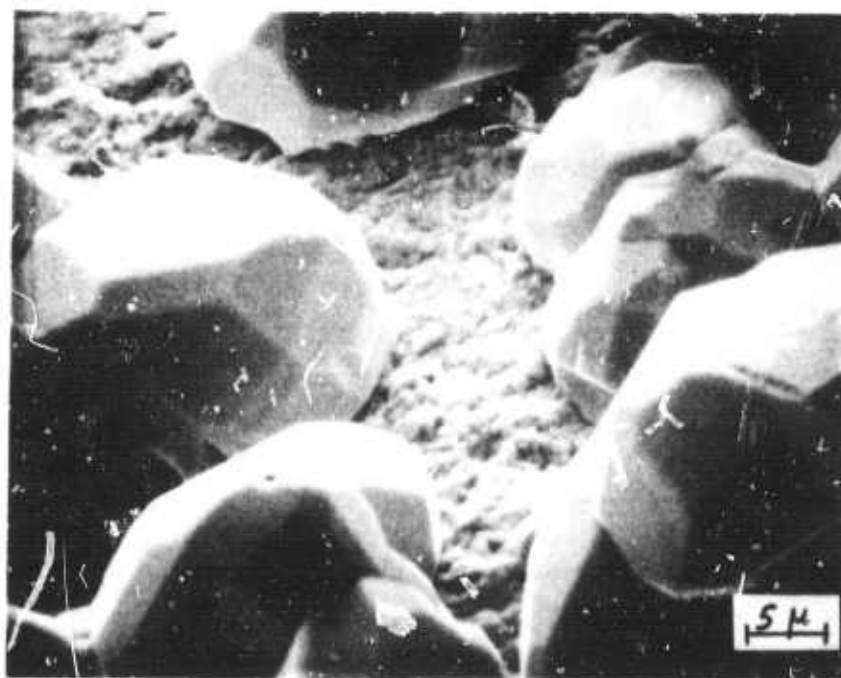
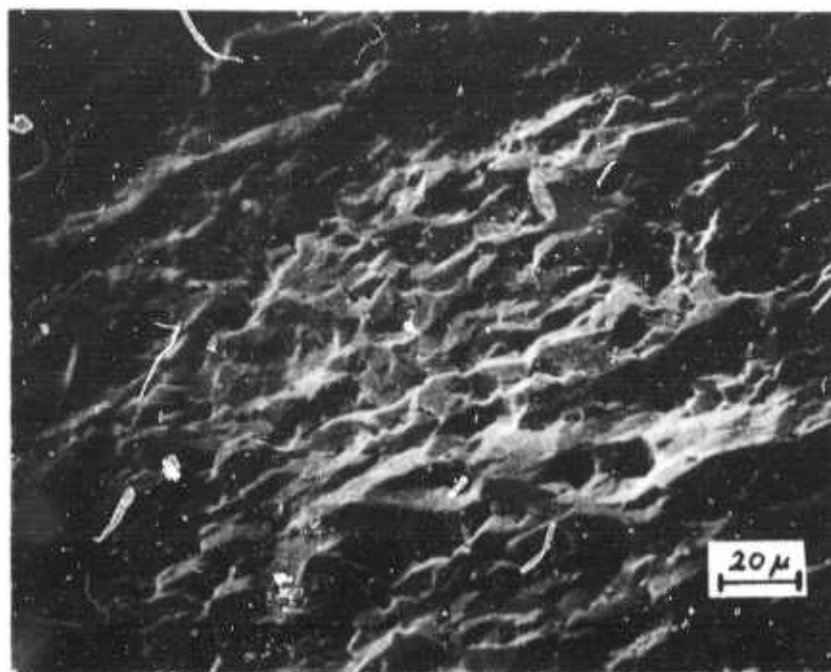


Figure 8. Scanning electron micrograph (SEM) of NbGe<sub>2</sub> coating surface.

(a)



(b)

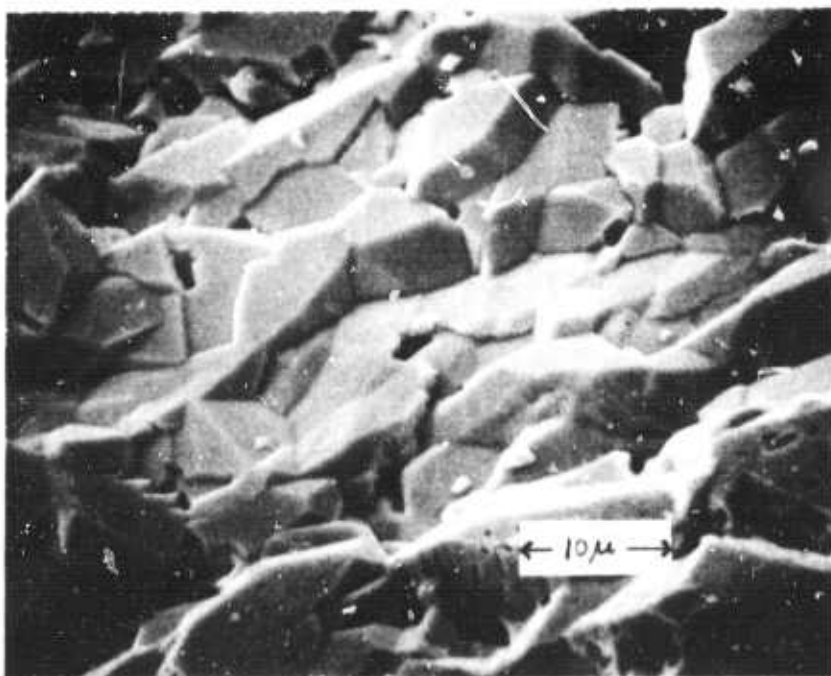


Figure 9. SEM of Nb<sub>3</sub>Ge<sub>2</sub> coating surface.

### Nb<sub>5</sub>Ge<sub>3</sub>

This compound was obtained from the low germanium concentration solutions by electroplating under a constant potential corresponding to the base of a single-step first cathodic wave, as in Fig. 6.

Figure 10 shows SEM photographs of this compound coating surface. Typical growth parameters were 5 mol. % K<sub>2</sub>NbF<sub>7</sub>, 0.04 mol. % K<sub>2</sub>GeF<sub>6</sub>, 710°C, and constant potential of -45 mV.

### Nb<sub>5</sub>Ge<sub>3</sub> - Nb<sub>3</sub>Ge Mixture

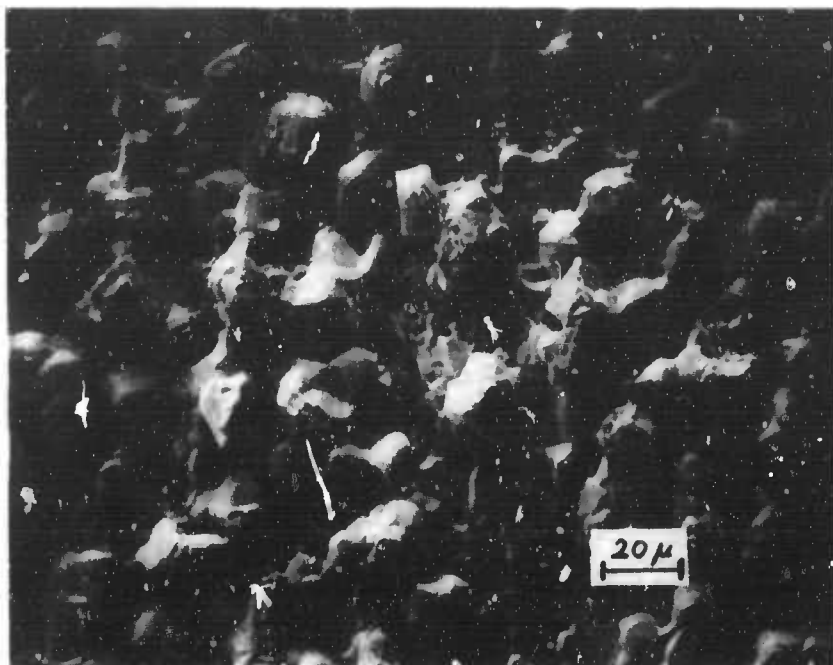
The mixture with Nb<sub>3</sub>Ge as the minor phase, was deposited under similar conditions to the deposition of Nb<sub>5</sub>Ge<sub>3</sub>. A higher temperature, however (815°C) was used. Fig. 11 shows SEM photographs of the deposit surface.

The Nb-Ge compounds thus obtained were characterized by x-ray diffraction, with lattice parameters being determined by a least square computer program. A comparison of the results with the bulk prepared materials, as reported in the ASTM X-ray diffraction file, is given in Table 1. The differences in the lattice parameters are believed to be due to different compound compositions, as the bulk preparation is a high temperature technique, whereas the electrodeposition is a relatively low temperature one.

#### (e) Morphology Control

Coherency and uniformity of electrodeposits begin to deteriorate as the rate of the electrodeposition is increased into the diffusion-controlled regime<sup>(20-21)</sup>. Improvement of the coating quality may be achieved by the increase of concentration, decrease of the deposition rate, agitation and sometimes by raising the temperature. The effect of diffusion-control may also be decreased by the application of reversal current<sup>(22-23)</sup>, or potentials<sup>(24-25)</sup>. Molten alkali fluorides, due to their high decomposition potentials, may be used for both electrodeposition and electropolishing. Application of anodic electropolishing pulses, as schematically shown in Fig. 12, was found to substantially increase the rate of the electrodeposition of coherent Nb coatings. Inconclusive results were obtained when the technique was applied to

(a)



(b)

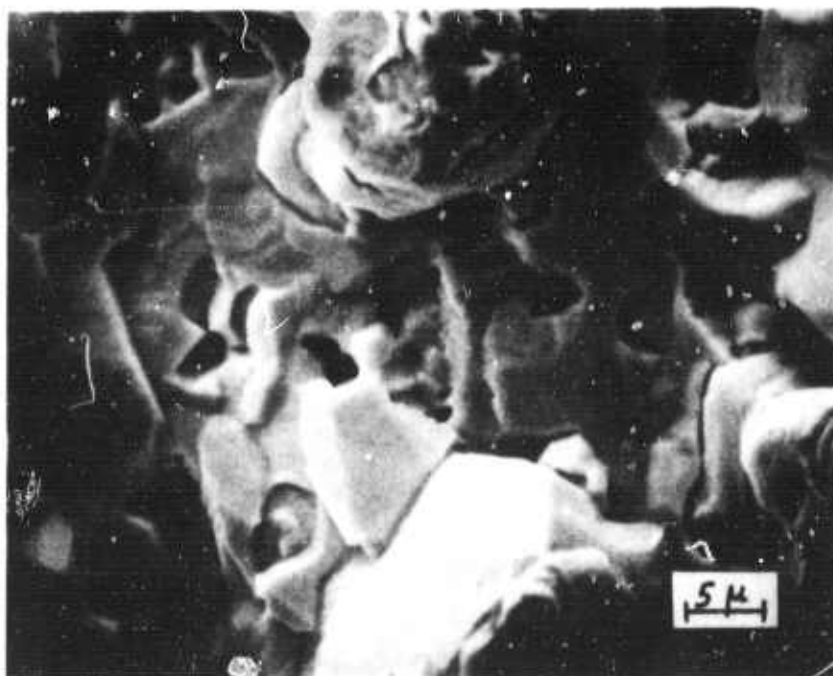
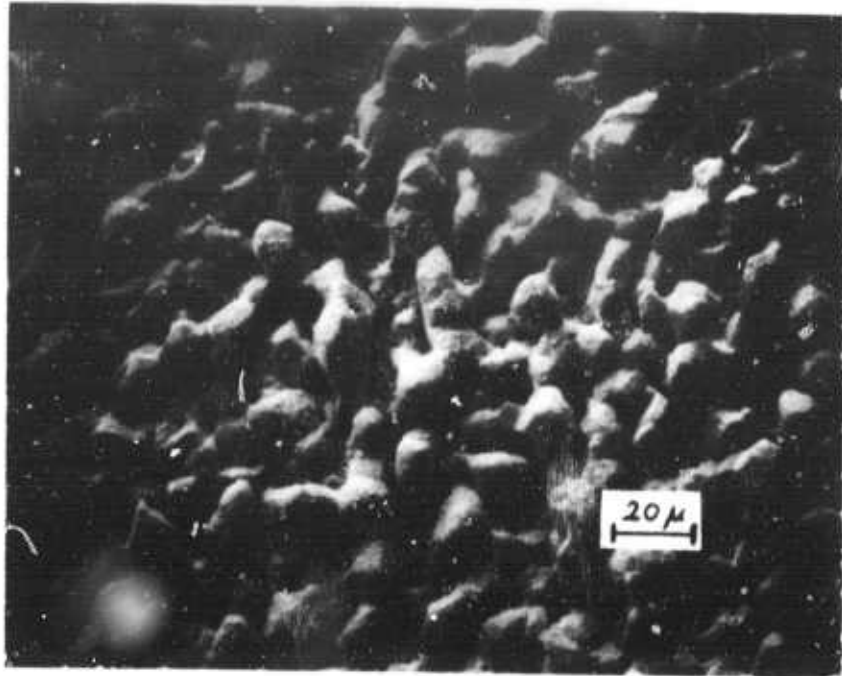


Figure 10. SEM of Nb<sub>5</sub>Ge<sub>3</sub> coating surface.

(a)



(b)

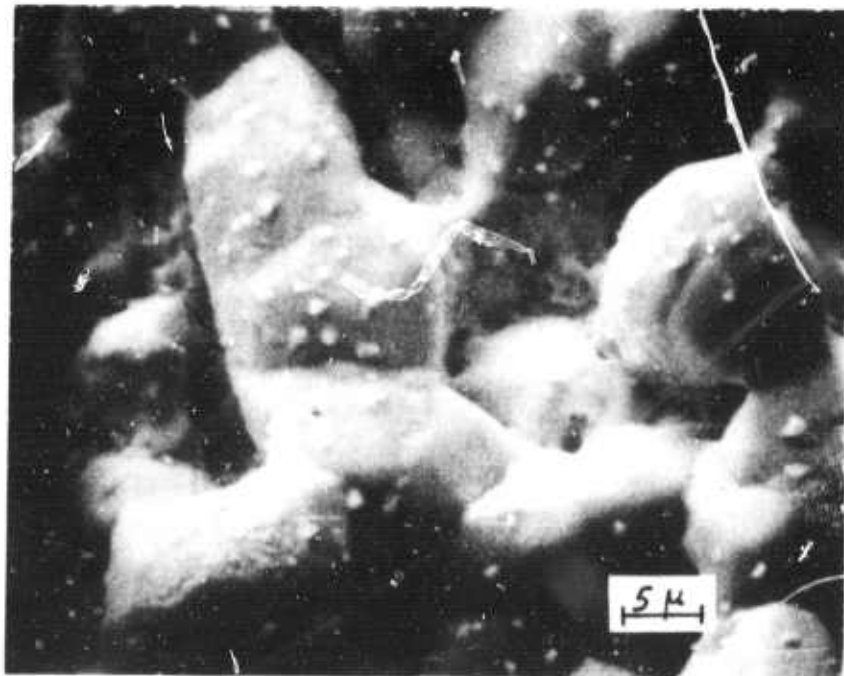


Figure 11. SEM of the mixture  $\text{Nb}_5\text{Ge}_3 + \text{Nb}_3\text{Ge}$  (minor) coating surface.

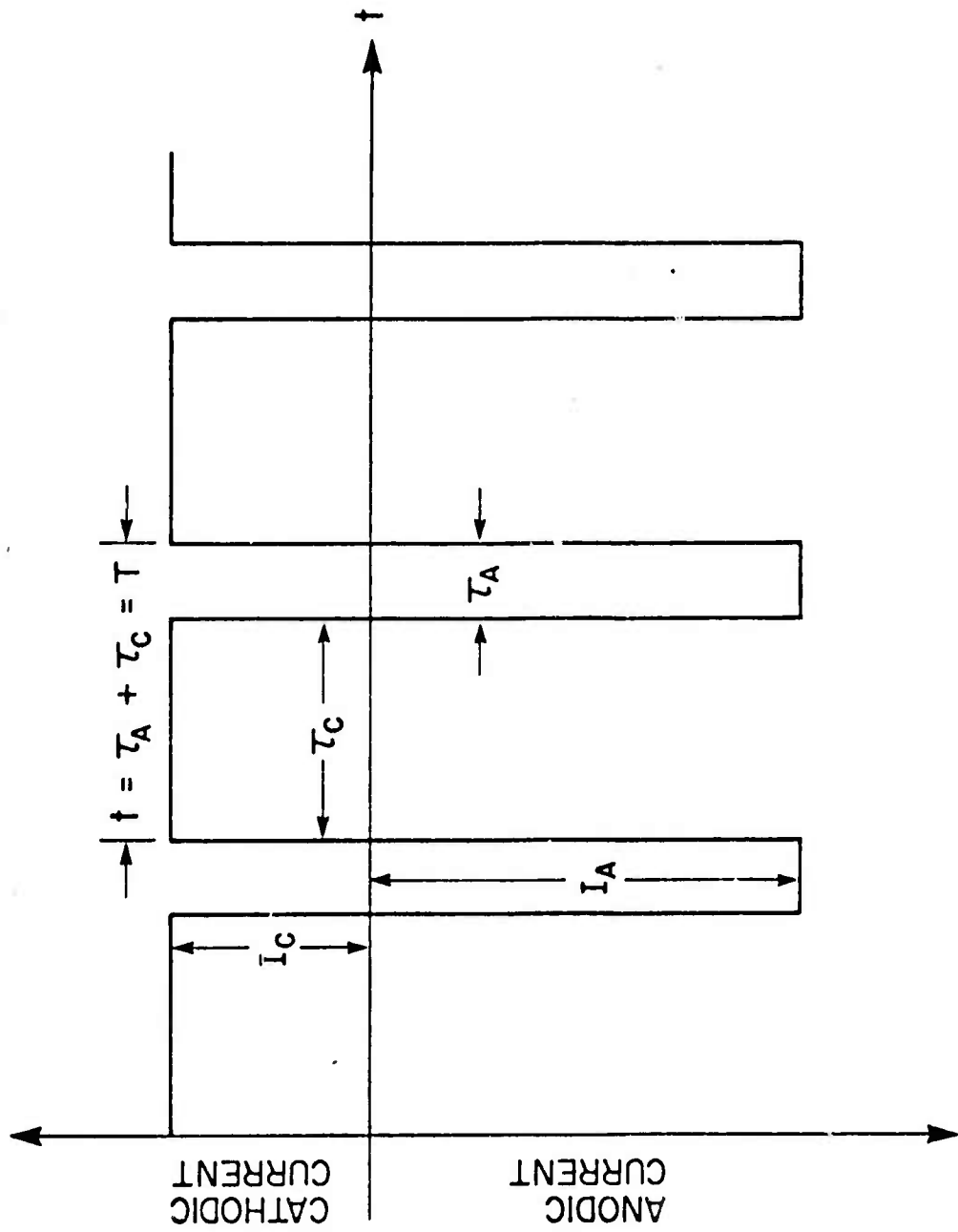


Figure 12. Reversal current square wave, and its parameter.

TABLE 1

Nb-Ge Compounds

	ASTM Reported (Bulk Prepared)	Present Work (Electrochemically Prepared)
$\text{Nb}_3\text{Ge}$	Cubic $a_o = 5.168\text{\AA}$	Cubic $a_o = 5.14 - 5.17\text{\AA}$
$\text{Nb}_5\text{Ge}_3$	Tetragonal $a_o = 10.148\text{\AA}$ $c_o = 5.152\text{\AA}$	Tetragonal $a_o = 10.149 \pm 0.005\text{\AA}$ $c_o = 5.085 \pm 0.010\text{\AA}$
$\text{Nb}_3\text{Ge}_2$	Hexagonal $a_o = 7.718\text{\AA}$ $c_o = 5.370\text{\AA}$	Hexagonal $a_o = 7.774 \pm 0.002\text{\AA}$ $c_o = 5.380 \pm 0.002\text{\AA}$
$\text{NbGe}_2$	Hexagonal $a_o = 4.966\text{\AA}$ $c_o = 6.781\text{\AA}$	Hexagonal $a_o = 4.964 \pm 0.006\text{\AA}$ $c_o = 6.786 \pm 0.009\text{\AA}$

the electrodeposition of Nb-Ge alloys. The difficulties encountered with the application of the technique to the Nb-Ge alloys are believed to be due to the separate stripping potentials of the various alloys. This separation is evident in any cyclic voltammogram of the first cathodic wave and the corresponding separated anodic peaks.

The rate increase is facilitated by the polishing of the newly formed interface protrusions created during the preceding cathodic pulse. Thus, the cathodic pulse may drive into the diffusion-controlled regime, giving rise to interface protrusions forming after some "initiation" period<sup>(21)</sup>. The protrusions are then taken off during the anodic polishing pulse, as schematically shown in Fig. 13. The next cathodic deposition starts again at a fresh smooth interface. The net growth is thus that which was deposited during the initiation periods.

Experiments to increase the deposition rate of Nb were performed with a solution of 6 mol. %  $K_2NbF_7$ , and at  $750 \pm 5$  °C. Cu strips of 1 cm width were used as cathodes, and a niobium sheet was used as a dissolving anode. Cu/Nb(IV), Nb(V) was used for a reference electrode. No mechanical agitation was used.

Anodic polarization curves failed to reveal the characteristic electropolishing plateau. Instead, linear curves were obtained up to current densities of  $10 \text{ A/cm}^2$ . This is in agreement with other works done on electropolishing in chloride and fluoride melts<sup>(26-27)</sup>.

Reversal potential pulses (shown in Fig. 14) as well as reversal current pulses (shown in Fig. 15) were examined. The deposit shown in Fig. 16 was grown by the application of the reversal potential square wave shown in Fig. 14. The average deposition current density on this sample was  $90 \text{ mA/cm}^2$ . The average dissolution anodic current density was  $110 \text{ mA/cm}^2$ . The Q-ratio for this sample was 4.0, where Q is defined by

$$Q = Q_C/Q_A = T_C i_C / T_A i_A$$

The wave parameters are defined in Fig. 12. Note the superior quality of this deposit and its polished and shiny appearance.

Fig. 17 shows another sample which was grown by the application of a reversal potential square wave. For this sample, however, the

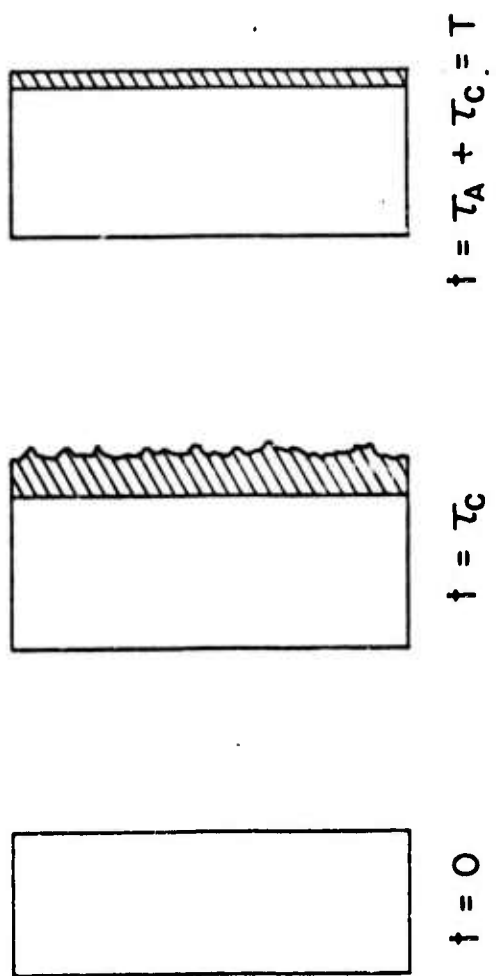


Figure 13. Schematic profile cross-section of the cathode and its coating.

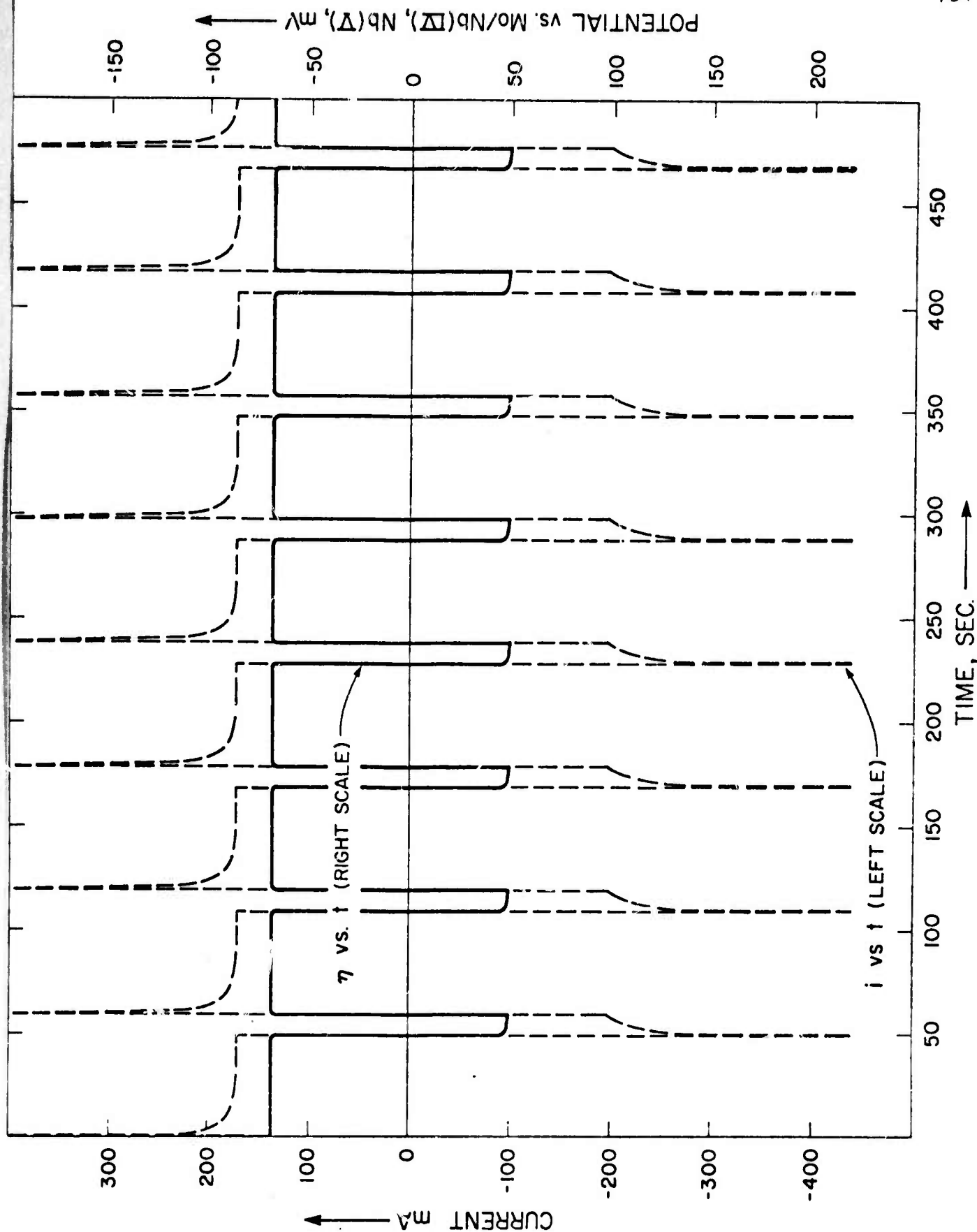


Figure 14. Reversal potential pulses for the deposition of Nb from 6 mol. %  $K_2NbF_7$  solution.

$\eta_c = -70$  mV,  $\eta_A = +50$  mV,  $t_c = 50$  sec,  $t_A = 10$  sec,  $Q \approx 4.0$

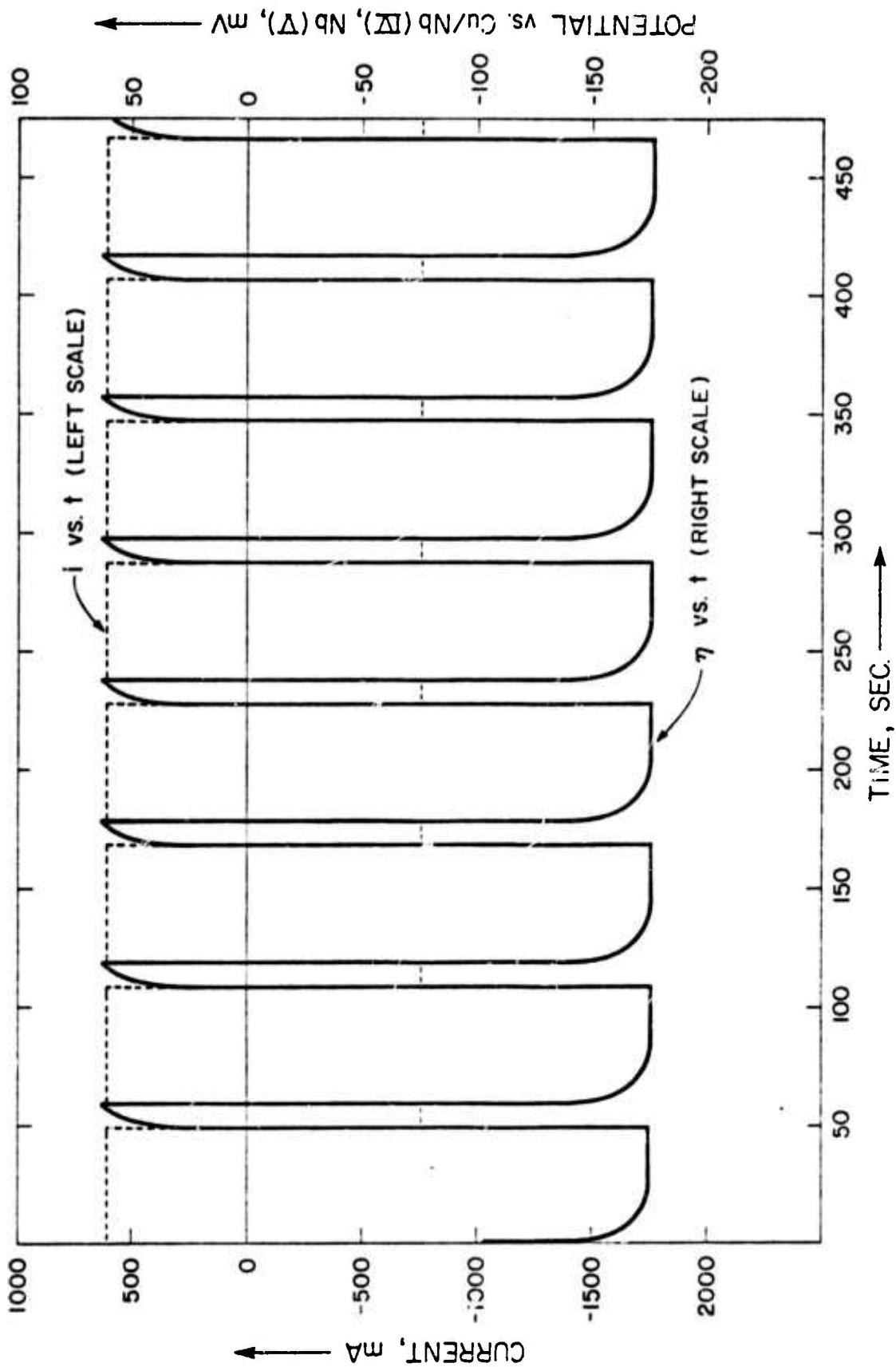
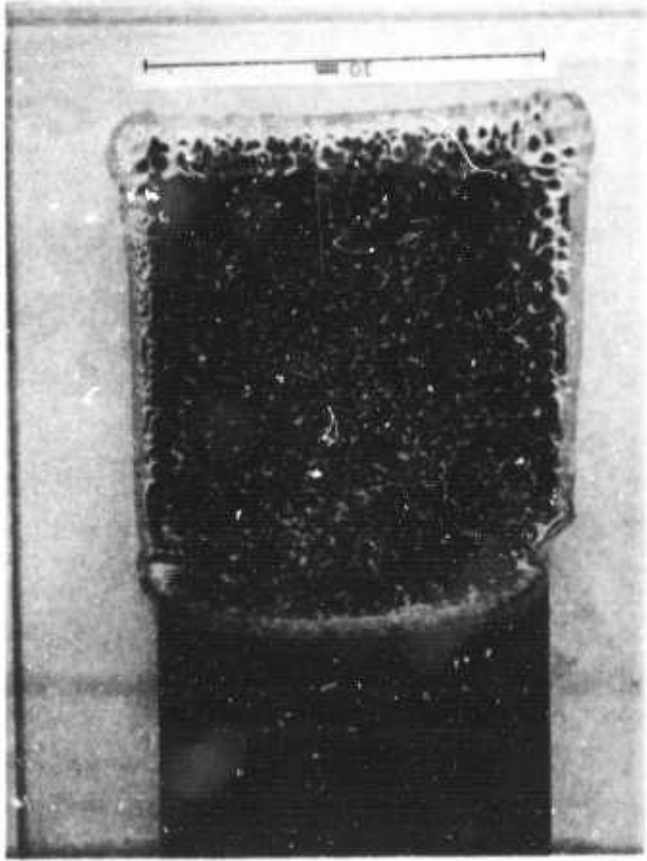


Figure 15. Reversal current pulses for the deposition of Nb from 6 mol. %  $K_2NbF_7$  solution.

$i_c = 600$  mA,  $i_A = 750$  mA,  $t_c = 50$  sec,  $t_A = 10$  sec,  $Q = 4.0$



(a)



(b)

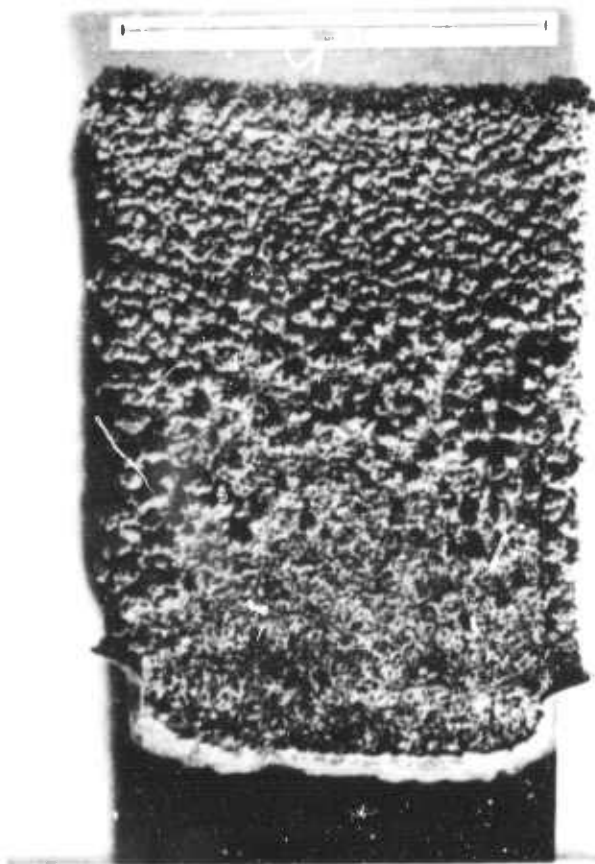


(c)

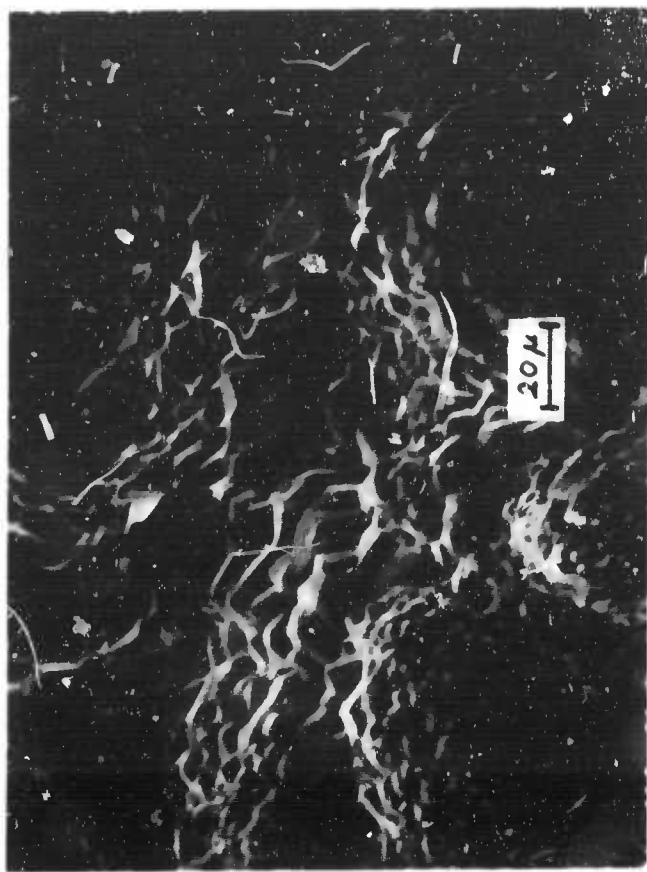
Figure 16. Nb coating obtained by reversal potential pulses.

$\eta_c = -70$  mV,  $\eta_A = +50$  mV,  $t_c = 50$  sec,  
 $t_A = 10$  sec,  $Q = 4.0$

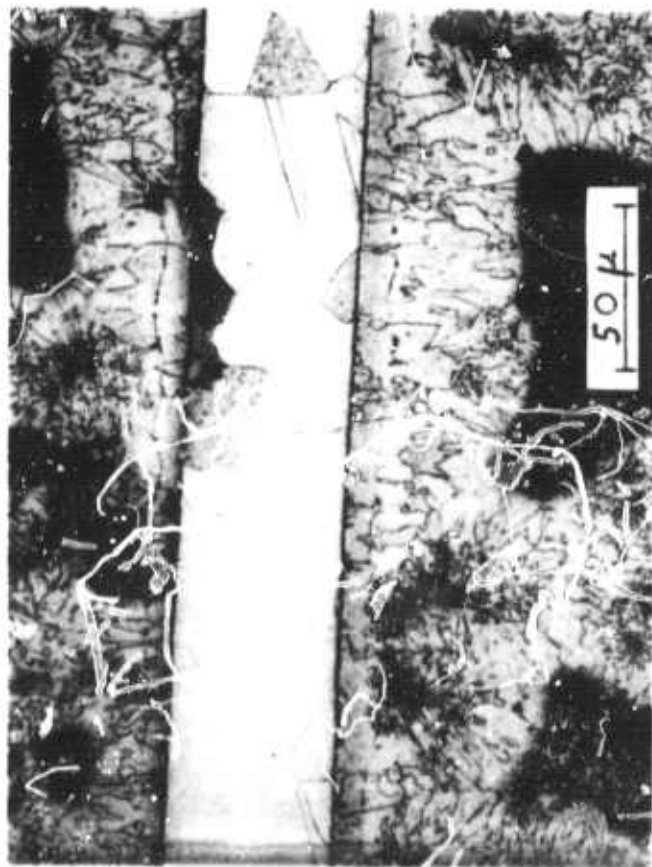
(a) full view, (b) SEM photograph,  
 (c) vertical cross-section



(a)



(b)



(c)

Figure 17. Nb deposit obtained by reversal potential pulses.

$v_c = -155$  mV,  $r_A = 5$  mV,  $t_c = 50$  sec,  
 $t_A = 10$  sec,  $Q = 8.0$

(a) full view, (b) SEM photograph,  
(c) vertical cross-section

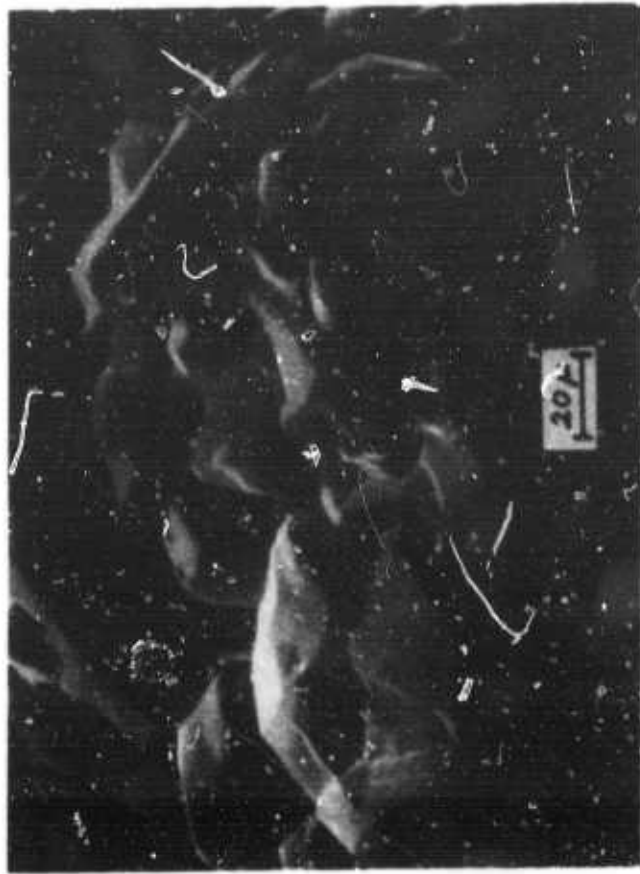
average deposition current density was  $300 \text{ mA/cm}^2$ , and  $Q = 8.0$ . Note the bad morphology of this deposit: the large grains with poor filling and coherency. The more the deposit grows, the worse its quality becomes.

Reversal current square waves offer a better control of Q-ratio as the currents do not drift during the deposition run. Figs. 18 and 19 show the effect of reducing the Q-ratio. The sample shown in Fig. 18 had  $Q = 4.0$ , and this of Fig. 19 had  $Q = 2.0$ . Both samples were grown with identical cathodic current densities,  $i_c = 300 \text{ mA/cm}^2$ .

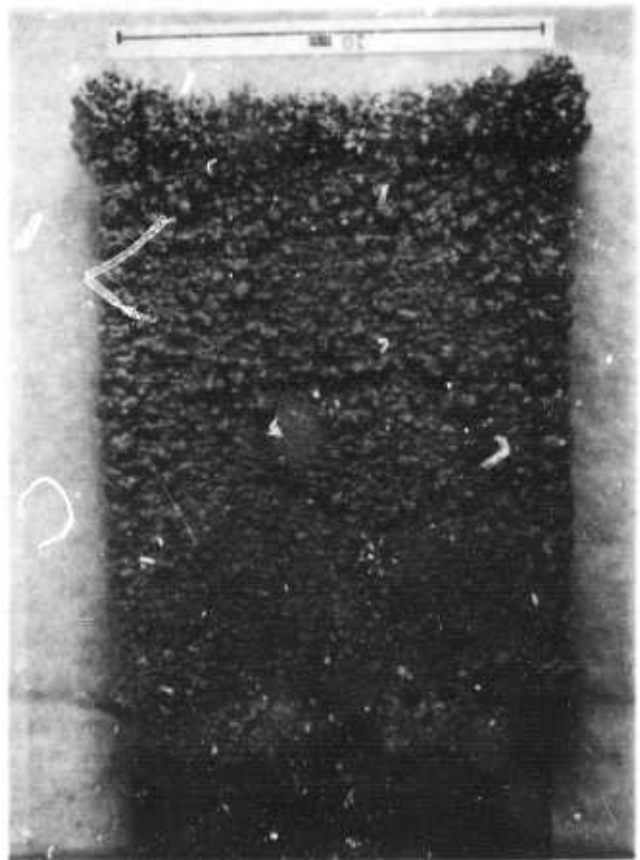
The most important parameter seems to be the Q-ratio. The closer its value to unity, the better the coherency and smoothness of the deposit. In general, potential pulses offer less control of the morphology, due to the drift of the currents and Q-ratio during the run. It is desirable to employ anodic pulse amplitudes as high as possible, to ensure electropolishing rather than electroetching. (Note the pits in the sample of Fig. 16.) Anodic current densities in excess of  $100 \text{ mA/cm}^2$  were found essential for successful polishing. The pulse periods  $T_C$  and  $T_A$  were found to have greatest influence through their influence on the Q-ratio.

Very long periods,  $T_C > 1 \text{ min.}$  are deleterious, due to the formation of large protrusions, which can not be removed by electropolishing. The frequency was found to have only a small effect. Increasing the frequency showed limited improvement in the deposit coherency and brightness. See Fig. 20.

Constant current experiments were performed for comparison. The sample shown in Fig. 21 was prepared by pre-electrolysis at a constant cathodic current density of  $3.3 \text{ mA/cm}^2$ . The deposit is of high quality and coherency. It is preferentially oriented along the [100] direction, and is of dull appearance. The typical pyramidal morphology is believed to be due to the adsorption of impurities during the pre-electrolysis. Application of a constant current density of  $5 \text{ mA/cm}^2$  to the pure solution yielded the sample shown in Fig. 22. Application of a constant cathodic current density of  $25 \text{ mA/cm}^2$  resulted in a deteriorated deposit of thickness-limited nature, as shown in Fig. 23.



(b)



(a)



(c)

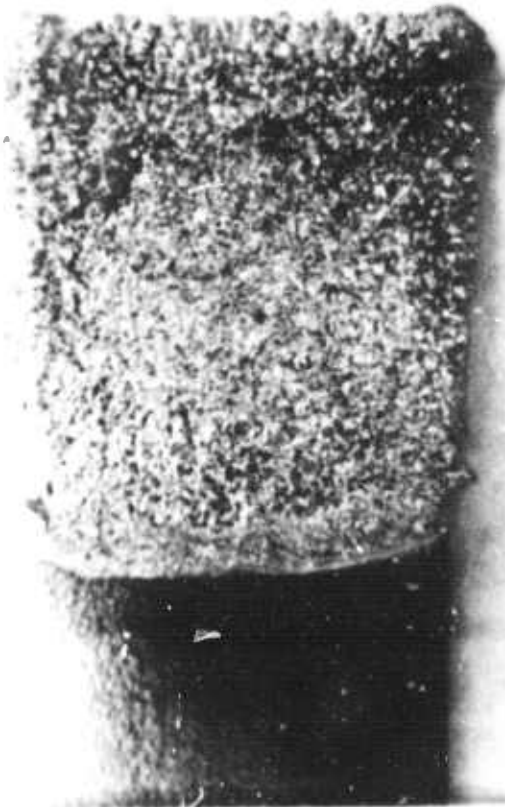
Figure 18. Nb deposit obtained by reversal current pulses.

$i_c = 600 \text{ mA}$ ,  $i_A = 750 \text{ mA}$ ,  $t_c = 50 \text{ sec}$ ,  
 $t_A = 10 \text{ sec}$ ,  $Q = 4.0$

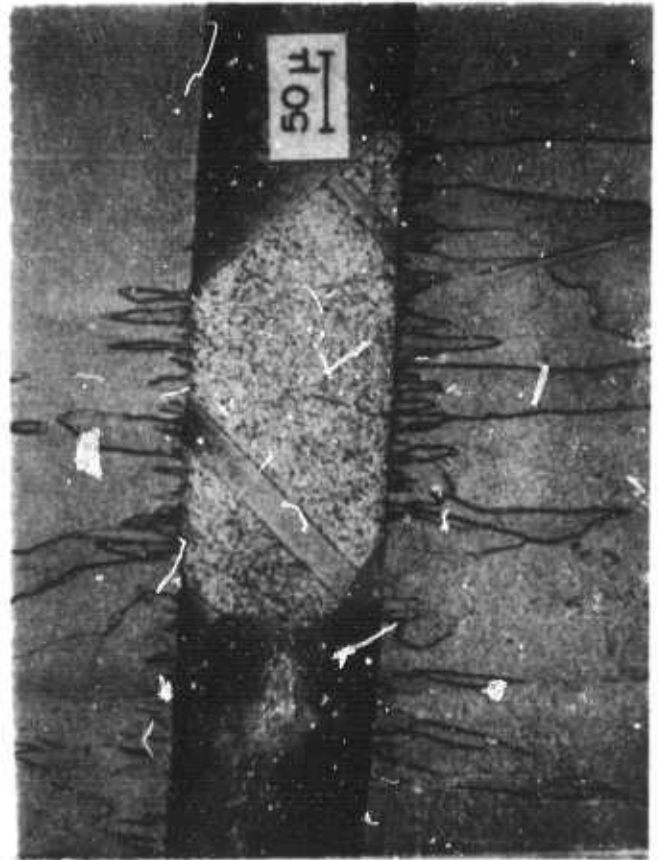
(a) full view, (b) SEM photograph,  
 (c) vertical cross-section



(b)



(a)

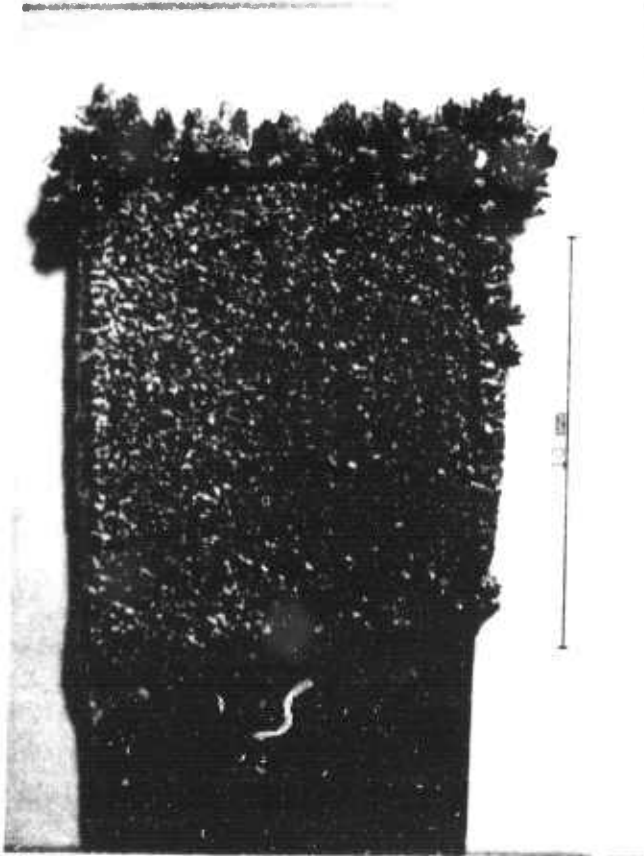


(c)

Figure 19. Nb deposit obtained by reversal current pulses.

$i_c = 600 \text{ mA}$ ,  $i_A = 750 \text{ mA}$ ,  $t_c = 25 \text{ sec}$ ,  
 $t_A = 10 \text{ sec}$ ,  $Q = 2.0$

(a) full view, (b) SEM photograph,  
 (c) vertical cross-section



(a)



(b)



(c)

Figure 10. Nb deposit obtained by reversal current pulses. As in Figure 19, but at 10 times higher frequency.

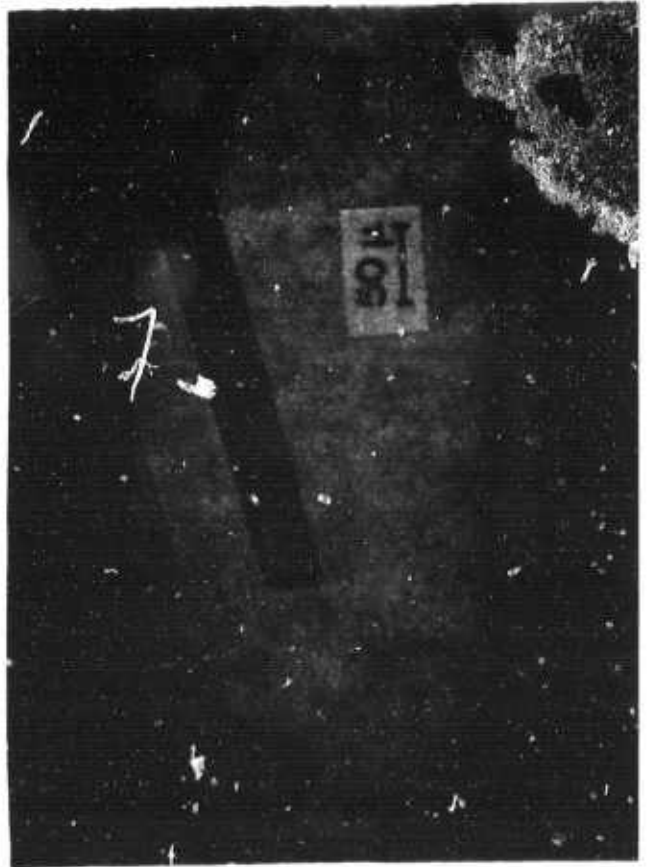
(a) full view, (b) SEM photograph, (c) vertical cross-section



(b)



(a)



(c)

Figure 21. Nb deposit obtained by steady-state current pre-electrolysis.

$i_c = 10 \text{ mA (5 mA/cm}^2\text{)}$ .

(a) and (b) SEM photographs,  
(c) vertical cross-section

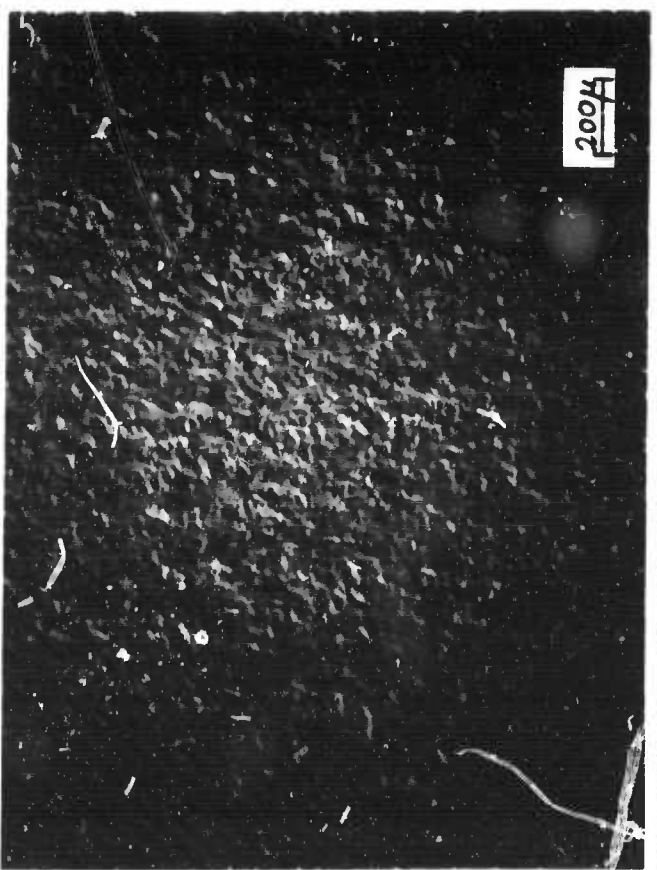


Figure 22. Nb deposit obtained at constant current density of 5 mA/cm<sup>2</sup>. Mo substrate, pure solution. SEM photographs.

(a)

(c)

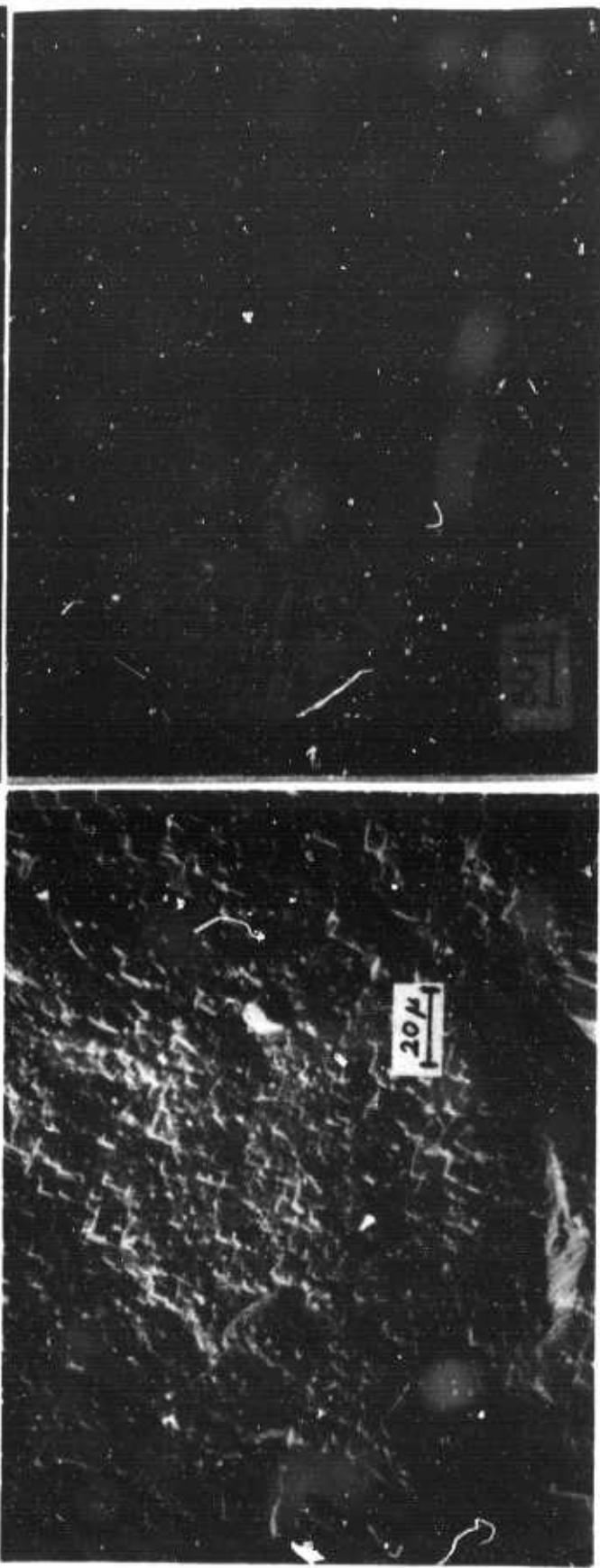
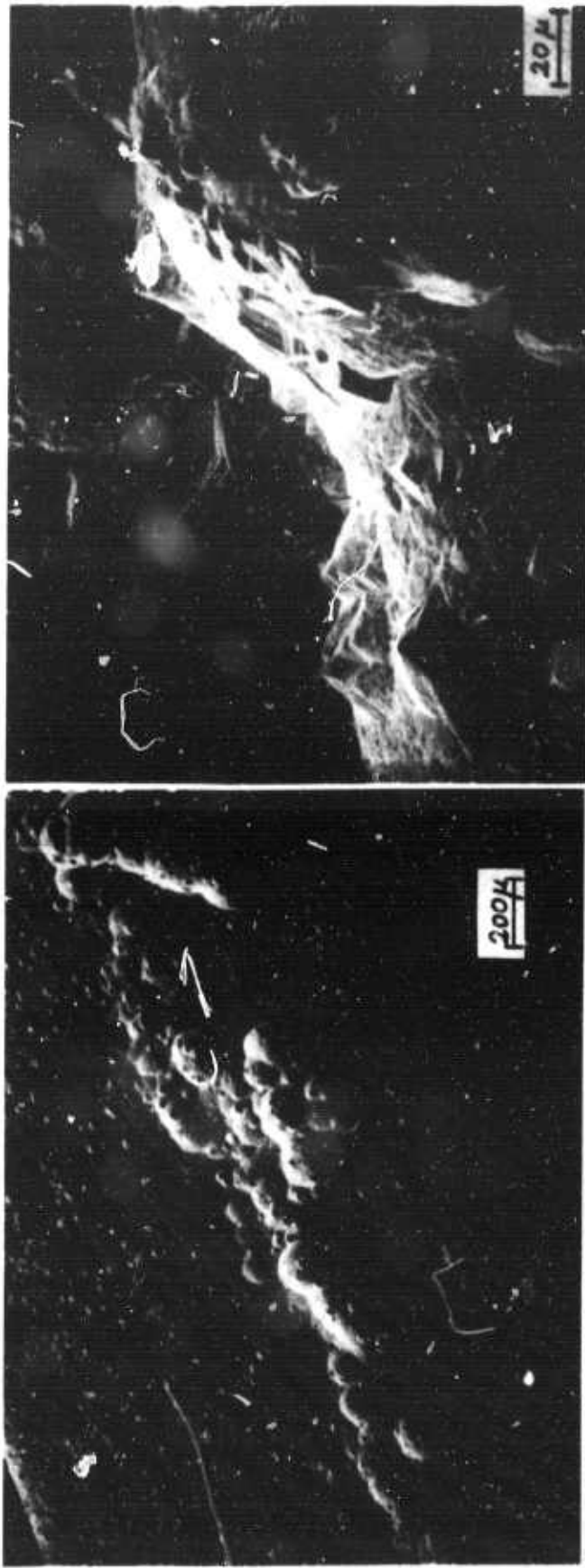


Figure 23. Nb deposit obtained by steady-state current,  $i = 50 \text{ mA (} 25 \text{ mA/cm}^2 \text{)}$ . (a) and (b) SEM of deteriorating surface. (c) SEM of smooth area. (d) vertical cross-section.

(a)

(b)

(c)

(d)

It is concluded that the reversal pulse technique for Nb electro-deposition may offer a rate increase by a factor of 10-50 over the steady-state current technique in molten fluoride baths.

(f) Silicon Epitaxy

Electrocrystallization Epitaxy (ECE) of Si was achieved for the first time. A solution containing 5 mol. % of  $K_2SiF_6$  in the KF-LiF eutectic and an operating temperature of  $750^\circ C$  were utilized. A high purity Si sheet was used as a dissolving anode, and a single-crystal Si wafer of the (111) orientation was the substrate. The substrate was mirror polished, and of n-type (resistivity  $\sim 10 \Omega\text{-cm}$ ).

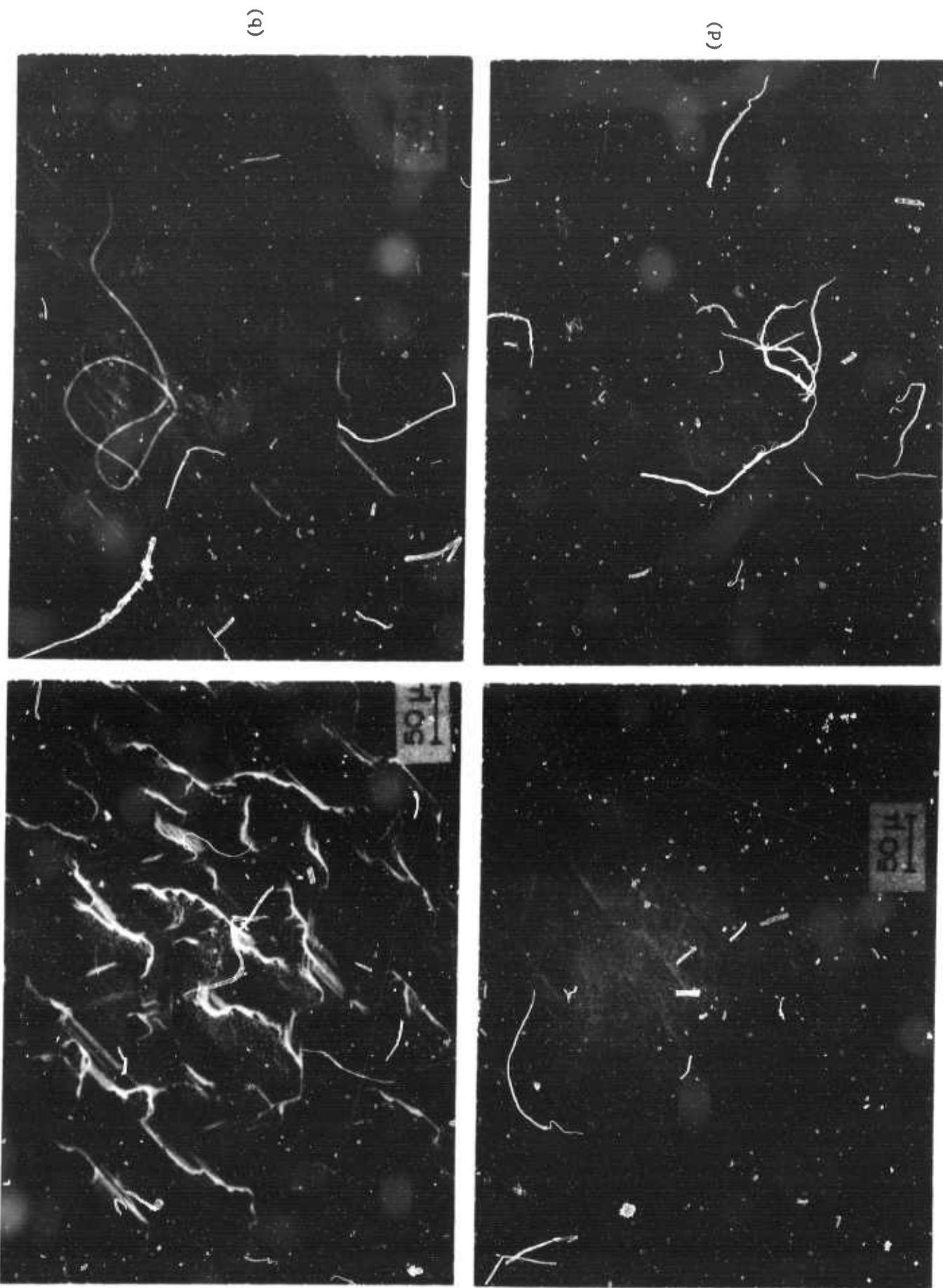
The grown layers were found to be of p-type ( $\rho \approx 0.04 \Omega\text{-cm}$ ). No impurities could be detected by either electron microprobe or Auger spectroscopy. The current density was found to have an important influence upon the morphology of the deposit. Fig. 24 shows SEM photographs of samples which were grown at 1, 2, 4, and  $6 \text{ mA/cm}^2$ . The improvement obtained with the increase of the current density is believed to be due to the favoring of step propagation, while the adsorption rate is constant for a given impurity concentration. It is believed that the adsorption of foreign species hinders the propagation of kinks and steps.

Electroplating at  $10 \text{ mA/cm}^2$  resulted in an epitaxial layer of  $\sim 10 \mu$  thickness covered with polycrystalline deposit.

4. Conclusions and Future Plans

(a) Nb-Ge alloys may be simultaneously co-deposited into high quality coatings from the molten fluoride baths. The compounds  $NbGe_2$ ,  $Nb_3Ge_2$ , and  $Nb_5Ge_3$  were prepared as single-phase coatings. Binary-phase mixtures, including the mixtures  $Nb_5Ge_3 - Nb_3Ge$  and  $Nb_3Ge - Nb$  were also prepared.

(b) The compound  $Nb_3Ge$  has not yet been electro-deposited as a single phase coating. It is believed that the difficulties in its preparation result from either a too small value of the solution activities ratio  $a_{Nb(IV)}/a_{Ge(IV)}$ , or from thermodynamical<sup>(28)</sup> instability of the pure phase.



(a)

(b)

(c)

(d)

Figure 24. SEM photographs of (111) Si epitaxial layers grown at (a) 1 mA/cm<sup>2</sup> (10 μ thick), (b) 2 mA/cm<sup>2</sup> (10 μ thick), (c) 4 mA/cm<sup>2</sup> (2 μ thick), (d) 6 mA/cm<sup>2</sup> (10 μ thick).

(c) Electrochemical investigations have produced valuable information. The (hypothetical) standard electrode potential for Ge deposition from the KF-LiF solution containing  $K_2NbF_7$  and  $K_2GeF_6$ , is  $E_{Ge}^{\circ} = -0.114$  volts versus the Mo/Nb(IV), Nb(V) electrode. For comparison, the value  $E_{Nb}^{\circ} = -0.05$  volts was calculated from the data<sup>(15)</sup> for the deposition reaction  $Nb(IV) + 4e^- = Nb$  (versus the redox couple potential). The reaction is reversible and involves the transfer of  $n = 4$  electrons. The diffusion coefficient of the tetravalent species are  $D_{Ge(IV)} = 3.8 \times 10^{-6}$  cm<sup>2</sup>/sec, and  $D_{Nb(IV)} = 5.4 \times 10^{-5}$  cm<sup>2</sup>/sec. The niobium deposition reaction is activation-controlled, and obeys the Tafel law with  $i_0 = 12$  mA/cm<sup>2</sup>, and  $\beta = 0.053$  volts. The solution resistivity (at 750°C), as estimated from iR-drop measurements, is  $\delta = 0.03$  ohm-cm.

(d) The electrodeposition rate of niobium coatings was substantially increased by the application of alternating square wave current or potential pulses. An improvement by a factor of 10-50 over the constant-cathodic current technique was found with no mechanical agitation. The technique is inherent in the electrodeposition process, and could be easily applied to any substrate shape. In contrast, external auxiliary techniques, such as mechanical agitation (stirring or bubbling) or ultrasonic vibrations may leave dead areas on the substrate of poor solute supply, and other areas of enhanced supply, thus varying the morphology and uniformity of the coatings.

(e) The application of square wave pulses to the deposition of the Nb-Ge alloys requires further study. The difficulties which are encountered result from the separated anodic stripping potentials of the various Nb-Ge compounds. The technique, if successful, will permit a substantial increase in the deposition rate. It may even prove to be useful for a selective preparation of certain compounds.

(f) The feasibility to epitaxially grow Si by the ECE technique has been established. High quality layers of better than 99.99% purity have been obtained, with good control of the thickness. The technique may offer very attractive features for the production of inexpensive

solar cells on low grade Si substrates." The low operating temperature (750°C) should minimize the diffusion of impurities from the underlying substrates. Other possible advantages for use in integrated circuit technology are described elsewhere<sup>(19)</sup>.

(g) A further investigation of the possibility of preparing multi-layered deposits of alternating compounds will be performed. Initial experiments in this field show good prospects. The idea is to prepare the alternating phases by stepping or sweeping the potential (or current) between the potentials corresponding to the desired compounds. Another possibility is to use a selective stripping process for this purpose. The multi-layered deposition may have a great technological importance, since two-dimensional superconductors are expected to possess unique properties. The process, if feasible, will allow great flexibility (not to be found in other technique) in controlling the number of layers, and their thicknesses. Full control will then be obtained by electronic signals, which can be easily programmed for the desired frequency, pulse, duration and magnitude.

5. References

- (1) J. E. Cavalier, Appl. Phys. Lett. 23, 280 (1973).
- (2) L. R. Testardi, J. H. Wernick and W. A. Foyer, Solid State Commun. 15, 1 (1974).
- (3) J. J. Hanak, Metallurgy of Advanced Electronic Materials, Ed., G. E. Brock, Interscience, Inc., New York (1963).
- (4) R. E. Enstrom, J. J. Hanak and G. W. Cullen, R.C.A. Review 31, 702 (1970).
- (5) A. Echarrri and M. Spadoni, Cryogenics 11, 274 (1971).
- (6) A. R. Kaufmann and J. J. Pickett, J. Appl. Phys. 42, 58 (1971).
- (7) M. Suenga and W. B. Sampson, Appl. Phys. Lett. 18, 584 (1971).
- (8) K. Tachikawa, Y. Yoshida and L. Rinderer, J. Mater. Sci. 7, 1154 (1972).
- (9) B. T. Matthias, T. H. Geballe and V. B. Compton, Rev. Mod. Phys. 35, 1 (1963).
- (10) G. W. Mellors and S. Senderoff, J. Electrochem. Soc. 112, 266 (1965).
- (11) S. Senderoff and G. W. Mellors, J. Electrochem. Soc. 112, 841 (1965).
- (12) G. W. Mellors and S. Senderoff, Ibid. 113, 60 (1966).
- (13) G. W. Mellors and S. Senderoff, Ibid. 113, 66 (1966).
- (14) G. W. Mellors and S. Senderoff, Ibid. 114, 586 (1967).
- (15) G. W. Mellors and S. Senderoff, Ibid. 118, 220 (1971).
- (16) C. Decroly, A. Mukhtar and R. Winand, Ibid. 115, 905 (1968).
- (17) U. Cohen, Ph.D. Dissertation, Stanford University (1976).
- (18) U. Cohen, "Electrodeposition of Niobium Alloys Superconductors from Molten Fluorides", in Long Range Materials Research, DAHC 15 75 G15, First Annual Technical Report, CMR, Stanford (1974).
- (19) U. Cohen and R. A. Huggins, "Silicon Epitaxial Growth by Electrodeposition from Molten Salts", presented at the ECS Meeting (#RNP259), Dallas, Texas, October 5-10, 1975. Also to be published in the J. Electrochemical Society 123, 381 (1976).
- (20) A. R. Despic, J. W. Diggle and J. O'M. Bochriss, J. Electrochem. Soc. 115, 507 (1968).
- (21) J. W. Diggle, A. R. Despic and J. O'M. Bochriss, J. Electrochem. Soc. 116, 1503 (1969).

- (22) G. T. Bakhvalov, "New Technology of Electrodeposition of Metals", Metallurgy (1966).
- (23) S. Arouete, K. F. Blurton and H. S. Oswin, J. Electrochem. Soc. 116, 166 (1969).
- (24) A. R. Despic and K. I. Popov, J. Appl. Electrochem. 1, 275 (1971).
- (25) A. R. Despic and K. I. Popov, in Modern Aspects of Electrochemistry, Vol. 7, Eds. B. E. Conway and J. O'M. Bochriss, Plenum Press, New York, New York (1972), p. 295.
- (26) P. R. Rowland, Nature 171, 931 (1959).
- (27) D. P. Brouillet and I. Epelboin, Rev. Met. 51, 693 (1954).
- (28) T. H. Geballe and A. B. Hallak, private communications.